A detailed hydrologic evaluation of tile-drained macroporous soils: A field and modelling study

by

Steven K. Frey

A thesis
presented to the University of Waterloo
in fulfillment of the
thesis requirement for the degree of
Doctor of Philosophy
in
Earth Sciences

Waterloo, Ontario, Canada, 2011

Author’s Declaration

I hereby declare that I am the sole author of this thesis. This is a true copy of the thesis, including any required final revisions, as accepted by my examiners.

I understand that my thesis may be made electronically available to the public.

Abstract

The underlying objective of this research is to improve the overall understanding of how spatial and temporal variability in macroporosity and soil hydraulic properties in the shallow subsurface influence the long term mobility of agricultural nutrients, and specifically the movement of liquid swine manure, in macroporous, tile drained soils. The principal motivation for the work was to provide insight into dynamic nutrient mobility in this type of agricultural environment in order to guide both the efficiency and environmental sustainability of nutrient management practices. The results of this work facilitate the advancement of our conceptual understanding and our ability to simulate preferential flow and transport in structured agricultural soils that are subject to seasonal hydrologic patterns similar to those found in the humid continental climate of southwestern Ontario.

In order to quantitatively assess impacts of preferential flow on surface and groundwater resources, knowledge of macropore geometry and spatial variability is required. At the primary field research site for this work, near Kintore Ontario, investigations were conducted on: plot scale spatial relationships between macroporosity and tile drains, intra-field variability in macroporosity, and macroporosity/hydraulic conductivity (K) correlations. Results from the macroporosity characterization show that tile drains do not significantly influence lateral macropore distribution; however, macroporosity did vary significantly throughout the single field where the work was conducted. In addition, macroporosity was found to be much greater in the top 0.5 m of the soil profile than at tile depth, which ranged from 0.7 to 1.0 m. In general, smaller macropores were most abundant in the A horizon while larger macropores were most abundant near the top of the B horizon. It was also found that the hydraulic conductivity of both the A and B horizons were most strongly correlated with macroporosity in the 0.45 to 0.75 m depth interval. At two of the three locations investigated, dye infiltration patterns revealed that 20+ year old tile installation scars were actively channeling infiltrate from the surface to tile drains.

Preferential flow in structured agricultural soil is also heavily influenced by significant temporal and spatial variability in soil hydraulic properties. As part of the work conducted at Kintore, a series of tension and double ring infiltration tests were performed during relatively wet, and dry, soil conditions to elucidate the influence of both tile drains and soil moisture content on saturated and unsaturated soil hydraulic properties and soil structure. At each infiltration test location, comparisons were made between visible, and hydraulically effective (HE) macroporosity. Results from the infiltration tests show that field saturated hydraulic conductivity (K_{fs}) was greatest over the tile drains at the locations with relatively low B horizon permeability; however, where the B horizon permeability was relatively high, K_{fs} increased away from the tile drains. Although the unsaturated soil hydraulic properties were not influenced by the local presence of tile drains, they were subject to significant temporal variability. The HE macropore size distribution was also observed to have significant temporal variability. During relatively dry soil conditions, total HE macroporosity, and HE macroporosity attributable to small pores was less than during wetter soil conditions; conversely, HE macroporosity attributable to larger pores and K_{fs} were both greater when the soil was drier. In general, near surface HE macroporosity was approximately 100 times lower than the visible macroporosity.

In addition to detailed site characterization, a tracer experiment was also conducted at Kintore to quantify the potential for short and long term nutrient loss to tile drainage after a fall liquid manure application. As part of the experiment, bromide and chloride tracer solutions were applied over two parallel strips of soil adjacent to a tile drain. Following tracer application, the area was irrigated for nine hours to replicate heavy precipitation. The tracers were applied in early November 2007 and tracer concentrations in the tile discharge were subsequently monitored for 1 year. Bromide (which was applied directly beside the tile) reached the tile drain within 1 hour of application, thus indicating that preferential flow and transport processes were active; however, there was no noticeable increase in chloride (which was applied 2.3 m from the tile) concentration in the tile effluent over the entire one year monitoring period. By September of 2008, bromide was not regularly detected in the tile effluent and soil cores were extracted to determine the residual tracer mass stored in the soil profile. Mass balance calculations indicate that practically all of the bromide was accounted for over the course of the year, with the bulk (>98 %) being captured by the tile. Although very little (<10 %) of the surface applied bromide reached the tile quickly (within 48 hrs) following application; the majority of the total applied bromide reached the tile by April 1, 2008. Winter melts were most important influence on bromide movement to the tile drain and approximately 25 % of the total bromide mass was discharged during a single 10 day event in January 2008. Results from the tracer test indicate that the majority of soluble nutrients applied within approximately 2 m of tile drains, during fall liquid manure applications, will potentially be transported to surface water prior to the following growing season, and that winter and spring melt events are responsible for most of the soluble nutrient flux between tile drained agricultural land and surface water.

While water and solutes are typically used to characterize flow and transport processes in field soils, there is a scarcity of information regarding how these same processes influence the movement of liquid manure through macroporous soils in tile drained fields. To investigate this question, viscosity dependant, dual-permeability, flow and transport models were developed and employed to simulate liquid swine manure application experiments that were conducted on macroporous, tile drained soils near Sebringville Ontario. Using data from the field experiment as a benchmark for the models, simulations were conducted to establish how ammonium and phosphate are transported and ultimately distributed between tile drains, groundwater, and the unsaturated zone, in response to surface banding and subsurface injection manure application techniques, and different manure loading rates. Simulation results show that surface banding increases the shallow lateral distribution of both ammonium and phosphate, while injection application increases the vertical distribution. With injection application, higher application rates induce more rapid transport of ammonium and to a lesser degree phosphate to the tile drain. When the primarily vertical orientation of the macropores is considered, the tile drain rapid capture zone is limited to a narrow region immediately overlying the tile. The models also show that increasing liquid manure viscosity can result in a significant reduction in the amount of nutrients transmitted to tile drains shortly after application. As a result, fluid properties of the manure of interest need to be considered when assessing potential environmental risks associated with liquid manure land application.

Acknowledgements

Perhaps most notably, I would like to thank my advisor, Dr. David Rudolph, for his guidance and support over the 5 plus years I have spent at Waterloo. Although it occasionally seemed as though I was given extraordinary leeway to investigate anything with any perceived relevance to the general subject of hydrogeology, macropores, and tile drains; the end product of my efforts is a thesis that largely incorporates thoughts and ideas that Dave and I discussed very early on in the work. Upon reflection, I can only recall two instances where he reined in my grand schemes, and had I been left to my own devices in either instance, I would still quite literally be entrenched in a swine manure quagmire and not anticipating thesis completion anytime soon.

To my advisory committee members I also extend my gratitude and thanks for their support, encouragement, and assistance. In addition to always being very helpful as I learned my way around the lab, field equipment, and the purchasing department (which should not be understated), Dr. Brewster Conant can also deservingly lay claim the title of chief surveyor for the field work conducted in support of my research. As the lone soil physicist on the committee, Dr. Gary Parkin was an incredible asset as I found myself ‘digging’ further and further into the realm of soil science. Finally, I was also extremely privileged to not only have Dr. Ed Sudicky’s direct support on my advisory committee but to also have support from the numerical modelling community that he oversees at the University of Waterloo.

Keeping with the subject of numerical modelling, I would specifically like to thank Rob Mclaren and Dr. Young Jin Park, who were both paramount in my HydroGeoSphere ambitions.

I would also like to acknowledge the highly constructive input I received from Dr. Dan Reynolds, who served as the external examiner for the thesis defense; and Dr. Neil Thomson who served as the internal-external advisory committee member.

It can be said that if you surround yourself with good people you will accomplish good things and hopefully my research efforts support this proverb. I had the true pleasure of working with a group of graduate students, technicians, and co-op students whose helpfulness, commitments, and tenacity made the scope of the field research manageable. Accordingly, I extend a sincere thank you to: Candice Williams, Sean Sinclair, Julia Charlton, Joanna Passmore, Graham Pope, Cailey McCutcheon, Paul Johnson, Bob Ingleton, Wayne Noble, Kayla Siefried, Kelly Molnar, Dr. Ed Cey, Mark Waldick, Andrew Weibe, and Scott Piggot.

In addition to those aforementioned, it is imperative that Jeff ‘Kintopia’ Melchin receives special recognition for his contributions to the work described in this thesis. My good fortune for having Jeff’s assistance and company throughout our various field adventures cannot be overstated.

If for whatever reason two people are required to spend their days together within confines equivalent to a graduate student office in the Physics building at the University of Waterloo, for the benefit of all humanity, it is best if they get along. I was not only lucky enough to get paired up with someone who is tremendously easy to get along with, but who also turned into a great friend and whose conversations helped put the Ph in PhD. So to Marcelo Sousa, I also extend a big thank you.

From Agriculture and Agri-Food Canada I would like to thank Dr. David Lapen and Dr. Bonnie Ball-Coelho for their interest and assistance with my work and the field data sets they provided.

Without a doubt, much of my research could not have been accomplished without ‘no holds barred’ access to a very unique field site and for that I truly thank Frank Aarts and his family. Instead of cringing every time I asked if it would be OK to dig yet another hole (or crater) in his field, Frank was always most encouraging and was constantly interested in our discoveries as they unfolded.

And last but not least, I would like acknowledge the huge amount of support I received during my PhD adventure from my wife Katy, who undoubtedly knows more about the movement of liquid swine manure to tile drains than she ever dreamed possible, and has been forever patient in waiting to find out ‘where home is going to be’ (hopefully soon I’ll have an answer); and from my parents, who ultimately created the opportunity for me to spend the biggest part of the last decade as a student.

Funding

Primary financial assistance for this research was provided by the Natural Sciences and Engineering Research Council of Canada, Agriculture and Agri-Food Canada, Ontario Ministry of the Environment, and Ontario Pork. Additional funding was provided by the Canadian Water Network and the Canadian Foundation for Innovation.

Dedication

To Zoey and ? ,

I hope you both have as much fun in school as dad did!

Table of Contents

Author’s Declaration ii

Abstract… iii

Acknowledgements vi

Dedication. viii

Table of Contents ix

List of Figures xiii

List of Tables xviii

Chapter 1 Introduction 1

- 1.1 Background 1
- 1.2 Objectives 4
- 1.3 Thesis Organization 6

Chapter 2 Characterization of plot and field scale macropore spatial variability in tile drained soil in southwestern Ontario 7

- 2.1 Introduction 7
- 2.2 Methods and materials 10
  - 2.2.1 Field site description 10
  - 2.2.2 Plot characterization 11
  - 2.2.3 Plot layout 11
  - 2.2.4 Hydraulic property estimation 11
  - 2.2.5 Dye infiltration 12
  - 2.2.6 Macropore counting 12
  - 2.2.7 Statistical methods 13
- 2.3 Results and discussion 14
  - 2.3.1 Plot characterization 14
  - 2.3.2 Dye infiltration patterns 15
  - 2.3.3 Macropore distribution 16
  - 2.3.4 Tile drain influence on macroporosity 20
  - 2.3.5 Inter-plot macropore area fraction variability 21
  - 2.3.6 Macroporosity – hydraulic conductivity correlation 21
- 2.4 Conclusions 23
- 2.5 Figures and Tables 25

Chapter 3 Spatial and temporal influences on the hydraulic and structural properties of tile drained soil in southwestern Ontario ... 38
- 3.1 Introduction ... 38
- 3.2 Methods and materials ... 42
  - 3.2.1 Site description ... 42
  - 3.2.2 Experimental plot configuration ... 42
  - 3.2.3 Soil analysis ... 43
  - 3.2.4 Tension infiltration tests ... 43
  - 3.2.5 Double ring infiltration tests ... 45
  - 3.2.6 Macropore characterization ... 45
  - 3.2.7 Effective Porosity ... 46
  - 3.2.8 Statistical methods ... 47
- 3.3 Results ... 47
  - 3.3.1 Soil analysis ... 47
  - 3.3.2 Weather and soil conditions ... 47
  - 3.3.3 Macropore characterization ... 48
  - 3.3.4 Spatial variability in hydraulic properties with respect to tile drain location ... 49
  - 3.3.5 Temporal variability in hydraulic properties ... 49
  - 3.3.6 Effective Porosity ... 50
- 3.4 Discussion ... 51
  - 3.4.1 Tile drain influence on hydraulic properties ... 51
  - 3.4.2 Visible vs. hydraulically effective macroporosity ... 51
  - 3.4.3 Temporal variability ... 52
  - 3.4.4 Infiltration dynamics – tension vs. double ring infiltrometer ... 53
- 3.5 Conclusions ... 54
- 3.6 Figures and Tables ... 56

Chapter 4 Assessing potential nutrient losses in tile drained, macroporous soils over an annual cycle through conservative tracer tracking ... 63
- 4.1 Introduction ... 63
- 4.2 Study site and methods ... 66
  - 4.2.1 Site description ... 66
  - 4.2.2 Plot characterization ... 66

4.2.3 Plot instrumentation ... 70
4.2.4 Hydraulic response / tracer test ... 70
4.2.5 Tile discharge monitoring ... 71
4.2.6 Chemical analysis ... 71
4.2.7 Hydrograph separation ... 72
4.2.8 Residual tracer analysis ... 72
4.2.9 Water level – tile drain discharge correlation ... 73
4.2.10 Short term and long term bromide mass discharge estimates ... 73
4.3 Results ... 74
4.3.1 Plot characterization ... 74
4.3.2 Tile drain response to irrigation ... 75
4.3.3 Tracer breakthrough to tile: days 0 - 21 ... 76
4.3.4 Residual tracer distribution ... 77
4.3.5 Tile discharge – water level correlation ... 78
4.3.6 One year tracer movement ... 79
4.4 Discussion ... 81
4.5 Conclusions ... 84
4.6 Figures and Tables ... 86
Chapter 5 Viscosity dependant, two-dimensional, dual-permeability numerical modelling of liquid swine manure flow in a layered, macroporous, and tile drained soil ... 99
5.1 Introduction ... 99
5.2 Background ... 100
5.2.1 Preferential flow ... 100
5.2.2 Soil crust and plowpan layers ... 102
5.2.3 Liquid swine manure fluid properties ... 103
5.3 Methods ... 104
5.3.1 Field Experiments ... 104
5.3.2 Model Description ... 104
5.3.3 Domain Configuration – Boundary Conditions – Initial Conditions ... 109
5.3.4 Hydraulic Property Derivation ... 110
5.3.5 Transport Parameters ... 112
5.3.6 Model Calibration ... 112

5.4 Results and discussion 112
  5.4.1 Parameter estimation / model calibration 112
  5.4.2 Evaluation of model performance 115
  5.4.3 Hydraulic conditions, and nutrient movement to the tile drain 116
  5.4.4 Viscosity sensitivity 117
  5.4.5 Plowpan and soil crust sensitivity 118
5.5 Conclusions 121
5.6 Figures and Tables 124
Chapter 6 Conclusions and Recommendations 137
6.1 Summary of Conclusions 137
6.2 Recommendations for future research 142
References........ 144
Appendix A Kintore soil data 162
Appendix B Kintore infiltration test data 164
Appendix C Kintore macroporosity data 174
Appendix D Soil analysis process pictures 180
Appendix E Tile discharge, tracer and climate data 183
Appendix F Residual tracer distribution in plot 1 soil cores extracted Sept 2008 184
Appendix G Sebringville tile drain nutrient concentration data converted for 2D model application 186
Appendix H Extended dual-permeability model evaluation for tile discharge. 189
Appendix I Dual-permeability model water and solute exchange parameter sensitivity. 190
Appendix J Density influence on liquid manure movement in macroporous soil. 194
J1. Hydrostatic Domain 194
J2. Steady-state Flow – Unit Gradient 196
J3. Steady-state Flow – 0.1 Gradient 197

List of Figures

Figure 2.1. a) Location of the research site in southwestern Ontario, Canada, and b) relative location of the three experimental plots with respect to topography and the field boundary at the research site. . 25

Figure 2.2. Row-wise orientation of the infiltration and macropore counting areas relative to tile drain location at the three experimental plots. 26

Figure 2.3. Photograph showing plot 1 after the infiltration tests, dye application and trenching had been conducted. 26

Figure 2.4. Soil profile cross-section at a) plot 1, b) plot 2, and c) plot 3, that shows how the visible tile scars at plot 1 and 3, direct surface applied dye to the tile drain as opposed to plot 2 where a tile scar was not visible and worm burrows were the observed conduit for dye to reach the tile drain. 27

Figure 2.5. Example of the 0.25 m^2 horizontal surfaces that were prepared for macropore counting and photographing. In this case the surfaces were located at depths of; a) 0.5 m, and b) 0.8 m, in the sampling row furthest from the tile drain at plot 3. 27

Figure 2.6. Photograph taken at plot 3 that shows the typically vertical orientation of the worm burrows in the B horizon, and how the macropores terminated as the soil composition transitioned to coarser material. 28

Figure 2.7. Row-wise representation of macropore area fraction distribution at plot 1 relative to depth for macropores in the a) 0.5-5 mm, b) 5-8 mm and, c) 8-10 mm diameter ranges, as well as for d) total macroporosity. 29

Figure 2.8. Row-wise representation of macropore area fraction distribution at plot 2 relative to depth for macropores in the a) 0.5-5 mm, b) 5-8 mm and, c) 8-10 mm diameter ranges, as well as for d) total macroporosity. 30

Figure 2.9. Row-wise representation of macropore area fraction distribution at plot 3 relative to depth for macropores in the a) 0.5-5 mm, b) 5-8 mm and, c) 8-10 mm diameter ranges, as well as for d) total macroporosity. 31

Figure 3.1. Relative location of the three experimental plots with respect to tile drain positions, topography, and the field boundary. 56

Figure 3.2. Plan view of the row-wise orientation of infiltration test areas relative to the tile drain location, at the three experimental plots. 56

Figure 3.4. Mean macroporosity as a function of depth at plots 1, 2, and 3. 57

Figure 3.5. Plot 1 row-wise comparison of the $\alpha'(\psi)$ relationships for, a) August 2009 (wet), and c) September 2009 (dry); and the $K(\psi)$ relationships and K_{fs} estimates for, b) August 2009 (wet), and d) September 2009 (dry). 58

Figure 3.6. Plot 2 row-wise comparison of the $\alpha'(\psi)$ relationships for, a) August 2009 (wet), and c) September 2009 (dry); and the $K(\psi)$ relationships and K_{fs} estimates for, b) August 2009 (wet), and d) September 2009 (dry). 59

Figure 3.7. Plot 3 row-wise comparison of the a) $\alpha'(\psi)$ relationships, and b) $K(\psi)$ relationships and K_{fs} estimates for August 2008. 59

Figure 3.8. Comparison of the plot 1, a) $\alpha'(\psi)$ relationships, and b) $K(\psi)$ relationships and K_{fs} estimates for the August 2009 (wet) and September 2009 (dry) infiltration experiments. 60

Figure 3.9. Comparison of the plot 2, a) $\alpha'(\psi)$ relationships, and b) $K(\psi)$ relationships and K_{fs} estimates for the August 2009 (wet) and September 2009 (dry) infiltration experiments. 60

Figure 3.10. Inter-row comparison of mean hydraulically effective porosity for: a) plot 1 in August 2009, b) plot 2 in August 2009, c) plot 3 in August 2008, d) plot 1 in September 2009, and e) plot 2 in September 2009. 61

Figure 4.1. General location of the research site in southwestern Ontario, Canada (modified from http://atlas.gc.ca). 86

Figure 4.2. Experimental plot location relative to the field topography and boundaries. 86

Figure 4.3. Experimental plot configuration showing the location of the bromide and chloride tracer application areas relative to the: irrigation area, shallow (W1, W2, W3, W4, W5) and deep (W6, W7) piezometers, and tile drain monitoring station. 87

Figure 4.4. Mean macroporosity distribution at the experiment plot, for circular macropores of different sizes, and total macroporosity including fractures, from the surface to tile drain depth. 88

Figure 4.5. Tile discharge relative to precipitation and irrigation water input for (a) October 22 to 26, and (b) November 6 to 10. 89

Figure 4.6. Soil moisture content fluctuation in response to the 3 hour irrigation events on (a) October 22, and (b) October 24; and (c) the 9 hour irrigation event on November 7. 90

Figure 4.7. Vertical soil moisture profile before and immediately after the 3 hour irrigation events on October 22 (a) and October 24 (b), and the 9 hour irrigation event on November 7 (c). 91

Figure 4.8. November 7 to 28 (a) tile discharge relative to precipitation and irrigation water inputs, and (b) tile effluent bromide and chloride concentrations and cumulative bromide mass as a percent of the total mass applied. 91

Figure 4.9. Tile discharge, bromide (Br) concentration, and irrigation, for the first 20 hours of the tracer test, after the dilutive influence from tile discharge sourced from outside the test plot were removed with hydrograph separation. 92

Figure 4.10. Residual bromide and chloride distribution in the tracer application area, as observed in mid September of 2008, relative to the initial application areas identified on top surface. 92

Figure 4.11. Normal distribution probability plots of the (a) raw, and (b) transformed tile discharge data, and the water level data from piezometers 1, 2, and 4 – 7 (c – h). 93

Figure 4.12. Cross-correlation between tile discharge and water levels in piezometers W1, W2, W4, W5, W6, and W7 94

Figure 4.13. Water-level in relation to tile drain elevation in the seven piezometers (a), the two water level signals that compose the empirical tile discharge model (b), and modelled versus measured, transformed tile discharge data (c). 95

Figure 4.14. Cross-correlation between the modelled and measured transformed tile discharge data from October 27 to November 28, 2007. 95

Figure 4.15. Bromide and chloride concentration in the tile effluent (a), temperature (b), precipitation (c), instantaneous bromide flux rate (d), and bromide (as % of initial mass applied) captured by the tile drain (e), between October 2007 and November 2008. 96

Figure 4.16. Bromide and chloride concentration in the tile effluent (a), temperature (b), precipitation (c), water content at 23 cm depth (d), and lateral hydraulic gradient between W5 and W3(e), during the January 2008 precipitation/melt event. 97

Figure 5.1. Conceptual model of the physical system showing: (a) the subdivisions of the soil profile, (b) simulation domain geometry for the liquid swine manure (LSM) injection scenario, and (c) simulation domain geometry for the LSM surface banding scenario. Note that the macroporous B layer extends from the bottom of the macroporous plowpan to tile drain depth. 124

Figure 5.2. Simulation results compared to field observations for: tile discharge (a & d), NH_4 concentration (b & e), and total P concentration (c & f); for liquid swine manure application with injection at a rate of 74 m^3/ha (top row), and surface banding at a rate of 56 m^3/ha (bottom row)... 125

Figure 5.3. Simulated macropore NH_4 concentrations, and soil matrix and macropore zone water table positions for: (a) liquid swine manure (LSM) injection with an application rate of 74 m^3/ha at 0.048

days after application, and (b) LSM surface banding with an application rate of 56 m^3/ha at 0.208 days after application. 126

Figure 5.4. Simulation results compared to field observations for: tile discharge (a, d & g), NH_4 concentration (b, e & h), and total P concentration (c, f & i); for liquid swine manure injection at a rate of: 28 m^3/ha (top row), 37 m^3/ha (middle row), and 56 m^3/ha (bottom row). 127

Figure 5.5. Simulated viscosity/dry matter influences on tile effluent NH_4 concentrations after liquid swine manure (LSM) injection (top row), and surface banding (bottom row), with an application rate of 74 m^3/ha. LSM dry matter contents (with viscosity) of: 1.25% (a & d), 2.5% (b & e), and 5% (c & f), are each compared to the scenario where LSM viscosity has not been considered (no viscosity). 128

Figure 5.6. Simulated viscosity/dry matter influences on residual soil matrix NH_4 concentrations one day after liquid swine manure (LSM) injection (top row), and LSM surface banding (bottom row), with application rates of 74 m^3/ha. LSM dry matter contents of: 0% (a & e), 1.25% (b & f), 2.5% (c & g), and 5% (d & h), are considered. 129

Figure 5.7. Simulated viscosity/dry matter influence on the infiltration rate of liquid swine manure beneath a single application row with unit thickness after injection (a), and surface banding (b), with application rates of 74 m^3/ha. 130

Figure 5.8. Pressure heads in the soil matrix 1 cm and 5 cm below the 74.8 m^3 ha^{-1} liquid swine manure application surface nearest to the tile drain for injection (a), and 1 cm and 5 cm below the top of the macroporous A layer for surface banding (b), for dry matter contents of 0% (DM_0), and 5% (DM_5). 131

Figure 5.9. Proportion of total applied NH_4 mass stored in the soil matrix and macropore zones of the injection (a), and surface banding (b) scenarios; for liquid swine manure application at a rate of 74.8m^3 ha^{-1}; and dry matter contents of 0% (DM_0) and 5% (DM_5). 131

Figure 5.10. Simulated effects of the plowpan layer on tile discharge rates (a & c), and tile effluent NH_4 concentrations (b & d); for liquid swine manure injection (top row), and surface banding (bottom row), with an application rate of 74 m^3 ha^{-1}. 132

Figure 5.11. Concentration (a & c) and pressure head (b & d) non-equilibrium status, observed at a horizontal distance of 412.5 cm from the tile drain, at depths of 15 cm (A Layer) and 40 cm (B Layer) from the surface; for liquid swine manure injection (top row) and surface banding (bottom row) at a rate of 74 m^3 ha^{-1}, with and without plowpan layers. 133

Figure 5.12. Residual NH_4 distribution in the soil matrix 2 days after liquid swine manure application at a rate of 74 m^3 ha^{-1}; for injection with (a), and without (b), a plowpan layer; and surface banding with

a soil crust and plowpan layer (c), with a soil crust but without a plowpan layer (d), and without a soil crust layer but with a plowpan layer (e). 134

Figure 5.13. Simulated effects of the soil crust layer on tile discharge rates and tile effluent NH_4 concentrations for liquid swine manure surface banding with an application rate of 74 m^3 ha^{-1}. 135

Figure 5.14. Concentration (a), and pressure head (b), non-equilibrium status observed at a horizontal distance of 412.5 cm from the tile drain, at depths of 15 cm (A Layer) and 40 cm (B Layer) from the surface; for liquid swine manure surface banding at a rate of 74 m^3 ha^{-1}, with, and without, a soil crust. 135

List of Tables

Table 2.1. Mean physical characteristics of the A horizon soil at the three experimental plots. 33

Table 2.2. Mean physical characteristics of the B horizon soil at the three experimental plots. 33

Table 2.3. Depth dependant mean macropore area fraction and the associated coefficient of variation (CV) for macropores in the 0.5-5mm, 5-8mm, and 8-10mm size ranges, as well as for total macroporosity, at each of the three experiment plots. 34

Table 2.4. Statistical significance (P) values of the inter-row, depth averaged, macropore area fraction comparisons between the three rows located at different distances from the tile drain. $P \leq 0.1$ indicates that the probability of the median macropore area fraction values being equal is 0.1 or less. 35

Table 2.5. Statistical significance (P) values of the inter-plot, depth averaged, macropore area fraction comparisons. $P \leq 0.1$ indicates that the probability of the median macropore area fraction values being equal is 0.1 or less. 36

Table 2.6. Linear correlation (r) between total macropore area fraction at the four depth/depth intervals and mean hydraulic conductivity ($\log_{10}K$) of the surface, and B horizon soils. 37

Table 3.1. Physical characteristics of the A horizon soil at the three experimental plots (from chapter 2). 62

Table 3.2. Physical characteristics of the B horizon soil at the three experimental plots (from chapter 2). 62

Table 3.3. Effective porosity attributable to pores with equivalent cylindrical diameter greater than 0.02 cm and the associated coefficient of variation (CV). 62

Table 4.1. Mean values for selected physical properties of the A and B horizon soils as determined with core analysis, and for B horizon hydraulic conductivity. 98

Table 4.2. Mean initial (θ_i) and final (θ_f) moisture contents, and surface soil unsaturated ($K_{x,y}$), and saturated (K_{fs}) hydraulic conductivity. Row 1, and row 2, are located above, and 2 m away, from the tile drain, respectively. 98

Table 5.1. Physical soil properties (from *Ball-Coelho et al.*, 2007) from the liquid swine manure injection (INJ), and surface banding (SB), experiment site. 136

Table 5.2. Hydraulic properties assigned to the soil matrix zones. 136

Table 5.3. Hydraulic properties assigned to the macroporous zones. 136

Chapter 1

Introduction

1.1 Background

Since the mid 20th century, tremendous progress has been made by the soil physics, agronomic and hydrogeology communities to improve our understanding of water and nutrient dynamics in agricultural soils. Although significant advancements have been made, scientific discovery in this field must continue in order to keep agricultural productivity growth on pace with the growing population. In addition, significant pressure continues to be applied on the agricultural community to reduce the environmental impact of farming practices, specifically with respect to impacts on water quality. Between 1950 and 2008, the world's population grew from 2.5 to 6.8 billion people and with the help of science, global food production has been striving to keep pace. By 2050 global population is projected to reach over 9 billion, requiring that food production rise by 70%, with the increase coming largely from improvements in agricultural productivity, not by additional land cultivation (*FAO*, 2009). One of the most recognized methods of increasing crop yields is through fertilization; however, increased use of fertilizers often has deleterious effects on groundwater and surface water quality (*Scanlon et al*., 2007). Balancing this agricultural/environmental quandary necessitates that we continue to improve our understanding of soil/water/nutrient interactions in order to optimize nutrient availability for plant growth while reducing nutrient flux to groundwater and surface water.

Much of the productive agricultural land in North America is the result of major land modification initiatives that include both surface and subsurface drainage installation, and *Skaggs et al.* (1994) reported that approximately one quarter of all the cropland in North America has undergone drainage improvements. Subsurface (tile) drainage provides many benefits from an agricultural perspective but also has many potentially negative environmental impacts including increased peak runoff rates, increased nitrate-nitrogen losses to surface water, and by providing a conduit for substances such as liquid manure (*Shipitalo and Gibbs*, 2000; *Hoorman and Shipitalo*, 2006; *Ball-Coelho et al.*, 2007), herbicides (*Moorman et al*., 1999), pesticides (*Kladivko et al*., 1991; *Kladivko et al*., 1999) and pharmaceuticals (*Lapen et al*., 2008a) to reach surface water. The environmental impacts of tile drains are increasingly becoming the subject of debate between groups representing environmental, agricultural and political interests; however, basic questions of how tile drains dynamically interact with the hydrologic environment remain unanswered. Increased scientific knowledge is required to facilitate productive dialog among the stakeholders currently engaged in these debates.

Inherent to areas with extensive tile drainage installations are structured soils with poor natural drainage (*Skaggs et al*., 1994), that typically contain various types of preferential flow paths (macropores) that facilitate rapid water and solute flux under wet hydrologic conditions (*Flury et al*., 1994). When macropores interact with tile drains, agricultural products and chemical tracers can be detected in tile effluent within hours or even minutes after application (*Kung et al*., 2000; *Stamm et al*., 2002; *Ball-Coelho et al*., 2007). Past research has shown that only macropores in the immediate vicinity of tiles are likely to transmit solutes to the tile drains (*Mohanty et al*., 1998; *Shipitalo and Gibbs*, 2000); however, macropores located away from tiles still pose an environmental risk since they have the ability to rapidly transmit potential contaminants below the plant root zone and into shallow groundwater.

Proper quantification of the impact that tile drains and macropores have on groundwater and surface water is a complex issue that requires a multi-faceted approach. Perhaps the best method is through the conjunctive use of field tracer experiments that show the bulk system behavior; and physically-based, non-equilibrium flow and transport models that allow the bulk system to be dissected into its component parts for detailed analysis. The dual-permeability flow and transport formulation from *Gerke and van Genuchten* (1993a) is currently one of the most widely used models for simulating preferential flow and transport in macroporous field soils and is the method implemented in the popular Hydrus (*Simunek et al*., 2006) and HydroGeoSphere (*Therrien et* al., 2009) numerical models. While these models can simulate the physical complexities of flow through macroporous soil, they are extremely parameter intensive (*Simunek et al*., 2003) and require soil information that is not typically available at the plot and field scale.

One of the most fundamental requirements for parameterizing dual-permeability models is to have knowledge of macropore geometry and spatial distribution at the location of interest; however, to date there is very little field data available that provides this vital information. Although the subject of preferential flow has received considerable scientific attention, much of the existing field-based quantitative data for agricultural soil macroporosity relates to studies that focused on: (1) wheel traffic influences on soil hydraulic properties (*Ankeny et al*., 1990), (2) tillage effects (*Ehlers*, 1975; *Ankeny et al*., 1990; *Logsdon et al*., 1990; *Dunn and Phillips*, 1991), (3) hillslope position (*Bodhinayake et al*., 2004b), and (4) flow and transport dynamics in macroporous soil (*Ehlers*, 1975; *Villholth et al*., 1998; *Cey and Rudolph*, 2009); and not on field scale characterization of macropore spatial distribution. To further complicate the matter of selecting appropriate macropore parameters for use in dual-permeability models, macroporous agricultural soils are often tile drained and the spatial relation between macroporosity and tile drains is very poorly understood.

In addition to significant spatial variability, the hydraulic properties of agricultural soils are subject to temporal variability that can often overshadow spatial effects (*Messing and Jarvis*, 1993; *van Es et al*., 1999; *Zhou et al*., 2008). While it is accepted that the magnitude of temporal variability is largely governed by deterministic factors such as tillage (*Murphy et al*., 1993; *Moret and Arrúe*, 2007), crop type (*Bodner et al*., 2008), root growth (*Bodner et al*., 2008; *Mubarak et al*., 2009), climate (*van Es*, 1993; *Bodner et al*., 2008), irrigation (*Mubarak et al*., 2009), moisture content (*Zhou et al*., 2008) and wheel traffic (*Alakukku*, 1996a/b); very little information currently exists pertaining to the influence of tile drainage on soil variability from either a temporal or spatial perspective. Because macropores can typically transmit a large proportion of the total water flux in relatively wet soil (*Mohanty et al*., 1996; *Lin et al*., 1997), macropore temporal variability and associated temporal influences on soil structure are especially important considerations when evaluating the infiltration characteristics of agriculture soil. However, the amount of information currently available to describe temporal influences on macroporosity in tile drained soils is notably sparse.

While the dynamic response of tile drains to incident water is undoubtedly influenced by temporal variability in soil hydraulic properties, a disproportionately large amount of the annual water and nutrient-mass flux through tile drains can occur in a relatively short amount of time (*Drury et al*., 1996; *Cambardella et al*., 1999; *Tomer et al*., 2003; *Kladivko et al*., 2004), during extremely wet conditions. As a result, it is important to understand flow and transport processes in macroporous soil during ‘extreme’ hydrologic events in order to properly define the potential risks that tile drains pose to surface water resources on an annual basis; however, previous research has largely avoided this subject. Because ‘extreme’ event tile drainage research is complicated by the realism that tile drain monitoring is challenging during periods of high flow, new and innovative methodology is required to facilitate further scientific development in this field.

The understanding of nutrient fluxes in soil/groundwater/surface-water systems is further complicated by the number of different products available to serve as fertilizers; however, in geographical areas with large confined animal feeding operations, liquid manure is commonly used. To give perspective on the volume of manure under consideration, in Canada alone it is estimated that 16 million tonnes of liquid swine manure were applied to agricultural land in 2006 (*Hofmann*, 2008). Because past work (*Landry et al*., 2004; *Keener et al*., 2006) has shown that liquid manure has significantly different fluid properties than water, flow and transport characteristics specific to liquid manure need to be taken into account in order to accurately predict the risk that land application of liquid manure poses to water resources. To date however, the influence of manure specific fluid properties on the movement of liquid manure through macroporous soil has largely escaped scientific attention.

1.2 Objectives

The primary objective of this PhD thesis is to elucidate tile drain interactions with macroporous soils, and to improve the ability to simulate flow and transport of nutrients in shallow groundwater agricultural environments. As noted above, gaps currently exist in our understanding of the temporal and spatial variability of soil hydraulic properties; so by necessity, significant efforts were made during the course of this work to alleviate these gaps in order to address the primary objective with the detail required to contribute new insight on the subject. This work entailed a combination of field studies that were conducted on different soil types and during different seasons, and numerical modelling activities that utilize a modified version of the HydroGeoSphere numerical model that accounts for the influences of fluid viscosity on variably saturated flow through macroporous soils. Synthesizing the results from this work will improve the ability to more effectively manage fertilizer use in macroporous tile drained agricultural soil in order to optimize nutrient benefits and reduce environmental risk, by improving nutrient utilization by crops from both a predictive and conceptual perspective. Specific scientific contributions are as follows:

- Quantification of the influence that tile drainage has on soil hydraulic properties and macropore distribution in different soil types by evaluating the three dimensional spatial distribution of macroporosity, and the two-dimensional distribution of soil hydraulic properties, with respect to tile drain location. This was carried out in three unique settings that include: a flat lying field position with fine sandy loam soil underlain by a silty clay deposits; a slightly sloping location with loam soil underlain by silt, sand and gravel lenses; and a hillside location with loam soil underlain by sandy silt deposits.
- Quantifying the influence that post cropping season temporal variability has on the hydraulic properties and soil structure of flat lying sandy loam, and hillside loam soils.
- Conduct plot scale irrigation and transient tracer experiments on well characterized, macroporous soil in a shallow groundwater environment to: a) demonstrate the dynamic

nature of tile drain hydraulic response to precipitation, b) show how macropore interactions with tile drains influence nutrient flux after fall liquid manure applications, and c) quantify the relative proportion of surface applied solutes that can be captured overtime by tile drains after a late fall liquid manure application.

- Demonstrate how correlation between groundwater levels and tile drain discharge can be used to develop empirical tile drain discharge models, and: a) demonstrate how such models can be used to estimate tracer mass flux through a tile drain over a one year period following surface application of a conservative tracer, and b) illustrate the significance of 'extreme' hydrologic events on nutrient fluxes through tile drains.
- Demonstrate the importance of considering distinct soil layers such as plowpans and surface crusts in dual-permeability simulations of flow and transport in macroporous field soils by calibrating a plot scale, HydroGeoSphere model with results from a field-scale liquid manure application experiment.
- Show the importance of including fluid viscosity and physically realistic boundary conditions when simulating liquid manure application on layered, macroporous, and tile drained agricultural soils using a modified version of HydroGeoSphere.

1.3 Thesis Organization

The contents of this thesis are organized into six chapters, with this first chapter providing both a general introduction to the topic of preferential flow in tile drained agricultural land, and the basis and objectives for the scientific work described in detail throughout chapters 2 to 5. It is intended that chapters 2 through 5 will be published in international scientific journals and in order to expedite the publication process they have been prepared in manuscript format. Chapters 2 and 3 specifically focus on detailed site characterization work that was conducted at the primary field site near Kintore, Ontario where soil hydraulic property spatial and temporal variability was investigated with a series of infiltration tests and shallow excavations. Chapter 4 is focused on a tracer experiment that was conducted at the Kintore site in order to characterize conservative solute transport to tile drains over an annual climate cycle, and is supported by the site characterization work described in chapters 2 and 3. Chapter 5 investigates the movement of liquid swine manure to tile drains in structured soils using dual-permeability numerical models, and is based on field experiments conducted near Sebringville, Ontario by Agriculture and Agri-Food Canada. Chapter 6 restates the most significant conclusions from chapters 2 through 5, and also provides suggestions for future research.

Chapter 2

Characterization of plot and field scale macropore spatial variability in tile drained soil in southwestern Ontario

2.1 Introduction

Tile drains are ubiquitous features of the agricultural landscape across the most productive agricultural regions in North America and have been integral to improving our agricultural productivity. In temperate climate regions, tile drains are typically installed with the objective of removing excess soil moisture in order to: (1) allow farmers to plant crops earlier and harvest later, (2) reduce the detrimental effects of wheel traffic soil compaction, (3) improve root zone aeration, and (4) allow the root zone to warm quicker in the spring. Whereas in arid/semi-arid climate regions, where irrigation is common, tile drains are primarily intended to reduce salt accumulation in the soil. Although the many benefits of tile drainage are well known, environmental problems associated with tile drainage; such as increased: nitrate, pathogen, pesticide and salt loading in surface water; have also been documented. Because tile drainage is such a vital component of modern agriculture, yet potentially manifested with serious environmental issues, there is a need to increase our knowledge of how tile drains interact with the soil – groundwater – surface water system.

In temperate climate regions, tile drains are often installed in poorly drained, structured soils that contain secondary porosity features (macropores), such as biopores, root holes and fractures (*Beven and Germann*, 1982). Macropores are generally characterized as pores greater than 0.3 mm in equivalent cylindrical diameter that allow for non-equilibrium flow conditions to exist between the soil matrix and the secondary porosity when soil water pressure head exceeds the range of -10 to -6 cm (*Jarvis*, 2007). Within their hydraulically active pressure range, macropores are very important in governing the infiltration characteristics of agricultural soils and can have significant influence on infiltration processes, and on the transient hydraulic response of tile drains to precipitation and irrigation events. It has been repeatedly shown that a disproportionately large amount of water flux is transmitted through macropores as structured soils approach saturation (e.g. *Dunn and Phillips*, 1991; *Mohanty et al.*, 1996; *Lin et al.*, 1997). Because macropores can be so effective at rapidly transmitting water and solutes in the shallow soil environment, their influence on tile drains can be important. Numerous past studies have led to the conclusion that macropore flow processes are responsible for the rapid arrival of compounds derived from liquid manure (*Shipitalo and Gibbs*, 2000), liquid municipal biosolids (*Gottschall et al*. 2009), and pesticides and fertilizers (*Kladivko et al.* 1991) at tile drain outlets.

Because tile drainage has been shown to increase the structure (*van de Graaff*, 1979) and hydraulic conductivity (*Bouma et al*., 1979a) of some soil types, it has been hypothesized that macroporosity will increase in the vicinity of tile drains (*Alakukku et al*., 2010). Although the issue of macropore distribution relative to tile drain location has been considered in previous work involving both earthworm abundance and macropore distribution in agricultural soils, the results do not consistently show that tile drain location influences macroporosity. In a silt loam soil in Ohio that was planted in no-till soybean, *Shipitalo and Gibbs* (2000) found that macropores created by *Lumbricus terrestris* L. earthworms, and located within 0.5 m of the drain, are most likely to have a direct connection with the drain; however, they did not observe increased earthworm abundance over the drain. Conversely, work conducted in southwestern Finland has found that higher numbers of adult *Lumbricus terrestris* L. earthworms do exist over tile drains (*Nuutinen et al*., 2001), and that they tend to burrow deeper over tile drains (*Pitkänen and Nuutinen*, 1997) as compared to midway between drains. In more recent work by *Alakukku et al*. (2010), macroporosity was not found to increase above tile drains even though there were a greater number of earthworms in the soil above the tile drain.

In order to accurately quantify the potential for macropores to transmit contaminants to tile drains, their spatial distribution and geometric properties need to be known. Although dual-permeability models generally perform well when predicting water and solute flux in macroporous soils (*Vogel et al*., 2000; *Gärdenäs et al*., 2006; *Gerke et al*., 2007), they are parameter intensive (*Simunek et al*., 2003) and require a detailed description of the macropore/bulk soil volumetric ratio. To date, there is very little field data available that describes the spatial distribution of macroporosity in different soil types in order to support the parameterization of these complex models. Much of the existing field-based quantitative data for agricultural soil macroporosity relates to studies that focused on: (1) wheel traffic influences on soil hydraulic properties (e.g. *Ankeny et al*., 1990), (2) tillage effects (e.g. *Ehlers*, 1975; *Ankeny et al*., 1990; *Buczko et al*., 2006; *Logsdon et al*., 1990; *Azooz et al*., 1996; *Dunn and Phillips*, 1991), (3) hillslope position (e.g. *Bodhinayake et al*., 2004b), and (4) flow and transport dynamics in macroporous soil (e.g. *Ehlers*, 1975; *Villholth et al*., 1998; *Cey and Rudolph*, 2009); and not on field scale characterization of macropore spatial distribution.

Various techniques exist for quantifying macroporosity in soil; however, none are without problems. The most basic of the methods involves manually counting macropores on exposed soil surfaces and has been used extensively (e.g. *Ehlers*, 1975; *Lauren et al*., 1988; *Logsdon et al*., 1990; Cey and Rudolph, 2009). As with any manual procedure though, human bias will inherently induce variability and lack of reproducibility to the data (e.g. *Logsdon et al*., 1990). Image analysis of digitized soil images is also extensively used (e.g. *Edwards et al*., 1988; *Ringrose-Voase*, 1996; *Mallants et al*., 1997, *Cey and Rudolph*, 2009). Aside from the purely technical issues (*Thompson et al*., 1992), image analysis often involves quantification of dye stained surface area, which becomes problematic when considering that dye will invariably stain areas of the soil matrix as well as the walls of hydraulically active macropores. Methods have also been derived to determine macroporosity using tension infiltrometers (*Watson and Luxmoore*, 1986; *Bodhinayake et al*., 2004a) and hanging water columns (e.g. *Flint and Flint*, 2002) that are based on capillary theory. While both methods are widely used (e.g. *Watson and Luxmoore*, 1986; *Ankeny et al*., 1990; *Mallawatantri et al*., 1996; *Bodhinayake et al*., 2004a), their applicability is limited to situations where the only macropores of interest are connected to the infiltrometer base, or suction plate surface (*Beven and Germann*, 1982). In more recent advances in preferential flow research, soft x-ray radiography (*Mori et al*., 1999), and CAT scanning (*Perret et al*., 1999) technology has been applied to macropore characterization. While technically appealing, these technologies are currently limited to those who have access to the required equipment, and who are interested in lab scale soil core analysis.

While the inherent difficulty of macropore quantification is acknowledged, there is tremendous need for spatially distributed macroporosity data in order to better understand macropore influence on infiltration dynamics at the plot and field scale, and to quantify macropore spatial variability in numerical models that account for the presence of a preferential flow continuum. It is the objective of this component of the work to address the current gaps in our understanding of field scale macroporosity distribution in shallow water table agricultural settings by characterizing and comparing the spatial distribution of macroporosity with respect to: saturated hydraulic conductivity, soil type, topographical setting, and tile drain location in southwestern Ontario field soils. In total, macropores on one hundred and forty nine 0.25 m^2 horizontal surfaces, located at depths ranging from 0.02 to 1 m, and distances up to 4 m from tile drains, were manually counted and classified into five different size categories. Double-ring infiltrometer tests were conducted on the field surface above each sub-surface area where macropores were counted. Macroporosity spatial variability relative to tile drain location and field position was assessed with robust, non-parametric, statistical methods. The results provide quantitative data to support both the parameterization of preferential flow models, and assessments of environmental impacts associated with preferential flow and tile drainage systems, in agricultural settings. The extensive dataset obtained over the course of this work provides new insight into the spatial distribution of soil macroporosity at both the plot and field scale.

2.2 Methods and materials

2.2.1 Field site description

The experiment site is an actively cropped field that is located at N43°09’55”, W81°01’08”, near the town of Kintore in southern Ontario, Canada (Figure 2.1a). Systematically spaced, 10 cm diameter, plastic tile drains were installed at the site in 1985 with a tile plow. According to the regional soil survey (*Experimental Farms Service*, 1987), soils at the site are primarily poorly drained dark grey Gleysolic, Maplewood silt loam series, underlain by clay, and clay loam till that is bordered at the north edge of the field by well drained grey brown Luvisol of the Honeywood silt loam series that is underlain by calcareous loam till.   Beneath the surface soils is a complex layering of Quaternary sediments consisting of subglacial diamictons and glacifluvial deposits (*Rudolph and Parkin*, 1998) that extend to a depth of approximately 45 m (*Sado and Vagners*, 1975). The glacial sediments overlie Middle Devonian limestone of the Detroit River Group (*Ontario Geological Survey*, 1986). Topography at the site ranges from relatively flat (south-west end of the field) to gently rolling (north half of the field), and local soil conditions tend to vary in conjunction with topography. Minimum tillage practices have been utilized at the site since 1995. Prior to 2004 both liquid swine manure and commercial fertilizers were used as soil nutrient amendments; however, between 2004 and 2009 only commercial fertilizer was used. In 2007 and 2009 the field was planted in soybeans (*Glycine max L.*) that were harvested in late September and in 2008 the field was planted in winter wheat (*Triticum aestivum* L.) that was harvested in mid July. The topographic and surface – subsurface soil variability, combined with the uniform land management practice and climate conditions that are characteristic of a single field, made this site ideal to study soil type and topographic influences on macroporosity. Past research on nitrate flux in agricultural settings and riparian zone denitrification has been conducted at the same site (*Cey et al*., 1998; *Cey et al*., 1999).

2.2.2 Plot characterization

Three locations (plot 1, plot 2 and plot 3) at the site were chosen for study (Figure 2.1b), with each plot having a unique soil property/topography combination. The A horizon was characterized with 0.05 m diameter by 0.1 m long soil cores that were extracted from the 0.05 to 0.15 m depth interval. Six such cores were obtained from each plot, of which three were taken from immediately over the tile drain and three from a parallel transect 2 m away; coring locations were spaced 2 m apart along each transect. The B horizon was characterized with 0.08 m diameter by 0.1 m long soil cores that were extracted from various depths between 0.3 to 1 m. The B horizon samples were not taken from an evenly spaced grid but were instead intended to represent the different shallow sub-surface soil types observed. Organic matter content in the topsoil cores was determined using the Walkley-Black acid digestion method (Walkley and Black, 1934), particle size distribution for all of the cores was determined with the pipette method (Gee and Or, 2002), and bulk density was determined by assuming that the volume of soil inside the cores was undisturbed. The tile drains at each plot were located with an electronic drain inspection/location system. Prior to the infiltration experiments, soil moisture content in the top 5 cm of the soil profile was measured at twelve locations at each plot with a Campbell Scientific Inc, TDR 100, time domain reflectometry (TDR) system.

2.2.3 Plot layout

Twelve individual test areas at each plot were arranged on a rectangular grid oriented parallel to the tile drain (Figure 2.2). The three individual rows of test areas were spaced approximately 0, 1.5, and 3.5 m from the tile drain. Along each row, the four test areas were spaced approximately 2 m apart. All of the areas were all carefully located to avoid soil affected by wheel traffic with the exception of two test areas in row 1 of plot 3.

2.2.4 Hydraulic property estimation

Double-ring infiltrometer tests were used to obtain estimates of field saturated hydraulic conductivity (K_{fs}) on the soil surface above each sub-surface area where macropores were counted. In the process of setting up the infiltrometer tests, both the inner and outer rings were hammered approximately 5 cm into the soil. A water level of approximately 10 cm was maintained throughout the experiment in both the inner and outer reservoirs by separate 40 liter Mariotte bottles. Infiltration rates were monitored until quasi steady-state conditions were observed in the inner ring, which usually required two to three hours. Estimates of K_{fs} were obtained from the double ring infiltration data using the method prescribed by *Reynolds et al*. (2002). The saturated hydraulic conductivity (K_{sat}) of each B horizon soil core was measured in the lab with either a constant, or falling head permeameter, for the visibly coarse, or fine grained material, respectively (*Reynolds*, 2008).

2.2.5 Dye infiltration

Between the double-ring infiltrometer tests and macropore counting, 20 liters of blue dye (Brilliant Blue FCF) was infiltrated into the soil beneath each test area from within a 0.5 m by 0.5 m square sheet metal frame that was hammered approximately 0.02 m into the soil. The dye infiltration occurred under falling head conditions with the initial level usually around 0.08 m. The purpose of the dye infiltration was to visualize both the macropore hydraulic continuity from surface to tile drain depth and the spatial distribution of infiltration via preferential flow. Vertical soil faces that extended from the near surface to tile drain depth along one edge of each dye infiltration area were excavated and smoothed with a mason’s trowel and then photographed in order to document the vertical dye infiltration patterns.

2.2.6 Macropore counting

Macropores were counted on 4 or 5 horizontal soil surfaces beneath all but one of the surface test areas. To reduce the amount of manual digging required, 1 m deep trenches were excavated around one or two sides of the dye infiltration area with a mini-excavator (Figure 2.3). Manual preparation of the 0.5 by 0.5 m square counting surfaces involved the following steps; 1) digging with a spade to a position approximately 20 mm above the target elevation, 2) removing the next 15 mm with a handheld scraper blade, and 3) cutting vertical slices into the rough finished surface and then cracking off the final 5 mm of soil so that the soil structure was exposed with minimal smearing. Each surface was cleaned with a vacuum immediately before the macropores were counted. At plot 1, forty-eight surfaces were excavated on four levels situated between depths of 0.02-0.76 m, at plot 2 there were fifty-three surfaces on five levels excavated between depths of 0.02-1.00 m. At plot 3 there were sixty surfaces excavated on five levels between depths of 0.02-0.80 m; however, macropores were only counted on the forty-eight surfaces located between 0.02-0.5 m since the soil below a depth of approximately 0.6 m became increasingly coarse grained/gravelly and visible macropores seemed to terminate at the transition.

A 0.5 by 0.5 m square wire frame was placed on the prepared counting surface in order to define the counting area. The wire frame was subdivided into 4 equal quadrants and the counting process involved tallying the number of macropores in diametric size classifications of 0.5-5 mm, 5-8 mm, 8-10 mm and 10-12 mm within each quadrant; as well as tallying the length of all the fractures observed on each surface. Although somewhat arbitrary, the size classification was chosen for the following reasons: 1) pores less than 0.5 mm were difficult to discern from surface voids created during the surface preparation process, 2) the average size of the different size categories was approximately the median size, 3) pores in the 0.5-5 mm size were a combination of root holes and biopores whereas the larger sizes were mostly worm burrows lined with a dark film, and 4) fractures were included because they were obviously ubiquitous to the soil and dye infiltration patterns indicated that they were actively transmitting water. To reduce measurement bias circle templates were used to aid in size categorization. The potential data repeatability problems associated with manually classifying and counting macropores (e.g. *Logsdon et al.*, 1990) are acknowledged; however, the field methods needed to be relatively simple in order to accommodate the scale of the project.

Fractures were quantified during the counting exercises by using a ruler to physically measure the total length of fractures on each surface. An estimate of the area occupied by fractures was obtained by assuming that the average fracture width was 0.5 mm, which was based on field measurements taken in the A horizon layer of plot 3. It should be noted that the fracture values are slightly less reliable than the macropore values since additional fractures formed rapidly as the exposed surfaces dried; and on occasion it was difficult to ensure that the observed fractures had existed prior to surface exposition. Because fractures were found to make up a very small proportion of total macroporosity at each of the three plots, the uncertainty associated with fracture measurement has minimal influence on the overall macroporosity quantification results. Macropore area fraction (MAF), which is defined as the ratio of macropore area to total surface area, was obtained by multiplying the mean area of each macropore size interval by the observed number of macropores in that interval. Total MAF on each counting surface was obtained by summing the MAF associated with the individual macropore size intervals and the total fracture area. Ten megapixel digital pictures were taken of each counting surface to provide reference during data analysis and for possible future image analysis.

2.2.7 Statistical methods

The two sided rank-sum test (as defined in *Helsel and Hirsch*, 2002) was used to determine if the median MAF in the row of sample areas located above the tile drain was statistically indifferent from MAF in the two rows positioned parallel to the tile drain, and also to determine if the median MAF among the three plots was statistically indifferent. The MAF of 0.5-5 mm, 5-8 mm, and 8-10 mm macropores, and total macroporosity, at each depth level, were considered in the comparisons. Macropores in the 10-12 mm size category were rarely encountered and therefore not compared, and fractures were not compared because of the low proportion of macroporosity attributable to fractures and to the uncertainty surrounding the fracture data. Although the MAF attributable to 10-12 mm macropores, and to fractures, was not individually tested, their respective contributions to total macroporosity are included in the total MAF values.

2.3 Results and discussion

2.3.1 Plot characterization

Select soil compositional properties, bulk density, and mean hydraulic conductivity, at the three experimental plots identified in Figure 2.1b are presented in Tables 2.1 and 2.2. Plot 1, which is located on the relatively flat (1.6% grade) south end of the field where tile drains are located at a depth of about 0.75 m, consists of fine sandy loam topsoil with approximately 6% organic matter and is underlain by a silty clay B horizon with approximately 8% gravel content. Plot 1 is in an area of the field where hydraulic gradients direct the shallow groundwater towards surface year round, and where the tile drains flow during all but the driest conditions. Plot 2 is located on a slope (9% grade) along the eastern edge of the field where tile drains are located at a depth of about 0.95 m and A horizon soils are classified as loam that contains approximately 3% organic matter. The B horizon soil at plot 2 is composed of relatively uniform silty sand with approximately 4.3% gravel. The tile drain at plot 2 is seasonally active and water was not flowing in it at the time of this work. In comparison to plot 1, the water table at plot 2 is approximately 0.3 to 0.5 m deeper, which results in lower surface soil moisture content that in turn increases potential for carbon based organic materials to breakdown, hence the comparatively low proportion of A horizon organic matter. Plot 3 is located in the relatively flat (1.9% grade) center of the field where tile drains are located at about 0.85 m depth and the topsoil is classified as loam with approximately 5% organic matter. Water was flowing in the tile drain at plot 3 at a very low rate when the work was conducted. At all three plots, a hardpan layer was observed at the base of the A horizon, at depths of approximately 0.15 to 0.2 m. Near surface, mean soil moisture content at plots 1, 2, and 3, prior to the experiments being conducted were 0.29, 0.22, and 0.23 $m^3 m^{-1}$, respectively.

Similar to the large differences in soil composition, the hydraulic conductivity of both the surface, and B horizon soils, varies markedly between the three plots. Geometric mean hydraulic conductivity of the surface soil ranges from a low of 13 cm d^{-1} at plot 2, to a high of 251 cm d^{-1} at plot 3. Hydraulic conductivity of the B horizon has even greater variability and ranges from a low of 0.25 cm d^{-1} at plot 1 to a high of 63 cm d^{-1} at plot 3.

2.3.2 Dye infiltration patterns

Visible tile installation scars at plots 1 and 3 appeared to have preferentially funneled dye from the surface to the tile drain (Figure 2.4a,c). The tile scars were approximately 1.5 m wide at the top of the B horizon and tapered towards the base of the tile drain. Visual inspection indicated that within the tile scar regions, dye was transmitted towards the tile drain through cylindrical macropores, structural faces within and along the edges of the tile scars, and topsoil material that appeared to have washed into voids created during the tile installation process. It is important to note that in addition to serving as preferential flow conduits, the structural and compositional features within the tile scar areas are capillary barriers that will potentially impede lateral flow under partially saturated B horizon soil conditions. At plot 2 there was no evidence of a tile installation scar and cylindrical macropores were the only structural features that appeared to be transmitting dye to the tile (Figure 2.4b).

In the A horizon, the dye was widely distributed throughout the soil matrix and the macropores beneath the application area. Similar to the observation made by *Shipitalo et al*. (2004), it appeared that the hardpan layer at the top of the B horizon promoted the lateral spreading of the infiltrate and that macropore flow was the primary means of dye movement through the hardpan. Throughout the top of the B horizon, dye staining was generally limited to soil in the immediate vicinity of macropore features (e.g. Figure 2.5a) and from visual observations it did not appear that any single macropore size range was more or less stained than the others. All of the macropore sizes, including fractures, had obviously transmitted dye. At plots 1 and 2, macropores smaller than 0.5 mm, including some that had very fine roots inside them, were observed to have dye staining at tile depth. Although the very small pores were not precisely measured, some of them appeared to have diameters less than the generally suggested 0.3 mm minimum diameter of macropores. This observation suggests that small, vertically continuous capillary pores are also preferentially transmitting water and solutes to tile depth at this site.

At plot 3 the soil transitioned to noticeably coarser material at a depth of approximately 0.7 m, at which point the majority of the B horizon macroporosity appeared to terminate (Figure 2.6). The observed loss of macroporosity at a soil textural boundary is consistent with previous work that has shown *Lumbricus terrestris* L. earthworms were deterred by sand layers within loamy soil cores (*Hawkins et al*., 2008), and that burrows terminated at the transition to unweathered parent material (*Ehlers*, 1975) below a silt soil. Figure 2.6 provides a visual perspective on the soil composition/structural change that generally occurred between the 0.5 m and 0.8 m depths at plot 3. Due to the dramatic decline in the number of vertically continuous macropore features and the change in soil composition, dye staining patterns changed noticeably across the textural boundary. Within the coarse grained material below the boundary, the dye appeared widely dispersed (Figure 2.5b) and not focused around individual macropores (Figure 2.5a). These differences in dye staining patterns between soil layers with different structure and textural features are consistent with results reported by *Flury et al*. (1994) for agricultural soils in Switzerland that were underlain by coarse deposits. Based on observations from plot 3 and noting that the dye was applied with positive pressure, it appears that the B horizon macropores have the potential to act as vertical pipes that provide a direct hydraulic connection between the top of the hardpan layer and deeper, more permeable deposits. When the permeable deposits extend into the saturated zone, the groundwater flow system, as well as tile drain effluent, could be rapidly impacted by surface activity in conditions where shallow B layer macropores are hydraulically active.

2.3.3 Macropore distribution

2.3.3.1 Plot 1

The MAF estimation for plot 1 is presented in Figure 2.7. The MAF for macropores in the 0.5-5 mm size range (Figure 2.7a) is greatest near surface and progressively decreases to tile depth (0.75 m). The MAF attributed to macropores larger than 5 mm was low in relation to the smaller macropores for all depths. For macropores in the 5-8 mm size range (Figure 2.7b), the greatest MAF was observed at the top of the B horizon (0.15-0.45 m depth interval). Similarly, the MAF distribution for 8-10 mm macropores (Figure 2.7c) was also found to be greatest at the top of the B horizon. With the exception of a single worm burrow in the 8-10 mm size range, only macropores less than 5 mm in diameter appeared to reach tile depth at plot 1. Because the MAF at plot 1 is dominated by macropores in the 0.5-5 mm size range, the total MAF distribution (Figure 2.7d) largely reflects the distribution of the smallest macropores.

2.3.3.2 Plot 2

Results of the MAF estimation for plot 2 are presented in Figure 2.8. The MAF of 0.5-5 mm macropores (Figure 2.8a) is greatest near surface, and generally decreases until the 0.45-0.6 m depth interval, at which point it remains relatively stable to tile drain depth (0.95 m). The MAF of both 5-8 mm macropores (Figure 2.8b), and 8-10 mm macropores (Figure 2.8c), was greatest at the top of the B horizon (0.15-0.45 m depth interval), and rapidly declined below 0.45 m. Only a single macropore in the 5-10 mm size range was observed below the depth of 0.7 m. There were approximately 60% fewer 5-8 mm macropores near surface than at the top of the B horizon and macropores in the 8-10 mm size range were not observed near surface at all. The only macropores to reach tile depth were in the 0.5-5 mm size range. The total MAF distribution at plot 2 (Figure 2.8d) has two local peaks that largely reflect the high proportion of 0.5-5 mm macropores near surface, and the combination of 0.5-5 mm and 5-8 mm macropores within the 0.15-0.6 m depth range.

2.3.3.3 Plot 3

Although macropore counting surfaces at plot 3 were excavated to tile depth (0.85 m), macropores appeared to terminate in the vicinity of a textural boundary that existed at an approximate depth of 0.7 m. As a result, MAF is only reported for the 0.02-0.5 m depth interval. It is also important to note that at plot 3, two of the four test locations within row 1 appeared to have been affected by wheel traffic from the front wheel of a John Deere 9500 series combine during wheat harvest (based on wheel track imprints on the near surface macropore counting areas), which occurred approximately 3 weeks before this work. Although the inter-row MAF data is quite sparse, and large natural variability reduces the opportunity to conduct a meaningful comparison between wheel-affected and non-wheel-affected areas, a brief evaluation of the MAF datasets from row 1 suggests that wheel traffic may have reduced the MAF by up to 50%, with the greatest reductions observed near the field surface. Previous work by *Ankeny et al*. (1990) has shown that wheel traffic preferentially destroys or prevents the formation of macropores, and provides support for this observation.

The MAF estimation for plot 3 is presented in Figure 2.9. MAF attributed to 0.5-5 mm macropores (Figure 2.9a) was greatest in top 0.2 m, where it was also relatively constant. Between the depths of 0.2-0.5 m, the MAF of 0.5-5 mm macropores declined substantially. MAF of 5-8 mm macropores (Figure 2.9b) was greatest near the top of the B horizon and least near surface. MAF attributed to 8-10 mm macropores (Figure 2.9c) continuously increased with depth and peaked just above the level where the soil transitioned to coarser material. Of the three plots, plot 3 was the only site where macropores larger than 10 mm in diameter were observed, and in all instances, they were located in the 0.15-0.3 m depth interval. The large macropores typically composed less than 10% of the MAF, with one exception being a surface located at 0.15 m depth, beneath a non wheel impacted area of row 1, where 11-12 mm macropores composed approximately 20% of the MAF. The total MAF at plot 3 (Figure 2.9d) is greatest at the top of the B horizon, where it was relatively evenly composed of macropores in the 0.5-5 mm, 5-8 mm, and 8-10 mm, size ranges. The MAF near surface and at a depth of 0.5 m is approximately the same, although the majority of near surface macroporosity is composed of macropores in the 0.5-5 mm size range, and the majority of macroporosity at a depth of 0.5 m is composed of macropores greater than 5 mm in size.

2.3.3.4 Macropore distribution summary

A summary of MAF distribution at five depths/depth intervals is presented in Table 2.3. In general, intra-plot variability was larger within the individual MAF size ranges than it was for total MAF. The greatest amount of variability was observed for MAF associated with macropores in the 5-8 mm, and 8-10 mm size ranges at plots 1 and 2, where the distribution of these larger sized macropores was quite uneven relative to plot 3. In comparison, the distribution of macropores in the 0.5-5 mm size range was much more consistent within each of the depth intervals at each of the three plots and as a result the variability in MAF attributable to smaller macropores is less. The coefficient of variation (CV) for the total MAF at the different depths reported here ranges from 10 to 48% and is comparable to results from past work. *Logsdon et al*. (1990), who also counted macropores manually, reported that CV ranged from 14 to 94% for a count of the total number of pores in the upper B horizon of four different soil types in Minnesota and Wisconsin. *Mallants et al*. (1997) reported a CV of 51% for macroporosity data obtained from quantifying dye stained area in soil cores extracted from the A horizon of a sandy loam soil in Belgium.

Both the macropore distribution, and the magnitude of the MAF observed in this work correspond well with results from previous work that characterized macroporosity with respect to depth in an agricultural soil. As to the question of ‘where does maximum MAF occur within the soil profile?’ the answer varies depending on which work is cited; however, it is most often either at the near surface or in the top of the B horizon. Noting that MAF can be considered equivalent to macroporosity [%] / 100, the results from this work can be directly compared to past work that has quantified macroporosity. In work conducted in Germany that investigated the vertical distribution of 2-11 mm macropores, Ehlers (1975) observed a maximum macroporosity of approximately 0.8% at a depth of

0.6 m, while near surface macroporosity was approximately 0.2%. Logsdon et al. (1990) observed that maximum macroporosity attributable to macropores greater than 0.4 mm in size ranged from 0.2 to 1.66% and was most often located within the 0.15-0.5 m depth interval. In work conducted on a hillside (35% grade) silt loam soil in eastern Washington State, Mallawatantri et al. (1996) reported that a maximum macroporosity of 1.1% existed at a depth of 1.4 to 1.9 m in the B horizon, while macroporosity near surface was 0.7%. In a silt loam soil in Minnesota, Munyankusi et al. (1994) noted that the maximum macroporosity was approximately 2% and was located near surface, and at a depth of 0.75 m, macroporosity had declined to less than 0.5%. Alakukku et al. (2010), who conducted their work on a clay soil in southern Finland, also noted that the maximum macroporosity of 3% occurred in the near surface and by a depth of 0.38 to 0.5 m it had declined 0.3%. Because of the many factors that will influence the dynamic behavior of macroporosity distribution within a soil profile, the above works cannot be directly compared without giving consideration to things such as soil composition, soil fauna, crop type, tillage practices, drainage status, timing of investigations and climatic factors. Nevertheless, it can be concluded from even a cursory overview of the previous work, along with the results from this work, that the maximum macroporosity of silt and clay soils will likely be in the range of 0.2 to 3 % and will occur in either the A horizon or the top of the B horizon. In a general sense, the vertical extent of the majority of soil macropores will depend on numerous factors including rooting depth, presence of textural discontinuities, and water table position; however, for silt loam soils where the water table is tile drain controlled, such as the case in this work, it can be expected that the MAF at tile depth will be very low in comparison with the maximum value.

2.3.3.5 Fractures

Although the fracture area quantification process was considerably less precise than the method employed to quantify the cylindrical macropores, it is still relevant to report the observed fracture distribution characteristics. MAF occupied by fractures was typically very small in comparison to cylindrical features. The maximum fracture related macroporosity comprised approximately 15% (at 0.15 m depth), 2% (at 0.02 m depth), and 7% (at 0.15 m depth), of the total MAF at plots 1, 2, and 3, respectively. At plots 1 and 3 there were very few fractures observed below a depth of about 0.4 m and at plot 2 there were very few fractures below the A horizon. Although an average fracture aperture width of 0.5 mm was used to estimate the total fracture area of each 0.25 m^2 macropore counting surface, visual evidence suggests that average fracture aperture width decreases with depth.

Reduced fracture occurrence with depth in Ontario silt loam/loam soils has also been reported by *Cey and Rudolph* (2009) who noted that fracture density peaked at a depth of 0.1 m and was absent by a depth of 0.3 m. The low fracture volume observed in this work needs to be considered within the context of soil composition (most notably clay content) if comparisons are to be made with other work conducted on soils with higher clay content. As an example, *Lauren et al*. (1988) report that planar features in a silty clay loam occupied approximately 1.5% of the total sample area, whereas the total fracture area did not exceed 0.05% of the total sample area in this work.

2.3.4 Tile drain influence on macroporosity

Results from the rank-sum test to determine the probability that the MAF data from the row of test areas located immediately above the tile drain (row 1) is similar to MAF in the rows located approximately 1 m (row 2), and 3 m (row 3) away from the tile drain, are given in Table 2.4. The results are reported in terms of P values; accordingly, P values less than 0.1 suggest that there is less than a 10% chance that the intra-row MAF median values are equivalent. If the 90% confidence level is considered the acceptance criteria for the hypothesis test, then the results show that the tile drains at the plots 1 and 2 do not influence the MAF. At plot 3 there is significantly lower MAF at depths of 0.02 and 0.5 m in the test row located above the tile drain as compared to the row furthest from the drain; however the results are potentially biased by wheel traffic. It is also possible that the disruption of the natural soil layering during tile installation at plot 3 created a less hospitable environment above the tile drain for earthworms by pulling coarse sediments from below the textural boundary nearer to the surface.

These results from plots 1 and 2 generally agree with observations made by *Shipitalo and Gibbs* (2000), who reported that earthworm populations within a silt loam soil, at a field site with a 2 to 6% slope in Ohio, did not vary in relation to tile drain location. In contrast however, work conducted in southwestern Finland on a sandy clay soil found over twice as many *Lumbricus terrestris* L. earthworms above, as opposed to between tile drains (*Nuutinen et al*., 2001), and that the burrows were deepest above tile drains (*Nuutinen and Butt*, 2003). In work conducted on a clay soil with a 2 to 4% slope in southern Finland, *Alalukku et al*. (2010) found that soil macroporosity was not influenced by tile drain position even though the number of earthworm burrows was significantly greater above the drain. The lack of corroboration between results from these studies suggests that factors other than the mere presence of a tile drain will at least partially influence macropore spatial variability with respect to the drain.

2.3.5 Inter-plot macropore area fraction variability

Using the rank-sum test, comparisons were made to determine if total MAF was statistically similar among the three plots chosen for study at the site. For the comparison, MAF at each plot was divided into four depths/depth intervals. Interval 1 considered MAF at a depth of 0.02 m and was used to represent the near surface conditions. Interval 2 considered MAF from 0.05 m to 0.2 m depth and was used to represent mid to low A horizon conditions. The third interval considered MAF between depths of 0.2 m and 0.45 m and was used to represent the shallow B horizon. Finally, interval 4 considered MAF within the 0.45 to 0.75 m depth range and was used to represent the deeper B horizon. Because the minimum tile drain depth was 0.75 m (at plot 1), the comparison tests did not consider depths below 0.75 m.

Statistical probability (P) values for the inter-plot MAF comparison tests are reported in Table 2.5. The results show that median MAF among the three test plots is statistically similar ($P > 0.10$) for only 6 of the 48 comparison scenarios; which were as follows: 8-10 mm macropores within the 0.21-0.75 m depth interval between plots 1 and 2, total macroporosity within the 0.46-0.75 m depth interval between plots 1 and 2, 0.5-5 mm macropores at a depth of 0.02 m between plots 1 and 3, 5-8mm macropores within the 0.21-0.45 m depth interval between plots 2 and 3, and total macroporosity at a depth of 0.02 m between plots 2 and 3.

The inter-plot MAF differences are not without precedence. In a silt loam soil in Ohio, *Edwards et al*. (1988) observed statistically significant differences ($P=0.001$) in the number of macropores within the 0.4-5 mm size range at different sampling sites that were spaced no more than 75 m apart in the same field; however, they did not observe significant variability in macropores greater than 5 mm. *Lauren et al*. (1988) found that range of dependence for planar and cylindrical macropore features was 75 m and 60 m, respectively, in a silty clay loam in New York State.

2.3.6 Macroporosity – hydraulic conductivity correlation

To identify if the significant MAF differences between the three plots are related to differences in hydraulic conductivity, mean total MAF within each of the four depth intervals considered in the previous section was plotted against the surface soil K_{fs} (Figure 2.10a), and B horizon K_{sat} (Figure 2.10b), values presented in Tables 2.1, and 2.2, respectively. Inspection of Figure 2.10 reveals that MAF tends to increase as both the surface soil and B horizon hydraulic conductivity increases, although the trend is disrupted by the fact that A horizon K_{fs} was higher at plot 1 than plot 2 even though plot 2 had a generally greater MAF. Noting that the A horizon at plot 2 had higher bulk density and lower organic matter content than plot 1 (factors that potentially reduce K_{fs}), it is possible that the relatively uniform B horizon soils with higher K_{sat}, less gravel, and better natural drainage (as compared to plot 1), are conducive to macropore generation, and counteract effects associated with lower surface K_{fs} which may promote lower macroporosity. It is also possible that the lower surface K_{fs} at plot 2 actually promotes the existence of earthworms by reducing infiltration and enhancing surface runoff during extreme hydrologic events, thereby creating a soil environment less prone to occasional saturation.

The MAF - hydraulic conductivity relationships presented in Figure 2.10 were quantified with linear correlation tests. Results from the correlation tests (Table 2.6) show that total MAF has a much stronger correlation with B horizon K_{sat} than with surface soil K_{fs} for each of the four depth/depth intervals considered. When the surface soil and B horizons are considered collectively, hydraulic conductivity is most strongly correlated with MAF within the 0.46-0.75m depth interval, which is also the deepest interval considered here.

The relatively strong correlation between the field surface K_{fs} and the MAF in the 0.46-0.75 m depth interval can be at least partially explained by the conditions imposed during the infiltration experiments. Because the double-ring infiltrometer tests created near surface saturated conditions that promoted water flux within the macropores that were vertically continuous through the hardpan (verified by dye staining patterns), the infiltration rate observed at surface is largely governed by the ease which water can move from the hydraulically active macropores beneath the hardpan into the surrounding soil matrix. Because dye staining patterns indicated that an appreciable amount of the hydraulically active macroporosity in the B horizon terminated in the 0.45-0.75 m depth interval, increased MAF in that depth interval will provide more surface area for macropore-matrix water exchange, and will therefore promote surface drainage when the B horizon macropores extend through the hardpan.

The strong correlation between B horizon hydraulic conductivity and MAF can also be explained by the experimental conditions. Because B horizon hydraulic conductivity was determined using vertical soil cores with discrete lengths, some macropores could readily extend across the entire core. Therefore, increased MAF relates to increased macropore hydraulic activity, and leads to enhanced water flux during saturated flow conditions. Similar results have been observed in smaller scale experiments where the amount of soil cross-sectional area actively transmitting preferential flow has been shown to correspond closely with K_{sat} (*Anderson and Bouma*, 1973; *Bouma et al*., 1979b; *Sollins and Radulovich*, 1988).

2.4 Conclusions

In each of the three soil types that were investigated, the greatest MAF of 0.5-5 mm macropores occurred in the top 0.2 m of the soil profile, whereas the greatest MAF of 5-10 mm macropores occurred at the top of the B horizon, in the 0.2-0.5 m depth range. At the two plots with the lowest subsoil hydraulic conductivity (plots 1 and 2), the majority of the MAF at tile drain depth was composed of macropores in the 0.5-5 mm size range; whereas at the plot with the highest surface, and B horizon, hydraulic conductivity (plot 3), the majority of the macroporosity appeared to terminate at a textural boundary located at an approximate depth of 0.7 m. The soil material became noticeably coarser grained and more permeable below the textural boundary at plot 3, which resulted in much better natural subsurface drainage as compared to the plots 1 and 2, and appeared to promote deeper penetration of macropores in the 5 to 10 mm size range in the fine grained material above the boundary. From these observations, increased natural subsurface drainage appears to have the ability to increase shallow soil MAF.

Maximum mean MAF at the three plots ranged from 0.0035 to 0.009 and was observed at either the near surface, or top of the B horizon, depending on the relative proportion of macropores in the 0.5-5 mm and 5-12 mm size ranges. MAF at tile depth was always much lower than the maximum value and did not exceed 0.001. At all three plots, fractures were most common near surface and estimates suggest that they never comprised more than 15% of the total MAF, or 0.1% of total porosity.

Dye staining patterns indicated that within the topsoil layer, flow readily occurred within both the soil matrix and macropores; however, at the top of the hardpan layer the dye appeared to spread laterally and flow into open macropores. Below the hardpan layer, within the macroporous section of the B horizon, dye staining in the soil matrix generally only occurred in localized halos surrounding macropores that had obviously transmitted dye. At plot 3, where the soil at tile depth was relatively coarse grained, the dye staining patterns indicated that macropores in the B horizon acted as vertical pipes that transmitted dye from the near surface to the coarse grained material, and that matrix flow was the predominant flow mechanism within the coarse grained material. At all three plots, dye movement was not restricted to specific macropore size ranges and macropores of all sizes appeared equally likely to have transmitted dye under the positive pressure application conditions. At plot 2, where the B horizon was the most uniform of the three plots, pores less than 0.3 mm in diameter also appeared to have transmitted dye to tile depth. At plots 1 and 3, where the shallow B horizon was less uniform and clay contents ranged from approximately 10 to 15%, preferential flow paths and coarse grained lenses within the soil scars resultant from the tile drain installation process were found to be preferentially funneling dye from the surface to the tile drain. However at plot 2, where the B horizon had a more uniform composition and clay content was approximately 5%, there was no evidence of any tile installation scars and cylindrical macropores that were continuous from the top of the hardpan layer to tile depth were the primary pathway for dye to reach the tile drain.

Statistical analysis revealed that tile drains do not induce significant spatial trends in MAF distribution within any of the three plots that were investigated here; however, there are statistically significant differences in MAF between the plots, which were spaced between 100 and 250 m apart within the same field. The coefficient of variation for depth averaged MAF was larger for individual macropore size ranges (13 to 53% for 0.5 to 5 mm macropores, 28 to 332% for 5 to 8 mm macropores, and 29 to 346% for 8 to 10 mm macropores) than it was for total macroporosity (10 to 48%). Correlation testing between MAF, and the hydraulic conductivity of the surface soil, and B horizon soil, indicates that there is relatively strong ($r \geq 0.84$) correlation between MAF below 0.02 m depth and B horizon hydraulic conductivity, whereas the correlation between MAF at depths less than 0.45 m and surface soil hydraulic conductivity is relatively weak. Conversely, MAF below 0.45 m was strongly correlated ($r = 0.79$) to surface soil hydraulic conductivity.

At all three of the plots investigated here, surface applied solutes have the ability to be rapidly transmitted to tile drains via preferential flow paths that originate from within a localized area surrounding the drains. As a result, tile discharge, and ultimately, surface water receptor water quality, in settings where structured soils are underlain by a hydraulically active tile drain system, will invariably be influenced by land management practices that induce preferential flow. Shallow groundwater quality at each of the three plots also has the potential to be impacted by land management practices that induce preferential flow. However, the risk for rapid, widespread groundwater contamination is greatest at the plot where macropores that are vertically continuous through the hardpan are effectively drained by highly permeable subsurface deposits. At the other two plots, the combination of macroporosity that diminishes with depth, and subsurface deposits with relatively low permeability, will greatly reduce the impact of preferential flow on shallow groundwater quality.

2.5 Figures and Tables

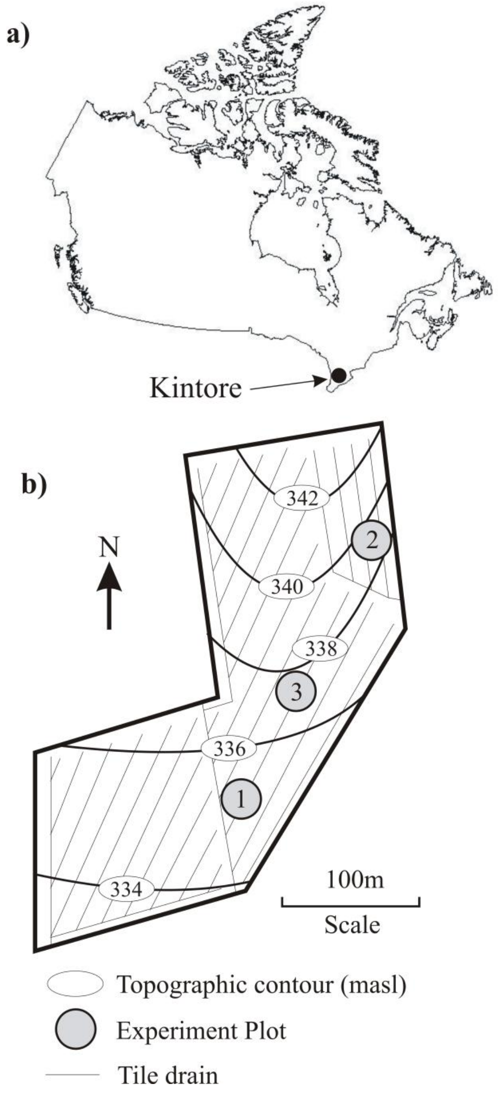

Figure 2.1. a) Location of the research site in southwestern Ontario, Canada, and b) relative location of the three experimental plots with respect to topography and the field boundary at the research site.

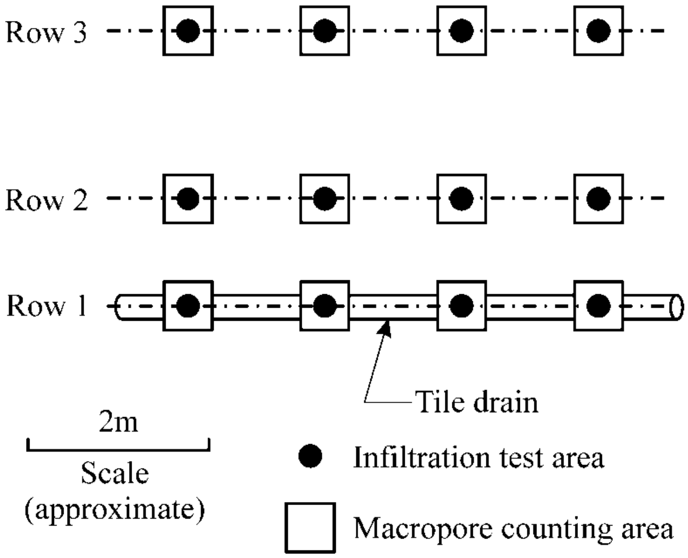

Figure 2.2. Row-wise orientation of the infiltration and macropore counting areas relative to tile drain location at the three experimental plots.

Figure 2.3. Photograph showing plot 1 after the infiltration tests, dye application and trenching had been conducted.

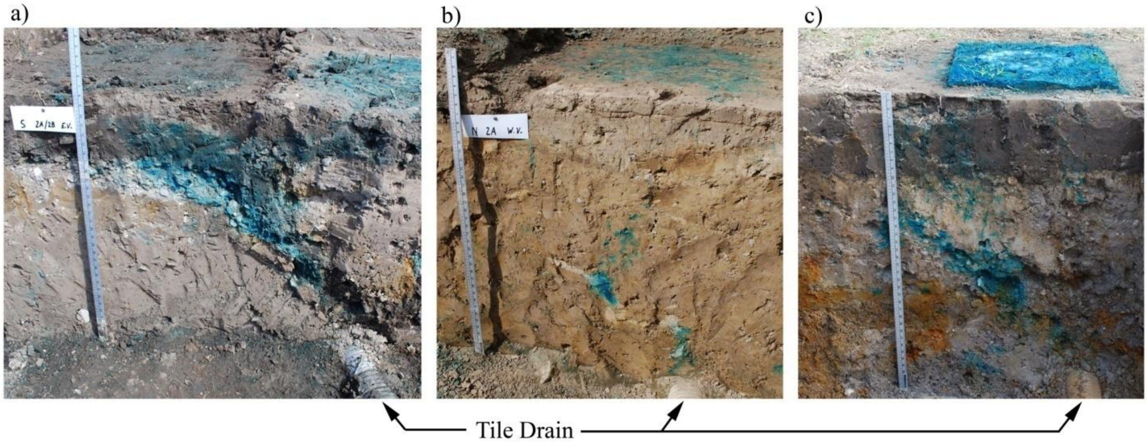

Figure 2.4. Soil profile cross-section at a) plot 1, b) plot 2, and c) plot 3, that shows how the visible tile scars at plot 1 and 3, direct surface applied dye to the tile drain as opposed to plot 2 where a tile scar was not visible and worm burrows were the observed conduit for dye to reach the tile drain.

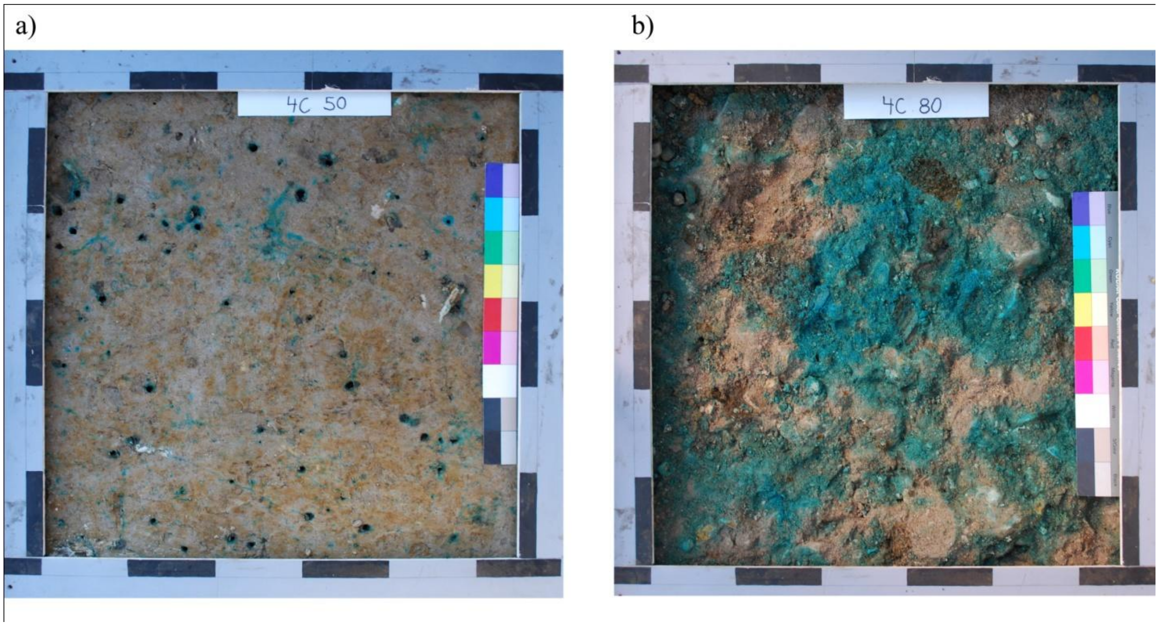

Figure 2.5. Example of the 0.25 m^2 horizontal surfaces that were prepared for macropore counting and photographing. In this case the surfaces were located at depths of; a) 0.5 m, and b) 0.8 m, in the sampling row furthest from the tile drain at plot 3.

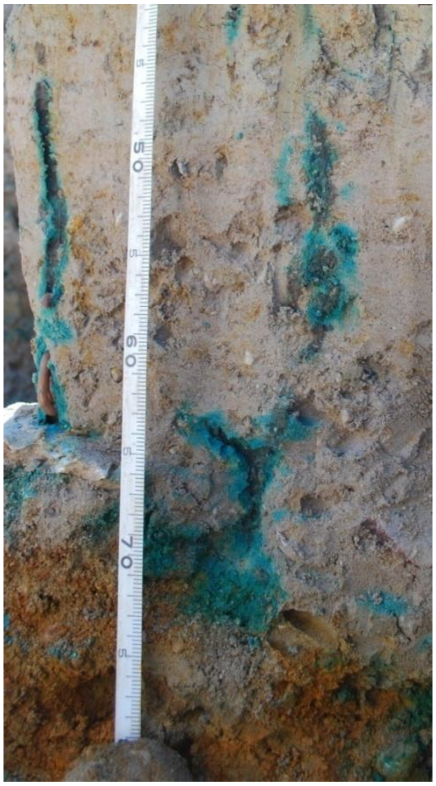

Figure 2.6. Photograph taken at plot 3 that shows the typically vertical orientation of the worm burrows in the B horizon, and how the macropores terminated as the soil composition transitioned to coarser material.

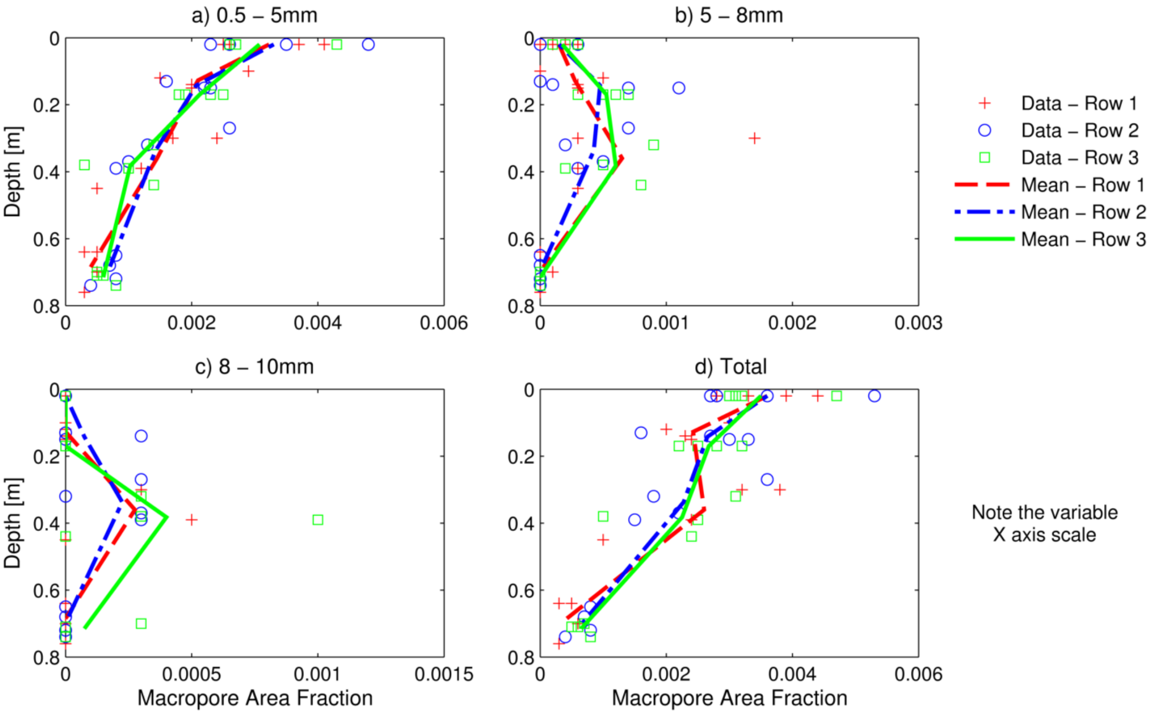

Figure 2.7. Row-wise representation of macropore area fraction distribution at plot 1 relative to depth for macropores in the a) 0.5-5 mm, b) 5-8 mm and, c) 8-10 mm diameter ranges, as well as for d) total macroporosity.

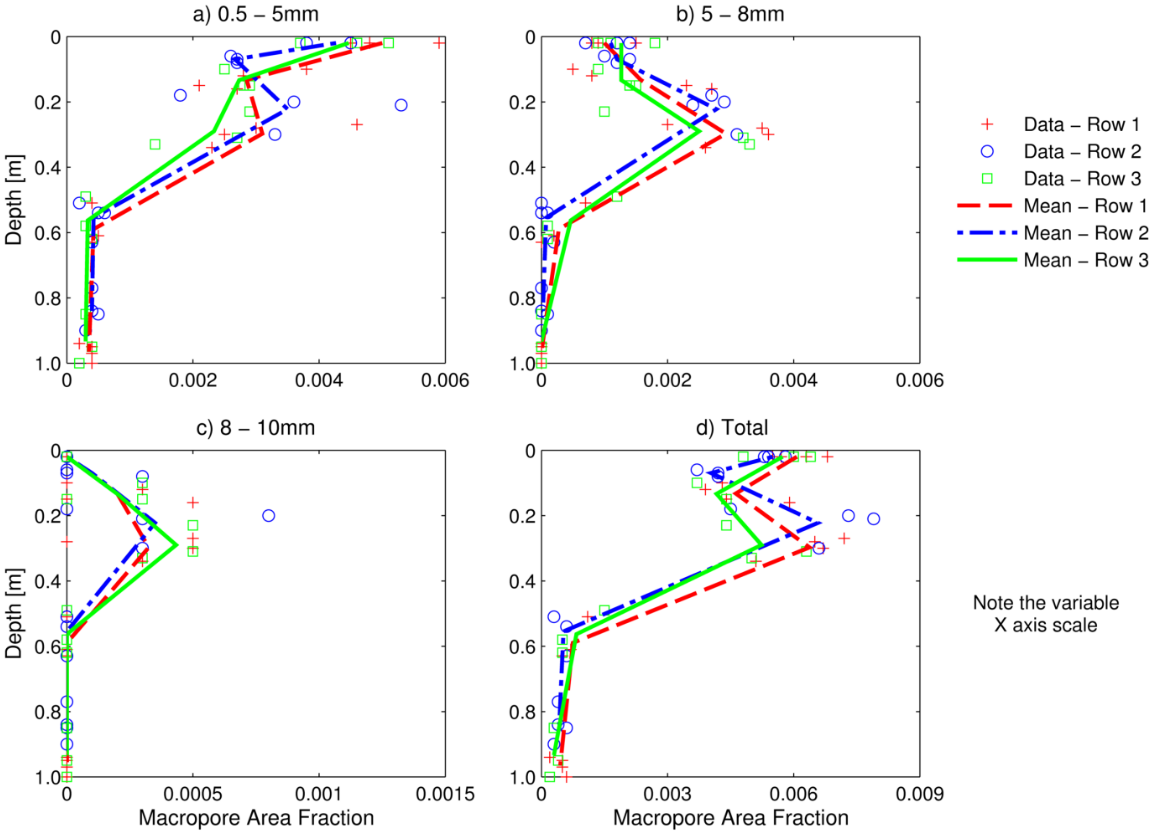

Figure 2.8. Row-wise representation of macropore area fraction distribution at plot 2 relative to depth for macropores in the a) 0.5-5 mm, b) 5-8 mm and, c) 8-10 mm diameter ranges, as well as for d) total macroporosity.

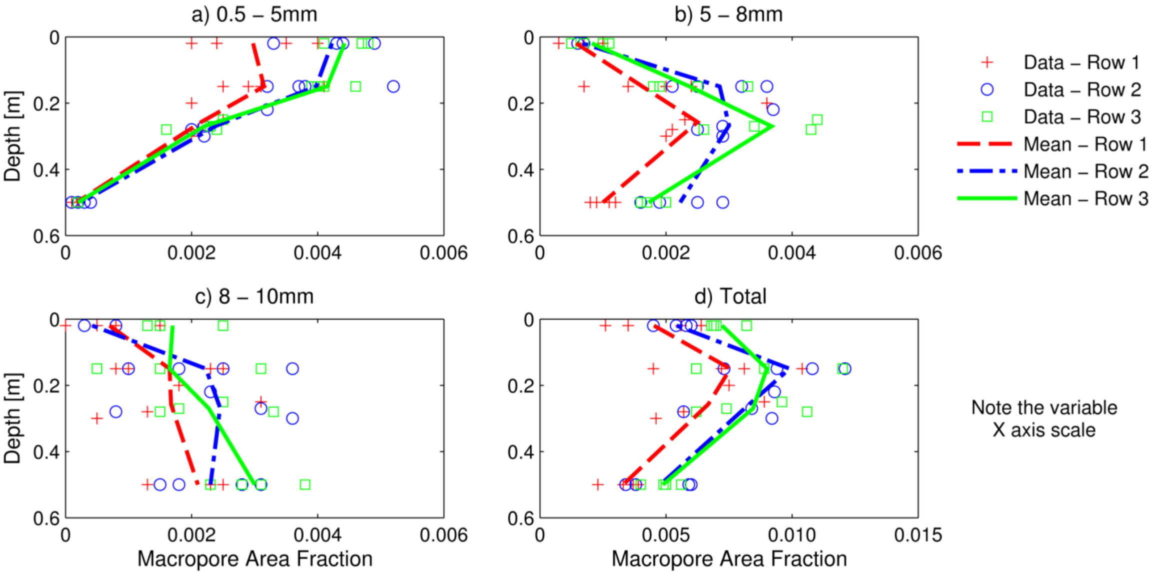

Figure 2.9. Row-wise representation of macropore area fraction distribution at plot 3 relative to depth for macropores in the a) 0.5-5 mm, b) 5-8 mm and, c) 8-10 mm diameter ranges, as well as for d) total macroporosity.

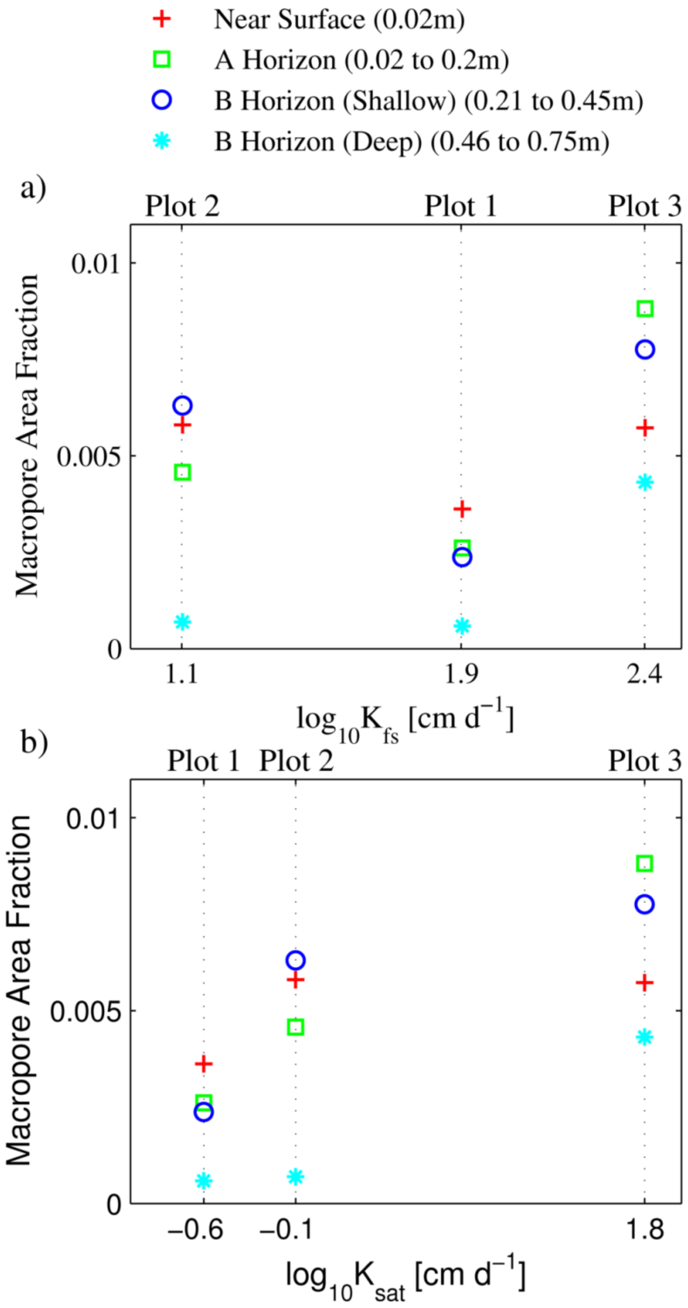

Figure 2.10. Mean macropore area fraction versus; a) surface soil mean $\log_{10}K_{fs}$ as determined from field measurements using the double ring infiltrometer method, and b) B horizon soil mean $\log_{10}K_{sat}$ as determined from lab measurements using either the constant, or falling head permeameter method.

Table 2.1. Mean physical characteristics of the A horizon soil at the three experimental plots.

Plot	Sand [%]	Silt [%]	Clay [%]	Gravel [%]	Bulk Density [g cm^{-3}]	Organic Matter [%]	Log$_{10}$K$_{fs}$ [cm d^{-1}]†
1	49.9 (1.5)	30.4 (1.5)	13.2 (0.7)	6.5 (1.7)	1.2 (0.0)	6.3 (0.3)	1.9 (0.3)
2	47.4 (1.7)	35.4 (1.0)	14.2 (1.0)	2.9 (1.0)	1.4 (0.1)	3.2 (0.1)	1.1 (0.5)
3	29.5 (1.2)	47.2 (1.2)	20.1 (1.1)	3.2 (2.7)	1.1 (0.1)	5.3 (0.2)	2.4 (0.5)

Values in parentheses denote standard deviation

Number of samples (n) equals 6 except where † indicates n equals 12

Table 2.2. Mean physical characteristics of the B horizon soil at the three experimental plots.

Plot	Sand [%]	Silt [%]	Clay [%]	Gravel [%]	Bulk Density [g cm^{-3}]	Log$_{10}$K [cm d^{-1}]
1†	28.8 (3.9)	48.3 (3.1)	14.6 (1.2)	8.3 (3.2)	1.9 (0.1)	-0.6 (1.1)
2	51.8 (5.7)	38.3 (4.4)	5.5 (1.7)	4.3 (3.1)	1.9 (0.2)	-0.1 (0.7)
3	51.9 (21.5)	29 (15.8)	9.4 (6.4)	9.7 (11.9)	1.7 (0.1)	1.8 (1.1)

Values in parentheses denote standard deviation

Number of samples (n) equals 6 except where † indicates n equals 4

Table 2.3. Depth dependant mean macropore area fraction and the associated coefficient of variation (CV) for macropores in the 0.5-5mm, 5-8mm, and 8-10mm size ranges, as well as for total macroporosity, at each of the three experiment plots.

Plot	Depth [m]	n	Macropore size range							
			0.5-5mm		5-8mm		8-10mm		Total	
			mean	CV%	mean	CV%	mean	CV%	mean	CV%
1	0.02	12	0.0032	26	0.0002	78	0	-	0.0036	24
	0.05-0.2	12	0.0021	18	0.0004	76	<0.0001	346	0.0026	20
	0.21-0.45	12	0.0013	53	0.0006	77	0.0003	90	0.0024	39
	0.46-0.75	11	0.0006	30	<0.0001	332	<0.0001	332	0.0006	28
	>0.75	1	0.0003	0	0	-	0	-	0.0003	-
2	0.02	10	0.0046	13	0.0011	32	0	-	0.0058	10
	0.05-0.2	12	0.0027	20	0.0016	52	0.0002	124	0.0046	22
	0.21-0.45	9	0.0031	38	0.0027	31	0.0004	47	0.0062	18
	0.46-0.75	11	0.0004	27	0.0003	145	0	-	0.0007	48
	>0.75	11	0.0004	26	<0.0001	332	0	-	0.0004	35
3	0.02	12	0.0039	24	0.0007	37	0.0009	77	0.0057	27
	0.05-0.2	13	0.0036	24	0.0024	37	0.0018	50	0.0087	26
	0.21-0.45	11	0.0023	18	0.003	28	0.0022	49	0.0078	25
	0.46-0.75	12	0.0002	38	0.0017	38	0.0025	29	0.0043	27
	>0.75	0	-	-	-	-	-	-	-	-

Table 2.4. Statistical significance (P) values of the inter-row, depth averaged, macropore area fraction comparisons between the three rows located at different distances from the tile drain. $P \leq 0.1$ indicates that the probability of the median macropore area fraction values being equal is 0.1 or less.

Comparison Test	Depth [m]	Macropore size range			
		0.5-5mm	5-8mm	8-10mm	Total
Plot 1 Rows 1-2	0.02 (0.00)	0.97	1.00	1.00	0.74
	0.14 (0.02)	0.60	0.71	1.00	0.54
	0.35 (0.06)	1.00	1.00	1.00	0.69
	0.69 (0.05)	0.11	1.00	1.00	0.11
Plot 1 Rows 1-3	0.02 (0.00)	0.77	1.00	1.00	0.89
	0.15 (0.03)	1.00	0.20	1.00	0.49
	0.37 (0.06)	0.46	0.91	0.97	0.66
	0.70 (0.04)	0.17	1.00	1.00	0.14
Plot 2 Rows 1-2	0.02 (0.00)	0.17	1.00	1.00	0.23
	0.11 (0.04)	0.63	1.00	0.91	0.23
	0.26 (0.06)	0.69	0.89	1.00	0.69
	0.57 (0.05)	0.89	0.40	1.00	0.11
	0.90 (0.08)	0.71	1.00	1.00	0.74
Plot 2 Rows 1-3	0.02 (0.00)	0.63	0.29	1.00	0.86
	0.13 (0.03)	0.97	1.00	1.00	0.86
	0.29 (0.04)	0.63	0.63	0.91	0.11
	0.58 (0.06)	0.23	1.00	1.00	0.91
	0.95 (0.05)	0.74	1.00	1.00	0.34
Plot 3 Rows 1-2	0.02 (0.00)	0.11	0.77	0.63	0.69
	0.15 (0.00)	0.20	0.06	0.46	0.20
	0.26 (0.04)	0.49	0.17	0.40	0.23
	0.50 (0.00)	0.51	0.03	0.63	0.20
Plot 3 Rows 1-3	0.02 (0.00)	0.03	0.34	0.11	0.03
	0.15 (0.00)	0.14	0.34	1.00	0.46
	0.26 (0.00)	0.71	0.11	0.40	0.34
	0.50 (0.00)	1.00	0.03	0.11	0.03

Values in parentheses denote standard deviation

Table 2.5. Statistical significance (P) values of the inter-plot, depth averaged, macropore area fraction comparisons. P ≤ 0.1 indicates that the probability of the median macropore area fraction values being equal is 0.1 or less.

Depth [m]	Plot 1 compared with plot 2				Plot 1 compared with plot 3				Plot 2 compared with plot 3			
	Macropore size range				Macropore size range				Macropore size range			
	0.5-5mm	5-8mm	8-10mm	Total	0.5-5mm	5-8mm	8-10mm	Total	0.5-5mm	5-8mm	8-10mm	Total
0.02	0.00	0.00	†	0.00	0.12	0.00	0.00	0.00	0.06	0.01	0.00	0.69
0.05-0.2	0.01	0.00	0.03	0.00	0.00	0.00	0.00	0.00	0.01	0.05	0.00	0.00
0.21-0.45	0.00	0.00	0.24	0.00	0.00	0.00	0.00	0.00	0.03	0.76	0.00	0.09
0.46-0.75	0.01	0.00	0.36	1.00	0.00	0.00	0.00	0.00	0.00	0.00	0.00	0.00

† No macropores in this size range observed

Table 2.6. Linear correlation (r) between total macropore area fraction at the four depth/depth intervals and mean hydraulic conductivity ($\log_{10}K$) of the surface, and B horizon soils.

K Subject area	Depth [m]			
	0.02	0.02 - 0.2	0.2 - 0.45	0.45 - 0.75
Surface	0.14	0.57	0.02	0.79
B Horizon	0.64	0.99	0.83	0.98

Chapter 3

Spatial and temporal influences on the hydraulic and structural properties of tile drained soil in southwestern Ontario

3.1 Introduction

Infiltration in agricultural settings with structured soils is heavily influenced by the significant temporal and spatial variability of soil hydraulic properties. While natural heterogeneity is undoubtedly a large source of in-field soil hydraulic property variability (e.g. *Nielsen et al*., 1973; *Vieira et al*., 1981), and is often treated stochastically (e.g. *Russo and Bresler*, 1981; *Yeh et al*., 1985), temporal variability has been found to have a more significant influence on soil properties (*Messing and Jarvis*, 1993; *van Es et al*., 1999; *Zhou et al*., 2008). It is well understood that the magnitude of temporal variability is largely governed by deterministic factors such as tillage (e.g. *Murphy et al*., 1993; *Moret and Arrúe*, 2007), crop type (*Bodner et al*., 2008), root growth (*Bodner et al*., 2008; *Mubarak et al*., 2009), climate (*Van Es et al*., 1993; *Bodner et al*., 2008; *Hu et al*., 2009), irrigation (*Mubarak et al*., 2009), moisture content (*Zhou et al*., 2008) and wheel traffic (*Alakukku*, 1996a; *Alakukku*, 1996b). In addition to temporally dependent factors, subsurface drainage can also be considered as a deterministic influence on soil variability, in the sense that subsurface drains inherently regulate/lower soil moisture at known locations which can in turn lead to reduced organic matter content (*Fausey and Lal*, 1992; *Frison et al*., 2009), and increased soil structural development (*Bouma et al*., 1979a). Subsurface drainage is a common feature in North American and European agricultural landscapes and should be considered as a potential factor in any comprehensive investigation of soil temporal and spatial variability.

The temporal variability of soil hydraulic properties is largely governed by wetting and drying cycles and macropore generative processes. In soils that have been recently tilled, wetting can promote aggregate disintegration (*Shiel et al*., 1988), and increased capillary forces associated with subsequent drying can potentially reduce structural porosity which results in a shift in the inter-aggregate pore size distribution towards smaller pores (*Ghezzehei and Or*, 2000). Conversely, desiccation cracks that form later in the growing season can increase intra-aggregate porosity (*Bodner et al*., 2008). It has been repeatedly shown that field saturated hydraulic conductivity (K_{fs}), and hydraulically effective mean pore radius (λ_m), can decrease rapidly immediately after tillage (e.g. *Starr*, 1990; *Murphy et al*., 1993), as a result of hydraulic compaction (*Mubarek et al*., 2009). Later in the growing season, K_{fs} has been shown to have an inverse correlation to soil moisture content (θ) in numerous studies (*Murphy et al*., 1993; *van Es*, 1993; *Lin et al*., 1998; *van Es et al*., 1999; *Zhou et al*., 2008) due to increased macroporosity; although, *Das Gupta et al*. (2006) found that hydraulic conductivity (K) was positively correlated to θ, which they attributed to increased hydraulic activity within the macropore network. While it is generally understood that soil infiltration capacity can fluctuate considerably late in the cropping season, quantitative assessments of late season temporal variability in soil pore size distribution and saturated/unsaturated hydraulic properties are notably scarce. Because evapotranspiration tends to decrease significantly during the post crop period, there is increased likelihood of downward water and solute flux; as a result, there is also greater risk for potential contaminants to be transmitted to tile drains and groundwater. Understanding the magnitude of seasonally variable risks to water resources requires thorough knowledge of seasonal influences on soil hydraulic property variability.

While the effects of tile drainage on soil hydraulic properties have been causally investigated in numerous previous works, the different combinations of soil types, geological and climate settings, and management practices that have been considered makes any attempt at broad scale interpretation and generalization difficult. However, there is abundant evidence within the existing body of literature to support the hypothesis that tile drains do in fact influence soil physical and hydraulic characteristics. In work conducted on a sandy clay soil in southwest Finland, *Shipitalo et al*. (2004) found that infiltration rates were twice as large above, as opposed to between, the tile drains. *Hundal et al*. (1976) observed that the installation of subsurface drainage led to greater hydraulic conductivity over the course of a longer term study of drainage system effects on the properties of a silty clay soil in Ohio. An explanation for why tile drainage may increase hydraulic conductivity was given by *Bouma et al*. (1979a) who noted in their work on clay soils in the Netherlands that the drier soil conditions associated with tile drainage promote drying and cracking, and deeper earthworm activity. Increased earthworm activity in the vicinity of tile drains has also been noted for sandy clay (*Nuutinen et al*., 2001), and clay (*Alakukku et al*., 2010), soils in Finland. However, as shown by *Alakukku et al*. (2010), increased earthworm abundance does not necessarily translate into greater hydraulic conductivity because at their site there was not a significant difference in hydraulic conductivity above as opposed to between tile drains. Similar results were observed in work conducted on a silt loam soil in Ohio where proximity to tile drains did not influence infiltration rates or sorptivity (*Fausey and Lal*, 1989); however, the presence of tile drainage reduced soil organic matter content (*Lal and Fausey,* 1993), which in turn led to differences in pore size distribution. In heavy clay soil in the Netherlands, *Bouma et al*. (1981) observed that the hydraulic conductivity of soil in the scar region above a tile drain was actually reduced in relation to comparable undisturbed soil, which they attributed to the disruption of natural soil structure during the tile installation process.

A number of methodologies exist to quantify changes in unsaturated soil hydraulic properties. Two of the more common approaches are based on either capillary theory (*Watson and Luxmoore*, 1986; *Dunn and Phillips*, 1991; *Bodhinayake et al*., 2004a), or tracking variation in empirical curve fitting coefficients such as the α parameter of *Gardner* (1958) (e.g. *Messing and Jarvis*, 1993; *Mohanty et al*., 1994; *Hu et al*., 2009).

The α parameter is an empirical fitting coefficient in the expression $K(\psi) = K_{fs} \exp(\psi\alpha)$, subject to $0 < \alpha < \infty$, and $-\infty < \psi \leq 0$; where *K* is hydraulic conductivity, *fs* denotes field saturated, and ψ is soil water pressure head. It was noted by *Philip* (1968) in the advent of quasilinear infiltration analysis that the value assigned to the α parameter reflects the relative importance of gravity and capillarity on infiltration processes, with smaller values being indicative of fine textured soils where capillary forces dominate and larger values being indicative of coarse textured soils where gravity tends to dominate. The dynamic nature of α within individual soils was identified by *Parlange* (1972) who noted that α is a function of ψ in real soils. By relating α to sorptive length (e.g. *Philip*, 1985), the effective cylindrical pore radius can be calculated according to capillary theory by $R = \sigma\alpha / \rho g$, where *R* is pore radius, σ and ρ are surface tension and density of water respectively, and *g* is acceleration due to gravity. The concept of using α to estimate an effective hydraulic radius was developed further by *White and Sully* (1987) with their description of micro-, and macro-scopic capillary length scales. *Lin et al*. (1997) effectively used the *White and Sully* (1987) approach to estimate hydraulically active pore size in structured soils as a function of applied pressure using a tension infiltrometer, and showed that the effective pore radius increases with increased clay content at higher application pressures. However, because factors such as tortuosity, pore-wall surface roughness, and pore connectivity all affect flow in real soils, *Reynolds and Topp* (2008) propose that it is more accurate to view α as an index parameter.

The use of capillary theory to quantify hydraulically effective porosity is based on the assumption that flow pathways with progressively larger effective diameters will contribute to unsaturated flow as soil moisture pressure head increases. With this method, the specific contribution to flow from individual hydraulically effective pore size intervals can be determined. This concept has been extensively used in past work (e.g. *Watson and Luxmoore*, 1986; *Dunn and Phillips*, 1991; *Azevedo et al*., 1998; *Bodhinayake et al*., 2004a; *Buczko et al*., 2006) where it has been repeatedly shown that very little porosity in structured soils is attributable to macropores and yet they typically transmit a large proportion of total water flux in wet soil conditions.

There is currently very little quantitative information regarding the influence that tile drains have on soil hydraulic properties and field scale infiltration patterns; however, there is considerable interest in assessing both groundwater and surface water quality and quantity in tile-drained agricultural settings. In order to improve our ability to predict water and solute movement in these environments, we need a greater understanding of spatial and temporal soil hydraulic property variability. Within the same context, greater understanding of soil structure and macroporosity temporal variability is of particular importance because of the strong influence that macropores have on infiltration. Currently, very little scientific attention has been given to macropore distribution relative to tile drains, or to differences between observed, and hydraulically effective macroporosity, relative to tile drains. Because tile drains influence soil moisture distribution, it is reasonable to expect that soil structure will also be influenced by the presence of tile drains. Although it is known that soil structure will change over time, the question of whether or not tile drains impart a spatial element to this change has not yet been addressed.

The objectives of this part of the overall study are: 1) to evaluate temporal changes in soil structure based on measurements of unsaturated and saturated soil hydraulic properties made during wet and dry soil conditions, 2) to evaluate the influence of tile drains on the soil hydraulic properties, and 3) to compare measurements of hydraulically effective macroporosity with measurements of visible macroporosity that were made at the same field locations.

To accomplish the objectives, soil structure and hydraulic properties are quantified and compared based on: piecewise linear $\alpha'(\psi)$ and $K(\psi)$ relationships, K_{fs} values, and hydraulically effective pore size distributions; that were all measured before and after an extended period of dry weather. The field activities involve a series of tension and double ring infiltrator tests that were conducted at known positions relative to tile drains at three locations within an individual cropped field that exhibits variable A and B horizon composition. In total, 54 tension and 54 double ring infiltration tests were conducted. Subsequent to the infiltration tests, extensive macropore characterization was carried out at each plot in order to quantify macroporosity between the near surface and tile drain depth. Data from the two different infiltration testing methods, combined with the results of the macropore characterization, facilitates an evaluation of infiltration dynamics that sheds light on the influence that macropores have on water distribution in structured, tile drained, soils.

3.2 Methods and materials

3.2.1 Site description

The agricultural field where the work was conducted is located at N43°09’55”, W81°01’08”, near the town of Kintore in southern Ontario, Canada. Soils at the site are mapped as poorly drained dark grey Gleysolic, Maplewood silt loam series underlain by clay, and clay loam till at the south end of the field and well drained grey brown Luvisol of the Honeywood silt loam series underlain by calcareous loam till at the north end (*Experimental Farms Service*, 1987). Beneath the surface soils is a complex layering of Quaternary sediments consisting of subglacial diamictons and glacifluvial deposits (*Rudolph and Parkin*, 1998) that extend to a depth of approximately 45 m (*Sado and Vagners*, 1975). Perforated plastic tile drains, 10 cm in diameter, were installed at the field in 1985. The tiles are spaced 12-15 m apart and are buried at depths of 0.6-1 m.

Minimum tillage practices have been utilized at the site since 1995. Prior to 2004 both liquid swine manure and commercial fertilizers were used as soil nutrient amendments; however, between 2004 and 2009 only commercial fertilizer was used. In 2008 the field was planted in winter wheat (*Triticum aestivum* L.) that was harvested in mid July and in May of 2009 the field was planted in soybean (*Glycine max L.*) that were harvested in late September. A meteorological monitoring station that recorded air temperature and precipitation on an hourly basis was in operation at the site between July 2007 and October 2009. Past research on nitrate flux in agricultural settings and riparian zone denitrification has been conducted at the same site (*Cey et al.*, 1998; *Cey et al.*, 1999).

3.2.2 Experimental plot configuration

Within the single field, three individual locations with different soil properties and topographic settings were selected for study, which will hereinafter be referred to as plots 1, 2 and 3 (Figure 3.1). Infiltration experiments were conducted at plots 1 and 2 during mid-August and then again in mid-

September of 2009, and at plot 3 during mid-August 2008. To avoid soil that had been influenced from prior work, the September 2009 experiments at plots 1 and 2 were conducted approximately 5 m up-gradient from where the August experiments were conducted, but still along the same tile lines. Each plot consisted of three rows of infiltration test areas, with each row parallel to the tile drain (Figure 3.2). Row 1 is located immediately above the drain, and rows 2 and 3 are located 1-1.5 m and 3-4 m from the drain respectively. Each row contained three or four test areas, each spaced 1-2 m apart. Tile drains at each plot were located with a subsurface pipe inspection/location system prior to the infiltration tests.

3.2.3 Soil analysis

At each plot, A horizon soil characterization is based on the laboratory analysis of six, 5 cm diameter by 10 cm long soil cores that were extracted from the 5 to 15 cm depth interval. Three of the A horizon cores were extracted directly above the tile and the other three were extracted along a transect 2 m from the tile; core spacing along each transect was 2 m. The B horizon was characterized with 8 cm diameter by 10 cm long soil cores that were extracted between depths of 30 to 100 cm. The B horizon samples were extracted from selected locations in an attempt to reflect the variety of subsoil conditions present at each plot. There were 4, 6, and 6, B horizon cores extracted from plots 1, 2, and 3, respectively.

Organic matter content in the A horizon cores was determined using the Walkley-Black acid digestion method (Walkley and Black, 1934), particle size distribution for all of the cores was determined with the pipette method and bulk density was determined by oven drying, assuming that the volume of soil inside the cores represented undisturbed soil. Prior to the soil physical property analysis, the hydraulic conductivity (K_{sat}) of the B horizon soil cores, in generally undisturbed condition, was determined with either the falling, or constant head permeameter method (*Reynolds*, 2008).

3.2.4 Tension infiltration tests

A tension infiltrometer (TI) with a 20 cm diameter base (Soil Measurement Systems) was used to characterize unsaturated soil hydraulic properties. Progressively decreasing tension settings of 15, 10, 5, 2, 1 and 0 cm were used during each TI test. The tension values were selected with the intention of obtaining data for relatively wet soil conditions typical of shallow water table, tile drained settings and to characterize soil hydraulic properties at relatively low tensions where it has been shown that macropores become hydraulically active (*Jarvis*, 2007). During each TI experiment a 10 cm long TDR probe was installed below the disk at approximately a 30° angle from horizontal and water content was monitored continuously in 10 s intervals with a Campbell Scientific Inc. TDR 100 time domain reflectometry system. Initial soil water contents at each test area were also recorded using the same system. The soil surface where the TI disk was placed was carefully prepared by cutting any vegetation down to ground level and smoothing the surface to the extent that all surface irregularities were masked by a 3-5 mm layer of fine sand that was emplaced to provide a level surface for the TI disk to sit, and to ensure good hydraulic connection between the disk and the soil (*Reynolds and Zebchuk*, 1996). Care was taken to minimize smearing of the soil surface and to avoid areas with excessive soil compaction from wheel traffic. At each tension setting, infiltration rates were usually measured in five minute intervals until quasi-steady-state conditions were observed before the applied tension was reduced to the next setting. In some cases, very high infiltration rates were observed for low tension settings and the measurement time intervals were reduced accordingly.

In order to determine values for $K(\psi)$ and $\alpha'(\psi)$, the tension infiltrometer (TI) data was analyzed according to the method presented by *Reynolds* (2008), which is briefly defined as follows:

$$\alpha'_{x,x+1} = \frac{\ln(Q_x / Q_{x+1})}{(\psi_x - \psi_{x+1})} \qquad \text{where } \psi \le 0 \tag{3.1}$$

$$K'_{x,x+1} = \frac{G\alpha'_{x,x+1} Q_x}{a(1 + G\alpha'_{x,x+1}\pi r)(Q_x / Q_{x+1})^P} \tag{3.2}$$

$$K(\psi_x) = \frac{\left[K'_{x-1,x} \exp\left(\alpha'_{x-1,x}\psi_x\right) + K'_{x,x+1} \exp\left(\alpha'_{x,x+1}\psi_x\right)\right]}{2} \qquad \text{x = 2,3,...n-1} \tag{3.3}$$

$$K(\psi_x) = K'_{x,x+1} \exp\left(\alpha'_{x,x+1}\psi_x\right) \qquad \text{for x = 1} \tag{3.4}$$

$$K(\psi_x) = K'_{x-1,x} \exp\left(\alpha'_{x-1,x}\, \psi_x\right) \qquad \text{for } x = n \qquad (3.5)$$

where x represents the applied pressure head (ψ) settings (L); G is a shape factor which was set constant at 0.237; Q is the observed quasi steady state flow rate ($L^3\ T^{-1}$); *a* is the disk radius (L); and $P = \psi_x / (\psi_x - \psi_y)$.

3.2.5 Double ring infiltration tests

Following each TI infiltration test, the contact sand was vacuumed off the soil surface and a double ring (DR) infiltration test was conducted at the same position in order to obtain an estimate of K_{fs}. Both the 30 cm diameter inner and 55 cm diameter outer rings were hammered approximately 5 cm into the soil. A constant water level of approximately 10 cm was maintained throughout the experiment in both the inner and outer reservoirs by separate 40 liter Mariotte bottles. Infiltration rates were measured by tracking water level in the Mariotte bottles. The final infiltration rates were obtained after quasi steady-state conditions were observed in the inner ring, which usually required two to three hours. Estimates of field saturated hydraulic conductivity were obtained from the double ring infiltration data using the method prescribed by *Reynolds et al*. (2002) as follows.

$$K_{fs} = q_s \Big/ \left(\left[\frac{h}{0.316\pi d + 0.184\pi a} \right] + \left[\frac{1}{\alpha^*(0.316\pi d + 0.184\pi a)} \right] + 1 \right) \qquad (3.6)$$

Where q_s is the observed quasi steady-state infiltration rate , *h* is depth of ponded water, *d* is the ring insertion depth, *a* is the inner ring radius and α^* is the calculated α' value for the 1 to 0 cm tension interval of the TI experiment that was conducted at the same test location.

3.2.6 Macropore characterization

Macropore characterization was conducted at each plot after the first set of infiltration experiments was conducted. Between the infiltration tests and macropore characterization, 20 liters of blue dye solution (Brilliant Blue FCF) was applied to the soil from within a 50 cm by 50 cm square reservoir that was positioned on center with each of the individual infiltration test locations. The dye was applied under falling head conditions with an initial head of approximately 8 cm. Following dye application, horizontal surfaces were excavated beneath each infiltration test area in order to characterize macroporosity between the surface and tile drain depth. On each excavated surface, the number of macropores in 0.5-5 mm, 5-8 mm, 8-10 mm, and 10-12 mm diametric size intervals were manually counted. Total cylindrical macropore surface area was calculated by multiplying the mean area of each size interval by the number of macropores observed within that interval. Fracture area was estimated by measuring the total length of fractures on each surface and then multiplying the result by 0.5 mm, which is an approximate average fracture width. Total macroporosity is the sum of the cylindrical and fracture macropore areas.

At plot 1, forty-eight surfaces were excavated on four levels situated between depths of 0.02-0.76 m, and at plot 2 there were fifty-three surfaces on five levels excavated between depths of 0.02-1.00 m. At plot 3 there were sixty surfaces excavated on five levels between depths of 0.02-0.80 m; however, macropores were only counted on the forty-eight surfaces located between 0.02-0.5 m because the soil below approximately 0.6 m became increasingly coarse grained/gravelly and visible macropores terminated at the transition.

For considerably more detail on the macropore characterization methodology, readers are referred to Chapter 2, which deals specifically with macropore spatial variability.

3.2.7 Effective Porosity

The hydraulically effective porosity ($\bar{\varepsilon}$) for each pore size interval (r) associated with the tension settings applied during the TI tests was calculated using the method of *Dunn and Phillips* (1991). According to this method, the mean number of hydraulically active pores ($\overline{N}(r)$) is calculated according to:

$$\overline{N}(r) = \left[8\mu\Delta I/(\pi\rho g)\right]\cdot\left[\int_{r(x)}^{r(y)} r^{-4}dr \Big/ \int_{r(x)}^{r(y)} dr\right] \tag{3.7}$$

Where: $r = -0.15/\psi$ (for r and ψ in units of centimeters according to *Dunn and Phillips*, 1991), subject to $\psi < 0$; μ is the dynamic viscosity of water ($ML^{-1}T^{-1}$); ΔI is the difference in infiltration rate (LT^{-1}) between tension settings x and y; ρ is the density of water (ML^{-3}); and g is acceleration due to gravity (LT^{-2}). From $\overline{N}(r)$, $\bar{\varepsilon}(r)$ is calculated according to:

$$\bar{\varepsilon}(r) = \overline{N}(r)\pi\int_{r(x)}^{r(y)} r^{2}dr \Big/ \int_{r(x)}^{r(y)} dr \tag{3.8}$$

The pore radii associated with tension settings of 15, 10, 5, 2, and 1 cm are 0.01, 0.015, 0.03, 0.075, and 0.15 cm respectively. A pore radius of 0.5 cm was used as the effective pore size for $\psi(0)$ because 0.5 cm was the maximum radius of macropores observed near surface at any of the three plots.

3.2.8 Statistical methods

The two sided rank-sum test (as defined in *Helsel and Hirsch*, 1992) was used to determine the level of statistical significance in the hydraulic parameter comparison tests. The null hypothesis for the rank-sum test is that the two groups of data being compared have the same median value; accordingly, if the rank-sum P is less than 0.10, there is less than a 10% chance that the groups share the same central value.

3.3 Results

3.3.1 Soil analysis

Results from the A and B horizon soil analysis are presented in Tables 3.1 and 3.2 respectively. The physical properties of the A and B horizon soils are considerably different between the 3 plots, and classification of the A horizon soils is in subtle disagreement with the regional soil survey (Experimental Farms Service, 1987). At plot 1, the A horizon consists of a fine sandy loam with 6.3 % organic matter that is underlain by a poorly sorted sandy-silt B horizon. At plot 2, the A horizon consists of a loam with 3.2 % organic matter that is underlain by a well sorted silty-sand B horizon. At plot 3, the A horizon consists of a silt loam with 5.3 % organic matter that is underlain by a poorly sorted silty-sand with up to 34% gravel in some areas. Geometric mean field saturated hydraulic conductivity of the surface soil was 79.4, 12.6, and 251.2 cm d^{-1}, at plots 1, 2, and 3, respectively. The hydraulic conductivity of the B horizon was also highly variable between the three plots, and the geometric mean values were 0.25, 0.8, and 63.1 cm d^{-1}, at plots 1, 2, and 3, respectively.

3.3.2 Weather and soil conditions

Temperature and precipitation at the site during the July to October time frame in both 2008 and 2009 are shown in Figure 3.3. Work at plot 3 commenced on August 18th, 2008, and in the week prior to the infiltration experiments, 7 mm of precipitation was received. During the 4-day period that the infiltration experiments were underway, another 2 mm of precipitation was received. The mean initial soil moisture content (Θ_i) at the beginning of the TI experiments was 0.23 (n = 12, CV = 17%)

and assuming that the soil beneath the infiltrometer disk at the end of each TI experiment represented field-saturated conditions, the mean field saturated soil moisture content (Θ_s) was 0.43 (n = 12, CV = 3%) at the end of the TI experiments.

The first set of infiltration experiments at plots 1 and 2 commenced on August 14th, 2009. Between August 7th and the 14th there was 51 mm of rainfall received. Over the 4-day period that the infiltration experiments were conducted the site received less than 1 mm of rainfall. Mean Θ_i at the start of the infiltration testing was 0.29 (n = 12, CV = 13%) at plot 1, and 0.22 (n = 12, CV = 8%) at plot 2. Again assuming that the soil beneath the infiltrometer disk at the end of each TI experiment represented field-saturated conditions, mean Θ_s was 0.44 (n = 12, CV = 2%) at plot 1 and 0.34 (n = 12, CV = 5%) at plot 2.

Between the first and second set of infiltration experiments at plots 1 and 2, the site received 44 mm of rainfall, of which less than 1 mm was received after September 9th, and as a result, soil conditions at plots 1 and 2 were significantly drier ($P < 0.1$) for the second set of infiltration experiments which commenced September 16th. The mean Θ_i for the second set of experiments was 0.21 (n = 9, CV = 21%) at plot 1, and 0.16 (n = 9, CV = 21%) at plot 2. Mean Θ_s, as observed at the end of the second set of TI experiments was 0.43 (n = 9, CV = 3%) at plot 1, and 0.37 (n = 9, CV = 8%) at plot 2. There was no precipitation received at the site during the second set of infiltration tests.

At plots 1 and 2 there was no significant ($P < 0.1$) difference in the soil moisture content above vs. laterally away from the tile drain; although, during August 2008 at plot 1, there was some indication that moisture contents were lower in the vicinity of the tile drain because mean Θ_i was 0.27, 0.29, and 0.32, in rows 1, 2, and 3, respectively (Figure 3.2). At plot 3 the mean initial soil moisture content was significantly ($P < 0.1$) less in row 3 than in row 1 (0.20 vs. 0.26); however, the field saturated soil moisture content data obtained at the end of the TI experiments did not indicate the same trend. In the case of plot 3, it is important to note that the B horizon soil cores extracted from beneath row 3 had the highest percentage of coarse material and the DR tests conducted on row 3 had the largest K_{fs} values, which suggests comparably good natural subsurface drainage in that area of the field.

3.3.3 Macropore characterization

Dye infiltration patterns verified macropore hydraulic continuity from the surface to tile drain depth at plots 1 and 2; however, it is important to note that the number of dye stained pores at tile depth was very low in comparison to the A horizon and the top of the B horizon. At plot 3, visible macropores appeared to terminate at a textural boundary located at a depth of approximately 70 cm, where the deeper soil became noticeably coarser grained. Dye infiltration patterns at plot 3 showed that macropores serve as preferential flow paths connecting the field surface to highly permeable subsurface deposits.

The highest macroporosity was located in the top 40 cm of the soil profile at each of the three plots (Figure 3.4), where the mean values of maximum macroporosity were 0.3%, 0.6%, and 0.9% at plots 1, 2, and 3, respectively. The lowest macroporosity was located at tile depth at plots 1 and 2, where macropores occupied less than 0.1% of the exposed soil surfaces. As reported in chapter 2, the presence of tile drains did not induce significant variability in macroporosity at any of the three plots.

3.3.4 Spatial variability in hydraulic properties with respect to tile drain location

Arithmetic mean values of $\alpha'(\psi)$, $K(\psi)$, and K_{fs}, for each row of test areas at plot 1, 2, and 3, are presented in Figures 3.5, 3.6, and 3.7. Mean K_{fs} values at plots 1 and 2, were a respective 50% and 140% higher, in row 1 than in row 3 during the August 2009 experiments, and a respective 56% and 162% higher, in row 1 than in row 3 during the September 2009 experiments; however, the difference is only statistically significant (at $P = 0.1$) at plot 2 during the September experiments. At plot 3 during August 2008, mean K_{fs} was actually 126% lower in row 1 than in row 3; however, the difference is not statistically significant. Again it is important to note that the B horizon at plot 3 also had the highest mean K_{sat} and the soil composition was the least well sorted of the three plots; in addition, the row 3 soil surface areas that exhibited the highest K_{fs} values were very close to the subsurface areas with the highest gravel content. Tile drain influences on $\alpha'(\psi)$ and $K(\psi)$ were not statistically significant at any of the three plots.

3.3.5 Temporal variability in hydraulic properties

Differences in mean $\alpha'(\psi)$, $K(\psi)$, and K_{fs} values between wet and dry soil conditions at plots 1 and 2, are presented in Figures 3.8 and 3.9. Between August 2009 and September 2009, mean K_{fs} increased significantly ($P < 0.1$) at plot 1 and 2 by 67% and 25%, respectively.

The general trend observed with TI results at the lowest tension interval (-1 to 0 cm) is consistent with results from the DR. At both plots 1 and 2, mean $K(\psi_{-1,0\mathrm{cm}})$ increased between August and September; however, the difference is only statistically significant ($P < 0.1$) at plot 2. At tensions greater than 2 cm, $K(\psi)$ was consistently higher in August as compared to September and in all but two instances (the 15 to 10 cm and 5 to 2 cm tension intervals at plot 2), the differences were statistically significant.

Differences in $\alpha'(\psi)$ values between the August and September experiments generally follow the same pattern as the $K(\psi)$ data. For the two lowest tension intervals, α values increased between August and September whereas for the three highest tension intervals, the α values generally decreased. Differences in α' values between the August and September experiments were statistically significant ($P < 0.1$) in all but three instances (the 2 to 1 cm tension interval at plot 1 and the 15 to 10 cm and 5 to 2 cm tension intervals at plot 2).

3.3.6 Effective Porosity

Results from the effective porosity calculations are presented in Table 3.3. At plots 1 and 2 during August 2009, and plot 3 during August 2008, the highest effective porosity for pores 0.02 to 1 cm in diameter was attributed to pores within the 0.03 to 0.15 cm size range. At plot 1, porosity attributable to pores 0.03 to 0.15 cm in size decreased significantly ($P < 0.01$) between August 2009 and September 2009; whereas porosity attributable to pores 0.3 to 1 cm in size increased, although the difference was not significant ($P = 0.24$). Between August 2009 and September 2009 at plot 2, the effective porosity attributable to pores greater than 0.15 cm increased significantly ($P < 0.1$); whereas porosity attributable to pores 0.03 to 0.15 cm in size decreased, although the differences were not significant ($P = 0.12$ for 0.03 – 0.06 cm pores, and $P = 0.27$ for 0.06 – 0.15 cm pores). At both plots 1 and 2, total hydraulically effective macroporosity decreased between August 2009 and September 2009, although the difference was only statistically significant at plot 1. While the presence of tile drains was not found to significantly influence the effective porosity distribution at any of the plots (Figure 3.10), intra-plot differences were significant ($P < 0.1$) for effective porosity measured at plot 3 during August 2008, and at plots 1 and 2 during August 2009. In contrast, differences in effective porosity between plot 1 and 2 under the drier conditions experienced during the September 2009 experiments were not significant. Mean total effective macroporosity (i.e. pores 0.03 to 1 cm in diameter) varied from a low of 0.0032 % at plot 2 during the September 2009 experiments to a high of 0.0082% at plot 1 during the August 2009 experiments.

The coefficient of variation (CV) for the effective porosity measurements was highly variable among the different pore size intervals. For pores 0.02 to 0.03 cm, and 0.3 to 1.0 cm in size, the CV was generally large, and ranged from 50 to 1776 %, and 87 to 158 % for the two respective size intervals;

whereas the CV for pores 0.03 to 0.3 cm in size was overall much smaller, and ranged from 22 to 79%.

3.4 Discussion

3.4.1 Tile drain influence on hydraulic properties

The influence of tile drains on K_{fs} was not consistent among the three plots. At plots 1 and 2, the respective mean K_{fs} was approximately 50% and 150% higher over the drains, which correlates well with the observations made by *Shipitalo et al*. (2004) who noted that infiltration rates in a sandy clay soil in Finland were twice as high above, as opposed to between, the tile drains. Furthermore, at plots 1 and 2, the maximum and minimum individual K_{fs} values were consistently observed in the row of test areas above the drain, and furthest from the drain, respectively. However at plot 3, the pattern was reversed and the maximum, and minimum, individual K_{fs} values were observed in the row of test areas furthest from, and above, the drain respectively; while average K_{fs} was 126% lower in the row above the drain than in the row furthest from the drain. It is important to note that the soil in row 1 at plot 3 was impacted by wheel traffic that potentially influenced K_{fs}. Once again, it is also important to note that the shallow subsurface soil at plot 3 was considerably more permeable than at plot 1 and 2, and would therefore provide relatively effective natural subsurface drainage in that area of the field. In such a case, the disruption of the natural soil structure and layering during the tile installation process can reduce soil permeability. This phenomenon has been previously noted by *Bouma et al*. (1981) who observed that disturbed soil above a tile drain in a Netherlands clay soil had a K_{sat} that was half that of the surrounding undisturbed soil.

3.4.2 Visible vs. hydraulically effective macroporosity

The hydraulically effective macroporosity (Table 3.3) attributed to pores 0.03-1.0 cm in diameter was approximately 100 times less than the near surface visible macroporosity (Figure 3.4). Similarly large differences have been reported in previous work. In example, *Buczko et al*. (2006) used data from *Trojan and Linden* (1998) to show that the hydraulically effective macroporosity in a Minnesota silt loam was approximately 600 times less than the macropore area identified with soil staining. Similarly, *Bodhinayake and Si* (2004c) found that hydraulically effective macroporosity was 1000 times less than macroporosity calculated from soil core moisture retention data. When comparing the near surface macroporosity values determined with the two methods used in this work it is important to note some important differences. Firstly, the TI measurements were obtained from the soil surface, where raindrop impact can potentially seal macropores up to 0.5 cm in diameter (*Ela et al*., 1992), while visible macroporosity was calculated from surfaces that were approximately 2 cm below ground surface and were therefore not subject to raindrop surface compaction. Secondly, calculating effective porosity using Poiseuille's law in conjunction with capillary theory assumes laminar, vertical flow through a straight sided cylindrical tube. Such an ideal flow scenario is highly unlikely in near surface macroporosity, where worm burrow orientation is not necessarily vertical (*Mckenzie and Dexter*, 1993), and macropores can routinely host plant roots (*Stewart et al*., 1999). As a result, flow efficiency through near surface macropores can be expected to be greatly reduced in relation to ideal conditions; therefore, more macropores would be required to transmit an equivalent flow.

3.4.3 Temporal variability

The assessment of hydraulic property temporal variability demonstrated that the surface soils at both plots 1 and 2 experienced significant structural modification between the comparably wet August 2009 conditions and the drier conditions experienced during September 2009. Because crop root growth was negligible during the one month interval between the infiltration tests, it can be expected that the majority of the variability was the result of wetting and drying processes. The observed trends in soil variability were consistent between the two plots. Results from the tension infiltration experiments show that both the piecewise linear $\alpha'(\psi)$, and $K(\psi)$ parameters, at applied tensions greater than 2 cm, decline between August and September; whereas the same two parameters increase at applied tensions less than 1 cm. The changes in the $\alpha'(\psi)$ relationship indicate that capillary forces become increasingly important for unsaturated flow processes as soil dries, while gravitational forces become more important in saturated, or nearly saturated, conditions. K_{fs} also increased as the soil at plots 1 and 2 dried, which is consistent with observations from previous investigations that considered antecedent soil moisture content influences on infiltration characteristics (*van Es et al*., 1993; *Lin et al*., 1998; *van Es et al*., 1999; *Zhou et al*., 2008). While the increase in K_{fs} may seem counterintuitive since hydraulically effective macroporosity decreased at both plots between August and September, it is important to note that the reduction in macroporosity was primarily attributed to a reduction in the number macropores with diameters less than 0.15 cm and 0.3 cm, at plots 1 and 2, respectively, whereas macroporosity attributable to pores larger than 0.3 cm increased by approximately 85% at both plots. Because the ability of a cylindrical macropore to conduct water increases in proportion to the 4th power of the radius, the increase in macroporosity attributable to large macropores was able to facilitate an increase in K_{fs} even though total hydraulically effective macroporosity decreased. Macroporosity has been noted to increase throughout the growing season for a number of reasons. *Starr* (1990) noted that worms can create additional macroporosity as they move to the surface in response to soil wetting that occurs in the fall, which in turn leads to higher infiltration rates; whereas *Murphy et al*. (1993) attributed increased late season K_{fs} to increased soil cracks, which is likely more akin to the scenario observed in this work. Because cracks have also been shown to promote macropore connectivity (*Shipitalo et al*., 2004), hydraulically effective macroporosity attributable to pores with diameters greater than 0.3 cm, and K_{fs} values, could have both increased between August and September as a result of increased macropore network continuity.

3.4.4 Infiltration dynamics – tension vs. double ring infiltrometer

When the $K(\psi)$ values obtained with the TI are compared to the K_{fs} values it is apparent that at plots 1 (Figure 3.5b,d and Figure 3.8b) and 2 (Figure 3.6b,d and Figure 3.9b), $K(\psi)$ estimates at the low tension settings are considerably greater than the K_{fs} estimates, which tend to be more closely aligned with the $K(\psi)$ values obtained for tension settings in the 3 to 7.5 cm range. It should be noted that macropores are not generally hydraulically active at tensions greater than 6 cm (*Jarvis*, 2007), so the K_{fs} values at plots 1 and 2 are generally more reflective of the soil matrix, without macropore contribution. However, at plot 3 (Figure 3.7b) this tendency is not evident and the low tension $K(\psi)$ values and the K_{fs} values are generally much closer together, suggesting that macropores are actively contributing to flow during the DR test.

When considering these method-dependent differences in infiltration characteristics, it is also important to note both the time, and volume of water, involved with the two infiltration methods. With the TI, quasi steady-state infiltration conditions were typically achieved after 15-25 minutes at each tension setting and the volume of water infiltrated at each setting was in some cases limited by the reservoir size, which is 1.65 liters. With the DR, 2-3 hours were required to reach quasi steady-state infiltration conditions and water volume was not a limiting factor. Based on these differences, quasi steady-state conditions are inherently different between the two methods.

Considering that the soil at each of the three plots contains abundant vertically continuous macropores, it is to be expected that a significant amount of vertical flow would take place beneath the TI disk at low applied tensions, and as a result, the infiltration pattern will be much different than that predicted with equation 3.2, which is based on ‘bulb’ shape three-dimensional infiltration geometry. It can therefore be surmised that equation 3.2 may not be entirely appropriate for determining $K(\psi)$ at low tensions. It is also quite possible that the TI reservoir used in this work did not hold enough water to bring the soil matrix and macropore regions into equilibrium at the low tension settings. The DR measurements on the other hand, would better reflect infiltration conditions when the soil matrix and macropores were in hydrostatic equilibrium, and would therefore better reflect the hydraulic behavior of the bulk soil. Accordingly, high K_{fs} values will therefore reflect conditions where macropores can remain hydraulically active over long periods of time, such as the case observed at plot 3 where macropores were connected to very permeable B horizon deposits. Conversely, low K_{fs} values reflect conditions where macropores cannot remain active as high velocity preferential flow conduits because they are essentially dead-end pores, such as the case for the majority of the macroporosity at plots 1 and 2. However, because the DR method is subject to influence from processes associated with continuous positive head conditions that can potentially reduce the infiltration rate, such as structure degradation, clay and organic matter swelling, slaking, eluviations, and air entrapment, it is quite likely that the K_{fs} values are somewhat underestimated.

Based on observations made in this work, it appears as though the DR tests provide insight on the ability of the macropores to remain hydraulically active under saturated conditions, at the point when pressure heads within the matrix and macropore regions have equilibrated. Comparatively, the TI tests appear to reflect the short-term capability of the macropores to transmit water during the early stages of a downward moving wetting front, at which time large hydraulic gradients between the matrix and macropore regions facilitate high rates of water imbibition into the matrix from the macropores, which emulates (albeit temporarily) the effect of having an increase in infiltration surface area. As a result, the TI method applied here will invariably overestimate K in nearly saturated conditions on surfaces underlain by low permeability deposits.

3.5 Conclusions

Although tile drains do not appear to significantly influence the unsaturated surface soil hydraulic properties at this site, evidence does suggest that they can influence K_{fs}. Of the three test plots investigated, the two with the lowest B horizon K_{sat} had notably higher surface soil K_{fs} values immediately above the tile drain; while the plot with the highest B horizon K_{sat} had the lowest K_{fs} values observed above the drain, which is thought to be the result of the tile installation process that disrupted the natural soil structure.

Post cropping season temporal variability caused significant changes in the saturated, and unsaturated soil hydraulic properties, as well as the hydraulically effective porosity pore size distribution. In the drier soil conditions, K_{fs} and $K(\psi)$ where $\psi \geq -1$ cm, were both higher than in the comparably wet soil conditions. The dry soil also had a greater proportion of hydraulically effective macroporosity attributed to large macropores (> 0.3 cm in diameter), while overall hydraulically effective macroporosity decreased as the soil dried. Changes in the piecewise linear $\alpha'(\psi)$ parameter values between wet and dry conditions support the observed changes in the hydraulically effective macropore distribution. In drier soil, the reduction in $\alpha'(\psi)$ when ψ is approximately less than -2 cm indicates that capillary forces become more significant within the smaller pores, while the increase in $\alpha'(\psi)$ at higher ψ values indicates that gravitational forces become more significant in the larger pores. These results suggest that soil shrinkage associated with drying causes a decrease in the size of small macropores that is concurrent with an increase in the size of large macropores (i.e. cracks may appear or enlarge).

The results from this work support the hypothesis that the application of high rates of liquid manure on dry soil may in fact increase the risk of nutrient loss to tile drains and shallow groundwater, as compared to soil that is slightly wetter. Because the post growing season surface soil hydraulic property variability was found to be so significant in this work, it is apparent that conceptual models of vadose zone flow and transport processes will become more physically realistic if soil temporal variability can be taken into account.

3.6 Figures and Tables

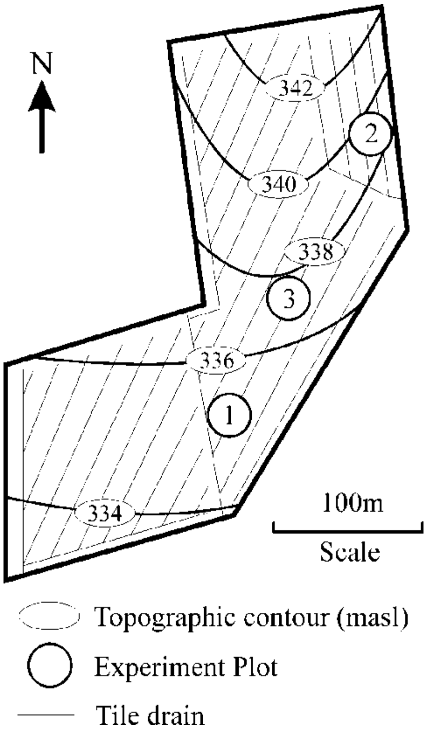

Figure 3.1. Relative location of the three experimental plots with respect to tile drain positions, topography, and the field boundary.

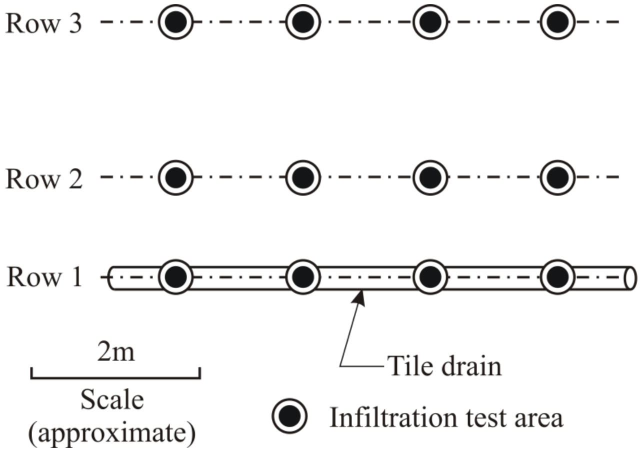

Figure 3.2. Plan view of the row-wise orientation of infiltration test areas relative to the tile drain location, at the three experimental plots.

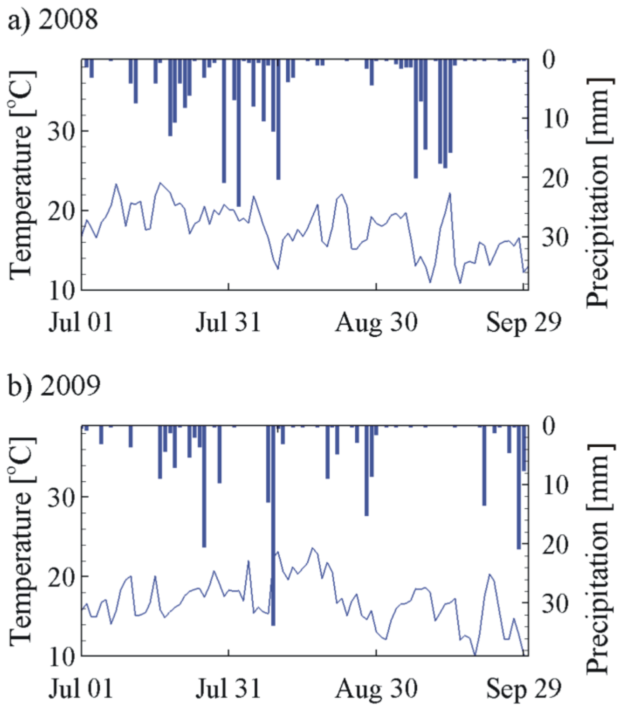

Figure 3.3. Daily mean temperature and precipitation at the field site for the July to October time interval during, a) 2008, and b) 2009.

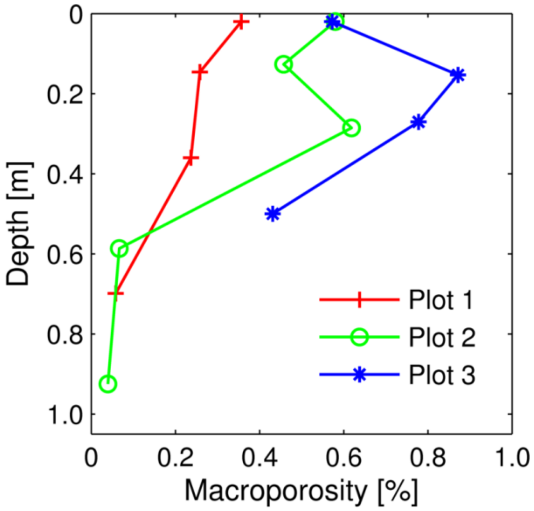

Figure 3.4. Mean macroporosity as a function of depth at plots 1, 2, and 3.

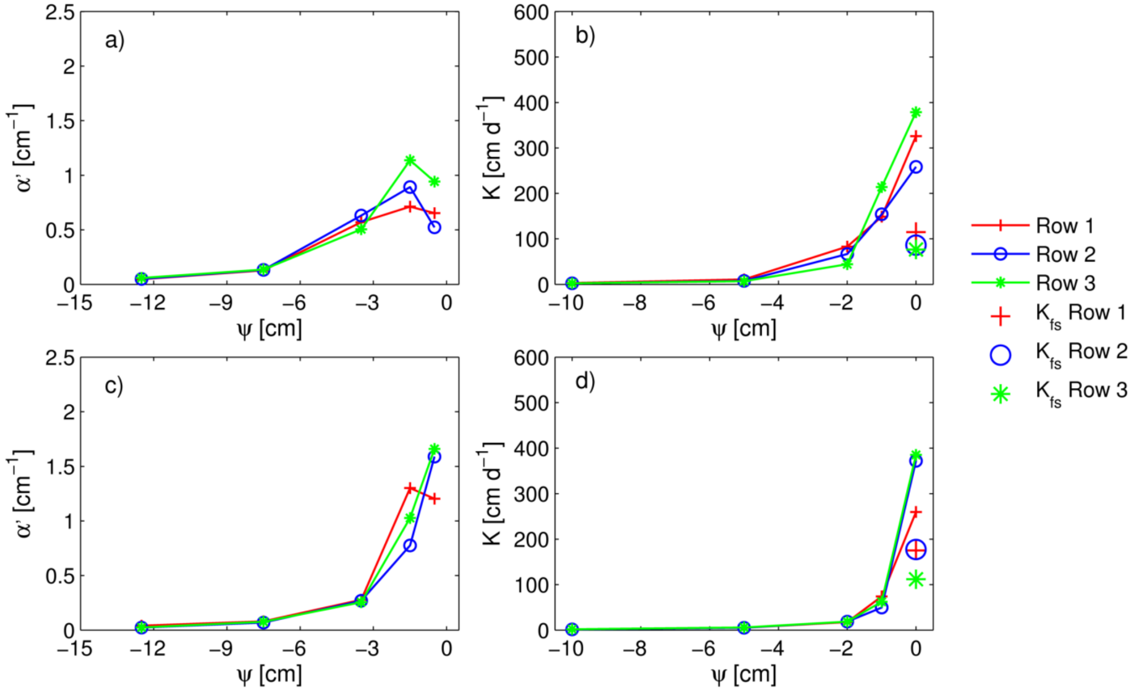

Figure 3.5. Plot 1 row-wise comparison of the $\alpha'(\psi)$ relationships for, a) August 2009 (wet), and c) September 2009 (dry); and the $K(\psi)$ relationships and K_{fs} estimates for, b) August 2009 (wet), and d) September 2009 (dry).

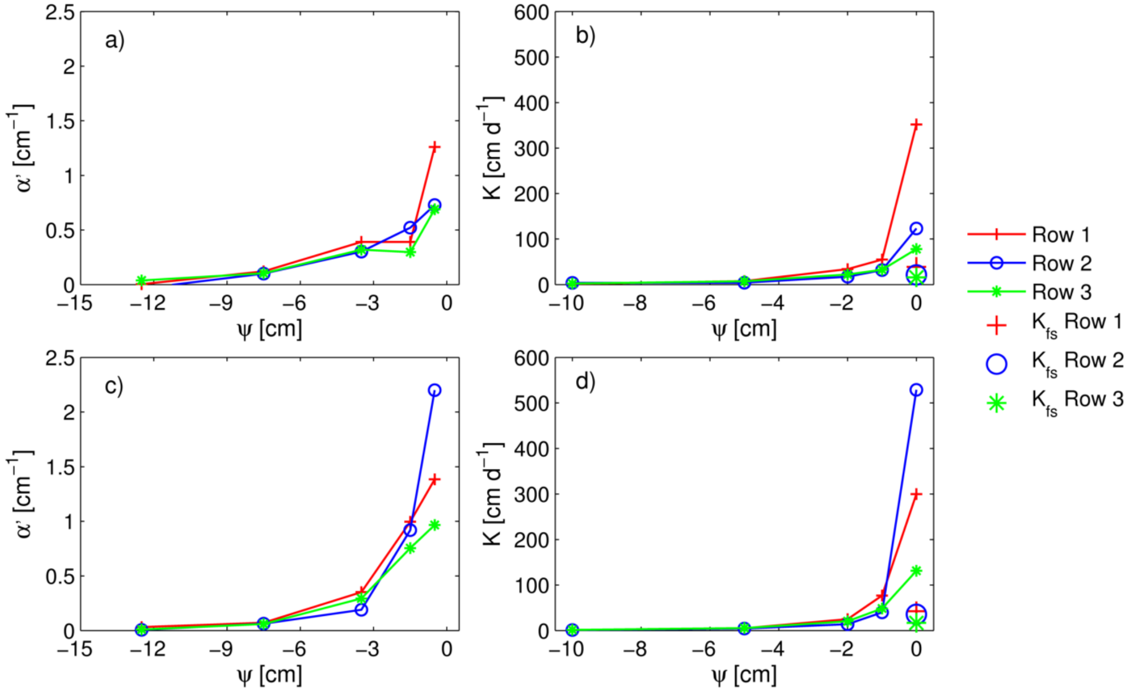

Figure 3.6. Plot 2 row-wise comparison of the $\alpha'(\psi)$ relationships for, a) August 2009 (wet), and c) September 2009 (dry); and the $K(\psi)$ relationships and K_{fs} estimates for, b) August 2009 (wet), and d) September 2009 (dry).

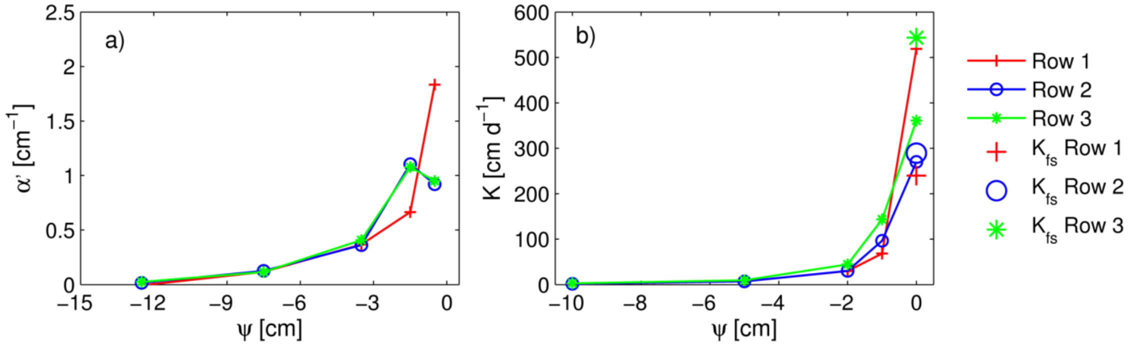

Figure 3.7. Plot 3 row-wise comparison of the a) $\alpha'(\psi)$ relationships, and b) $K(\psi)$ relationships and K_{fs} estimates for August 2008.

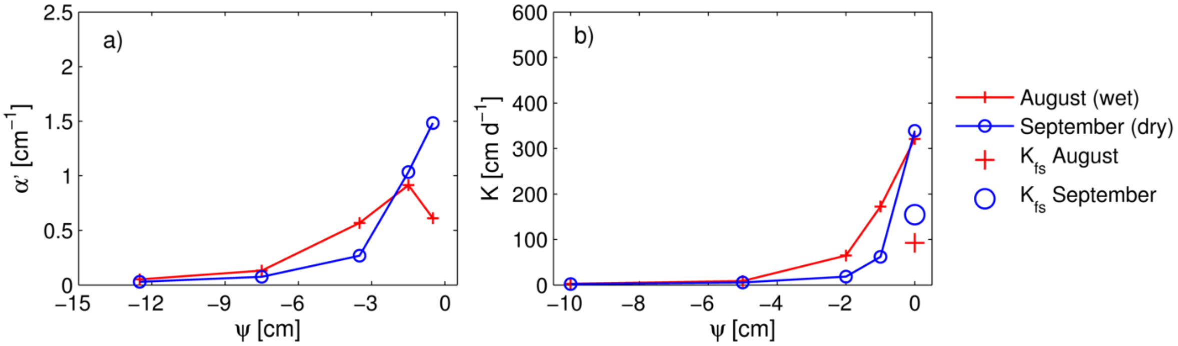

Figure 3.8. Comparison of the plot 1, a) $\alpha'(\psi)$ relationships, and b) $K(\psi)$ relationships and K_{fs} estimates for the August 2009 (wet) and September 2009 (dry) infiltration experiments.

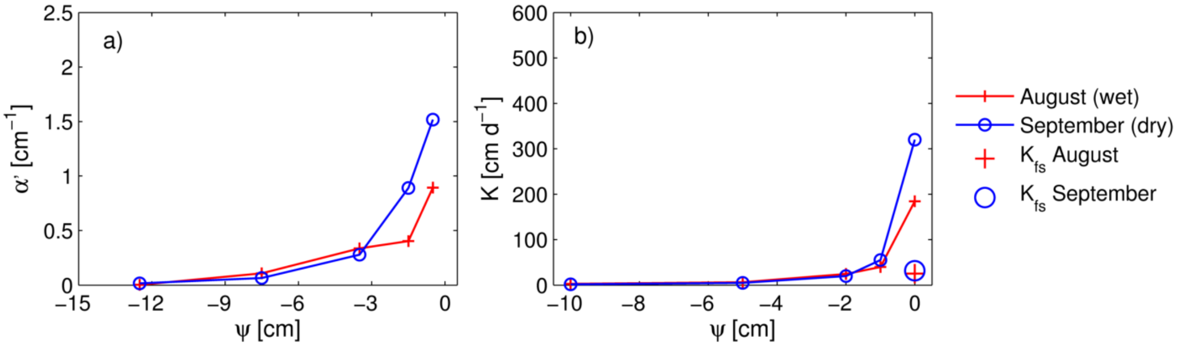

Figure 3.9. Comparison of the plot 2, a) $\alpha'(\psi)$ relationships, and b) $K(\psi)$ relationships and K_{fs} estimates for the August 2009 (wet) and September 2009 (dry) infiltration experiments.

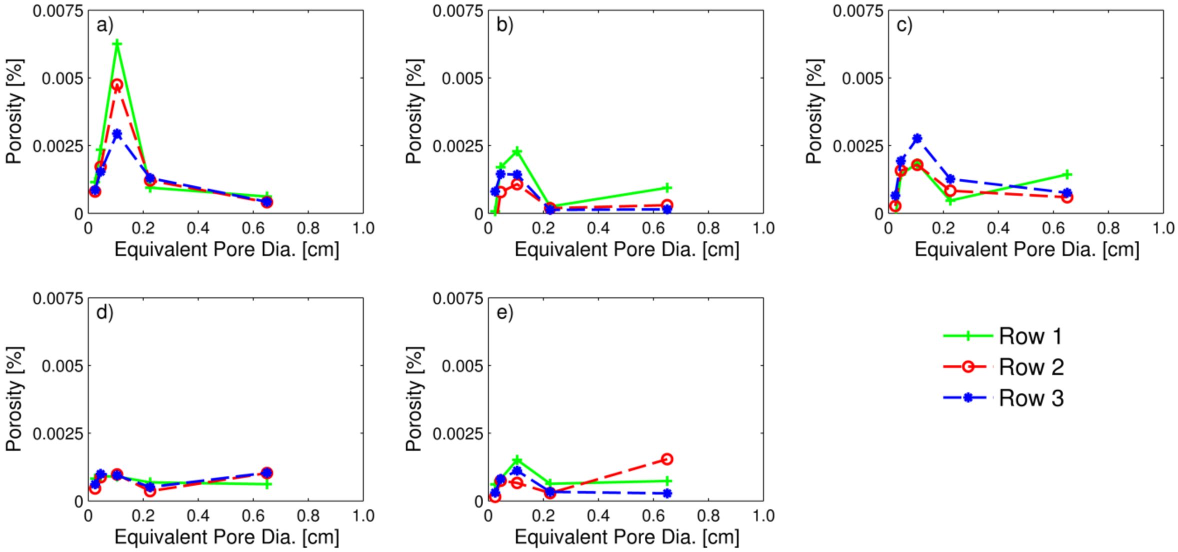

Figure 3.10. Inter-row comparison of mean hydraulically effective porosity for: a) plot 1 in August 2009, b) plot 2 in August 2009, c) plot 3 in August 2008, d) plot 1 in September 2009, and e) plot 2 in September 2009.

Table 3.1. Physical characteristics of the A horizon soil at the three experimental plots (from chapter 2).

Plot	Sand [%]	Silt [%]	Clay [%]	Gravel [%]	Bulk Density [g cm^{-3}]	Organic Matter [%]	Log$_{10}$K$_{fs}$† [cm d^{-1}]
1	49.9 (1.5)	30.4 (1.5)	13.2 (0.7)	6.5 (1.7)	1.2 (0.0)	6.3 (0.3)	1.9 (0.3)
2	47.4 (1.7)	35.4 (1.0)	14.2 (1.0)	2.9 (1.0)	1.4 (0.1)	3.2 (0.1)	1.1 (0.5)
3	29.5 (1.2)	47.2 (1.2)	20.1 (1.1)	3.2 (2.7)	1.1 (0.1)	5.3 (0.2)	2.4 (0.5)

Values in parentheses denote standard deviation

Number of samples (n) equals 6 except where † indicates n equals 12

Table 3.2. Physical characteristics of the B horizon soil at the three experimental plots (from chapter 2).

Plot	Sand [%]	Silt [%]	Clay [%]	Gravel [%]	Bulk Density [g cm^{-3}]	Log$_{10}$K$_{sat}$ [cm d^{-1}]
1†	28.8 (3.9)	48.3 (3.1)	14.6 (1.2)	8.3 (3.2)	1.9 (0.1)	-0.6 (1.1)
2	51.8 (5.7)	38.3 (4.4)	5.5 (1.7)	4.3 (3.1)	1.9 (0.2)	-0.1 (0.7)
3	51.9 (21.5)	29 (15.8)	9.4 (6.4)	9.7 (11.9)	1.7 (0.1)	1.8 (1.1)

Values in parentheses denote standard deviation

Number of samples (n) equals 6 except where † indicates n equals 4

Table 3.3. Effective porosity attributable to pores with equivalent cylindrical diameter greater than 0.02 cm and the associated coefficient of variation (CV).

Effective Pore Dia.	Plot 1				Plot 2				Plot 3	
	August 2009		September 2009		August 2009		September 2009		August 2008	
	Porosity	CV	Porosity	CV	Porosity	CV	Porosity	CV	Porosity	CV
[cm]	[%]									
0.02 - 0.03	9.4e-04	50	6.3e-04	51	9.0e-05	1776	3.6e-04	190	2.6e-04	240
0.03 - 0.06	1.9e-03	42	9.3e-04	22	1.3e-03	50	7.9e-04	31	1.6e-03	28
0.06 - 0.15	4.6e-03	66	9.4e-04	35	1.6e-03	79	1.1e-03	78	2.1e-03	56
0.15 - 0.3	1.2e-03	48	5.2e-04	50	1.9e-04	63	4.2e-04	74	8.6e-04	70
0.3 - 1.0	4.8e-04	94	8.9e-04	87	4.6e-04	158	8.5e-04	115	9.3e-04	94
0.03 - 1.0	8.2e-03	47	3.3e-03	37	3.6e-03	71	3.2e-03	56	5.6e-03	37

Chapter 4

Assessing potential nutrient losses in tile drained, macroporous soils over an annual cycle through conservative tracer tracking.

4.1 Introduction

Tile drains are a significant component of the drainage enhancements required to support productive agriculture on soils with poor natural drainage, and are common features of the modern agricultural landscape. Although tile drains are often perceived as environmental risks because of their ability to rapidly transmit nutrients and other potential contaminants to surface water (e.g. *Skaggs et al.*, 1994), these concerns are capitulated by global food demand that necessitates continuous increases in agricultural output. In North America, it is estimated that 62Mha, or 25% of the arable and permanent crop area, has undergone drainage improvements (International Commission on Irrigation and Drainage, 2010). Agriculture in humid, mid-latitude climate regions is particularly dependant on tile drains to help regulate the water table position during the growing season; and to remove excess soil moisture during the typically cool, wet winters, when a limited number of large precipitation and melt events can often dominate the hydrologic cycle. As a result, tile drain discharge is subject to large inter-seasonal, and inter-event, variability. An abundance of observational evidence exists to support the fact that a disproportionately large amount of the annual water and nutrient-mass flux through tile drains can occur in a relatively small amount of time (e.g. *Drury et al.*, 1996; *Cambardella et al.*, 1999; *Tomer et al.*, 2003; *Kladivko et al.*, 2004; *Royer et al.*, 2006; *Udawatta et al.*, 2006; *Macrae et al.*, 2007). While such evidence is valuable, a thorough understanding of the physical flow and transport processes at work in the soil profile during ‘extreme’ hydrologic events is required to optimize nutrient management practices on tile drained agricultural land.

In addition to seasonal and event based variability, flow and transport in tile drained soil is further complicated by the common presence of macropore features such as earthworm burrows, root holes, and cracks and fissures (*Thomas and Phillips*, 1979; *Beven and Germann*, 1982; *Jarvis*, 2007) that can facilitate preferential water flow and solute transport through the soil profile. Hydraulic activity within the macropore networks is not ubiquitous however, and the occurrence of preferential flow is heavily dependent on factors such as antecedent moisture content, rainfall intensity, and pore continuity (*Beven and Germann*, 1982; *Jarvis*, 2007). In relatively dry soils, light precipitation does not typically induce macropore flow and incident water infiltrates and redistributes within the matrix (e.g. *Coles and Trudgill*, 1985; *Köhne and Gerke*, 2005), whereas in relatively wet soil, even light precipitation can initiate macropore flow (e.g. *Coles and Trudgill*, 1985; *Villholth et al*., 1998). Macropore flow can occur in dry soil for a number of reasons, including: high precipitation rates (e.g. *Edwards et al*., 1992), low permeability (*Gerke and Köhne*, 2002) and/or hydrophobic (e.g. *Edwards et al*., 1992) macropore wall linings that impede imbibition into the soil matrix, and localized low permeability layers that induce localized water pressure increases (e.g. *Weiler and Naaf*, 2003). When macropores are hydraulically active they can transmit a large proportion of the total flow (e.g. *Dunn and Phillips*, 1991; *Mohanty et al*., 1996; *Lin et al*., 1997); however, because they are discrete features with a finite length, their hydraulic efficacy is largely governed by receptor (i.e. the surrounding soil matrix) conductivity. Consequently, when macropores are effectively drained by underlying permeable soil layers or tile drains they will impart a greater influence on flow and transport processes within the soil profile than when they are effectively dead end pores surrounded by a low permeability soil matrix (*Bouma*, 1982; *Shipitalo and Gibbs*, 2000; *Weiler and Naaf*, 2003).

The interaction between macropores and tile drains has been a popular research subject. Past studies have shown that macropores can transmit substances such as: nutrients (e.g. *Laubel et al*., 1999; *Cook and Baker*, 2001; *Ball Coelho et al*., 2007), pesticides (e.g. *Villholth et al*. 2000; *Kladivko et al*., 2001), pharmaceuticals (e.g. *Lapen et al*., 2008a), and bacteria (e.g. *Cook and Baker*, 2001; *Lapen et al*., 2008b), to tile drains. Because macropores beneath the top soil layer are predominantly vertical features (e.g. *Steenhuis et al*., 1988; *Shipitalo and Gibbs*, 2000), the tile drain 'rapid' capture zone is generally narrow in relation to tile spacing. For example, *Shipitalo and Gibbs* (2000) found that surface connected macropores within 50 cm of a tile drain installed in a silt loam soil in Ohio were most likely to have a direct connection with the drain.

Efforts to characterize flow and transport processes in tile drained, macroporous soils, have utilized irrigation along with surface applied conservative tracers to quantify breakthrough, and dye tracers to identify active flowpaths, (e.g. *Villholth et al*., 1998; *Larsson et al*., 1999; *Zehe and Fluhler*, 2001; *Stamm et al*., 2002). Rapid arrival of the tracer at the tile drain is a unifying theme amongst many of the past studies (e.g. *Richard and Steenhuis*, 1988; *Villholth et al*., 1998, *Lennartz et al*., 1999; *Jaynes et al*., 2001; *Zehe and Fluhler*, 2001; *Stamm et al*., 2002; *Gish et al*., 2004); however, low antecedent soil moisture content coupled with low irrigation rates (e.g. *Gish et al*., 2004; *Köhne and Gerke*, 2005) can reduce the likelihood of preferential flow. Although counter-intuitive, it has also been demonstrated that preferential flow can induce tile discharge even when the water-table is well below the drain elevation because hydraulically active macropores can be connected to the tile drain (e.g. *Steenhuis et al*., 1988; *Villholth et al*., 1998).

While it is well understood that macropores in tile drained agricultural soils can facilitate rapid movement of water and solutes in a wide variety of hydrologic conditions, the current understanding of how macropores influence solute partitioning between groundwater and surface water in tile drained soils is limited. Because the late fall to early spring time frame can often account for a large proportion of the annual nutrient movement to surface water in agricultural settings, and post harvest manure application is a common farming practice, consideration of seasonal influences on tile drainage is especially important. However, past research in this area has largely avoided the topic of tile drain dynamics during extreme hydrologic events such as winter and spring melts. Tile drainage research during extremely wet soil conditions that are common throughout the late fall to early spring time frame is complicated by the realism that tile drain monitoring is challenging during periods of high flow, and freeze-thaw activity. To facilitate further scientific development in this field, new and innovative methodology is required.

The intention of this component of the research work is to address the issue of flow and transport in macroporous, tile drained agricultural soil over an annual cycle, in the humid continental climate of southwestern Ontario. Because nutrient movement to surface water is notably higher from late fall to early spring in this region, large precipitation and melt events that occur within this period of increased hydrologic activity are given specific attention. The key objectives are as follows:

1) To determine the influence of macroporosity on short-term and long-term solute transport to tile drains.
2) Evaluate the relative significance of large; fall, winter, and spring, hydrologic events on the movement of soluble nutrients derived from late fall liquid manure application to surface water (via tile drains) and groundwater.
3) Quantify the correlation between groundwater levels and tile drainage, and demonstrate how such relationships can be used to predict tile drain discharge rates with high temporal resolution.

To achieve these objectives, an experiment was conducted at a tile drained agricultural field that has had extensive characterization of its soil hydraulic properties and macroporosity distribution. As part of the experiment, two different conservative tracers were applied to the field surface in parallel bands adjacent to a tile drain in early November, on wet soil. After tracer application, a three year return period rainfall was simulated with irrigation in order to generate soil conditions that pose a high risk for tile water contamination from liquid manure application. The movement of the tracers to both groundwater, and the tile drain, was monitored for one year following application. Near the end of the one year monitoring period, detailed measurements of residual tracer distribution within the soil profile were made.

4.2 Study site and methods

4.2.1 Site description

The experiment was conducted on an actively cropped field located at N43°09’55”, W81°01’08”, near the town of Kintore in southwestern Ontario, Canada (Figure 4.1). Soils at the site are mapped as poorly drained, dark grey Gleisolic, Maplewood silt loam series, which is underlain by clay, and clay loam till (*Experimental Farms Service*, 1987). Beneath the surface soils is a complex layering of Quaternary sediments consisting of subglacial diamictons and glacifluvial deposits (*Rudolph and Parkin*, 1998) that extend to a depth of approximately 45 m (*Sado and Vagners*, 1975). Perforated plastic tile drains, 10 cm in diameter, were installed at the field in 1985. The tiles are systematically spaced 12-15 m apart and are located at depths of 0.6-1 m.

Minimum tillage practices have been utilized at the site since 1995. Prior to 2004 both liquid swine manure and commercial fertilizers were alternately used as soil nutrient amendments; however, between 2004 and 2008 only commercial fertilizer was used. In May, 2007, the field was planted in soybean (*Glycine max L.*) that were harvested in late September. Following soybean harvest, the field was planted in winter wheat (*Triticum aestivum* L.) that was harvested in mid July 2008. Hourly measurements of air temperature, precipitation, relative humidity, wind speed, and solar radiation were collected at the site between June 2007 and October 2009. Past research on nitrate flux in agricultural settings and riparian zone denitrification has been conducted at the same site (*Cey et al*. 1998; *Cey et al*. 1999).

4.2.2 Plot characterization

4.2.2.1 Soil physical properties

The tracer test was conducted in the vicinity of an individual tile line located at the south area of the field (Figure 4.2) where the surface slopes gently (1.6 % grade) to a perennial steam that runs along the southern edge. Physical properties of the soil at the site were characterized with soil cores that were collected during September 2009 from an area located along the same tile drain but 40 m up-gradient from where the tracer experiment was conducted. From the A horizon, there were six, 5 cm diameter by 10 cm long soil cores, extracted from the 5 cm to 15 cm depth interval, on an evenly spaced 2 m by 3 m grid that had one long edge positioned above the tile drain. The B horizon was characterized with four selectively spaced, 8 cm diameter by 10 cm long, soil cores that were extracted at depths of 30-100 cm.

Organic matter content in the A horizon cores was determined using the Walkley-Black (Walkley and Black, 1934) acid digestion method, particle size distribution for all of the cores was determined with the pipette method (Gee and Or, 2002) and bulk density was determined by assuming that the soil volume contained within the cores was undisturbed. Hydraulic conductivity (K_{sat}) of the B horizon cores was determined with a falling head permeameter prior to the physical property tests (Reynolds, 2008).

4.2.2.2 Surface soil hydraulic properties

The saturated and unsaturated hydraulic properties of the surface soil were measured in November 2008 with a series of six tension (TI) and six double-ring (DR) infiltration tests. The infiltration tests were conducted along the same tile drain as the tracer test but 5 m down-gradient from where the tracers were actually applied to avoid heavily trafficked soil. The individual infiltration test locations were positioned on an evenly spaced 2 m by 3 m grid that had one long edge positioned above the tile drain. During the infiltration tests the soil was relatively wet, which is typical of late fall conditions at the site.

A tension infiltrometer (TI) with a 20 cm diameter disk and a 1.65 liter reservoir (Soil Measurement Systems model SW-080B) was used to characterize the unsaturated hydraulic properties of the soil. Decreasing tension settings of 10, 5, 2, 1 and 0 cm were used during each test. The TI disk was placed on soil surfaces that were carefully prepared by cutting any vegetation down to ground level and smoothed to the extent that all surface irregularities were masked by a 3-5 mm layer of fine sand that was emplaced to provide a level surface for the TI disk to sit and to ensure good hydraulic connection between the disk and the soil. Care was taken to minimize smearing of the soil surface and to avoid areas with signs of wheel traffic. At each tension setting, infiltration rates were usually measured in five minute intervals until quasi-steady-state conditions were observed before the applied tension was reduced to the next setting. At each individual tension setting, the duration of the TI tests was potentially limited by the volume of water in the reservoir. In the few cases where very high infiltration rates were observed and reservoir volume appeared to be the limiting factor, measurement time intervals were reduced accordingly. During each TI experiment, a 10 cm long time domain reflectometer (TDR) probe was installed below the disk at approximately a 30 degree angle from horizontal and water content was monitored continuously in 10 second intervals with a Campbell Scientific Inc. TDR100 system.

As per the methodology described in section 3.2, the tension infiltrometer (TI) data was analyzed according to the method presented by *Reynolds* (2008), which is again briefly defined as follows:

$$\alpha'_{x,x+1} = \frac{\ln(Q_x / Q_{x+1})}{(\psi_x - \psi_{x+1})} \quad \text{where } \psi \ \leq 0 \tag{4.1}$$

$$K'_{x,x+1} = \frac{G\alpha'_{x,x+1} Q_x}{a(1 + G\alpha'_{x,x+1} \pi r)(Q_x / Q_{x+1})^P} \tag{4.2}$$

$$K(\psi_x) = \frac{\left\lfloor K'_{x-1,x} \exp\left(\alpha'_{x-1,x}\, \psi_x\right) + K'_{x,x+1} \exp\left(\alpha'_{x,x+1}\, \psi_x\right)\right\rfloor}{2} \qquad x = 2,3,...n-1 \tag{4.3}$$

$$K(\psi_x) = K'_{x,x+1} \exp\left(\alpha'_{x,x+1}\, \psi_x\right) \qquad \text{for x = 1} \tag{4.4}$$

$$K(\psi_x) = K'_{x-1,x} \exp\left(\alpha'_{x-1,x}\, \psi_x\right) \qquad \text{for x} = n \tag{4.5}$$

where x represents the applied pressure head (ψ) settings (L); G is a shape factor which was set constant at 0.237; Q is the observed quasi steady state flow rate (L^3 T^{-1}); *a* is the disk radius (L); and $P = \psi_x /(\psi_x - \psi_y)$.

Following each TI test, the contact sand was vacuumed off the soil surface and a double ring (DR) infiltration test was conducted at the same position, with the objective of obtaining estimates of field saturated hydraulic conductivity (K_{fs}). Both the 30 cm diameter inner and 55 cm diameter outer rings were pressed approximately 5 cm into the soil. A constant water level of approximately 10 cm was maintained in both the inner and outer rings with separate 40 liter mariotte bottles. Infiltration rates were monitored until quasi-steady-state conditions were observed in the inner ring, which usually required two to three hours. Estimates of field saturated hydraulic conductivity were obtained from the DR infiltration data using the method prescribed by *Reynolds, et al.,* (2002) as follows.

$$K_{fs} = q_s / \left(\left[\frac{h}{0.316\pi d + 0.184\pi a} \right] + \left[\frac{1}{\alpha * (0.316\pi d + 0.184\pi a)} \right] + 1 \right) \tag{4.6}$$

Where q_s is the observed quasi steady-state infiltration rate (L^3 T^{-1}), h is depth of ponded water (L), d is the ring insertion depth (L), a is the inner ring radius (L), and $\alpha*$ is the calculated α value for the 1-0 cm tension interval of the TI experiment that was conducted at the same test area (L^{-1}).

4.2.2.3 Macropore characterization

Extensive macropore characterization at the test plot was conducted during August 2009 at the same up-gradient location where the six A horizon soil cores were obtained. The macropore related work is described in greater detail within the context of a large scale macroporosity – hydraulic property spatial variability assessment at the field site (Chapters 2 and 3). In total, macroporosity was quantified on forty-eight 0.25 m^2 horizontal soil surfaces positioned at depths ranging from 0.02 to 0.76 m from surface, and located at distances between 0 and 3 m from the tile drain. On each excavated surface, the number of macropores in 0.5-5 mm, 5-8 mm, 8-10 mm, and 10-12 mm diametric size intervals were manually counted. Total cylindrical macropore surface area was calculated by multiplying the mean area of each size interval by the number of macropores observed within that interval. Fracture area was estimated by measuring the total length of fractures on each surface and then multiplying the result by 0.5 mm, which is an approximate average fracture width. Total macroporosity is the sum of the cylindrical and fracture macropore areas. Prior to the macropore characterization, additional TI and DR infiltration tests were conducted on the field surface (Chapter 3) above each subsurface area where macroporosity was characterized. Between the infiltration tests and macropore characterization at each individual infiltration test location, 20 liters of blue dye solution (Brilliant Blue FCF) was applied to the soil under positive pressure, from within a 50 cm by 50 cm square reservoir.

4.2.3 Plot instrumentation

The experiment site (Figure 4.3) was heavily instrumented. Water levels were monitored in 5 shallow piezometers with 33 mm outside diameters that had 0.6 m long screens centered at 1.5 m depth (W1–W5), with pressure transducers recording water levels on 15 minute intervals; and 2 deep piezometers of the same design (W6, W7) that had screens centered at depths of 2.5 m, and 4.5 m respectively, that also contained pressure transducers that recorded water level fluctuation in 15 minute intervals. Atmospheric pressure was measured with a barometer that logged atmospheric pressure in 15 minute intervals. Soil moisture content was measured with a multilevel TDR system (Environmental Sensors Inc.) positioned 1.5 m from the tile drain and midway along the irrigated section, to measure soil water content in 15 to 30 cm intervals over a depth range of approximately 5 to 120 cm. Irrigation water was applied with a sprinkler system capable of supplying 13 mm hr^{-1} of water to the 9 m by 9 m plot area. Tile discharge was monitored at the down gradient end of the test plot using an electronic flow-meter with approximately 800 l hr^{-1} peak capacity that was configured to measure tile discharge in 15 minute intervals. Tile drain water samples were obtained with an automatic water sampler installed in an insulated enclosure at the tile discharge monitoring station and groundwater samples were obtained from 9 sets of multilevel sampling wells that were each screened at depths of 1.5 m, 2.5 m and 3.5 m. A meteorological monitoring station that recorded air temperature and precipitation on an hourly basis was in operation at the site between July 2007 and October 2009.

4.2.4 Hydraulic response / tracer test

Two preliminary irrigation tests were conducted to assess the hydraulic response of the tile drain at the plot to surface irrigation. The first test was conducted on October 22, 2007 when soil conditions were relatively dry and the second test was conducted two days later, after 15 mm of rain fell at the site, when the soil was wetter. Both of the preliminary tests involved 3 hours of irrigation using water application rates of 8.1 and 8.3 mm hr^{-1}, for the first and second tests respectively. Local municipal tap water was used for both of the preliminary tests.

The main tracer experiment began on November 7, 2007, with the application of 250 g m^{-2} of bromide (Br) to a 2.3 m by 6.1 m patch of soil adjacent to the tile drain, and the application of 250 g m^{-2} of chloride (Cl) to a 2.3 m by 6.1 m patch of soil adjacent to the Br zone (Figure 4.3). Both ions were manually applied in dissolved form with garden variety watering cans at concentrations of 125 g l^{-1}, over a 25 minute period. The source material for the two tracer ions was NaBr and NaCl. Although Na ions can cause flocculation of some clay minerals, the relatively high background Na concentrations (approximately 2 to 30 mg l^{-1}) in the groundwater at the Kintore site infers that the clay minerals in the soil have been previously exposed to Na and were therefore not likely to be significantly influenced by Na in the tracer solution. The irrigation system was activated immediately after tracer application and 5 mm hr^{-1} of water was applied to the plot for 9 hrs, using water pumped from the stream. The application rate is an approximate representation of a 3 year return period, 9 hour rain event at the site (*Prodanovic and Simonovic*, 2004). Minimal surface runoff was observed during the irrigation tests.

4.2.5 Tile discharge monitoring

Tile flow rates at the plot were continuously measured from October 10 to November 28, 2007, at which time the monitoring system pump was destroyed by sediment buildup in the submerged reservoir that it was housed. The pump was replaced in early January 2008 in preparation for a winter thaw; however, during the actual winter thaw event, discharge volumes often exceeded the system's 800 l hr^{-1} capacity. During select peak flow periods, manual tile discharge measurements were taken using a rudimentary bucket/stopwatch method to supplement the tile flow dataset. The pump had to be replaced because of excessive sediment buildup on three additional occasions during January 2008; as a result, the measured tile flow data for the month of January is somewhat sporadic. The measured tile discharge record ends at the end of January when the 180 liter plastic barrel that was serving as the pump reservoir imploded under pressure from the surrounding wet soil. Model estimates (described below) of tile discharge at the site were made for the entire 1 year period following tracer application.

4.2.6 Chemical analysis

Chemical tracer monitoring in the tile water and groundwater began immediately after the tracers were applied and continued for 1 year after the tracers were applied. The sampling interval was initially every 15 minutes at the tile and every 2 to 6 hours in the monitoring wells, with the shallowest wells sampled at the highest frequency. The sampling frequencies were progressively decreased to once per day at the tile drain and approximately once per month at the monitoring wells. Tile water sampling was unaffected by the problems that plagued the tile flow monitoring station. Br and Cl concentrations in the water samples were measured with an ion-chromatograph (IC) (Dionex ICS-3000) that was calibrated against Br and Cl standards that ranged from 0.1 to 100 mg l^{-1} in concentration. When individual samples had tracer concentrations that exceeded 100 mg l^{-1}, they were diluted by an appropriate factor and then re-analyzed. Background concentrations of Br and Cl in the tile drain discharge and the monitoring wells were measured prior to tracer application.

4.2.7 Hydrograph separation

Hydrograph separation was conducted with the objective of isolating tile discharge that had originated within the experimental plot area, from total tile discharge measured at the monitoring station during the 48 hour interval surrounding each irrigation event. Baseflow contribution to tile discharge during each event was estimated by linearly interpolating tile flow between the beginning and end points of the discharge peak induced by irrigation. Additional tile discharge that is assumed to be the result of localized irrigation is estimated as total discharge minus interpolated tile baseflow.

Because the land surface area contributing to tile flow at the monitoring station is large in relation to the irrigated test plot, and there was notable tile baseflow at the time of the November 7th experiments, measured tracer concentrations are diluted in relation to the actual concentrations transmitted to the tile from the tracer application area. The dilution masks the temporal dynamics of tracer transport to the tile drain. By combining tracer mass flux with the irrigation induced tile discharge obtained through hydrograph separation, a tracer breakthrough curve that better reflects flow and transport processes beneath the tracer application area can be obtained. Estimates of undiluted tracer concentration ($M\ L^{-3}$) are made by dividing mass flux ($M\ T^{-1}$) by irrigation induced tile discharge ($L^3\ T^{-1}$).

4.2.8 Residual tracer analysis

To determine the amount of residual tracer retained in the soil near the end of the year long tracer test, sixteen, 5 cm diameter by 2 m (theoretical) long, soil cores were extracted from the 6 m by 6 m area adjacent to the tile drain where the tracers were originally applied. Core extraction was conducted during September 2008. In total, 134 subsamples were removed from the cores in 10 cm increments and soil pore water from each subsample was extracted and analyzed for Br and Cl. Because core recovery varied from 50 to 100 %, the relative position of each subsample from within the obtained core was used to estimate the actual depth that each subsample would represent at the experiment plot according to $Z_t = Z_a L_t / L_a$, where Z_t is theoretical sample depth, Z_a is sample depth in the actual soil core, and L_t and L_a are the theoretical and actual core lengths, respectively. The core analysis results were assembled into a three-dimensional dataset that was spatially interpolated using kriging in order to generate three dimensional Br and Cl concentration and mass distribution profiles. Estimates of residual Br and Cl mass in the soil profile were obtained by numerical integration of the residual mass distribution profiles.

4.2.9 Water level – tile drain discharge correlation

In order to estimate tile drain discharge and cumulative tracer flux at the plot after the monitoring station was rendered inoperable, an empirical model was developed to predict tile discharge over the one year period of interest using groundwater level data. Prior to the application of parametric data analysis techniques to test for correlation between tile discharge and groundwater levels, water level and tile discharge data distribution was assessed using normal probability graphs to determine if data transformation would improve the normality of the data sets. During model development, cross-correlation between groundwater levels in each of the seven piezometers, and tile discharge was determined. Through an intuitive trial and error process, the model $Q_t = \mathrm{A}[Z_s + Z_d(n)] + \mathrm{B}$, was derived to predict tile discharge (Q_t), in units of liters / 15 min, as a function of two empirical fitting coefficients (A and B), and water-level in one shallow piezometer (Z_s), and one deep piezometer (Z_d) that had been smoothed with a centered moving average over n, 15 minute, time intervals. It was intended that the Z_s term would incorporate the high frequency tile drain response to precipitation and melt events, and the $Z_d(n)$ term would incorporate the low frequency seasonal variation in tile drain baseflow. The model was implemented into a simple FORTRAN program and optimal values for A, B, and n were determined by coupling the model with the PEST parameter estimation software package (*Doherty*, 2004). The performance of the model was assessed by visually comparing predicted tile flow rates against tile flow rates that were measured while the flow monitoring station was in operation, and by comparing predicted vs. measured cumulative Br flux between November 7th and November 28th.

4.2.10 Short term and long term bromide mass discharge estimates

Estimates of bromide mass (M_{br}) discharged through the tile drain were determined according to $M_{br} = \sum_{i=1}^{n} Q_i C_i$; where Q_i, and C_i are tile flow rate, and Br concentration respectively, for each 15 minute time step (i). Measured, and modelled values of Q_i were used to estimate Br mass flux over the respective three week (n = 2016), and one year (n = 35136) periods that followed tracer application. When the time interval between sampling was more than fifteen minutes, linear interpolation between measured data points was used to estimate tile effluent Br concentrations.

4.3 Results

4.3.1 Plot characterization

Results from the A and B horizon physical soil characterization are presented in Table 4.1. Based on grain size distribution, the A horizon soil is classified as a sandy loam which is in minor disagreement with the regional soil survey (Experimental Farms Service, 1987) that classified the surface soil at the test plot as a silt loam. The A horizon soil extends to a depth of approximately 25 cm, where a hardpan layer is encountered at the top of the silt loam B horizon soil. The B horizon soil extends to tile depth, and geometric mean K_{sat} is 0.25 cm d^{-1}. The saturated (K_{fs}) and unsaturated ($K_{x,y}$) hydraulic conductivity of the surface soil (Table 4.2) is considerably higher than the B horizon K_{sat}, which reflects both the contribution of macropores to vertical flow in such wet soil conditions, and the differences in soil composition and bulk density. With the exception of K_{0cm}, mean values of surface soil hydraulic conductivity are consistently higher in the infiltration test areas located immediately above the tile drain. Higher hydraulic conductivity above the tile drain indicates that macropores that are effectively drained (i.e. connected with tile drains or underlain by high permeability deposits) have the greatest potential to influence steady-state infiltration rates.

Mean macroporosity distribution at the plot is presented in Figure 4.4. The highest proportion of macroporosity was observed near surface where it amounts to approximately 0.35 % of the soil area. Macroporosity progressively declines with increasing depth, and accounts for approximately 0.06 % of the soil area at tile drain level. Cylindrical pores less than 5 mm in diameter compose most of the macroporosity within the entire depth range investigated. Macropores larger than 5 mm are most abundant near the top of the B horizon where they compose approximately 35 % of the total macroporosity. Fracture area also peaked at the top of the B horizon where it accounted for approximately 15 % of the total macroporosity.

Dye staining patterns indicated that dye movement occurred within all sizes of macropores and fractures. The soil matrix in the A horizon was extensively stained; however, the only staining in the B horizon soil matrix was observed in areas surrounding macropores that had obviously transmitted dye. The hardpan layer at the top of the B horizon appeared to have promoted lateral dye spreading, and vertical dye movement into the B horizon was limited to macropores that were continuous through the hardpan. The depth of dye penetration was dependent on the penetration depth of those macropores that were able to move dye through the hardpan layer. The primary means for dye to reach the tile drain was through cylindrical macropores and structural cracks that were located within and along the edges of relic, tile drain installation scars that extended from the top of the B horizon to tile depth.

4.3.2 Tile drain response to irrigation

Although the magnitude and duration of irrigation was similar during both the October 22nd and 24th tile drain hydraulic response tests (Figure 4.5a), there was considerably greater increase in tile discharge for the later of the two tests. Similar to the October 24th test, irrigation during the November 7th tracer experiment also caused a noticeable increase in tile discharge (Figure 4.5b). During both the October 24th and November 7th irrigation events, tile flow started to increase within 1 hour of irrigation, and continued to increase throughout the irrigation interval. Tile flow began to decline as soon as irrigation ceased on both October 24th and November 7th. Hydrograph separation conducted for the October 24th and November 7th irrigation events shows that the amount of additional tile discharge induced by irrigation is small in relation to the amount of water applied. Approximately 17%, and 14%, of the applied water volume was recovered within 24 hours for the irrigation events conducted on October 24th, and November 7th, respectively.

Initial soil moisture conditions were notably different between the two October tests. In the 7 day period leading up to October 22nd, only 5 mm of precipitation was received at the site, whereas between the 22nd and the 24th, there was 16 mm of precipitation received, not including irrigation. As a result of drier soil conditions, there was an additional 10 mm of water storage capacity in the soil profile prior to irrigation on October 22nd, as compared to October 24th. While the near surface soil moisture content increased substantially during both October tests (Figure 4.6a and 4.6b), there was minimal increase at a depth of 23 cm (top of hardpan) on October 22nd, whereas on October 24th, water content at 23 cm depth approached saturation. In the 24 hours prior to irrigation on November 7th there was 10 mm of rain received at the site; as a result, soil conditions were also quite wet in advance of tracer application. The magnitude and rate of soil moisture increase in response to irrigation on November 7th was similar to October 24th (Figure 4.6b and 4.6c), and peak moisture contents in the A horizon were achieved within 3 hours from the start of irrigation. Soil drainage characteristics were also similar between the October 24th and November 7th tests; in both cases rapid near surface soil drainage began very soon after irrigation stopped, and soil moisture content at 23 cm depth declined at a slightly faster rate than at 7.5 cm depth.

Results from the irrigation tests suggest that soil moisture content at the base of the A horizon is a good indicator of tile discharge temporal response to water application on the field surface. During both the October 24th and November 7th irrigation events, tile discharge begins to increase at the same time that soil moisture content at a depth of 23 cm (top of hardpan) increases. Upon cessation of irrigation on both October 24th and November 7th, soil moisture content at 23 cm begins to decline at roughly the same time that tile discharge starts to decline. During the October 22nd irrigation event, neither soil moisture content at a depth 23 cm nor tile discharge increased noticeably.

During all three irrigation events, the amount of water stored in the soil profile increased substantially between the beginning and end (Figure 4.7). At the point during each irrigation test where the soil moisture peaks, the additional water in the soil profile represents 75%, 149%, and 84 %, of the total volume of water applied during the October 22, 24, and November 7 tests, respectively. It is important to note that the somewhat erratic nature of the soil moisture increases is at least partially an artifact of interpolation error because soil moisture content was only measured by the TDR at 4 locations between the surface and tile depth.

4.3.3 Tracer breakthrough to tile: days 0 - 21

Irrigation, precipitation, and tile discharge, (Figure 4.8a) are closely related to the concentration and cumulative mass flux of Br in the tile effluent (Figure 4.8b) during the 3 weeks following tracer application; whereas, Cl concentration shows little variation during the same time period. The presence of Br in the tile effluent within 1 hour of application indicates that preferential flow has influenced tracer movement during the experiment. Br concentrations in the tile effluent rise continuously throughout the irrigation interval and peak 1 hour after irrigation stops. Following the initial peak, Br concentrations rapidly decline to less than 25 % of the maximum value within 24 hours, and generally undergo a more gradual decline in the following 20 days. While numerous small precipitation events do not have significant influence on tile effluent Br concentration during the 3 weeks following tracer application, relatively high intensity events on November 21st and November 27th both induce temporary increases in Br concentration and tile discharge rates. Based on the various precipitation events at the site during the latter part of November, in order for precipitation to notably influence Br breakthrough characteristics, rainfall intensity needs to exceed 2 mm hr^{-1}, which is very close to the mean unsaturated hydraulic conductivity values obtained from the TI tests for the 5 cm tension setting (Table 4.2). Because previous work has suggested that macropores become hydraulically active within this tension range (*Jarvis*, 2007), it can be surmised that precipitation in excess of 2 mm hr^{-1} within 3 weeks of tracer application was able to flush Br from the near surface soil matrix into macropores that were connected to the tile drain, thereby inducing temporary concentration increases.

Although Br concentrations in the tile effluent rise quickly after tracer application, and the wet soil conditions reflect ‘high risk’ conditions for tile drainage contamination from surface applied solutes via preferential flow, the amount of Br mass captured by the tile within 48 hours of tracer application is only 8 % of the applied mass (Figure 4.8b). A similar amount of Br was captured by the tile within 48 hours of the large precipitation event that began on November 21st, where 23 mm of rainfall was received over 24 hours. After 3 weeks of relatively wet soil/hydrologic conditions, the Br mass captured by the tile drain accounts for 27 % of the total amount applied.

While Figure 4.8b clearly shows that Br reaches the tile drain quickly, the short term temporal dynamics of tracer transport at the site become clearer after the effects of baseflow dilution have been removed. The modified Br breakthrough curve (Figure 4.9) shows that tile flow from outside the irrigation area has a significant impact on the concentration of Br in the tile drain. Instead of peak concentrations arriving one hour after irrigation stopped as shown in Figure 4.8b, the modified breakthrough curve shows that Br concentration in the water draining from the test plot actually peaked one hour after irrigation began, and concentrations declined rapidly as tile discharge increased. The high Br concentrations observed soon after tracer application are the result of preferential movement of tracer laden water to the tile drain prior to significant dilution from post tracer-application irrigation water. Br concentration remains low while irrigation induced tile discharge remains elevated; however, Br concentration increases again as discharge rates decline upon the cessation of irrigation.

4.3.4 Residual tracer distribution

Tracer concentrations in the soil pore water ranged from 0 to 113 mg l^{-1} for Br, and 5 to 194 mg l^{-1} for Cl, in the 16 soil cores that were extracted in September 2008. At low concentrations, the tracer distribution throughout the sampled soil volume is quite diffuse, and difficult to visualize. To enable easier comparison, and to clearly shown where the majority of the tracer mass is retained, both the Br and Cl residual concentration plumes are delineated by a 50 mg l^{-1} isosurface (Figure 4.10). Estimates of residual mass suggest less than 2 % of the original Br mass is retained in the soil, of which the majority is localized in the down-gradient end of the plot, within the A horizon. The maximum soil pore water Br concentration in the immediate vicinity of the tile drain was approximately 20 mg l^{-1} and was also localized in the down-gradient end of the plot. The amount of residual Cl tracer in the soil was difficult to determine because of the presence of legacy Cl from many years of liquid swine manure application at the site; however, if the 50 mg l^{-1} isosurface is used to approximate the position of the Cl tracer plume, it is apparent that the majority of the mass is retained between the surface and tile drain depth. Plan view perspective of Figure 4.10 shows that the centroid of the residual Cl plume has shifted down the topographic gradient and towards the tile drain, in relation to the position of the original Cl application surface. Even though Cl concentrations in the tile effluent did not appear to rise significantly over the 10 month period between tracer application and core extraction, pore water analysis results show that the Cl plume from the tracer experiment had reached the tile drain by mid-September 2008.

4.3.5 Tile discharge – water level correlation

Normal probability plots of tile discharge and water level in the piezometers are shown in Figure 4.11. The normality of the raw tile discharge data (Figure 4.11a) was considerably improved (Figure 4.11b) by applying a power transform of the form $Q_t(\lambda) = (Q \exp \lambda - 1)/\lambda$ where $Q_t(\lambda)$ is transformed tile discharge, Q is raw tile discharge, and λ is the power parameter. In this case, the optimal value of λ is -0.3423. Although the transformed tile discharge data does not perfectly follow a normal distribution, it does display distribution characteristics that are similar to the water-level data (Figure 4.11c-h), with the mid-range data tending to be aligned more closely to the normal distribution than the tail data which tends to diverge away from the normal distribution, in the direction of the mean value.

Water-level fluctuation is strongly correlated with transformed tile discharge for all six of the piezometers that were assessed (Figure 4.12), with cross-correlation coefficients ranging from 0.74 to 0.88. Lag time between water-level fluctuation and tile discharge is minimal for the 4 shallow piezometers, W1, W2, W4, and W5; however, water-level fluctuation in W6 (screened at 2.5 m), and W7 (screened at 4.5 m), lags tile discharge by 12, and 15 hours, respectively. The hydraulic response of W3 to precipitation and irrigation was muted because of its close proximity to the tile drain. Accordingly, there was very little water-level fluctuation in W3 during all but the most intense hydrologic events. As a result, the W3 water-level dataset was not ideally suited for cross-correlation analysis.

Water-level measured in relation to tile drain elevation for all seven piezometers, between October 27, 2007 and January 28, 2008, is shown in Figure 4.13a. With the exception of W3, all of the shallow piezometers exhibit relatively high frequency water-level fluctuations that correspond to the high frequency variability observed in the tile discharge rates. Compared to the shallow piezometers, the high frequency water level fluctuations in W6 and W7 are somewhat muted; however, the deeper wells appear to contain low frequency signals that becomes more obvious after the data has been smoothed (Figure 4.13b). The low frequency water-level variation in the deep wells closely resembles the tile drain baseflow variability that is apparent in Figure 4.13c, whereas the base water-level in the shallow piezometers is relatively constant. The low frequency water-level fluctuation in W6 and W7 indicates that the magnitude of the vertical hydraulic gradient within the shallow groundwater flow system at the site undergoes seasonal variation that coincides with variation in tile drain baseflow.

The strongest correlation between modelled and measured tile discharge was achieved by coupling the raw water-level in W1 with water-level from W7 that had been smoothed using a 1550 day centered moving average (Figure 4.13b). The combination of high frequency water-table fluctuation, with the low frequency deep water-level fluctuation, yielded an empirical model, of the form described in section 2.9, that can accurately replicate both the high frequency variability in tile discharge associated with individual precipitation events and the low frequency variability in tile base flow (Figure 4.13c). The A and B fitting parameters for the model were 2.374 and -1.767 respectively. The cross-correlation coefficient for the modelled vs. measured transformed tile discharge relationship is 0.93, with less than 1 hour of lag (Figure 4.14). The strong correlation between modelled and measured discharge demonstrates that predicting tile discharge as a function of water-levels is a viable alternative to long term continuous tile monitoring. Although the fitting parameters defined here are site specific, the general approach is readily transferable and easily applied.

4.3.6 One year tracer movement

Following tracer application, Br concentrations (Figure 4.15a) in the tile effluent tend to decline logarithmically with respect to a linear time scale; however, numerous short duration melt, (Figure 4.15b) and/or precipitation, (Figure 4.15c) events can cause temporary concentration increases/decreases. Because tile discharge rates increase in the late fall and remain elevated throughout the winter months, the tile drain Br mass capture rate (Figure 4.15d) tends to remain relatively stable over the first two and a half months following tracer application, even though concentrations decline; although once again, short duration climactic events can induce temporary variability. It is not until after a major winter melt event in mid January that the Br mass capture rate declines appreciably, at which point over 75 % of the applied Br (Figure 4.15e) has already been accounted for in the tile effluent. The next most significant decline in Br mass capture rate occurred following the spring melt that occurred at the end of March, when both tile flow rates and Br concentrations experienced significant concurrent declines. By the end of March, almost 100 % of the applied Br mass was accounted for in the tile effluent. Significant precipitation events in early May and early June both induce temporary increases in both Br concentration and mass capture rate; however, neither parameter reaches levels obtained during the winter, or spring, melt events. Bromide concentrations dropped below 0.1 mg l^{-1} at the beginning of August and remained undetectable until heavy precipitation in mid September caused concentrations to rise to approximately 1 mg l^{-1}. Concentrations dropped below 0.1 mg l^{-1} again by early October, where they remained until tile monitoring ceased.

Results of cumulative mass capture estimation, that utilized the modelled tile discharge, shows the relative importance of late fall precipitation, winter precipitation and melts, and spring melt events, on tracer movement. The single most significant event with respect to Br mass capture occurred over a ten day winter melt event in early January (Figure 4.16). During this period, the average temperature was 3 °C, 62 mm of precipitation was received at the site, and approximately 20 % of the total applied Br mass was discharged through the tile drain. In comparison, approximately 50 % of the total Br was discharged through the tile drain during the entire two month time frame that preceded the January melt. By the beginning of May, Br captured by the tile had risen to approximately 110 %, and between May and November, an additional 4 % of the Br mass is discharged. When the amount of residual mass in the soil profile is also considered, 116 % of the original Br mass is ultimately accounted for within one year of application.

Chloride concentrations in the tile effluent remained quite stable throughout the one year monitoring period and generally remained within the bounds of background levels measured prior to tracer application. Tile drain sampling during September 2007 at the site established that background Cl concentrations ranged from 4 to 11 mg l^{-1}. In the one year period following tracer application, concentrations only exceeded 11 mg l^{-1} on three very wet occasions (early December, mid January, and early May), when maximum concentrations of 15 mg l^{-1} were reached. Cl concentrations also experienced significant (albeit temporary) declines to as low as 1 mg l^{-1} during extremely wet conditions on numerous occasions, such as the melt events in mid January, mid February, and the end of March. Br concentrations declined in conjunction with the declines in Cl concentrations; however, the magnitude of the declines was always greater for Br.

The performance of the approach used to predict one year cumulative Br mass capture can be partially assessed by comparing the model based prediction for the November 7th to 28th time interval with the mass capture estimate obtained by using tile discharge data obtained from the monitoring station (i.e. comparing Figures 4.15e and 4.8b). Such a comparison shows that estimating Br mass capture with the tile discharge model underestimates cumulative mass by approximately 7 %, at the end of the 21 day time interval considered. These results indicate that although the model based estimates are not exact, cumulative mass calculated using modelled tile flow will give a relatively accurate perspective on solute loading to surface water via tile drains.

4.4 Discussion

The close relationship between the increase in soil moisture content at a depth of 23 cm and rapid tile discharge response to precipitation/irrigation is consistent with the dye infiltration tests that showed that macropore flow into the B horizon was initiated at the top of the hardpan layer. When the soil matrix at the base of the topsoil layer nears saturation, the opportunity for localized ponding at the top of the hardpan increases, and as a result, there is increased likelihood that water will laterally disperse until vertically continuous macropores are encountered that facilitate B horizon preferential flow. When these vertically continuous B horizon macropores extend into the soil surrounding the tile drain, they become effective conduits for water from the A horizon to be rapidly transmitted to the tile by bypassing the B horizon soil matrix. When the entire soil profile is nearly saturated, it is reasonable to expect diminished hydraulic activity within macropores that are enveloped by low permeability soil. In such situations, it can be envisioned that water will disperse laterally across the top of the hardpan until macropores are encountered that can remain hydraulically active because of effective subsurface drainage. Conversely, when the soil profile is not saturated, water application rates do not exceed the imbibition capacity of the topsoil layer, and there is adequate storage capacity in the topsoil layer for all the incident water, the opportunity for lateral water movement across the top of the hardpan will be reduced. In such a situation, incident water distribution within the soil profile will be largely controlled by matrix flow processes, and the dynamic response of tile discharge to precipitation/irrigation will be muted.

The highest tracer concentrations in the tile effluent were observed shortly after tracer application because preferential flow processes were able to transmit tracer laden incident water directly to the tile drain with minimal interaction with soil matrix pore water and minimal dilution from irrigation water. Although high solute concentrations can be toxic to aquatic life, and should not be disregarded, very little of the applied tracer reached the tile as a result of direct preferential flow. In actuality, the majority of the tracer mass was transmitted to the tile in response to large precipitation and/or melt events that occurred throughout the late fall and early winter time frame. During these significant but infrequent hydrologic events, tile drain baseflow was much higher; and as a result, dilution of surface derived solutes is enhanced, and concentrations are reduced accordingly. Results from this work show that even though concentrations are lower, total solute mass loading to surface water during significant hydrological events far exceeds the immediate post-application period, even when the post application period reflects 'worst case' conditions for solute land application (i.e. on wet soil with tiles flowing and followed by heavy precipitation).

During major melt events, such as the one experienced during mid January, tracer concentrations in the tile effluent tend to slowly rise (Figure 4.16a) in response to increasing temperatures (Figure 4.16b), and light precipitation (Figure 4.16c). As melting continues, the water content at 23 cm depth increases (Figure 4.16d) until saturation, at which point extensive macropore flow from the top of the hardpan layer to the tile drain can be expected. At the point when soil at 23 cm depth becomes saturated there is a concurrent decrease in tile effluent tracer concentrations, which indicates that tracer laden water leaching from the soil matrix is being diluted from incident water transmitted directly to the tile via macropore flow.

The magnitude of the hydraulic gradient measured perpendicular to the tile also relates to fluctuations in tracer concentration in the tile effluent. As shown in Figure 4.16e, the gradient between the W3 and W5 piezometers begins to increase at the same time that Br concentrations increase during the January melt event, which suggests that the soil in the vicinity of the tile drain underwent increased solute leaching during the early stages of the melt. However, as hydrologic activity increased during the January melt event, tracer concentrations began to drop sharply. At the point when concentrations drop, water levels in the piezometer closest to the tile drain (W3) rise sharply, and as a result, lateral hydraulic gradients towards the drain decline substantially. With lateral gradients essentially absent during these brief periods when hydrologic activity is most intense, flow through the soil matrix essentially becomes a one dimensional process; and therefore, the majority of the water that is transmitted to the tile drain through the soil profile is transmitted through an area immediately above the drain. As a result, the soil above the tile drain will be subject to increased solute leaching compared to soil away from the drain.

Macropore characterization identified that macroporosity was approximately 7 times higher near surface than at tile depth. Such a macropore spatial distribution indicates that the majority of macropores terminate above tile depth, and as a result, the majority of macropore flow in will occur in dead end pores that terminate far enough above the tile drain to preclude their direct contribution to tile discharge. When the primarily vertical orientation of the B horizon macropores is considered in conjunction their spatial distribution, it becomes evident that the ability of macropores to transmit solutes rapidly to tile drains is limited to relatively few B horizon macropores in close vicinity to the tile. Because there is limited opportunity for lateral solute transport through the macropores, the permeability of the soil matrix coupled with the magnitude of the lateral hydraulic gradient exerts major influence on solute movement to the tile drain. In this experiment, the cumulative Br flux pattern largely reflects the importance of matrix flow processes because only a small proportion of the total Br was preferentially transmitted to the tile drain relatively soon after application, even though the soil and hydrologic conditions at the time of tracer application represented an ideal scenario for macropore flow to occur.

Despite the limited preferential movement of solutes to the tile drain immediately after surface application, a significant portion of the total applied mass can be captured by the tiles over longer periods of time. As was demonstrated at this site in southwestern Ontario, when solutes are applied to the land surface post-harvest it can be expected that the majority of the mass applied within 2 m of the tile will be leached from the soil profile prior to the next growing season. When it is considered that tile drains are often spaced 10–15 m apart, upwards of 25% of soluble nutrients applied post-harvest will be potentially become surface water contaminants in settings with similar hydrogeological and climate conditions.

In addition to soil characteristics, shallow groundwater flow direction also influences solute flux and distribution. Because the vertical component of groundwater flow is directed upwards at this site (which is not uncharacteristic of tile drained sites in southwestern Ontario), the tracers did not migrate deep into the soil profile. In such settings, local groundwater is at relatively low risk of contamination from solutes applied at the field surface, and tile drains/surface water serve as the primary receptors for solutes exported from the soil profile.

4.5 Conclusions

In general, solute flux and distribution at any site with macroporous, tile drained soil, will be governed by many factors, including: antecedent moisture content, macropore extent and anisotropy, permeability of soil layers, hydraulic gradients induced by both the tile drains and shallow groundwater flow, and climate variability. For a proper understanding of nutrient fluxes in such complex settings, each of these factors must be given adequate consideration.

The results from this work demonstrate the importance of the regional shallow-groundwater flow system on water and solute flux in tile drained agricultural settings. At sites similar to the site investigated here, where shallow-groundwater is moving towards the surface, the hydraulic gradients act as a protective barrier that inhibits surface applied solutes from migrating deep into the soil profile. In these settings, tile drains, and ultimately surface water bodies, are the primary receptors for water and solutes that leach from the soil profile.

Although it has been shown that solutes can be rapidly transmitted to tile drains after surface application during high risk environmental conditions (i.e. initially wet, macroporous soil, where heavy precipitation succeeds application), the initial solute breakthrough to the tile accounts for a small proportion of the applied mass. The low initial mass capture ratio can be attributed to the primarily vertical orientation of the B horizon macropores that direct preferential flow in a downward direction. As a result, the permeability and hydraulic conditions of the soil matrix ultimately govern the lateral movement for the majority of the solutes transmitted into the B horizon via preferential flow paths that do not terminate in close proximity to tile drains.

The most important factors controlling the temporal pattern of solute flux in the tile drain were climate related, with the magnitude of the precipitation and/or melt event being directly proportional to the mass flux rate. As an example, approximately 20% of the solute mass applied within 2 m of the tile was discharged in response to a single winter melt event that spanned a 10 day interval in mid January. During the late fall/early winter time frame, smaller precipitation events also caused notable increases in the solute mass capture rate.

Tile drain flow rates can be exceptionally difficult to monitor over an annual cycle because of the wide measurement range required. While sensitive flow meters may be applicable during periods of relatively low flow, these types of devices do not withstand long term deployment in high flow conditions. Because the majority of tile drainage solute flux occurs in response to major hydrologic events, accurate tile discharge measurements during high flow conditions are imperative for quantifying water/solute/nutrient budgets in agricultural settings over annual cycles. To alleviate the need to constantly maintain flow monitoring equipment during peak flow conditions, the relationship between groundwater levels and tile flow rates can be utilized. In this work, knowledge of water-table position, along with water-level in a 4.5 m deep monitoring well was effectively used to develop an empirical model that estimated tile flow rates over a wide range of hydrologic conditions.

4.6 Figures and Tables

Figure 4.1. General location of the research site in southwestern Ontario, Canada (modified from http://atlas.gc.ca).

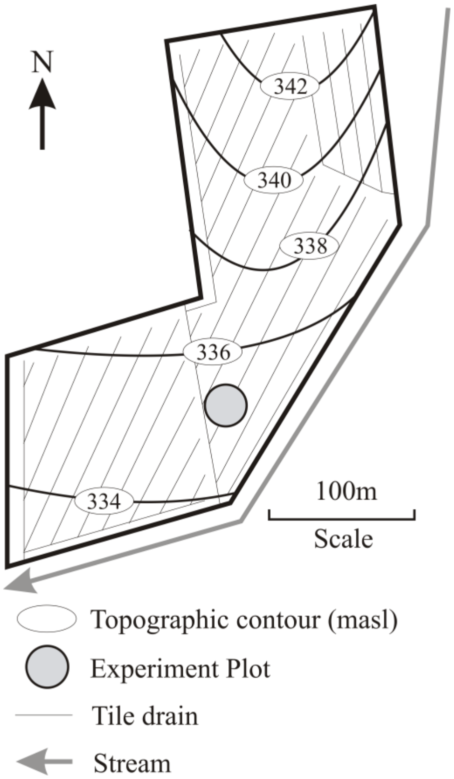

Figure 4.2. Experimental plot location relative to the field topography and boundaries.

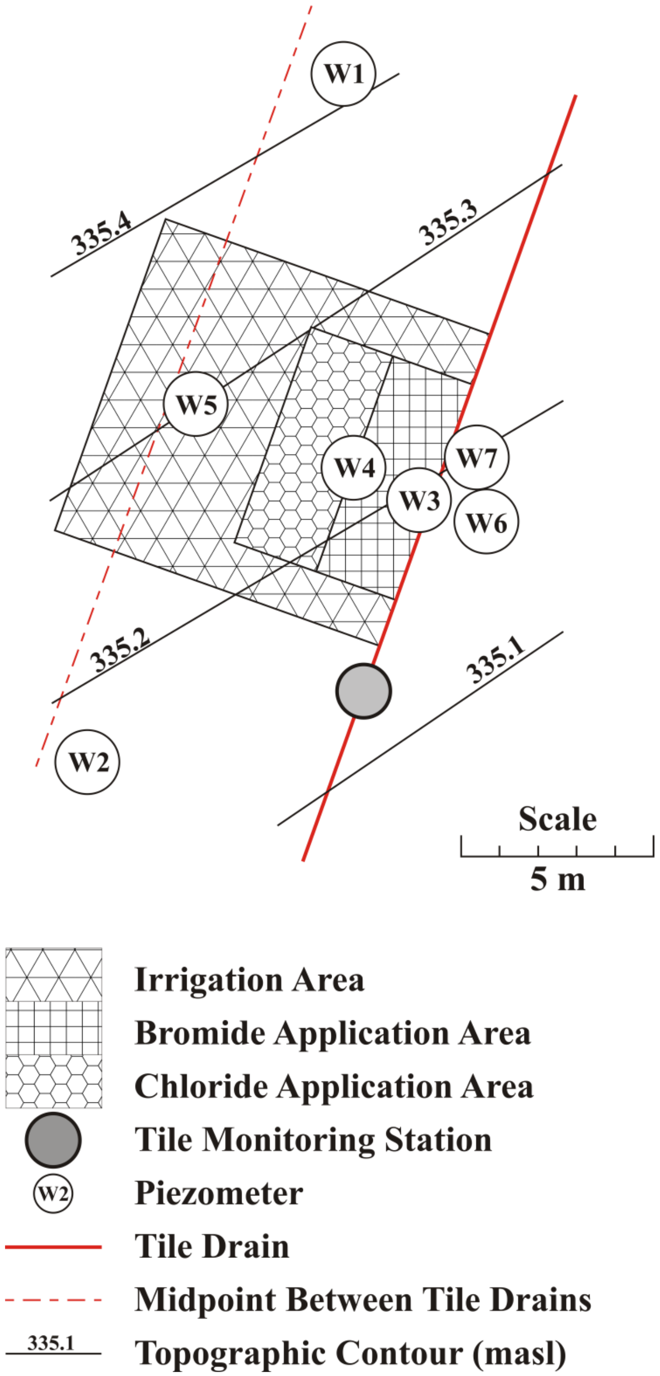

Figure 4.3. Experimental plot configuration showing the location of the bromide and chloride tracer application areas relative to the: irrigation area, shallow (W1, W2, W3, W4, W5) and deep (W6, W7) piezometers, and tile drain monitoring station.

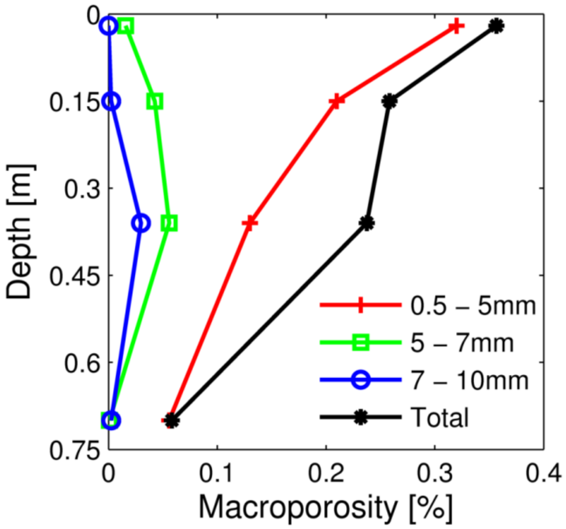

Figure 4.4. Mean macroporosity distribution at the experiment plot, for circular macropores of different sizes, and total macroporosity including fractures, from the surface to tile drain depth.

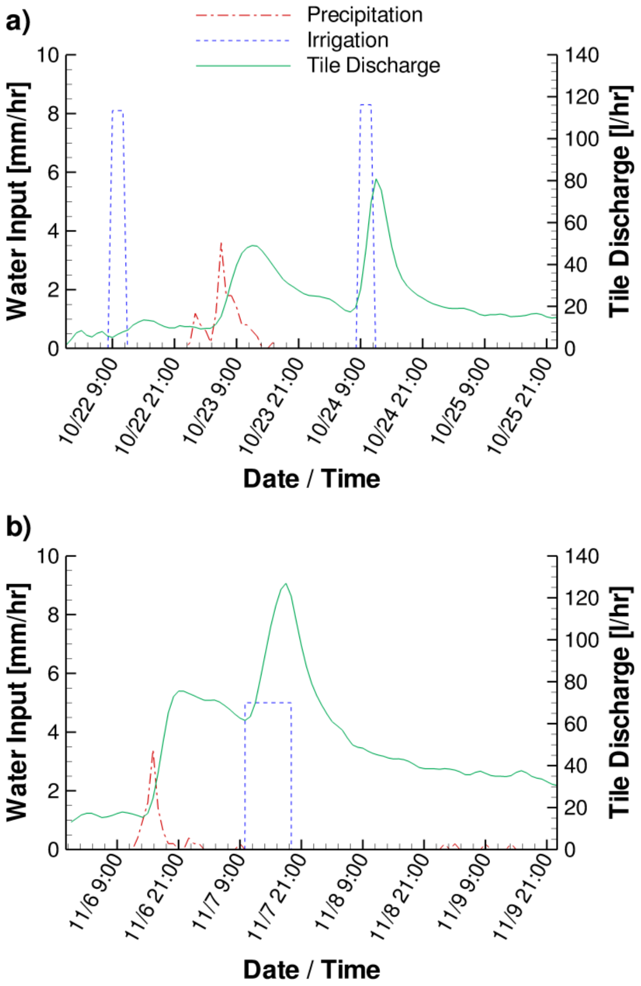

Figure 4.5. Tile discharge relative to precipitation and irrigation water input for (a) October 22 to 26, and (b) November 6 to 10.

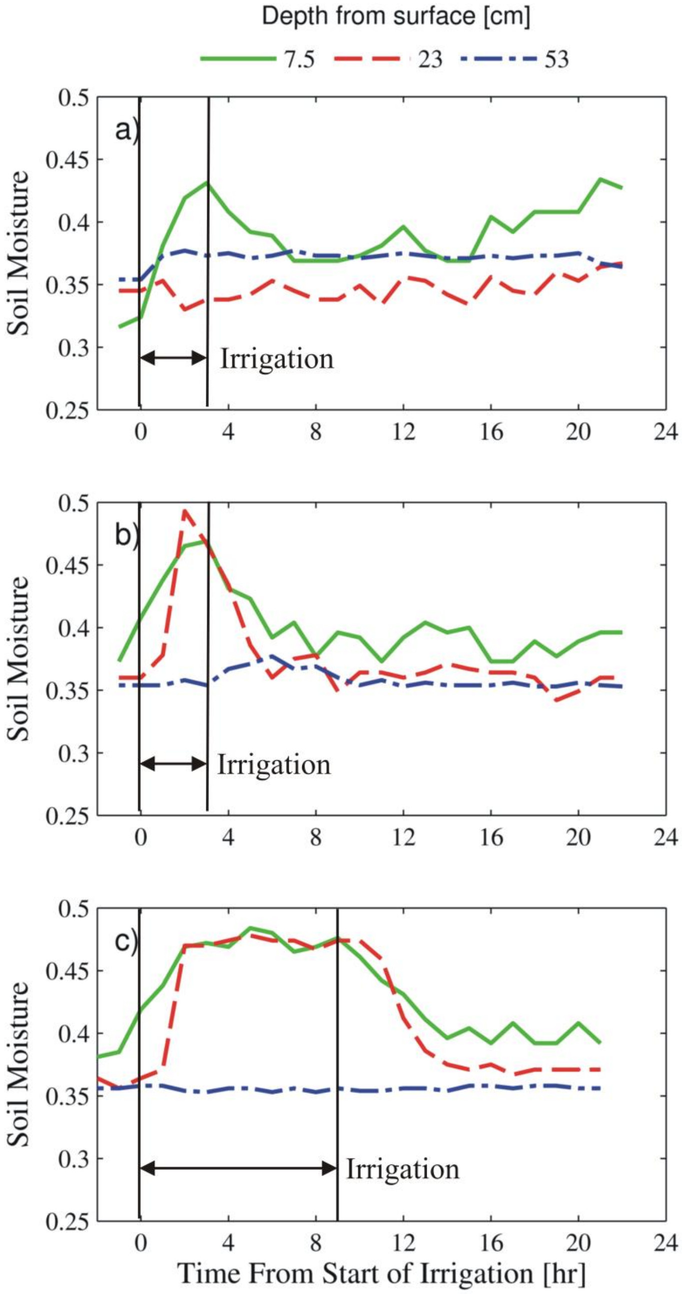

Figure 4.6. Soil moisture content fluctuation in response to the 3 hour irrigation events on (a) October 22, and (b) October 24; and (c) the 9 hour irrigation event on November 7.

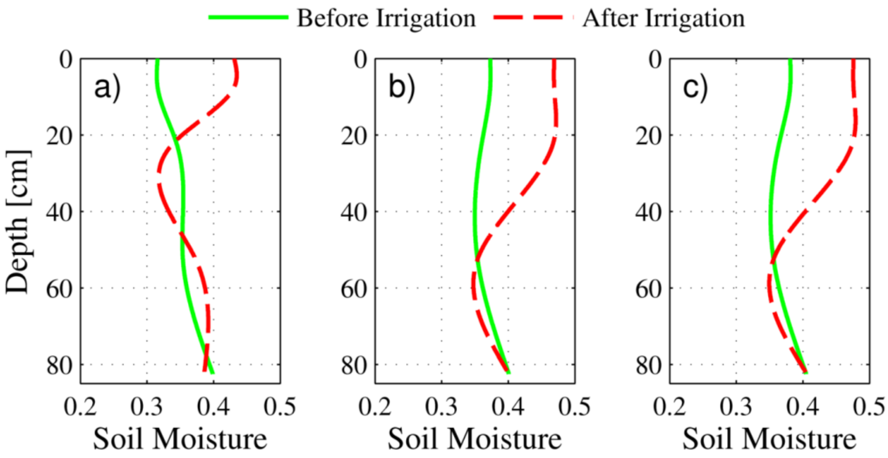

Figure 4.7. Vertical soil moisture profile before and immediately after the 3 hour irrigation events on October 22 (a) and October 24 (b), and the 9 hour irrigation event on November 7 (c).

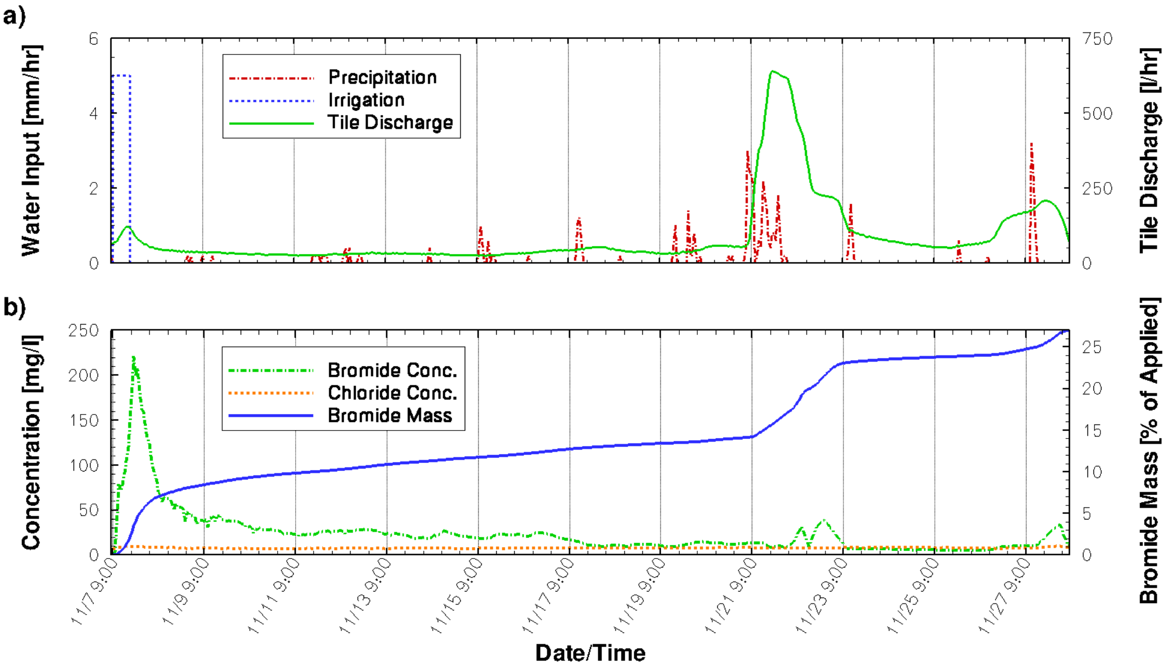

Figure 4.8. November 7 to 28 (a) tile discharge relative to precipitation and irrigation water inputs, and (b) tile effluent bromide and chloride concentrations and cumulative bromide mass as a percent of the total mass applied.

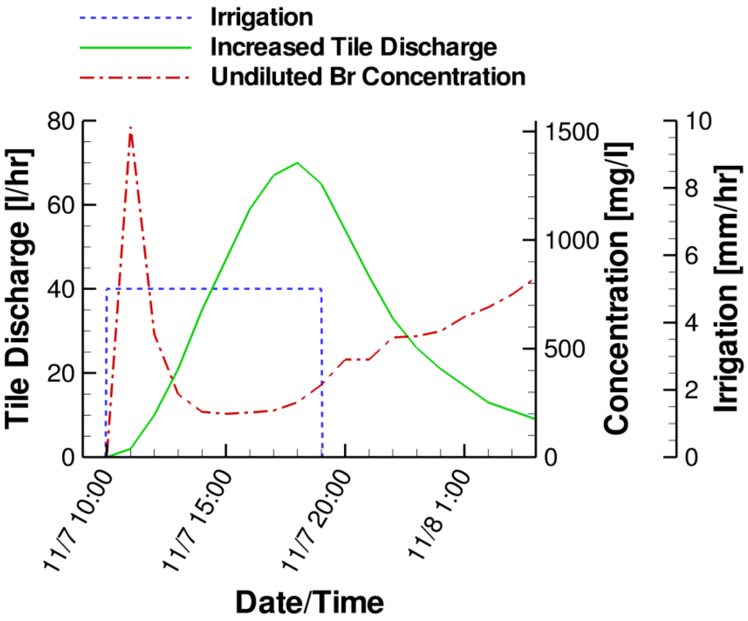

Figure 4.9. Tile discharge, bromide (Br) concentration, and irrigation, for the first 20 hours of the tracer test, after the dilutive influence from tile discharge sourced from outside the test plot were removed with hydrograph separation.

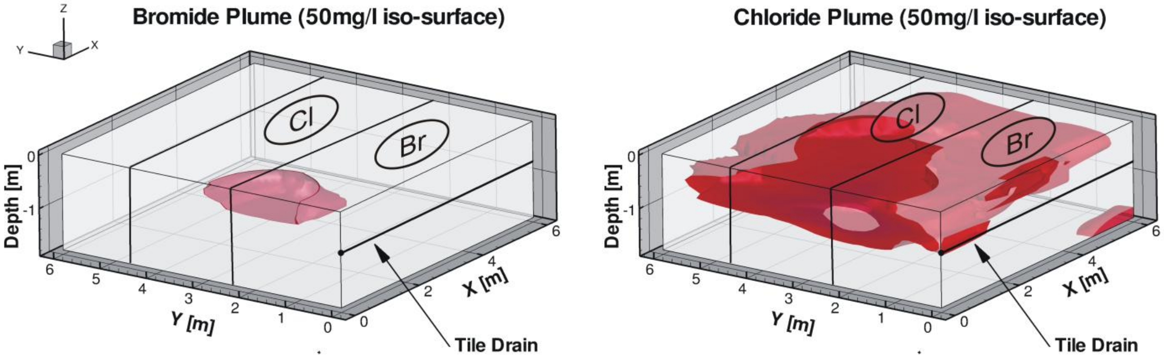

Figure 4.10. Residual bromide and chloride distribution in the tracer application area, as observed in mid September of 2008, relative to the initial application areas identified on top surface.

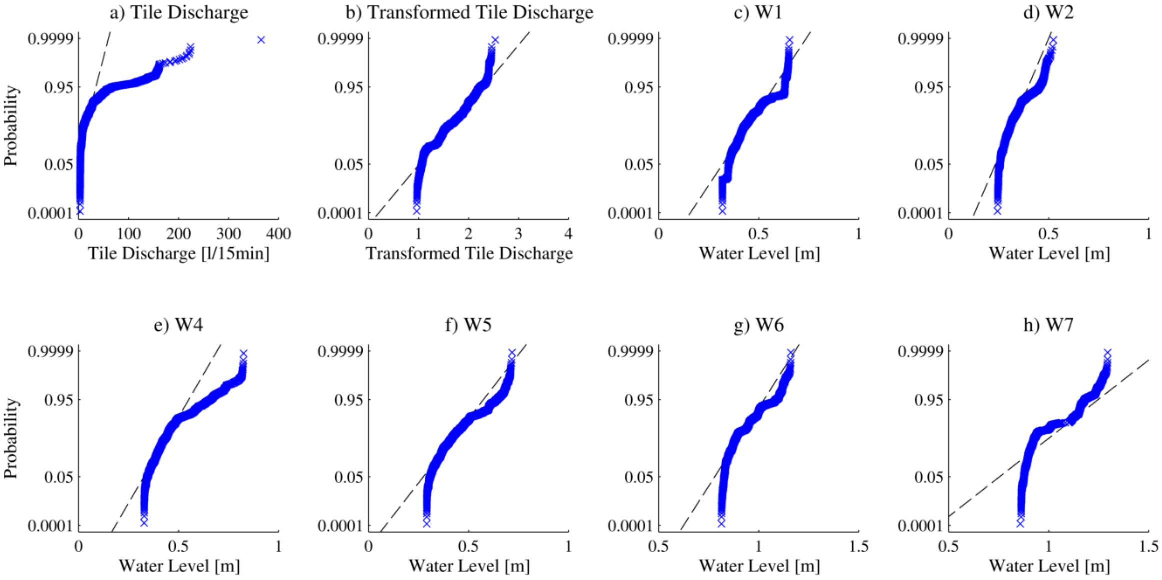

Figure 4.11. Normal distribution probability plots of the (a) raw, and (b) transformed tile discharge data, and the water level data from piezometers 1, 2, and 4 – 7 (c – h).

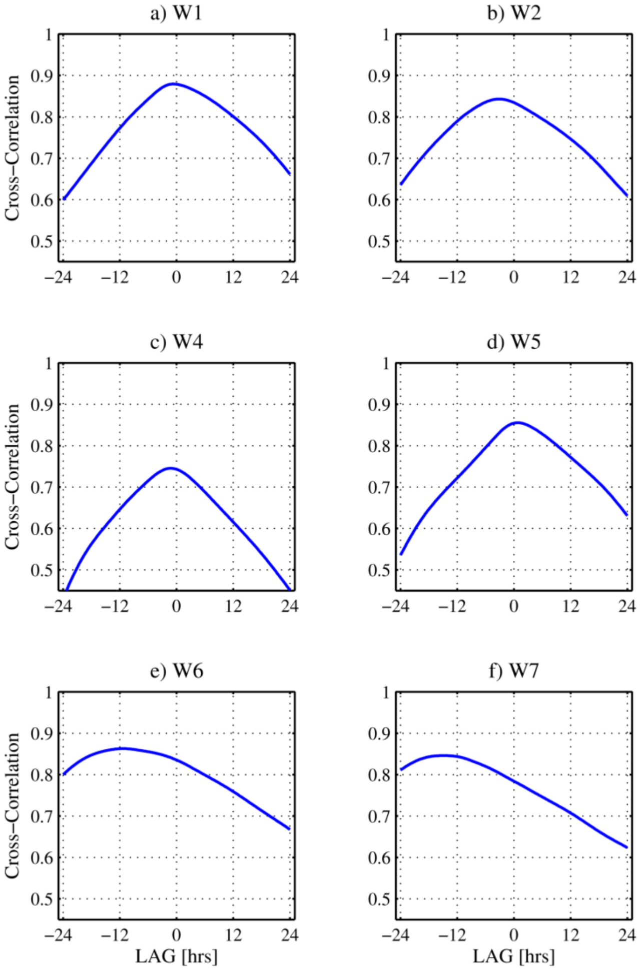

Figure 4.12. Cross-correlation between tile discharge and water levels in piezometers W1, W2, W4, W5, W6, and W7.

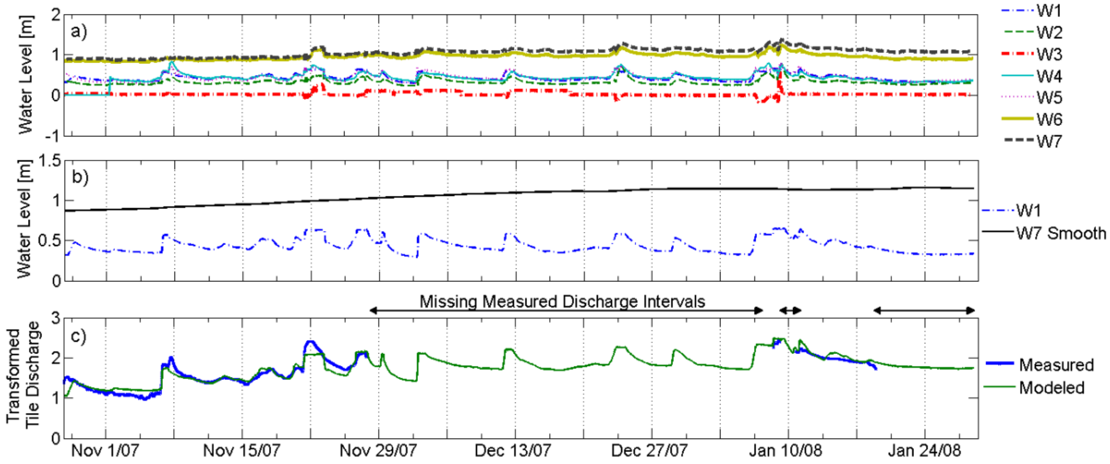

Figure 4.13. Water-level in relation to tile drain elevation in the seven piezometers (a), the two water level signals that compose the empirical tile discharge model (b), and modelled versus measured, transformed tile discharge data (c).

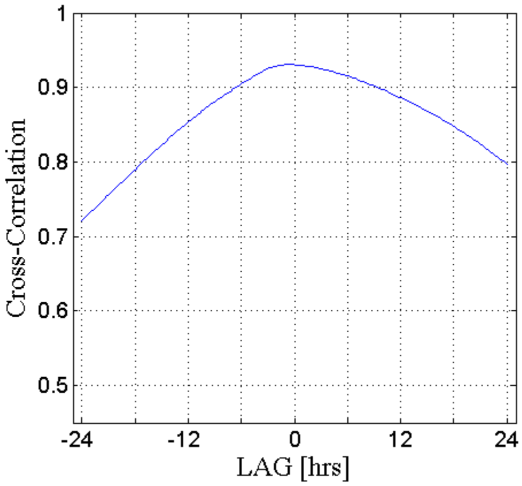

Figure 4.14. Cross-correlation between the modelled and measured transformed tile discharge data from October 27 to November 28, 2007.

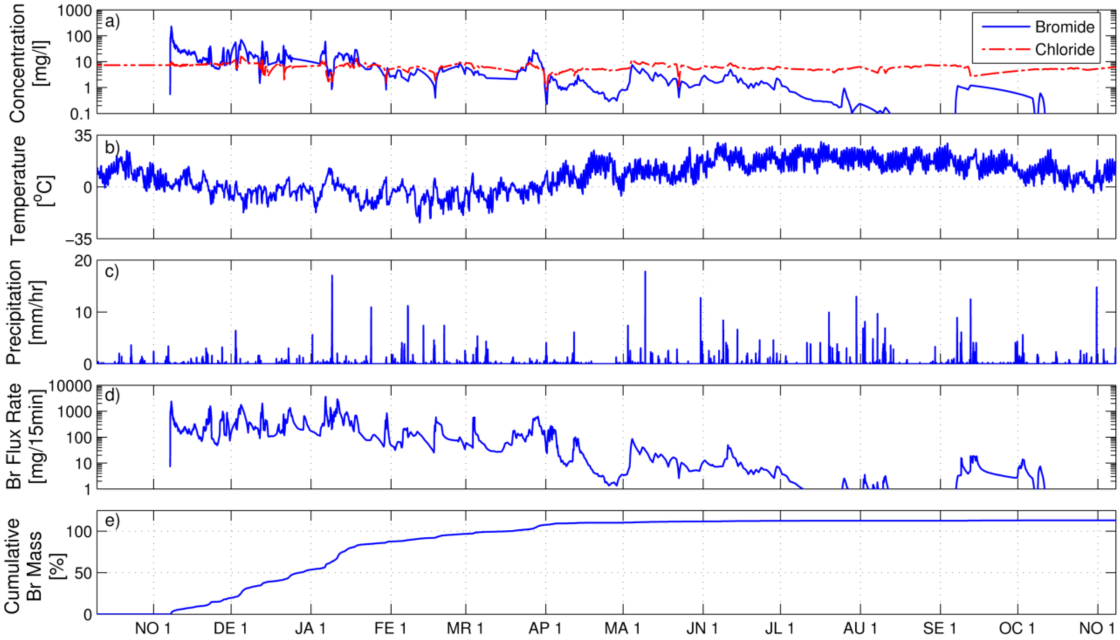

Figure 4.15. Bromide and chloride concentration in the tile effluent (a), temperature (b), precipitation (c), instantaneous bromide flux rate (d), and bromide (as % of initial mass applied) captured by the tile drain (e), between October 2007 and November 2008.

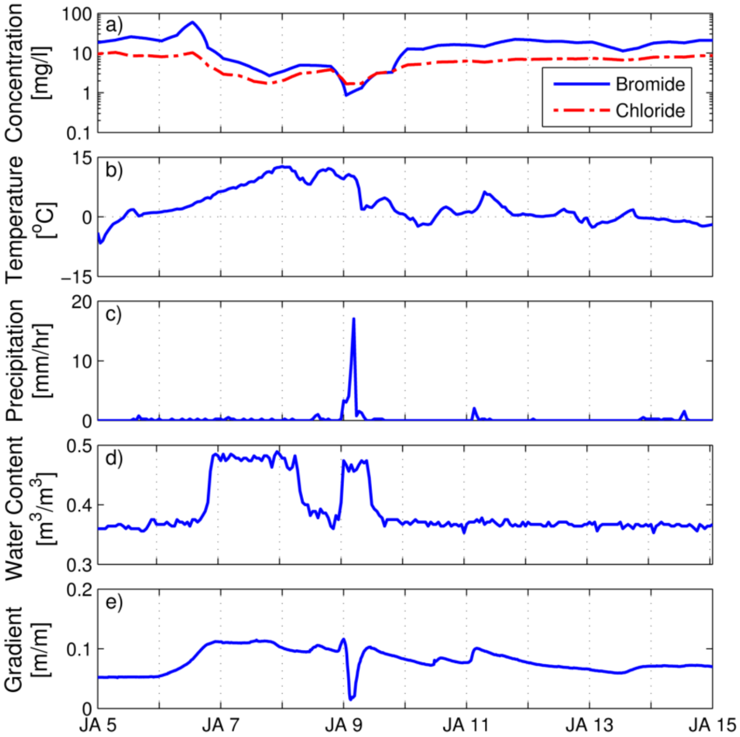

Figure 4.16. Bromide and chloride concentration in the tile effluent (a), temperature (b), precipitation (c), water content at 23 cm depth (d), and lateral hydraulic gradient between W5 and W3(e), during the January 2008 precipitation/melt event.

Table 4.1. Mean values for selected physical properties of the A and B horizon soils as determined with core analysis, and for B horizon hydraulic conductivity.

Soil Horizon	Sand [%]	Silt [%]	Clay [%]	Gravel [%]	Bulk Density [g cm^{-3}]	Organic Matter [%]	Log$_{10}K_{sat}$ [cm d^{-1}]
A†	49.9 (1.5)	30.4 (1.5)	13.2 (0.7)	6.5 (1.7)	1.2 (0.0)	6.3 (0.3)	-
B‡	28.8 (3.9)	48.3 (3.1)	14.6 (1.2)	8.3 (3.2)	1.9 (0.1)	-	-0.6 (1.1)

† n = 6

‡ n = 4

Values in parentheses denote standard deviation

Table 4.2. Mean initial (θ_i) and final (θ_f) moisture contents, and surface soil unsaturated ($K_{x,y}$), and saturated (K_{fs}) hydraulic conductivity. Row 1, and row 2, are located above, and 2 m away, from the tile drain, respectively.

Row	Θ_i	Θ_f	Log$_{10}K_{x,y}$ (cm d^{-1})				Log$_{10}K_{fs}$ [cm d^{-1}]
			Tension [cm]				
			5	2	1	0	
1†	0.34 (0.02)	0.42 (0.01)	0.68 (0.11)	1.26 (0.33)	1.60 (0.34)	2.25 (0.27)	2.01 (0.39)
2†	0.35 (0.02)	0.43 (0.01)	0.43 (0.16)	0.98 (0.13)	1.33 (0.10)	2.56 (0.42)	0.87 (0.48)

† n = 3

Values in parentheses denote standard deviation

Chapter 5

Viscosity dependant, two-dimensional, dual-permeability numerical modelling of liquid swine manure flow in a layered, macroporous, and tile drained soil

5.1 Introduction

Liquid swine manure (LSM) is a large source of non-point pollution across the agricultural landscape. In 2006 it was estimated that over 15 million swine in Canada produced approximately 16 million tonnes of manure (*Hofmann*, 2008), of which approximately 85% (*Statistics Canada*, 2002) could be expected to have been in liquid form. Primarily because of economies of scale, the current trend in livestock farming is progressing towards larger confined animal feeding operations, which is also leading to a greater geographical concentration of agricultural land receiving LSM soil amendments. While the nutrients contained in the LSM (e.g. nitrogen, phosphorus) have appreciable agronomic value if they can be utilized for crop growth, they also pose significant risk to water resources, which is exemplified in the numerous studies that have shown that nutrient constituents of LSM are often detected in tile drainage relatively soon after application (*Fleming and Bradshaw*, 1992; *Hoorman and Shipitalo*, 2006; *Ball-Coelho et al*., 2007). The release of excess nutrients to the environment can result in eutrophication of surface waters and elevated levels of potentially harmful nitrate in groundwater. In addition to nutrients, LSM is also known to contain pathogens, heavy metals, antibiotics, and hormones (*Bradford et al*., 2008), for which the environmental risks are not yet fully understood.

In order to continue to increase our level of understanding of the environmental risks associated with the land application of LSM, we must increase our level of knowledge regarding the processes that control the movement of LSM through the soil. This goal is complicated by the large number of interacting factors that affect the movement of LSM, including the method and rate of LSM application, fluid properties of the LSM, physical properties of the soil, soil structural features, antecedent soil moisture content, and subsurface drainage status. These factors are considered in the current component of the research work which specifically addresses the issue of LSM movement in structured soils, with specific focus given to the following:

i) Modification of an existing dual-permeability model to account for variable viscosity as a function of solute concentration, and apply it to field based LSM flow and transport scenarios based on conceptual models that include: soil crusts, plowpans, directionally variable (anisotropic) macropore permeability, and numerical boundary conditions specific to LSM application methods.

ii) Demonstrate parameterization of the new model using pedotransfer functions in conjunction with, bulk soil composition and hydraulic conductivity information, and literature data.

iii) Determine the relative sensitivity of the simulated tile drain discharge rates and nutrient concentrations to variations in LSM viscosity, and the presence or absence of soil crust and plowpan layers.

The numerical experiments are based on field data and soil hydraulic parameter measurements collected during a series of LSM application experiments performed at an agricultural field near Sebringville, in southwestern Ontario, Canada, for which additional details are provided below. The primary goal of the work is to enhance the modelling tools that can be used to investigate the fate of LSM in shallow agricultural soils and to determine the significance and sensitivity of LSM, and subsurface properties, in controlling nutrient movement in the soil profile.

5.2 Background

5.2.1 Preferential flow

In shallow water-table, tile-drained agricultural settings, preferential flow pathways (macropores) such as biopores, root holes and desiccation cracks (*Beven and Germann*, 1982) in the soil profile can serve as conduits for rapid downward movement of LSM (*Shipitalo and Gibbs*, 2000). Although hydraulically active macropores occupy a very small proportion of total porosity in structured field soils, they can transmit more than 75% of the water flow under saturated conditions (*Mohanty et al.*, 1996; *Lin et al.*, 1997). Because macropores are not typically hydraulically active until soil water pressure head exceeds the range of -10 to -6 cm (*Jarvis*, 2007), it might be concluded that LSM application on relatively dry soil does not pose an environmental risk with respect to preferential flow. In practice however, LSM is applied at such high rates that localized ponding often develops on the application surfaces, which can readily initiate macropore flow if macropores vent in the vicinity of the pond. Once LSM enters a macropore its movement back into the soil matrix can be impeded by low permeability skin layers that line the walls of the macropores (*Gerke and Köhne*, 2002).

While the greatest proportion of macroporosity in shallow water-table agricultural soils is commonly observed near surface, features such as worm burrows and root holes are routinely observed to reach tile drain depths (*Shipitalo and Gibbs*, 2000; *Nuutinen and Butt*, 2003; *Shipitalo et al*., 2004), and facilitate the rapid transmission of LSM to groundwater, and to surface-water via tile drain discharge.

It has been well established that dual-continuum numerical models are superior to their single-continuum counterparts for modelling flow and transport through macroporous soil (*Vogel et al*., 2000; *Gärdenäs et al*., 2006; *Gerke et al*., 2007). Comprehensive reviews of preferential flow and transport modelling methodologies and past work on the subject are given by *Köhne et al*. (2009); *Gerke*, (2006); and *Simunek et al*. (2003). One of the more widely used dual continuum modelling approaches was initially presented by *Gerke and van Genuchten* (1993a). In the *Gerke and van Genuchten* (1993a) formulation, volumetrically proportioned soil matrix and macropore zones are considered to be superimposed within the same model space, for which a coupled pair of Richards equations are used to describe flow processes, and a coupled pair of convection-dispersion equations are used to describe transport processes; while first order water and solute exchange terms are used to control interactions between the two continuum. Application of the *Gerke and van Genuchten* (1993a) formulation to field based modelling scenarios is complicated by the parameter intensiveness of the governing equations (*Simunek et al*., 2003), and by the impracticality of obtaining estimates for some of the most critical parameters at the plot and field scale.

The predominantly vertical nature of macropore features (*Bouma et al*., 1982; *Edwards et al*., 1988; *Mohanty et al*., 1998; *Cey and Rudolph*, 2009) infers that vertical fluxes will be much greater than horizontal fluxes in macropore networks. Recent past work (*Gerke et al*., 2007) has utilized two-dimensional (2D) dual-permeability models for analysis of preferential flow and transport in macroporous soils; however, the directional nature of macropore networks, and the associated influence on bulk flow direction, has not yet been carefully considered in multi-dimensional dual-permeability models. Because results from past field experiments have found that preferential flow intercepted by tile drains has originated at the surface and in close proximity to the drain (*Mohanty et al*., 1998; *Shipitalo and Gibbs*, 2000), the anisotropic nature of the macropores can be considered important for governing the lateral distribution of infiltrating water and solutes within the soil profile. The concept of an anisotropic macropore network is further supported by previous work that has documented that macropores are not always vertical features (*Perret et al*., 1999; *Shipitalo and Gibbs*, 2000) and may in fact be inclined. Failure to properly account for macropore flow direction will restrict the ability of a model to accurately predict the horizontal distribution of water and solutes, and poses a conceptual problem for multi-dimensional models that are used for purposes such as estimating time dependant tile drain capture, and determining the residence time of chemicals in the soil profile.

The use of multi-dimensional models is particularly important for investigating water and nutrient movement in fields with subsurface (tile) drainage. While tile drainage systems can act to integrate the effects of spatial variability in soil composition and structure, and allow tile drained fields to effectively serve as field scale lysimeters (*Richard and Steenhuis*, 1988), they can also induce relatively steep localized hydraulic gradients that necessitate the use of 2D models for realistic preferential flow and transport analysis (*Haws et al*., 2005; *Köhne and Gerke*, 2005).

5.2.2 Soil crust and plowpan layers

Shallow water-table, tile drained, agricultural soils typically contain distinct morphological layers, such as soil crusts and plowpans, that collectively govern infiltration processes that will act on both liquid manure and water. Soil crusts can readily form at the soil surface as result of raindrop or irrigation water impact forces which cause slaking of soil aggregates and dispersion and orientation of the finer soil particles. *McIntyre* (1957) found that soil crusts formed through simulated raindrops impacting on the surface of fine sandy loam soil had hydraulic conductivities that were approximately 4 orders of magnitude lower than the underlying soil. It has also been demonstrated that simulated raindrops can effectively seal macropores up to 5 mm in diameter (*Ela et al*. 1992).

In conventionally tilled soils, dense, low permeability plowpan layers often exist which restrict vertical infiltration through the soil matrix. In dye infiltration studies, plowpans have been observed to restrict the vertical migration of dyed water through the soil matrix and tend to cause the dye to spread laterally until it encounters vertically continuous macropores that can facilitate further downward movement (*Shipitalo et al*., 2004). In past numerical modelling work, *Abbaspour et al*. (2000) concluded that a plowpan layer, with hydraulic conductivity of approximately 0.001 and 0.018 times that of the overlying and underlying soil respectively, needed to be included in order to accurately simulate pressure heads and water contents observed during plot scale irrigation experiments. Similarly, *Rosenbom et al*. (2009) found that inclusion of a plowpan layer within their model domain improved the ability of the model to match field observations. In tile drained soils, cracks have been observed to be more abundant above as opposed to below the plowpan layer

(*Shipitalo et al*., 2004), which suggests that plowpan layers are located at an interface between two regions with different structural characteristics.

Although the importance of soil crusts and plowpan layers in controlling infiltration processes are generally well known, these features are not yet commonly incorporated into the numerical models that are used to simulate infiltration processes. In order to accurately simulate infiltration in agricultural soil, the inherent physical complexities of the layered soil profile need to be incorporated into the model domain.

5.2.3 Liquid swine manure fluid properties

When investigating movement of LSM through soil it is important to note that the viscosity of LSM is well correlated with its dry matter content (*Landry et al*., 2004; *Keener et al*., 2006). Analyzing the movement of LSM through partially saturated porous media using a Richards equation based approach is supported by past work that showed manure slurries with less than 5% total solids behave as Newtonian fluids (*Kumar et al*., 1972). *Keener et al*. (2006) found that a 5% LSM dry matter content resulted in approximately a one order of magnitude increase in the viscosity of the LSM, which would result in a one order of magnitude reduction in hydraulic conductivity (K) according to $K = k\rho g/\mu$; where k (L^2) is intrinsic permeability, ρ (M L^3) is fluid density, g (L T^2) is acceleration due to gravity, and μ (M L^{-1} T^{-1}) is fluid dynamic viscosity. While previous work has demonstrated the importance of considering viscosity influences when simulating variably-saturated flow of saltwater through one-dimensional columns (*Forkel and Celia*, 1992), and saturated flow through density stratified deep geological cross-sections (*Ophori*, 1998), little progress has been made on understanding the influence of viscosity on the flow of LSM through macroporous soil, even though it is quite clear that the movement of LSM through soil will be impeded in comparison to water. Because nutrients are often applied in the form of liquid manure, it is especially important to consider viscosity effects when predicting how nutrients and other manure constituents infiltrate and redistribute within the soil profile.

To provide some insight on ρ influences on LSM movement through macroporous soil, appendix J contains a cursory numerical investigation of density effects on flow and transport in saturated, macroporous soil columns.

5.3 Methods

5.3.1 Field Experiments

This numerical experimentation is based on field experiments that were designed to evaluate the effects of LSM application methods and loading rates on corn yield, nitrogen recovery, and tile effluent water quality (*Ball-Coelho et al*., 2005). These studies were conducted in late June – early July of 2000, 2001, and 2002, at a generally flat-lying agricultural field near Sebringville, in southwestern Ontario, Canada. Soil at the site is classified as Huron silt loam, for which selected properties are provided in Table 5.1. Tile drains at the site were installed in the early 1980's and are 10 cm in diameter, systematically spaced approximately 9 m apart, and positioned at a depth of about 70 cm.

During the experiments, LSM was applied to standing corn using either surface banding (SB) or subsurface injection (INJ) application methods. Following LSM application, NH_4-N (hereafter referred to as NH_4) and total phosphorus (P) were monitored in the tile effluent. Of the three years when field experiments were conducted, data from 2002 has the greatest temporal resolution for nutrient breakthrough at the tile drain; as a result, field data from 2002 is used as a basis for this work. In 2002, the LSM contained 2.5 % dry matter and was applied between corn rows at rates of: 0, 37.4, and 56.1 m^3 ha^{-1} with the SB method; and 0, 28.1, 37.4, 56.1, and 74.8 m^3 ha^{-1} with the INJ method. For INJ, the application depth was targeted at 10 to 15 cm below surface. Two replicates of each application method – loading rate combination were applied to individual plots that were 9.0 m wide (12 corn rows) by 206 m long, and centered over individual tiles. Not all tile drains were flowing at the time of the experiments in 2002; therefore, concentration data does not exist for all application method – loading rate scenarios. Because of considerable rainfall prior to the 2002 field experiments, there was an agronomically significant soil crust present.

5.3.2 Model Description

The numerical model utilized in this study was HydroGeoSphere (HGS) (*Therrien et al*., 2009). HGS is an integrated surface – subsurface flow and transport model that includes a three-dimensional extension of the original one-dimensional, dual-permeability model of *Gerke and van Genuchten* (1993a). For realistic simulation of flow and transport in dual-permeability media with directionally dependant hydraulic conductivity, HGS allows individual hydraulic conductivity values to be specified for the X, Y and Z directions for both continua, therefore making the model well suited for the conjunctive simulation of flow and transport within the predominantly vertical soil macropores and the relatively isotropic soil matrix. For the purpose of this study, where the infiltrating fluid is known to have a viscosity that is dependent on the concentration of a specific component (which in this case is the dry matter content of LSM), HGS has been modified to include continuously variable relative viscosity as a function of the concentration of a specific solute. The relative viscosity term is subsequently used as an adjustment factor for the relative permeability of each node in the domain. A conceptual overview of the modified model and the associated partial differential equations which govern flow and transport is given below. For further information on the HGS model, and the numerical solution of the dual-permeability flow and transport governing equations, the reader is referred to *Therrien et al*. (2009).

5.3.2.1 Flow

Dual-permeability porous media are considered to be a superposition of primary and secondary pore systems over the same volume. In the description that follows, the subscripts *m*, and *f*, are used to denote the respective primary (soil matrix), and secondary (macropore), pore systems. The dual-permeability, variably saturated flow solution is obtained by simultaneously solving two Richards equations for each grid node in the model domain that contains macropores in addition to the ubiquitous soil matrix. The pair of coupled equations is defined as follows:

$$\nabla \cdot \left[K_m \cdot k_{r,m} \cdot \mu_{r,m} \cdot \nabla \cdot \left(h_m + z\right)\right] + \frac{\Gamma_w}{(1 - w_f)} = \frac{\partial}{\partial t}\left(\theta_m\right) \tag{5.1}$$

$$\nabla \cdot \left[K_f \cdot k_{r,f} \cdot \mu_{r,f} \cdot \nabla \cdot \left(h_f + z\right)\right] - \frac{\Gamma_w}{w_f} = \frac{\partial}{\partial t}\left(\theta_f\right) \tag{5.2}$$

where ∇ is the gradient operator; *K* ($L\cdot T^{-1}$) is the saturated hydraulic conductivity tensor; *h* (L) is the pressure head; *z* (L) is the elevation head; w_f is the macroporosity volumetric fraction; θ_m and θ_f are the water contents in the matrix and macropores, respectively; and k_r (-) is relative permeability described with the *van Genuchten* (1980) unsaturated soil hydraulic property model as follows:

$$k_r = S_e^{0.5}\left[1 - \left(1 - S_e^{\frac{1}{m}}\right)^m\right]^2 \tag{5.3}$$

where $S_e = (\theta - \theta_r)/(\theta_s - \theta_r)$, $m = 1 - 1/n$, and $\theta = \theta_r + (\theta_s - \theta_r)\left(1 + |\alpha_{vg} h|^n\right)^{-m}$. S_e (-) is effective saturation, θ (L^3 L^{-3}) is water content, θ_r (L^3 L^{-3}) is residual water content, θ_s (L^3 L^{-3}) is saturated water content, α_{vg} (L^{-1}) and n (-) are soil specific empirical fitting coefficients. The saturation – pressure head relationship is considered to be non-hysteretic.

A simultaneous solution to the set of flow equations is obtained by coupling the two equations via Γ_w (T^{-1}) which is a water transfer term (*Gerke and van Genuchten*, 1993b) and is defined as $\Gamma_w = \alpha_w^* K_a (h_f - h_m)$ where α_w^* (L^{-2}) is a first-order mass transfer coefficient for water and K_a ($L \cdot T^{-1}$) is the effective hydraulic conductivity of the matrix – macropore interface, which is defined as $K_a = 0.5[K_a(h_f) + K_a(h_m)]$ where $K_a(h)$ is also described with the *van Genuchten* (1980) model. Although α_w^* has previously been defined as $\alpha_w^* = \lambda_w \beta / a^2$ (*Gerke and van Genuchten*, 1993a) where β is a geometry factor, a is the distance from the center of a fictitious soil matrix block to the fracture edge and λ_w is an empirical coefficient; the difficulty in quantifying these parameters led to the decision that it would be prudent in this work to consider α_w^* as an empirical fitting coefficient that can be adjusted during the model calibration process.

Viscosity dependence is incorporated into the flow governing equations through the $\mu_{r,m}$ (-) and $\mu_{r,f}$ (-) terms, which represent the respective matrix and macropore viscosity adjustment factors. The method employed here to incorporate variable fluid viscosity is generally applicable for any solute that has a predictable concentration – viscosity relationship. In our case, where LSM is the fluid of interest, the viscosity adjustment terms are based on the moisture content – viscosity relationships presented in *Keener et al*. (2006) which are approximated as follows:

$$\mu_{r,m} = \frac{1}{\exp\left(0.437 \cdot C_{DM,m}\right)} \tag{5.4}$$

$$\mu_{r,f} = \frac{1}{\exp\left(0.437 \cdot C_{DM,f}\right)} \tag{5.5}$$

where C_{DM} is the concentration of manure dry matter content (DM) obtained from the transport solution described below.

For the scenario considered here, fluid exchange between the surface and soil matrix flow domains is controlled with a first-order relationship that assumes the existence of a thin boundary layer to allow calculation of a vertical gradient. The exchange equation can be given as:

$$\Gamma = -k_r \mu_{r,m} K_{m,z} \frac{\left(h - h_o\right)}{l_{exch}} \tag{5.6}$$

where Γ ($L \cdot T^{-1}$) is exchange flux, k_r (-) is relative permeability, $\mu_{r,m}$ (-) is soil matrix viscosity adjustment factor, $K_{m,z}$ ($L \cdot T^{-1}$) is soil matrix vertical saturated hydraulic conductivity, h and h_o (L) are the soil matrix pressure head and water depth in the surface domain respectively, and l_{exch} (L) is the thickness of the boundary layer, which is set to 0.1 cm.

5.3.2.2 Transport

The dual-permeability transport solution utilized by HGS solves a pair of advection-dispersion equations that are coupled by an exchange term that accounts for solute mass flux between the primary and secondary porosity continua. Advective and dispersive transport controls the mass flux between the surface and sub-surface domains. The governing equations for subsurface transport are based on the description given by *Gerke and van Genuchten* (1993a), and are given as follows:

$$\Delta\left(\theta_m D_m \Delta C_m - q_m C_m\right) - \theta_m \lambda_m C_m + \frac{\Gamma_s}{\left(1 - w_f\right)} = \frac{\partial}{\partial t}\left(\theta_m C_m R_m\right) \tag{5.7}$$

$$\Delta\left(\theta_f D_f \Delta C_f - q_f C_f\right) - \theta_f \lambda_f C_f - \frac{\Gamma_s}{w_f} = \frac{\partial}{\partial t}\left(\theta_f C_f R_f\right) \tag{5.8}$$

where C ($M \cdot L^{-3}$) is solute concentration, λ (T^{-1}) is a first order decay coefficient, q ($L \cdot T^{-1}$) is the Darcy flux, R (-) is a retardation factors which is defined as:

$$R = 1 + \frac{\rho_b K_d}{\theta} \tag{5.9}$$

where ρ_b ($M \cdot L^{-3}$) is bulk density and K_d ($L^3 \cdot M^{-1}$) is a linear distribution coefficient. D ($L^2 \cdot T^{-1}$) is the hydrodynamic dispersion coefficient and is defined by *Bear* (1972) as:

$$\theta D = \left(\alpha_l - \alpha_t\right)\frac{q \cdot q}{|q|} + \alpha_t |q| \mathrm{I} + \theta \tau D_{free} \mathrm{I} \tag{5.10}$$

where α_l (L) and α_t (L) are the longitudinal and transverse dispersivities, I is the identity matrix, D_{free} ($L^2 \cdot T^{-1}$) is the free-solution diffusion coefficient, and $\tau(-)$ is the tortuosity which is defined by *Millington and Quirk* (1961) as:

$$\tau = \frac{\theta^{\frac{7}{3}}}{\theta_s^{\ 2}} \tag{5.11}$$

In equations 5.7 and 5.8, Γ_s ($M \cdot L^{-3} \cdot T^{-1}$) is a solute mass transfer term defined by *Gerke and van Genuchten* (1993a) as:

$$\Gamma_s = (1-d)\Gamma_w \Omega_f C_f + d\Gamma_w \Omega_m C_m + \alpha_s (1-w_f)\theta_m (C_f - C_m) \tag{5.12}$$

where *d* (-) determines the transfer direction according to:

$$d = 0.5\left(1 - \frac{\Gamma_w}{|\Gamma_w|}\right), \quad \text{subject to } \Gamma_w \neq 0 \tag{5.13}$$

and Ω_m (-) and Ω_f (-) are solute concentration relation terms defined as:

$$\Omega_m = (1-w_f)\frac{\theta_m}{\theta_{bulk}} \quad \text{and} \quad \Omega_f = w_f \frac{\theta_f}{\theta_{bulk}} \tag{5.14}$$

where θ_{bulk} is the water content of the bulk soil. In the solute mass transfer equation α_s (T^{-1}) is a solute mass transfer coefficient defined as $\alpha_s = D_{free}\beta/a^2$. Similar to the approach taken with α_w^*, α_s is treated as an empirical fitting coefficient that is adjusted during the model calibration process.

In this work, NH_4 and P are subject to first order decay and linear sorption, respectively; while DM is considered to be a conservative species in the transport solution.

5.3.2.3 Soil Matrix - Macropores - Bulk Soil Relationships

A set of relationships has been defined by *Gerke and van Genuchten* (1993a), and *Gerke et al*. (2007), which relate composite properties of the bulk soil with those of the soil matrix and macropore continua in dual-permeability models of the form used in this work. Constitutive equations for bulk porosity (ϕ_{bulk}); water content (θ_{bulk}); saturated hydraulic conductivity (K_{bulk}); Darcy flux (q_{bulk}); and solute concentration (C_{bulk}) are defined as follows:

$$\phi_{bulk} = w_f \phi_f + (1 - w_f)\phi_m \tag{5.15}$$

$$\theta_{bulk} = w_f \theta_f + (1 - w_f)\theta_m \tag{5.16}$$

$$K_{bulk} = w_f K_f + (1 - w_f)K_m \tag{5.17}$$

$$q_{bulk} = w_f q_f + (1 - w_f)q_m \tag{5.18}$$

$$C_{bulk} = \left\lfloor w_f \theta_f C_f + (1 - w_f)\theta_m C_m \right\rfloor / \theta_{bulk} \tag{5.19}$$

5.3.3 Domain Configuration – Boundary Conditions – Initial Conditions

The simulation domains (Figure 5.1) represent two-dimensional, unit thickness, cross sections of the INJ and SB LSM application field test plots. The 150 cm high soil profiles have been subdivided into five distinct layers (Figure 5.1a) that consist of: (1) a non-macroporous soil crust layer, (2) a macroporous A horizon, (3) a macroporous plowpan layer, (4) a macroporous B horizon, and (5) a non-macroporous B horizon. Both the INJ (Figure 5.1b) and SB (Figure 5.1c) domains represent one half of the symmetrical, 900 cm wide, field test plots. Both sides and the bottom of the domains are considered no-flow boundaries. A constant head boundary condition with the head fixed at atmospheric pressure was assigned to the exterior nodes located at a depth of 70 cm on the right side of the domain to represent the tile drains.

Steady-state initial conditions were developed by applying a constant water flux of 0.007 cm d^{-1} to the top surfaces, resulting in a steady-state water table that gently slopes towards the tile drain with about 2 cm of vertical relief across the width of the domain, and a constant tile discharge rate of 3.15 cm^3 d^{-1}. When the simulation-domain / field-experiment surface area ratio is taken into account, the simulated steady-state tile discharge is within the same order of magnitude as the discharge rates measured in the tiles that were flowing at the time of the field experiments.

LSM is applied to the simulation domain via surface-water zones that allow for advective flux of LSM into the soil matrix to vary as a function of both surface-water depth, and soil matrix pressure head. The surface-water zones are not directly coupled to the macropore zones in either of the application method scenarios. In SB, the soil crust was assumed to seal the macropores at the surface (*Ela et al*., 1992). In INJ, tillage action is assumed to minimize the direct connection between macropores and the LSM (*Turpin et al*., 2007b). Both the INJ and SB domains contain 6 individual surface-water zones, spaced 75 cm apart, that are specifically configured to reflect the physical reality of the two application methods. For INJ (Figure 5.1b), the surface-water zones are each 10 cm wide and recessed 10 cm into the top surface of the domain; whereas for SB (Figure 5.1c), they are each 50 cm wide and located on the top surface of the domain. Initial depth of LSM in the surface-water zones is proportional to the manure application rate. For INJ application rates of 28.1, 37.4, 56.1, and 74.8 m^3 ha^{-1}, the initial LSM depth was 2.1, 2.8, 4.3, and 5.7 cm, respectively; and for SB application rates of 56.1 and 74.8 m^3 ha^{-1}, the initial LSM depth was 0.9 and 1.1 cm, respectively. To reflect the maximum possible distance between a LSM applicator and a tile drain during the field experiments, the horizontal distance between the tile drains and the vertical centerlines of the surface-water zones located nearest to the tile drains is 37.5 cm.

The control volume finite difference method was used to solve the flow and transport governing equations. Vertical grid spacing was 1 cm above the tile drain elevation and graded from 1 to 15 cm, from tile drain elevation to the base of the domain. Horizontal grid spacing varied from 2.5 cm along the right side of the domain, to 5 cm throughout the middle of the domain, to 7.5 cm along the left side of the domain. The INJ and SB grids consisted of 13712 and 13832 nodes respectively, of which 6401 and 6496 were macropore nodes located within the 1 to 70 cm depth interval.

5.3.4 Hydraulic Property Derivation

Soil hydraulic properties required for the parameterization of the dual-permeability numerical model were primarily derived using a combination of: (1) field measured bulk hydraulic conductivity measured with a single ring pressure infiltrometer (*Ball-Coelho et al*., 2007), (2) soil physical properties in conjunction with the Rosetta pedotransfer-function based hydraulic property estimation program (*Schaap et al*., 2001), (3) macropore-area-fraction estimates reported for Plot 2 at the Kintore macroporosity characterization experiments (see chapter 2) where the soil has similar composition to Sebringville, (4) the constitutive relationship described in equation 5.17, and (5) model calibration.

5.3.4.1 Soil Matrix

Soil composition and bulk density data given for the 0-20 and 20-40 cm depth intervals in Table 5.1 were used in conjunction with Rosetta (*Schaap et al*. 2001) to derive the A and B layer soil matrix hydraulic properties. For the soil crust and plowpan layers, the hydraulic conductivities (K_s) were determined during model calibration, while the residual and saturated soil moisture contents, and the α_{vg} and n_{vg} empirical coefficients of the *van Genuchten* (1980) soil water retention function, were set equivalent to those of the the A layer.

5.3.4.2 Macropores

The macroporosity weighting factor coefficient (w_f) was held constant at 0.006 for the A and B layers of the SB scenario, and the B layer of the INJ scenario. Because tillage associated with subsurface manure injection creates additional macroporosity (*Turpin et al*., 2007a), w_f for the A layer of the INJ scenario was determined during model calibration.

The vertical, saturated hydraulic conductivity ($K_{s,z}$) for macropores in the A and B layers of both the INJ and SB scenarios was individually calculated using equation 5.17 in combination with the following: (1) bulk field saturated hydraulic conductivity (K_{fs}) values given in Table 5.1, where values from the 0-20 cm and 20-40 cm depth intervals are used to represent the A and B layers respectively; (2) estimated soil matrix saturated hydraulic conductivities (K_s); and (3) w_f . For the A layer of the INJ scenario, a new value of $K_{s,z}$ was calculated for each value of w_f that was tested in the model calibration process.

The vertical/horizontal macropore saturated hydraulic conductivity ratios ($K_{s,z}$ / $K_{s,x}$) were determined during model calibration. While it was assumed that $K_{s,z}$ / $K_{s,x}$ for the macropores in the B layer of both LSM application scenarios would be equal, application scenario specific $K_{s,z}$ / $K_{s,x}$ ratios were determined for the A layers.

Based on the assumption that the majority of the macropore zone is open pore space, saturated water contents (θ_s) were set to 0.9 for all of the macropore flow zones. Residual water contents (θ_r) were all set to 0.05, which in combination with the respective values for the α_{vg} and n_{vg} coefficients of 0.1 cm^{-1} and 2.0, lead to relatively dry macropores in the simulated soil profile when it is in a freely drained state.

The water (α^*_w) and solute (α_s) exchange parameters for the A and B layers were determined individually for both the INJ and SB scenarios during model calibration. The saturated hydraulic conductivity of the matrix-macropore interface (K_a) was set to 0.08 times that of the soil matrix in the corresponding layer. The 0.08 factor is based on work conducted by *Gerke and Köhne* (2002) that found K_a was reduced in comparison to the hydraulic conductivity of the soil matrix by a factor of approximately 12 at a soil water pressure head of -28.17 cm, which is very close to the average soil water pressure head observed in the 0 to 70 cm depth interval of the model domains here, in the initial condition prior to LSM application.

5.3.5 Transport Parameters

The value for α_l was set to 0.07 cm and was taken from data presented by Neuman (1990) for tracer tests conducted on a size scale similar to this work. The α_t value was set to 0.007 cm and is based on the work by Sudicky (1986) that showed dispersion in the direction perpendicular to flow is generally small when compared to dispersion parallel to flow.

5.3.6 Model Calibration

Models for the two application scenarios were primarily calibrated to NH_4, and P field data using results from the 74 m^3 ha^{-1} LSM injection, and 56 $m^3 ha^{-1}$ LSM surface banding experiments. Tile discharge was of limited focus during model calibration because of sparse field data. The calibration process involved successive iterations of manual parameter updating followed by model execution and results analysis. The objective of the calibration process was to enable the models for both the INJ and SB scenarios to predict the shape of the NH_4 and P breakthrough curves (BTC) at the tile drain outlet with respect to: arrival time, peak concentration, and late time (24-48 hrs after application) concentration. At the point when the field observed BTC shapes were simulated reasonably well for both the INJ and SB scenarios it was concluded that the models were realistically emulating the physical processes controlling the LSM infiltration. By concurrently calibrating two models with different LSM application surface configurations that both share similar soil hydraulic properties, it is hoped that uncertainty surrounding parameter equifinality can be reduced.

5.4 Results and discussion

5.4.1 Parameter estimation / model calibration

Although the calibrated INJ model does a somewhat better job than the calibrated SB model (Figure 5.2), both models are generally able to reproduce the observed NH_4 and P concentrations to within an order of magnitude, and the peak concentration arrival times to within approximately 1 hour.

Inclusion of a first order decay coefficient of 0.4 d^{-1} for NH_4 transport, and an equilibrium distribution coefficient of 0.3 $cm^3\ kg^{-1}$ for P transport, greatly improved the late time match between field data and model estimates of nutrient concentrations at the tile drain.

5.4.1.1 Soil Matrix

The final set of calibrated hydraulic parameters for the soil matrix zones are presented in Table 5.2. Using Rosetta, K_s is estimated to be 13.4 and 4.4 cm d^{-1} for the respective A and B soil layers. During model calibration, K_s of the soil crust was reduced by a factor of 8 relative to K_s of the underlying A layer soil matrix. K_s of the 10 cm thick plowpan layer, with its base located at a depth of 30 cm, was reduced by a factor of 335 and 110, relative to the soil matrix K_s of the A and B layers, respectively.

5.4.1.2 Macropores

The final set of calibrated hydraulic parameters for the macropore zones are presented in Table 5.3. Using the method described in section 5.3.4.2, $K_{s,z}$ values range from 13600 to 69700 cm d^{-1}. While it may seem that these $K_{s,z}$ values are quite large, it is important to note that the resulting flow velocities are generally within an order of magnitude of those reported in past field studies; such as *Cey and Rudolph* (2009) who report that flow velocity in partially saturated vertical macropores was approximately 4000 cm d^{-1}; and *Nimmo* (2007) who calculated that the field experiments of *Kung et al*. (2000) that were conducted under relatively wet conditions on a tile drained loam soil, yielded preferential flow velocities of 10000 cm d^{-1}.

While acceptable model calibration for the SB scenario was achieved by using mean w_f values obtained from similar soils 25 km away, calibration of the INJ scenario model was improved by accounting for local tillage effects on soil structure, which resulted in the A layer w_f being increased by a factor of 4 relative to that of the SB scenario. The B layer w_f in the INJ scenario did not require compensation, which highlights the obvious fact that tillage influences on soil structure are strongest in the A layer.

During model calibration, $K_{s,x}$ of the B layer macropores in both application scenarios were reduced by a factor of 50 relative to $K_{s,z}$. For the macropores in the A layer of the SB scenario, $K_{s,x}$ was reduced by a factor of 10 relative to $K_{s,z}$; while $K_{s,x}$ was equal to $K_{s,z}$ in the A layer of the INJ scenario. Consideration of macropore anisotropy was imperative for acceptable simulation of the NH_4 and P peak concentrations, and the peak concentration arrival time at the tile drain. The $K_{s,x}$/ $K_{s,z}$ ratios obtained here correspond well with field observations that have shown wormholes become increasingly vertical with increased depth (*Mckenzie and Dexter*, 1993), and that fractures and root holes (which could both readily facilitate lateral flow) tend to be greater near surface (*Cey and Rudolph*, 2009). Different anisotropy ratios for the two LSM application methods highlight the fact that tillage can disrupt existing macropores while at the same time also create new fractures in the A layer (*Turpin et al*., 2007a).

5.4.1.3 Water and solute exchange coefficients

Individual $\alpha*_w$ and α_s parameter values were determined for the A and B layers of both the INJ and SB scenarios. Optimal values of $\alpha*_w$ in the A layers were 8 cm^{-2} and 5 cm^{-2}, for the INJ and SB scenarios respectively; while in the B layer, a value of 0.005 cm^{-2} for $\alpha*_w$ worked well for both scenarios. The α_s parameter was finalized at values of 8 d^{-1} and 0.01 d^{-1}, in the A layers of the respective INJ and SB scenarios, while in the B layers, values of 1 d^{-1} and 0.1 d^{-1}, led to optimal model calibration.

Although α^*_w and α_s have both been treated as empirical fitting coefficients, some insight on water and solute exchange processes between the soil matrix and macropore zones in layered macroporous soils can be obtained by assessing the relative magnitudes of the final calibrated values (*Schwartz et al*., 2000) because larger values of α^*_w promote greater water exchange and related advective mass flux, and larger values of α_s promote greater diffusive mass flux, between the 2 continua. It can also be noted that α^*_w has a positive correlation with K_a, so the same simulation results could have been obtained by adjusting K_a; thus highlighting just one of the parameter equifinality issues currently surrounding dual-permeability model application.

The final value of α^*_w for the A layer is three orders of magnitude greater than the value obtained for the B layer for both the INJ and the SB scenarios. The difference in the α^*_w values between the A and B layers may reflect on the differences in the soil structure between the two layers as suggested by *Schwartz et al*. (2000). While the A layer consists of features that could be expected to undergo annual cycles of generation and destruction, such as: preexisting fractures, root holes, worm burrows, and tillage induced fractures; macropore features in the B layer primarily consist of root holes and worm burrows that could be expected to survive over a number of annual cycles, and develop dense, organic rich linings that inhibit exchange (*Gerke and Köhne*, 2002). Also, fractures are often more abundant in the A layer (*Cey and Rudolph*, 2009) and fractures could potentially provide more surface area for exchange to occur than cylindrical macropore features of equivalent volume.

The relatively low α^{*}_{w} value obtained for the B layers facilitates the development of non-equilibrium conditions between the macropores and the soil matrix that exist for up to a day after 74.8 m^3 ha^{-1} LSM application, and lead to steep lateral pressure-head gradients within the macropores in the vicinity of the tile (Figure 5.3). These gradients exist because macropores near the tile are in effect freely drained by the tile whereas away from the tile, macropore drainage occurs via lateral flow towards the tile (which is a controlled by macropore $K_{s,x}$), and through water movement into the soil matrix (which is restricted by relatively low matrix hydraulic conductivity and α^{*}_{w} values). It is the steep gradients in the macropores that allow the model to simulate the rapid movement of water and solutes, through a continuum with strong anisotropy, to the tile drain from a surface position that is horizontally displaced relative to the tile drain.

In comparison to the B layer, the relatively large values obtained for α^{*}_{w} in the A layer reduce both the magnitude and the duration of the pressure-head non-equilibrium conditions in the A layer. Because the conceptual model assumes that LSM first moves from the surface-water zone into the soil matrix, and then from the soil matrix into the macropores, easy inter-continuum exchange of water and solutes near the LSM application surface increases infiltration rates by reducing pressure head buildup in the soil matrix.

While there is not a clear layer dependant trend in the value of α_s for the two LSM application scenarios, the A layer α_s is two orders of magnitude larger for INJ as opposed to SB, which can be at least partially explained by the presence of new, tillage induced fracture surfaces that could promote more diffusive mass exchange between the macropores and the soil matrix than the surfaces of the preexisting macropore features in the SB scenario, which may have developed surface skins that restrict diffusive mass exchange (*Köhne et al*., 2002).

5.4.2 Evaluation of model performance

The performance of the models was evaluated by using the parameters derived during the calibration process in simulations using different LSM application rates and comparing the results with associated field data. For the INJ scenario, evaluation simulations were conducted using 28, 37, and 56 m^3 ha^{-1} LSM application rates, for which the results are shown in Figure 5.4. From the evaluation results it is apparent that the ability of the model to predict results from the INJ field experiments decreases as application rate decreases. While the INJ model predicted NH_4 and P concentrations in the tile effluent with a reasonable degree of accuracy for the 56 m^3 ha^{-1} application rates, and to a slightly lesser degree for the 37 m^3 ha^{-1} LSM application rates, it did a poor job of simulating results from the 28 m^3 ha^{-1} experiments.

The SB scenario model was evaluated using results from the 37 m^3 ha^{-1} SB field experiments where neither the model, nor the field data, showed a detectable increase in tile effluent NH_4 and P concentrations in response to LSM application.

5.4.3 Hydraulic conditions, and nutrient movement to the tile drain

Simulation results from the calibrated models (Figure 5.2) show that tile effluent NH_4 concentrations are predicted to peak approximately 0.048d, and 0.208d after LSM application for the 74.8 m^3 ha^{-1} INJ, and 56.1 m^3 ha^{-1} SB scenarios, respectively. When tile concentrations peak, the single LSM application surfaces located closest to the tile drain are the sole source of the tile effluent NH_4 for both the INJ (Figure 5.3a) and SB (Figure 5.3b) scenarios, and NH_4 remains centered beneath the other five application surfaces. From a hydraulic perspective, when the tile effluent NH_4 concentrations peak, the water table in the macropore zone is near its maximum, at which time water levels at a position 75 cm from the tile drain have risen by approximately 38 cm in the INJ scenario (Figure 5.3a), and 17 cm in the SB scenario (Figure 5.3b), relative to the initial position, and are considerably higher than the water table in the soil matrix zone. The relatively large water table rise in the macropores induces steep lateral pressure head gradients in the vicinity of the tile drains. When tile effluent NH_4 concentrations peak, the lateral gradient in the macropore zone across the 75 cm interval nearest the tile is 0.52 and 0.23, in the respective INJ and SB scenarios; and the concurrent lateral gradients in the soil matrix are 0.087 and 0.135. For both scenarios, lateral gradients in the soil matrix do not peak until approximately 0.8 d after LSM application, and reach maximum values of 0.166 and 0.143, in the INJ and SB scenarios respectively, across the 75 cm interval nearest the tile. Pressure heads in the macropore and soil matrix have nearly equilibrated when the soil matrix hydraulic gradients peak.

Away from the tile drain the lateral hydraulic head gradients in both the soil matrix and macropore zones remain relatively low throughout the simulation interval. At their peak 0.8 d after LSM application, the lateral gradients in the soil matrix across the 75 cm horizontal interval located furthest from the tile drain (Figure 5.3) are 0.004 in the INJ scenario, and 0.002 in the SB scenario.

5.4.4 Viscosity sensitivity

Sensitivity tests for both the INJ and SB scenarios, using an LSM application rate of 74 m^3 ha^{-1}, were conducted in order to determine the importance of considering the DM – viscosity relationship when predicting LSM movement in the soil profile. LSM dry matter contents of 0, 1.25, 2.5 and 5%, were considered in the evaluation, which according to equations 5.4 and 5.5, would lead to relative permeability multiplication factors of 1, 0.6, 0.3, and 0.1, respectively. The same LSM dry matter content values were also used to assess viscosity influences on both residual NH_4 distribution within the soil matrix and LSM infiltration from the soil surface, for both application scenarios. Model parameters established during the calibration process were used in all cases.

Predicted tile effluent NH_4 concentrations relative to LSM dry matter content are shown in Figure 5.5. When the viscosity effects associated with a LSM dry matter content of 1.25% are compared to the scenario where viscosity is not considered, peak concentrations decrease by 40 and 60%, and arrival times decrease by 7 and 22 min, for INJ (Figure 5.5a) and SB (Figure 5.5d), respectively. As would be expected, viscosity influences increase as DM content increases. When 5% DM is considered in the INJ scenario (Figure 5.5c), viscosity effects are responsible for a 30 minute delay in the arrival of NH_4 at the tile drain, and a reduction in peak concentration by a factor of 30. For the SB scenario, 5% DM content (Figure 5.5f) induces a 220 minute delay in the arrival of NH_4 at the tile drain, and a three order of magnitude reduction in peak concentration.

Simulated residual soil matrix NH_4 distributions beneath single LSM application surfaces adjacent to the tile drain, 48 hours after LSM application, are shown in Figure 5.6. With LSM dry matter content of 1.25%, there is very little difference in residual NH_4 distribution between simulations that do, and do not, consider viscosity effects for both the INJ (Figure 5.6a-b) and the SB (Figure 5.6e-f) scenarios. As DM content increases, NH_4 is progressively retained higher in the soil profile in both scenarios; however, the results suggest that increasing viscosity does have a stronger influence on SB than INJ. With a DM content of 5%, very little NH_4 is predicted to move below the base of the A layer in the SB scenario (Figure 5.6h), whereas for the INJ scenario (Figure 5.6d), NH_4 does move into the B layer, albeit with lower spatial distribution than in the simulations where DM content was lower.

Simulated infiltration rates for LSM to move into the soil profile, from a single application surface, are shown in Figure 5.7. Increased DM content reduces the infiltration rate and extends the associated infiltration time for both the INJ (Figure 5.7a) and SB (Figure 5.7b) scenarios. In the INJ scenario, the maximum infiltration rate of LSM with 5% DM is reduced by approximately 50%, and the time required for infiltration is approximately 3 times longer, than for the simulation where viscosity influence is not considered. In the SB scenario, the time required for infiltration of LSM with 5% DM is again extended by a factor of approximately 3 relative to the simulation where the influence of viscosity is not considered. However, the influence of viscosity on maximum infiltration rate is slightly less than in the INJ scenario, and viscosity effects associated with 5% DM content reduce the maximum infiltration rate by approximately 30% relative to the case where viscosity effects are not considered.

As shown in Figure 5.8, slower infiltration rates associated with 5% LSM dry matter content lead to reduced pressure heads in the soil matrix below the LSM application surface, and to delayed rise in pressure-heads for both application scenarios; however, the relative reduction in pressure-heads is greater for the SB scenario because of the additional dampening effect of the soil crust layer. Lower soil matrix pressure-head leads to a reduction in the magnitude of pressure-head non-equilibrium between the matrix and macropores, which in turn reduces LSM movement into the macropores (Figure 5.9). Because macropore flow is the mechanism for rapid vertical movement of LSM to the tile drain, a reduction in LSM movement into the A layer macropores also leads to delayed arrival of LSM at the tile drain and lower concentrations of LSM constituents in the tile effluent.

5.4.5 Plowpan and soil crust sensitivity

To determine the influence of the plowpan layer on the movement of LSM in the soil profile, results from simulations that included a plowpan were compared to results from simulations that did not include a plowpan for both application scenarios. Similarly, to determine the influence of the soil crust layer on LSM movement, results from a SB simulation that included the soil crust layer were compared to results from a simulation that did not include the soil crust. LSM movement in the INJ scenario is not influenced by the presence of a soil crust layer. Soil hydraulic properties established in the model calibration process were used for both the plowpan and the soil crust sensitivity tests; however, properties of the A layer soil matrix were extended to a depth of 30 cm for the simulations that did not include the plowpan; and in the simulation that did not include the soil crust, properties of both the A layer macropore and soil matrix continua were extended to the surface. An LSM application rate of 74 m^3 ha^{-1} was used in all of the plowpan and soil crust sensitivity simulations. In the results, the magnitude of non-equilibrium (NE) between the macropore and soil matrix zones for pressure-head (h_f - h_m), and NH_4 concentration (C_f - C_m), are reported for commonly located grid nodes that are horizontally centered beneath the leftmost LSM application surfaces (Figure 5.3), and located at depths of 15 and 40 cm, to represent hydraulic conditions in the A and B layers respectively.

5.4.5.1 Plowpan

Removing the plowpan in the INJ simulation caused a 47% reduction in peak tile discharge (Figure 5.10a), a 73% reduction in peak NH_4 concentration in the tile effluent (Figure 5.10b), and also delayed both the hydraulic response, and NH_4 arrival at the tile drain by approximately 15min. The effect of removing the plowpan is greater for the SB scenario. Results from the SB simulation with the plowpan removed show: peak tile discharge is reduced by 57% (Figure 5.10c), peak NH_4 concentration is reduced by over three orders of magnitude (Figure 5.10d), the hydraulic response of the tile drain is delayed by approximately 40 min, and NH_4 arrival at the tile drain is delayed by 120 min.

Removing the plowpan layer also changes characteristics of both the pressure head, and NH_4 concentration NE conditions, with more pronounced effects observed for SB as compared to INJ. When the plowpan is removed from the INJ simulation there is minimal change in the both the NH_4 concentration (Figure 5.11a), and the pressure-head (Figure 5.11b) NE conditions in the A layer; whereas in the B layer, the development of NH_4 concentration NE conditions is delayed by 15 min and the magnitude of the peak pressure-head NE condition is reduced by 42%. In the A layer of the SB scenario, removing the plowpan causes a 10% reduction in peak NH_4 concentration NE (Figure 5.11c), and delays the development of NH_4 concentration NE conditions by 37 min; whereas pressure-head equilibrium is not noticeably affected by the removal of the plowpan (Figure 5.11d). In the B layer of the SB scenario, NH_4 concentration NE conditions are effectively eliminated when the plowpan layer is removed and peak pressure-head NE conditions are reduced by 95%.

The residual NH_4 distribution is also affected because of changes in the hydraulic behavior of the macroporous soil profile caused by removal of the plowpan. For the INJ scenario, removal of the plowpan causes a slight reduction in the width of the NH_4 distribution profile (Figure 5.12a-b) and leads to more retention of NH_4 in the A layer. The plowpan has a much more pronounced effect on residual NH_4 distribution in the SB scenario, where practically all of the NH_4 gets retained in the A layer when the plowpan is removed (Figure 5.12c-d).

By restricting downward flow in the soil matrix, the plowpan leads to both increased pressure-head conditions in the A layer soil matrix during infiltration that promotes increased shallow lateral distribution of LSM, and increased LSM movement into the A layer macropores. Because the models consider macropores to be vertically continuous features, increased macropore flow in the A layer also leads to increased macropore flow in the B layer; as a result, inclusion of a plowpan also increases both the B layer pressure-head NE conditions, and vertical LSM distribution.

5.4.5.2 Soil Crust

Removing the soil crust layer from the SB scenario approximately doubles the peak tile discharge rate (Figure 5.13a), increases the peak NH_4 concentration by a factor of 28 (Figure 5.13b), decreases the time required for the tile to exhibit a hydraulic response to LSM application by approximately 40 min, and decreases the time required for NH_4 to reach the tile drain by approximately 107 min.

Removing the soil crust layer from the SB simulations also changes the NH_4 concentration, and pressure-head NE conditions between the macropore and soil matrix zones. When the soil crust is removed, peak NH_4 concentration NE (Figure 5.14a) increases by factors of 4.2 and 10.4 for the A and B layers respectively; and the associated NE conditions are established 65min earlier in the A layer, and 120min earlier in the B layer. Little change is observed in the A layer pressure-head NE conditions (Figure 5.14b) when the soil crust is removed since pressure-head equilibrium conditions exist for both cases (with and without soil crust) throughout the simulation time at a depth of 15 cm below the LSM application surface. However, at a depth of 40 cm, in the B layer, pressure-head NE increases by 50%, and pressure-head NE conditions are established approximately 80min earlier, when the soil crust is removed.

Residual NH_4 distribution in the soil profile also changes in response to removal of the soil crust layer from the SB simulation. Removal of the crust (Figure 5.12e) promotes both deeper movement of NH_4 into the soil profile, and B layer NH_4 concentrations that are an order of magnitude greater than when the crust is included (Figure 5.12c). By slowing down the infiltration rate of LSM from the surface, the presence of a soil crust reduces the pressure head in the A layer soil matrix which in turn reduces LSM movement into the macropores and increases LSM retention near surface. When the soil crust is absent from the SB scenario, the pressure-head from the LSM application surface is transmitted directly to the A layer soil matrix which leads to increased movement of LSM into the macropores and results in greater vertical LSM distribution.

5.5 Conclusions

Reasonably easy to collect soil physical property data and field-saturated hydraulic conductivity estimates from a macroporous silt loam soil were conjunctively used to parameterize a pair of 2D dual-permeability models that were successfully able to simulate LSM movement to tile drains in a variably saturated soil profile over a 48 hour time frame after SB, and INJ, application methods. To reflect the complexity of the both the soil structure and soil layer distribution at the field site, the models included distinct horizontally continuous layers to represent the soil crust, plowpan, and A and B horizons, and also accounted for macropore orientation by incorporating anisotropy into the hydraulic conductivity description for the macropore continuum. Soil crust and plowpan hydraulic conductivity, macropore anisotropy ratios, and LSM application method specific values for the water and mass exchange coefficients in the A and B layers were established during the model calibration process. For the INJ scenario model to accurately simulate field observed nutrient breakthrough to the tile drain, tillage effects needed to be accounted for by increasing the value of the A layer w_f coefficient by a factor of 4 relative to the value used in the SB scenario. To account for the viscosity related influences on relative permeability associated with liquid manure dry matter content, variable viscosity as a function of solute concentration was added into the dual-permeability numerical solution.

The complexity of the two models used for this work elucidates the influences of variable soil structure and soil layer properties, LSM viscosity, and LSM application methods on flow and transport processes in shallow water table, tile drained agricultural soils. Model results suggest that the macropore anisotropy ratio is considerably different between the A and B layers, and reflects the structural differences between predominantly vertical worm burrows and root holes in the B layer, and the more isotropic macropore features in the A layer. Tillage associated with LSM injection also influences macropore geometry by further reducing the anisotropy ratio in the A layer. The parameters that control exchange between the soil matrix and the macropores vary according to soil layers and LSM application methods. The exchange coefficients in the B layer are relatively low compared to those for the A layer which suggests that the regenerative processes that affect A layer macroporosity enhances water and solutes movement between the soil matrix and the macropores as compared to the B layer. For the INJ scenario, tillage effects on soil structure also appear to promote easier exchange of water and solutes between the soil matrix and the macropores. Relatively low water and solute exchange parameter values in the B layer support the development of large pressure-head non-equilibrium conditions between the soil matrix and the macropores, and lead to large horizontal hydraulic gradients in the vicinity of the tile within the macropore network as compared to the gradients in the soil matrix. The large hydraulic gradients near the tile facilitate lateral movement of water and solutes within the macropore continuum, and define the soil surface area which contributes preferential flow to the tile drain. Away from the tile drain, horizontal hydraulic gradients are much lower and macropore flow is primarily vertical.

In order to accurately estimate nutrient breakthrough to the tile drain, models for both LSM application methods required the inclusion of a macroporous plowpan layer with low matrix permeability at the base of the A layer. In addition to a plowpan layer, the SB scenario model also required a reduced permeability soil crust layer at the surface of the soil profile. In response to LSM application, the plowpan layer reduces the capability for vertical flow in the soil matrix which leads to increased pressure-heads in the A layer soil matrix. The increased soil matrix pressure-heads promote the exchange of LSM from the A layer soil matrix into the macropore network, which ultimately leads to rapid vertical movement of LSM and earlier arrival of nutrients at the tile drain, as compared to scenarios that do not include a plowpan layer. Inclusion of a soil crust layer reduces the infiltration rate of LSM into the A layer which reduces pressure-heads in the A layer soil matrix and leads to less LSM movement from the A layer soil matrix into the macropores, and leads to less vertical LSM movement and lower nutrient concentrations at the tile drain.

Due to the relationship between LSM dry matter content and viscosity, the relative permeability of LSM flow systems decreases as dry matter content increases, and as a result, increasing the dry matter content of the LSM has a large influence on nutrient distribution within the soil profile and breakthrough at the tile drain. Because LSM is most concentrated near the application surfaces, the soil matrix near the application surfaces has the greatest reduction in relative permeability and LSM infiltration rates decline considerably as LSM dry matter contents increase. Decreased infiltration rates lead to lower pressure-heads in the A layer soil matrix which leads to less LSM movement from the A layer soil matrix into the macropores. As a result, increasing the dry matter content of LSM causes appreciable reductions in nutrient concentrations in the tile drain effluent and leads to greater LSM retention in the A layer soil matrix near the LSM application surface.

Results from this work emphasize that increasing the liquid manure viscosity and/or reducing the ponding depth during the application of liquid manure, will reduce nutrient movement to tile drains over the 2 day time period following manure application. In addition, if manure application within approximately 0.75 m (horizontal distance) of a tile drain can be avoided, the risk of rapid nutrient movement to surface water via tile drains will be greatly reduced. Awareness of soil features such as crusts and plowpans is also important since these characteristics have strong influence on the subsurface movement of liquid manure and associated nutrients. In cases where uniform soil crusts exist, liquid manure can potentially be surface banded at higher rates than cases where crusts are absent, with no significant increase in nutrient movement to tile drains. In cases where shallow subsurface soil horizons with reduced soil matrix permeability are absent, liquid manure may also be surface banded, or injected, at higher rates than where these layers are present, with no significant increase in short term nutrient movement to tile drains.

5.6 Figures and Tables

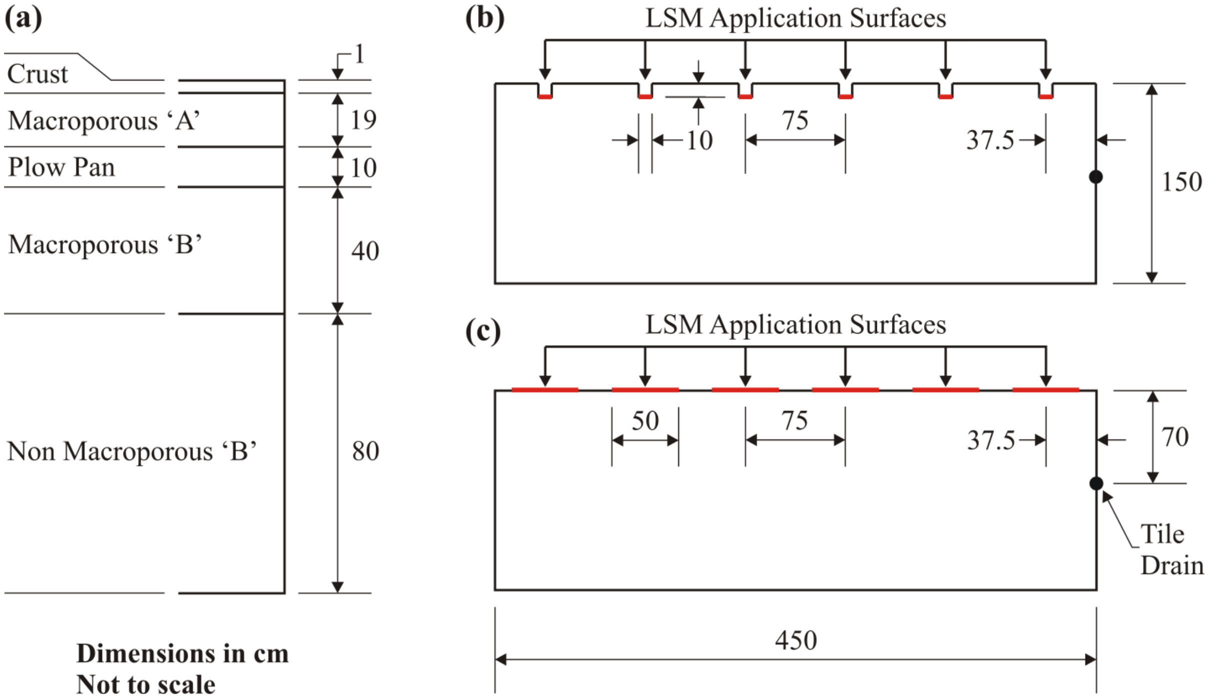

Figure 5.1. Conceptual model of the physical system showing: (a) the subdivisions of the soil profile, (b) simulation domain geometry for the liquid swine manure (LSM) injection scenario, and (c) simulation domain geometry for the LSM surface banding scenario. Note that the macroporous B layer extends from the bottom of the macroporous plowpan to tile drain depth.

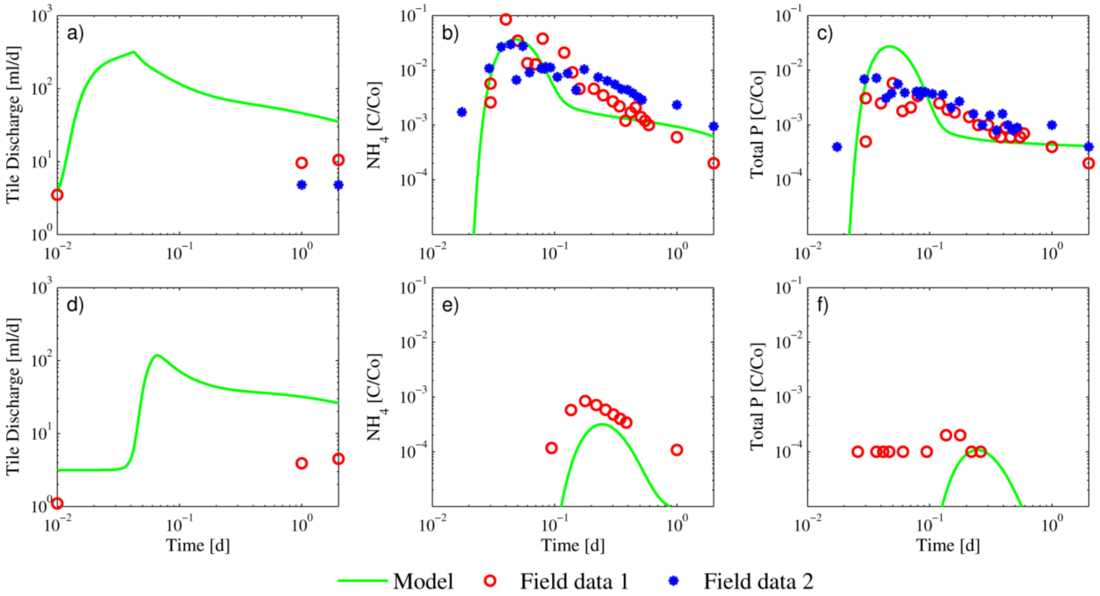

Figure 5.2. Simulation results compared to field observations for: tile discharge (a & d), NH$_4$ concentration (b & e), and total P concentration (c & f); for liquid swine manure application with injection at a rate of 74 m^3/ha (top row), and surface banding at a rate of 56 m^3/ha (bottom row).

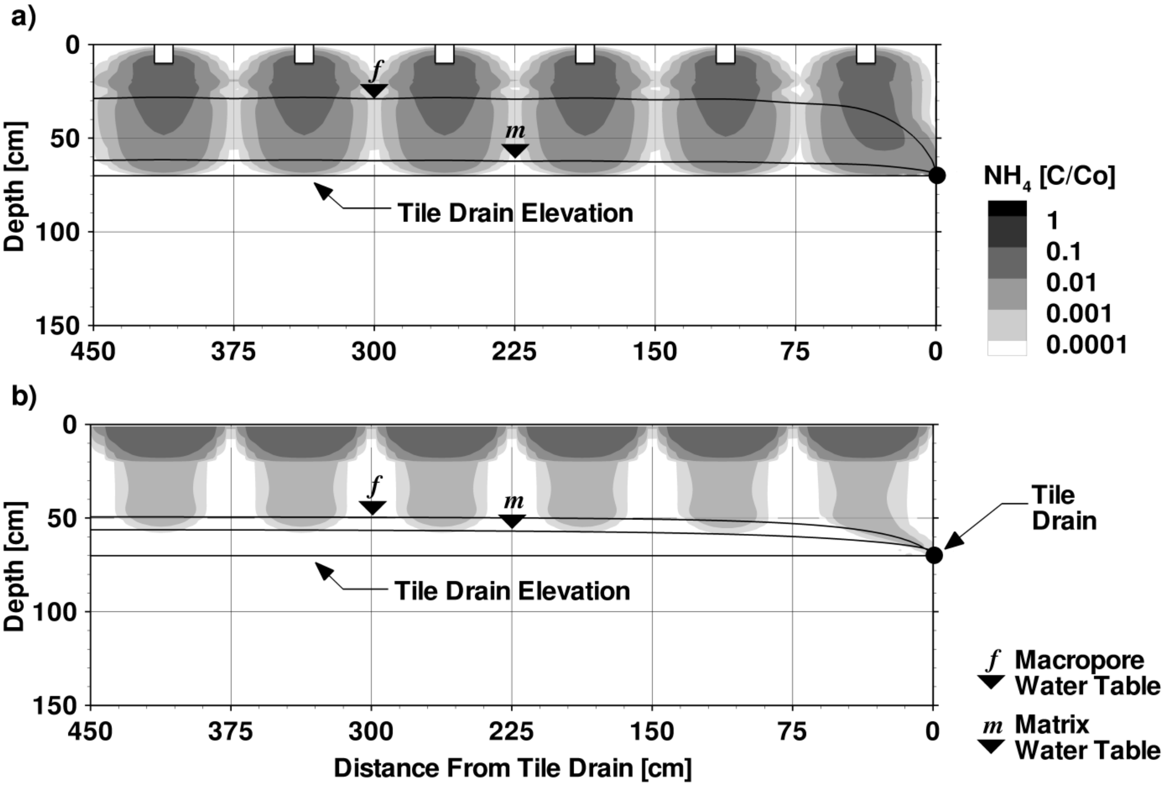

Figure 5.3. Simulated macropore NH_4 concentrations, and soil matrix and macropore zone water table positions for: (a) liquid swine manure (LSM) injection with an application rate of 74 m^3/ha at 0.048 days after application, and (b) LSM surface banding with an application rate of 56 m^3/ha at 0.208 days after application.

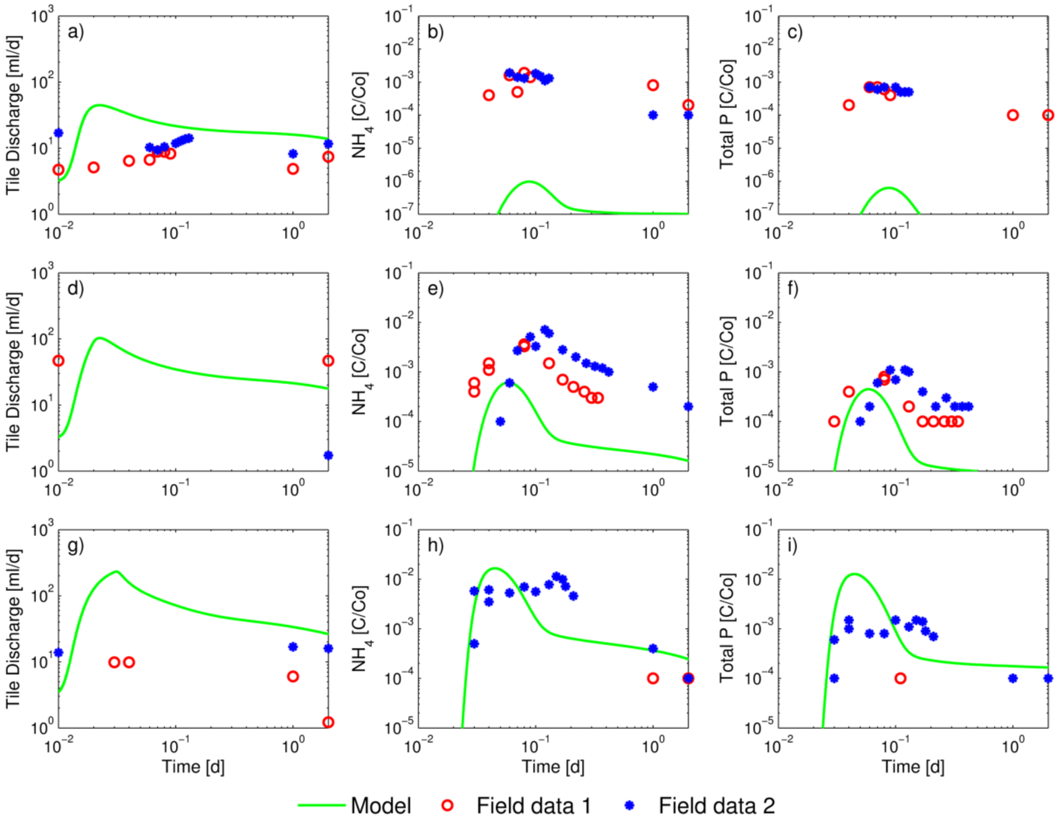

Figure 5.4. Simulation results compared to field observations for: tile discharge (a, d & g), NH_4 concentration (b, e & h), and total P concentration (c, f & i); for liquid swine manure injection at a rate of: 28 m^3/ha (top row), 37 m^3/ha (middle row), and 56 m^3/ha (bottom row).

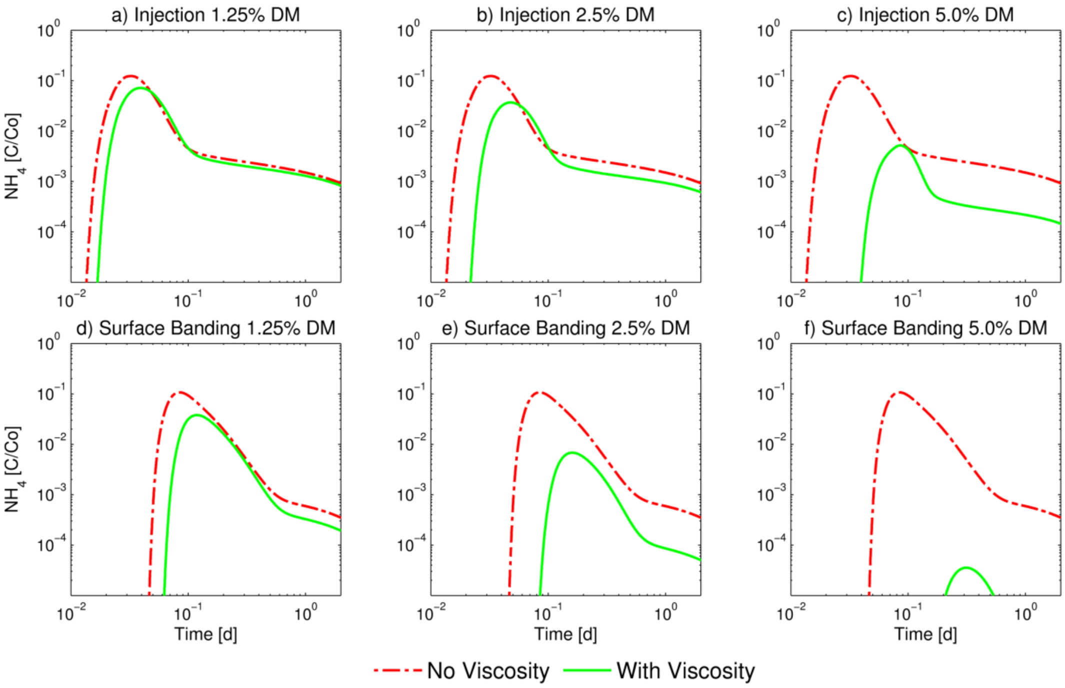

Figure 5.5. Simulated viscosity/dry matter influences on tile effluent NH_4 concentrations after liquid swine manure (LSM) injection (top row), and surface banding (bottom row), with an application rate of 74 m^3/ha. LSM dry matter contents (with viscosity) of: 1.25% (a & d), 2.5% (b & e), and 5% (c & f), are each compared to the scenario where LSM viscosity has not been considered (no viscosity).

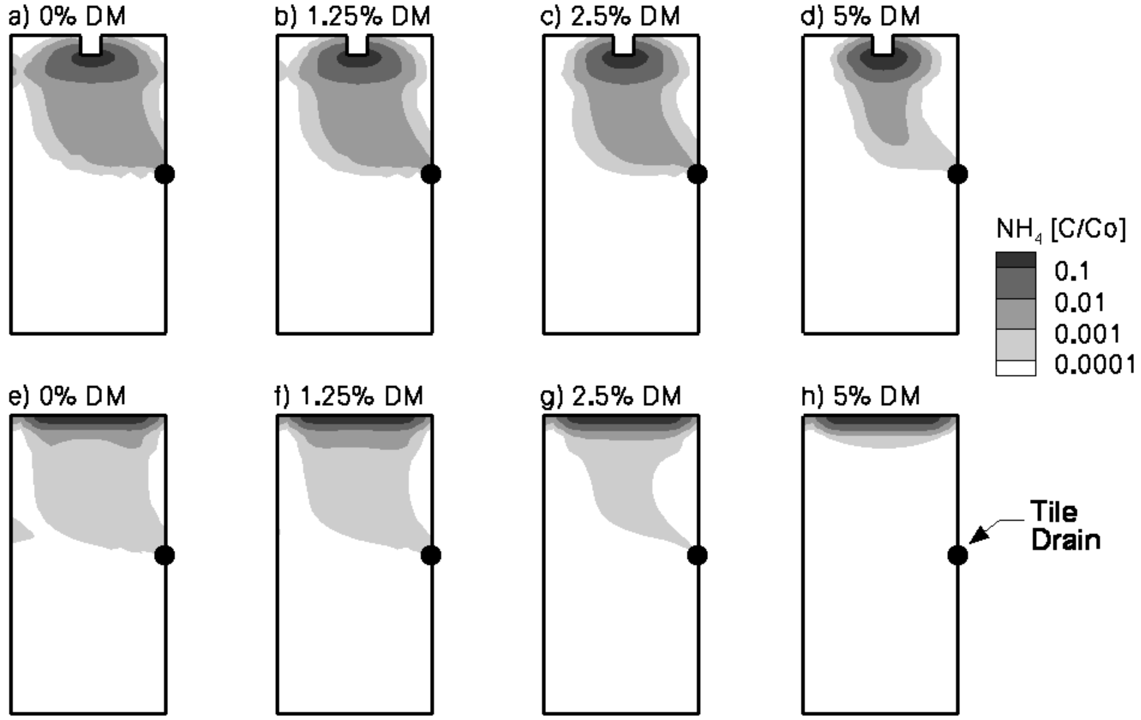

Figure 5.6. Simulated viscosity/dry matter influences on residual soil matrix NH_4 concentrations one day after liquid swine manure (LSM) injection (top row), and LSM surface banding (bottom row), with application rates of 74 m^3/ha. LSM dry matter contents of: 0% (a & e), 1.25% (b & f), 2.5% (c & g), and 5% (d & h), are considered.

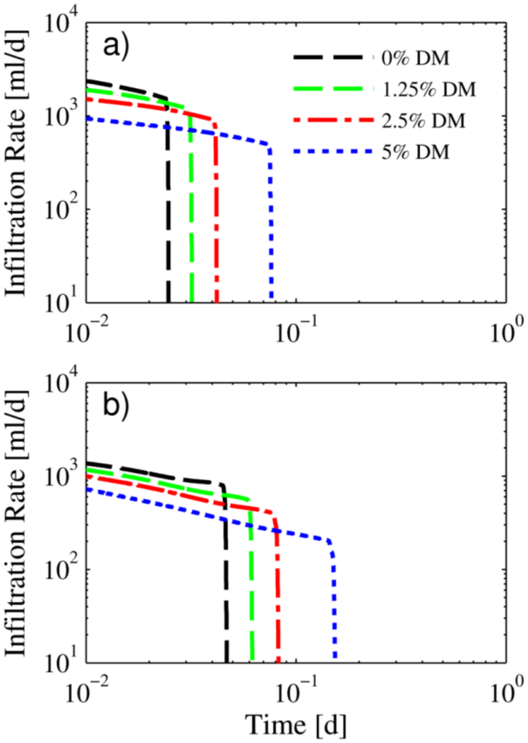

Figure 5.7. Simulated viscosity/dry matter influence on the infiltration rate of liquid swine manure beneath a single application row with unit thickness after injection (a), and surface banding (b), with application rates of 74 m^3/ha.

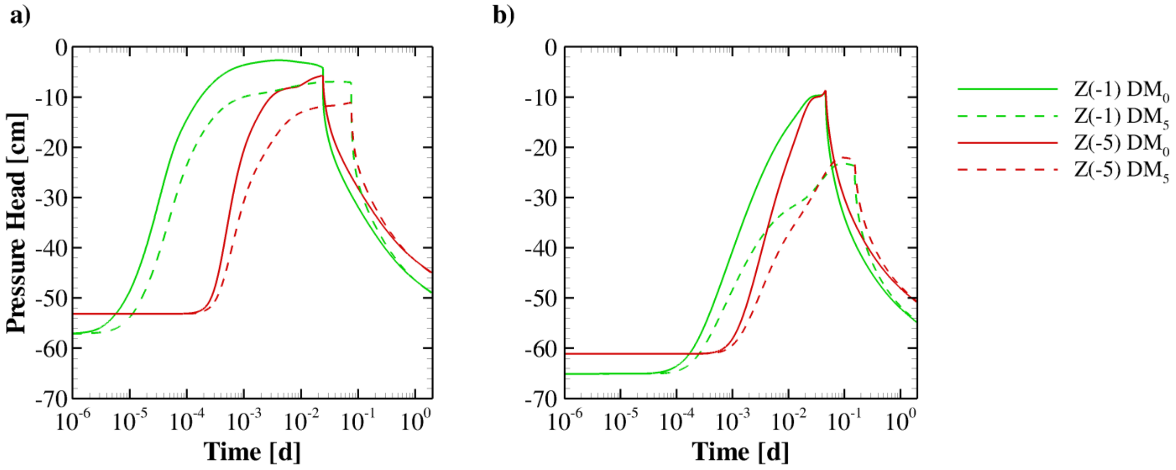

Figure 5.8. Pressure heads in the soil matrix 1 cm and 5 cm below the 74.8 m^3 ha^{-1} liquid swine manure application surface nearest to the tile drain for injection (a), and 1 cm and 5 cm below the top of the macroporous A layer for surface banding (b), for dry matter contents of 0% (DM_0), and 5% (DM_5).

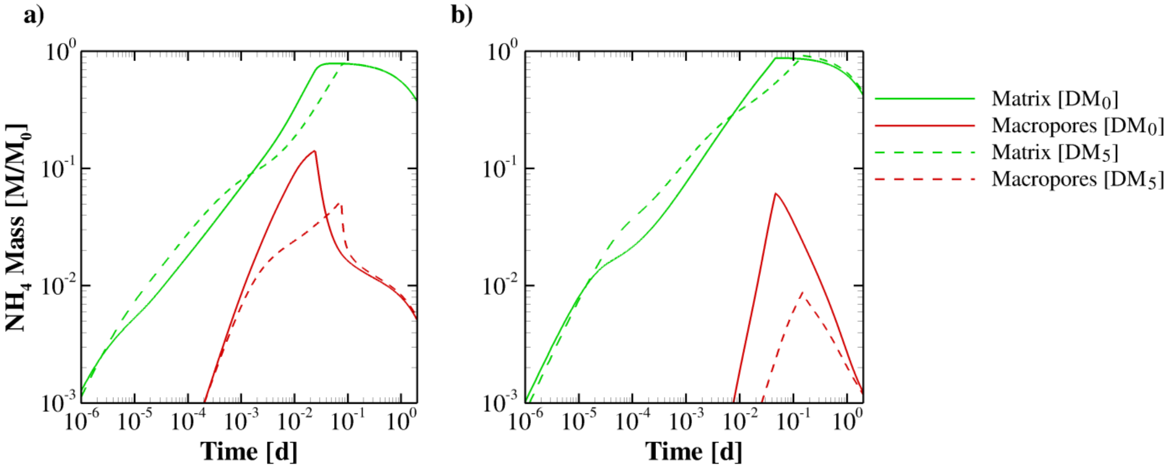

Figure 5.9. Proportion of total applied NH_4 mass stored in the soil matrix and macropore zones of the injection (a), and surface banding (b) scenarios; for liquid swine manure application at a rate of 74.8m^3 ha^{-1}; and dry matter contents of 0% (DM_0) and 5% (DM_5).

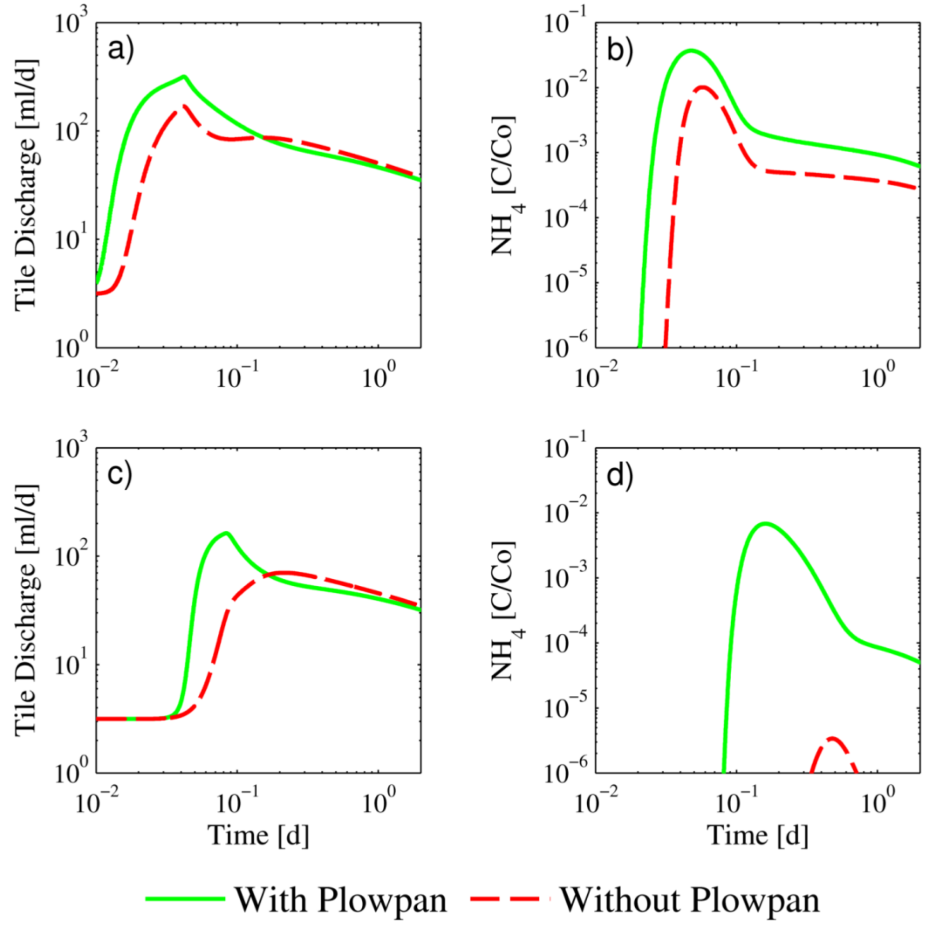

Figure 5.10. Simulated effects of the plowpan layer on tile discharge rates (a & c), and tile effluent NH_4 concentrations (b & d); for liquid swine manure injection (top row), and surface banding (bottom row), with an application rate of 74 m^3 ha^{-1}.

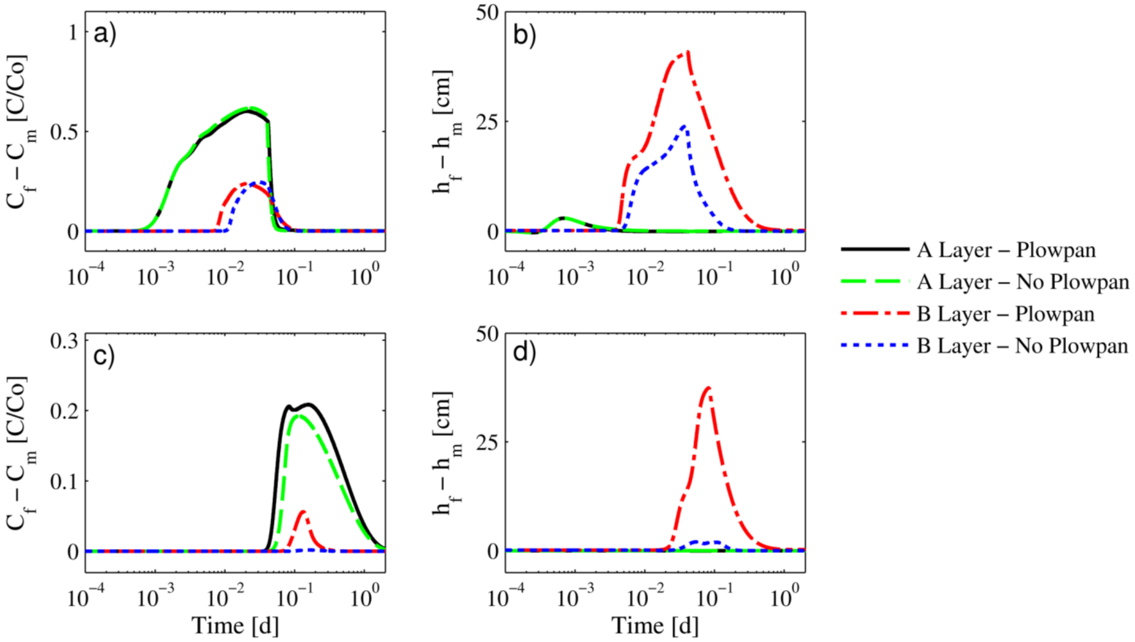

Figure 5.11. Concentration (a & c) and pressure head (b & d) non-equilibrium status, observed at a horizontal distance of 412.5 cm from the tile drain, at depths of 15 cm (A Layer) and 40 cm (B Layer) from the surface; for liquid swine manure injection (top row) and surface banding (bottom row) at a rate of 74 m^3 ha^{-1}, with and without plowpan layers.

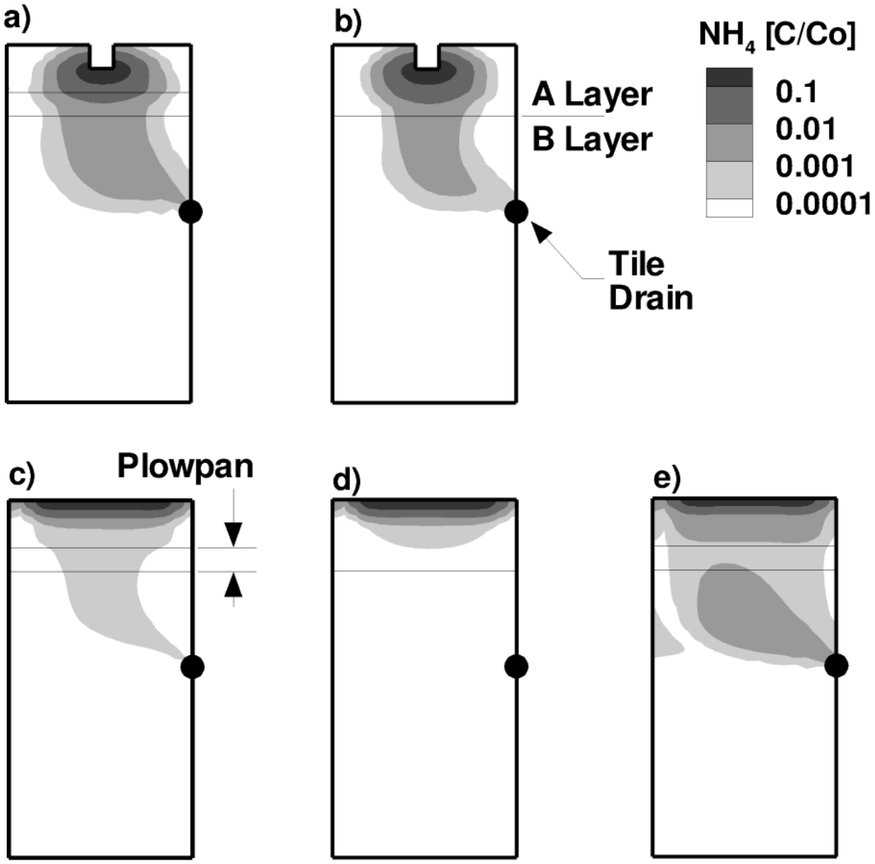

Figure 5.12. Residual NH_4 distribution in the soil matrix 2 days after liquid swine manure application at a rate of 74 m^3 ha^{-1}; for injection with (a), and without (b), a plowpan layer; and surface banding with a soil crust and plowpan layer (c), with a soil crust but without a plowpan layer (d), and without a soil crust layer but with a plowpan layer (e).

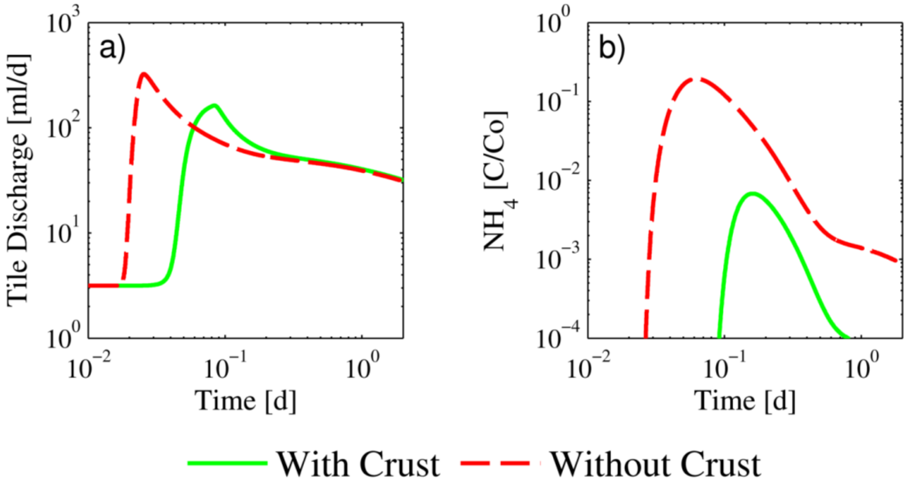

Figure 5.13. Simulated effects of the soil crust layer on tile discharge rates and tile effluent NH_4 concentrations for liquid swine manure surface banding with an application rate of 74 m^3 ha^{-1}.

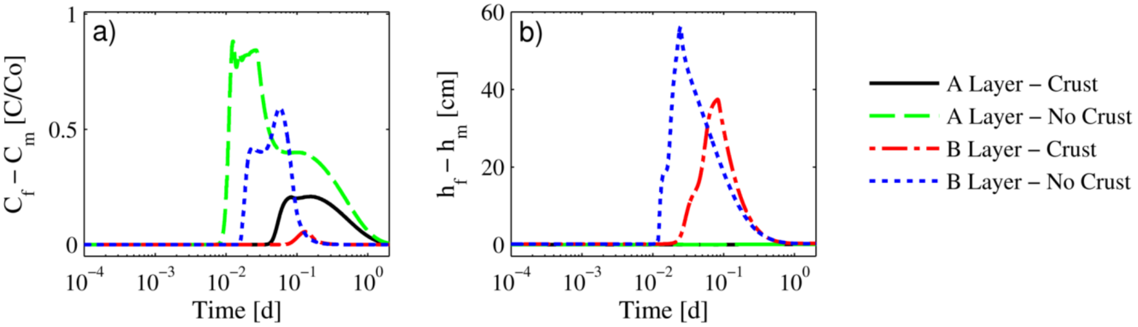

Figure 5.14. Concentration (a), and pressure head (b), non-equilibrium status observed at a horizontal distance of 412.5 cm from the tile drain, at depths of 15 cm (A Layer) and 40 cm (B Layer) from the surface; for liquid swine manure surface banding at a rate of 74 m^3 ha^{-1}, with, and without, a soil crust.

Table 5.1. Physical soil properties (from *Ball-Coelho et al.*, 2007) from the liquid swine manure injection (INJ), and surface banding (SB), experiment site.

Depth	Sand	Silt	Clay	Bulk Density	K_{fs} INJ	K_{fs} SB
[cm]		[%]		[g cm^{-3}]	[cm d^{-1}]	
0-20	20	56	24	1.39	717	95
20-40	16	54	30	1.56	423	190
40-60	15	55	30	1.64	n/a	
60-90	19	54	27	1.49		

Table 5.2. Hydraulic properties assigned to the soil matrix zones.

Soil Layer	Depth	Θ_r	Θ_s	α_{vg}	n_{vg}	K_s
	[cm]	-	-	[cm^{-1}]	-	[cm d^{-1}]
Crust	0-1	0.07	0.42	0.006	1.61	1.68*
A	1-20	0.07	0.42	0.006	1.61	13.4
Plow Pan	20-30	0.07	0.42	0.006	1.61	0.04*
B	30-150	0.08	0.40	0.008	1.49	4.4

* Values established during model calibration

Table 5.3. Hydraulic properties assigned to the macroporous zones.

Application Method	Soil	Depth	Θ_r	Θ_s	α_{vg}	n_{vg}	$K_{s,z}$	$K_{s,x}$	K_a	w	α_w	α_s
	Layer	[cm]	-	-	[cm^{-1}]	-		[cm d^{-1}]		-	[cm^{-1} d^{-1}]	[d^{-1}]
Injection	A	1-20	0.05	0.9	0.1	2	29300	29300*	1.12	0.024*	8*	8*
	B	20-70	0.05	0.9	0.1	2	69700	1400*	0.4	0.006	0.005*	1*
Surface Banding	A	1-20	0.05	0.9	0.1	2	13600	1360*	1.12	0.006	5*	0.01*
	B	20-70	0.05	0.9	0.1	2	30900	600*	0.4	0.006	0.005*	0.1*

* Values established during model calibration

Chapter 6

Conclusions and Recommendations

6.1 Summary of Conclusions

This research was an effort to accurately define the process of solute and nutrient movement to tile drains in macroporous agricultural soil, and to characterize the soil properties that influence such movement. While extensive field work was conducted in pursuit of soil property and solute flux data; the question of how nutrients entrained within liquid manure are transported through macroporous soil profiles was primarily addressed through the use of state of the art numerical modelling tools. Although southwestern Ontario served as the geographical focal point for the work, the results are relevant to any tile drained, macroporous, cropland soil that is subject to similar seasonal climate variability.

Soil hydraulic properties and macroporosity were characterized at three separate locations. Near surface macropore distribution with respect to depth was similar among the three locations. Macropores that ranged in size from 0.5-5 mm were most abundant in the topsoil and macropores that ranged from 5-10 mm were most abundant at the top of the B horizon. At the two locations with relatively low B horizon hydraulic conductivity, the majority of the MAF at tile drain depth was composed of macropores in the 0.5-5 mm size range whereas at the location with comparably high B horizon hydraulic conductivity, macroporosity appeared to terminate at a soil textural boundary located above the tile drain. Below the textural boundary, the soil material became noticeably coarser grained and more permeable which resulted in effective natural subsurface drainage, and appeared to promote deeper penetration of macropores in the 5 to 10 mm size range within the overlying fine grained material.

The mean maximum macropore area fraction (MAF) at the three locations ranged from 0.0035 to 0.009 and was observed at either the near surface or top of the B horizon, depending on the relative proportion of macropores in the 0.5-5 mm and 5-12 mm size ranges. MAF at tile depth was always much lower than the maximum value and did not exceed 0.001. Fractures were most common near surface and estimates suggest that they never comprised more than 15% of the total MAF, or 0.1% of total porosity. Results show that tile drains do not induce significant spatial trends in MAF distribution; however, intra-plot statistical comparison indicates that MAF is significantly different between the individual test locations, which were spaced between 100 and 250 m apart within the same field.

Dye staining patterns indicated that within the topsoil layer, flow readily occurred through both the soil matrix and macropores; however, at the top of the hardpan layer the dye appeared to spread laterally and flow into open macropores that penetrated a hardpan layer that existed at each of the three locations. At two of the three locations, preferential flow paths within the soil scars resultant from the tile drain installation process were channeling dye from the surface to the tile drain. However, at the third location there was no evidence of any tile installation scars and cylindrical macropores that were continuous through the hardpan appeared to be the primary pathway for dye to reach the tile drain.

At all three of the locations, surface applied solutes have the ability to be rapidly transmitted to tile drains via preferential flow paths that originate from within a localized area surrounding the drains. As a result, tile discharge, and ultimately, surface water receptor water quality, in settings where structured silt soils are underlain by a hydraulically active tile drain system, will invariably be influenced by land management practices that induce preferential flow. Shallow groundwater quality at each of the three plots also has the potential to be impacted by land management practices that induce preferential flow. However, the risk for rapid, widespread groundwater contamination is greatest at the location where macropores that are vertically continuous through the hardpan are effectively drained by highly permeable subsurface deposits. In the absence of highly permeable subsurface deposits, the impact of preferential flow on shallow groundwater quality is greatly reduced because the majority of macropores are in fact dead end pores that do not extend deep into the soil profile.

Although tile drains do not appear to influence the unsaturated surface soil hydraulic properties at the Kintore site, evidence does suggest that they do influence field saturated hydraulic conductivity (K_{fs}). Of the three locations investigated, the two with the lowest B horizon permeability had notably higher surface soil K_{fs} values immediately above the tile drain; while the plot with the highest B horizon permeability had the lowest K_{fs} values observed above the drain, which is thought to be the result of the tile installation process that disrupted the relatively permeable natural soil structure.

Post cropping season temporal variability was observed in the saturated, and unsaturated soil hydraulic properties, as well as the hydraulically effective porosity pore size distribution. In relatively dry soil conditions, K_{fs} and near saturated hydraulic conductivity were both higher than in the comparably wet soil conditions. The dry soil also had a greater proportion of hydraulically effective macroporosity attributed to large macropores; although overall hydraulically effective macroporosity was less in the dry soil because of reduced contribution from smaller pores.

Results from the conservative tracer experiment described in chapter 4 demonstrate that solutes can be rapidly transmitted to tile drains after surface application during high risk environmental conditions (i.e. initially wet, macroporous soil, where heavy precipitation succeeds application); however, the initial solute breakthrough to the tile accounts for a small proportion of the applied mass. The low initial mass capture can be attributed to the primarily vertical orientation of the B horizon macropores that direct preferential flow in a downward direction. As a result, the permeability and hydraulic conditions of the soil matrix ultimately govern the lateral movement for the majority of the solutes transmitted into the B horizon via preferential flow paths that do not terminate in close proximity to tile drains.

Despite the limited preferential movement of solutes to the tile drain immediately after surface application, a significant portion of the total applied mass can be captured by the tiles over longer periods of time. This work demonstrated that in southern Ontario, it can be expected that the majority of solutes applied to structured silty soils within 2 m of tile drains during the fall will be leached from the soil profile prior to the next growing season. When it is considered that tile drains are often spaced 10–15 m apart, upwards of 25% of soluble nutrients applied post-harvest will be potentially become surface water contaminants. In general, solute flux to the tile drain was heavily dependent on climate conditions and the occurrence of ‘extreme’ hydrologic events. As an example, approximately 20% of the solute mass applied within 2 m of the tile was discharged through the tile drain in response to a single winter melt event that spanned a 10 day interval in mid January, 2008.

Because of the wide range of flow conditions within tile drains over an annual cycle, long term monitoring of tile discharge rates can be exceptionally difficult. While sensitive flow meters are applicable during periods of relatively low flow, such devices did not withstand the perils of deployment during high flow conditions. Because the majority of tile drainage solute flux occurs in response to major hydrologic events, accurate tile discharge measurements during high flow conditions are imperative for quantifying water/solute/nutrient budgets in agricultural settings over annual cycles. To alleviate the need to constantly maintain flow monitoring equipment during peak flow conditions, the relationship between groundwater levels and tile flow rates can be employed. This work demonstrated a methodology that utilizes water-table position data, along with water-level data from a deep (4.5 m) well, to accurately estimate tile flow rates over a wide range of hydrologic conditions. This approach could be generally applicable at other sites.

The results from the tracer experiment also demonstrate the importance of the regional shallow-groundwater flow system on water and solute flux in tile drained agricultural settings. At sites where shallow-groundwater is moving towards the surface, the hydraulic gradients act as a protective barrier that inhibits surface applied solutes from migrating deep into the soil profile. Therefore, tile drains (and ultimately surface water bodies) in these types of hydrogeological settings are the primary receptors for water and solutes that leach from the soil profile.

Flow and transport of liquid swine manure (LSM) during field experiments conducted on a macroporous, tile drained soil was simulated with a version of HydroGeoSphere that was modified to account for the influence of manure dry matter (DM) content on fluid viscosity. Individual dual-permeability models were developed to evaluate the influence of manure application via injection (INJ) and surface banding (SB) on nutrient distribution in the soil profile and breakthrough to tile drains. To reflect the complexity of both the soil structure and soil layer distribution at the liquid manure application experiment field site, near Sebringville Ontario, the models included distinct horizontally continuous layers to represent the soil crust, plowpan, and A and B horizons. Macropore orientation was also accounted for by incorporating anisotropy into the hydraulic conductivity description for the macropore continuum. Model parameterization was achieved using a combination of soil physical property data, field saturated hydraulic conductivity values, pedotransfer functions, constitutive relationships between the soil matrix and macropore properties, and calibration.

The complexity of the models used for this work elucidated the influences of variable soil structure and soil layer properties, LSM viscosity, and LSM application methods on flow and transport processes in shallow water table, tile drained agricultural soils. Simulation results suggest that the macropore anisotropy ratio is considerably different between the A and B layers, and reflects the structural differences between predominantly vertical worm burrows and root holes in the B layer, and the more isotropic macropore features in the A layer. Tillage associated with LSM injection also influences macropore geometry by further reducing the anisotropy ratio in the A layer.

The parameters that control water and solute exchange between the soil matrix and the macropores vary according to soil layers and LSM application methods. The exchange coefficients that govern water and mass movement between the soil matrix and macropores are relatively low in the B layer compared to those in the A layer which suggests that near surface macropore regenerative processes and soil structure characteristics enhance water and solute movement between the soil matrix and the macropores. For the INJ scenario, tillage effects on soil structure also appear to promote easier exchange of water and solutes between the soil matrix and the macropores.

In order to accurately reproduce the field measured nutrient breakthrough to the tile drain, models for both LSM application methods required the inclusion of a macroporous plowpan layer with low matrix permeability at the base of the A layer. Model results show that the plowpan layer reduces the capability for vertical flow in the soil matrix, and leads to increased pressure-heads in the A layer soil matrix. The increased soil matrix pressure-heads promote the exchange of LSM from the A layer soil matrix into the macropore network, which ultimately leads to rapid vertical movement of LSM and earlier arrival of nutrients at the tile drain. In addition to a plowpan layer, the SB scenario model also required a reduced permeability soil crust layer. The presence of a soil crust layer reduces the infiltration rate of LSM and leads to a reduction in A layer soil matrix pressure-heads. As a result, there is less movement of LSM into macropores, less vertical LSM movement, and lower nutrient concentrations at the tile drain.

Due to the relationship between LSM dry matter content and viscosity, the relative permeability of LSM flow systems decreases as dry matter content increases. Therefore, increasing the LSM dry matter has a large influence on nutrient distribution within the soil profile, and associated nutrient breakthrough to the tile drain. Because LSM is most concentrated near the application surfaces, the soil matrix near the application surfaces undergoes the greatest reduction in relative permeability. Decreased infiltration rates lead to lower pressure-heads in the A layer soil matrix and results in less LSM movement from the soil matrix into the macropores. As a result, increasing the dry matter content of LSM causes appreciable reductions in nutrient concentrations in the tile drain effluent and leads to greater LSM retention in the A layer soil matrix near the LSM application surface.

In summary, this body of research work has shown that flow and transport processes at any site with macroporous, tile drained soil will be governed by many factors, including: macropore extent, anisotropy, and spatial – temporal variability; soil layering and the presence of hardpans/plowpans and surface crusts; soil hydraulic property spatial – temporal variability; hydraulic gradients induced by both the tile drains and shallow groundwater flow; and climate variability. Furthermore, if the solutes of interest are entrained in liquid manure, it is also important to consider the effects of manure specific fluid properties. For a proper understanding of nutrient fluxes in such complex settings, each of these factors must be given adequate consideration.

6.2 Recommendations for future research

The field component of this research was conducted partly with the intention of obtaining the data required to parameterize and calibrate high resolution, transient, dual-permeability models and to minimize parameter equifinality to a degree not yet realized by the vadose zone modelling community. While collecting the field data was an arduous task, so will be the task of utilizing the data to its full potential within a modelling framework. As such, the logical next step, which is already underway, will be to develop and calibrate a model of the Kintore tracer experiment. The calibrated model will have great utility as an environmental risk analysis tool for solute/manure application on macroporous, tile drained soils, in different climate/antecedent soil moisture conditions.

It can be easily argued that the greatest intrinsic value in numerical models is in their ability to simulate processes that occur on a larger scale or longer timeframe than what can be reasonably investigated in a research campaign solely based on field work. Future improvements in large scale models will in part be achieved by incorporating highly transient, plot/field scale phenomena into regional/watershed scale simulation scenarios. Upscaling relatively small scale processes so that they can be applied within a large scale model is not a trivial task, and is generally limited by the time required to compute a solution to intense numerical problems. Preferential flow and transport in tile drained soil is one example of a potential small scale process that can be readily envisioned to have significant influence on large scale hydrologic response to both transient climate events, and field scale land management practices. However, currently there is little quantitative data that supports the argument that preferential flow processes add significant value when they are incorporated into large scale models. Providing scientific basis to support such an argument would be a worthy task.

As of yet there is little understanding of the complex relationship that exists between soil structure and macroporosity distribution, soil hydraulic properties, and infiltration characteristics in layered soils. Although some insight on this problem is given throughout chapters 2 to 5, the data collected at the Kintore site provides great opportunity for an extremely focused investigation on this subject. In total, there are 36 individual test areas at the Kintore site where saturated and unsaturated surface soil hydraulic properties are defined above soil columns where visible macroporosity has been painstakingly characterized down to tile depth. In addition, high resolution images exist for each of the macropore counting surfaces. Such data is well tailored for evaluation via statistical methods that employ both traditional and spectral analysis techniques.

One last suggestion for future research stems from the conclusion that liquid manure fluid properties have significant influence on nutrient distribution within a soil profile. Accordingly, it seems logical to investigate the potential for tailoring manure properties so that they are ideally suited for specific manure application methods and/or soil types. Because manure fluidity is important from a handling/transfer perspective, it is quite likely that the best point to manipulate fluid properties for optimal nutrient distribution is at application. Considering the condition of many post harvest field surfaces that receive liquid manure, combine chaff or other crop residue would be readily available to potentially serve as a base material for fluid modification. Perhaps liquid manure spreaders could be outfitted with a pick-up/blender attachment. Or maybe there is also potential to use low cost coagulants that could also provide a value added benefit for overall soil quality.

References

Abbaspour, K., R. Kasteel, and R. Schulin (2000), Inverse parameter estimation in a layered unsaturated field soil, *Soil Science*, 165:109-123.

Alakukku, L. (1996a), Persistence of soil compaction due to high axle load traffic .1. Short-term effects on the properties of clay and organic soils, *Soil & Tillage Research*, 37:211-222.

Alakukku, L. (1996b), Persistence of soil compaction due to high axle load traffic .2. Long-term effects on the properties of fine-textured and organic soils, *Soil & Tillage Research* 37:223-238.

Alakukku, L., V. Nuutinen, E. Ketoja, H. Koivusalo, and M. Paasonen-Kivekas. (2010), Soil macroporosity in relation to subsurface drain location on a sloping clay field in humid climatic conditions, *Soil & Tillage Research* 106:275-284.

Anderson, J.L., and J. Bouma. (1973), Relationships between saturated hydraulic conductivity and morphometric data of an argillic horizon, *Soil Science Society of America Journal* 37:408-413.

Ankeny, M.D., T.C. Kaspar, and R. Horton. (1990), Characterization of tillage and traffic effects on unconfined infiltration measurements, *Soil Science Society of America Journal* 54:837-840.

Azevedo, A.S., R.S. Kanwar, and R. Horton. (1998), Effect of cultivation on hydraulic properties of an Iowa soil using tension infiltrometers, *Soil Science* 163:22-29.

Azooz, R.H., M.A. Arshad, and A.J. Franzluebbers. (1996), Pore size distribution and hydraulic conductivity affected by tillage in northwestern Canada, *Soil Science Society of America Journal* 60:1197-1201.

Ball-Coelho, B. R., R. C. Roy, and A. J. Bruin (2005), Optimization of liquid swine manure sidedress rate and method for grain corn, *Agronomy Journal*, 97:1322-1332.

Ball-Coelho, B. R., R. C. Roy, E. Topp, and D. R. Lapen (2007), Tile water quality following liquid swine manure application into standing corn, *Journal of Environmental Quality*, 36:580-587.

Bear, J. (1972), Dynamics of fluids in porous media, 764 pp., American Elsevier, New York

Beven, K., and P. Germann. (1982), Macropores and water-flow in soils, *Water Resources Research* 18:1311-1325.

Bodhinayake, W., B.C. Si, and C.J. Xiao. (2004a), New method for determining water-conducting macro- and mesoporosity from tension infiltrometer, *Soil Science Society of America Journal* 68:760-769.

Bodhinayake, W., B.C. Si, and K. Noborio. (2004b), Determination of hydraulic properties in sloping landscapes from tension and double-ring infiltrometers, *Vadose Zone Journal* 3:964-970.

Bodhinayake, W., and B.C. Si. (2004c), Near-saturated surface soil hydraulic properties under different land uses in the St Denis National Wildlife Area, Saskatchewan, Canada, *Hydrological Processes* 18:2835-2850.

Bodner, G., W. Loiskandl, G. Buchan, and H. P. Kaul (2008), Natural and management-induced dynamics of hydraulic conductivity along a cover-cropped field slope, *Geoderma*, 146:317-325.

Bouma, J., L.W. Dekker, and J. Haans. (1979a), Drainability of some Dutch clay soils: A case study of soil survey interpretation, *Geoderma* 22:193-203.

Bouma, J., A. Jongerius, and D. Schoonderbeek. (1979b), Calculation of saturated hydraulic conductivity of some pedal clay soils using micromorphometric data, *Soil Science Society of America Journal* 43:261-264.

Bouma, J., J.W. Vanhoorn, and G.H. Stoffelsen. (1981), Measuring the hydraulic conductivity of soil adjacent to tile drains in a heavy clay soil in the Netherlands, *Journal of Hydrology* 50:371-381.

Bouma, J., C. F. M. Belmans, and L. W. Dekker (1982), Water infiltration and redistribution in a silt loam subsoil with vertical worm channels, *Soil Science Society of America Journal*, 46:917-921.

Bradford, S., E. Segal, W. Zheng, Q. Wang, and S. Hutchins (2008), Reuse of concentrated animal feeding operation wastewater on agricultural lands, *Journal of Environmental Quality*, 37:S97-S115.

Buczko, U., O. Bens, and R.E. Huttl. (2006), Tillage effects on hydraulic properties and macroporosity in silty and sandy soils, *Soil Science Society of America Journal* 70:1998-2007.

Cambardella, C. A., T. B. Moorman, D. B. Jaynes, J. L. Hatfield, T. B. Parkin, W. W. Simpkins, and D. L. Karlen (1999), Water quality in Walnut Creek watershed: Nitrate-nitrogen in soils, subsurface drainage water, and shallow groundwater, *Journal of Environmental Quality*, 28:25-34.

Cey, E.E., D.L. Rudolph, G.W. Parkin, and R. Aravena. (1998), Quantifying groundwater discharge to a small perennial stream in southern Ontario, Canada, *Journal of Hydrology* 210:21-37.

Cey, E.E., D.L. Rudolph, R. Aravena, and G. Parkin. (1999), Role of the riparian zone in controlling the distribution and fate of agricultural nitrogen near a small stream in southern Ontario, *Journal of Contaminant Hydrology* 37:45-67.

Cey, E. E., and D. L. Rudolph (2009), Field study of macropore flow processes using tension infiltration of a dye tracer in partially saturated soils, *Hydrological Processes*, 23:1768-1779.

Coles, N., and S. Trudgill (1985), The movement of nitrate fertilizer from the soil surface to drainage waters by preferential flow in weakly structured soils, Slapton, S. Devon, *Agriculture Ecosystems & Environment*, 13:241-259.

Cook, M. J., and J. L. Baker (2001), Bacteria and nutrient transport to the lines shortly after application of large volumes of liquid swine manure, *Transactions of the Asae*, 44:495-503.

Das Gupta, S., B.P. Mohanty, and J.M. Köhne. (2006), Soil hydraulic conductivities and their spatial and temporal variations in a vertisol, *Soil Science Society of America Journal* 70:1872-1881.

Doherty, J. (2004), PEST Model-independent parameter estimation user manual: 5th edition, Watermark Numerical Computing.

Drury, C. F., C. S. Tan, J. D. Gaynor, T. O. Oloya, and T. W. Welacky (1996), Influence of controlled drainage-subirrigation on surface and tile drainage nitrate loss, *Journal of Environmental Quality*, 25:317-324.

Dunn, G.H., and R.E. Phillips. (1991), Macroporosity of a well-drained soil under no-till and conventional tillage, *Soil Science Society of America Journal* 55:817-823.

Edwards, W.M., L.D. Norton, and C.E. Redmond. (1988), Characterizing macropores that affect infiltration into nontilled soil, *Soil Science Society of America Journal* 52:483-487.

Edwards, W. M., M. J. Shipitalo, W. A. Dick, and L. B. Owens (1992), Rainfall intensity affects transport of water and chemicals through macropores in no-till soil, *Soil Science Society of America Journal,* 56:52-58.

Ehlers, W. (1975), Observations on earthworm channels and infiltration on tilled and untilled loess soil, *Soil Science* 119:242-249.

Ela, S.D., S.C. Gupta, and W.J. Rawls. (1992), Macropore and surface seal interactions affecting water infiltration into soil, *Soil Science Society of America Journal* 56:714-721.

Experimental Farms Service. (1987), Soil map of Oxford County, soil survey report No. 28. Reprinted 1987. Ottawa.

FAO. (2009), High Level Expert Forum - How to Feed the World in 2050. Rome October 12-13 2009: United Nations.

Fausey, N.R., and R. Lal. (1989), Drainage - tillage effects on Crosby-Kokomo soil association in Ohio II. Soil temperature regime and infiltrability, *Soil Technology* 2:371-383.

Fausey, N.R., and R. Lal. (1992), Drainage - tillage effects on a Crosby-Kokomo soil association in Ohio III. Organic matter content and chemical properties, *Soil Technology* 5:1-12.

Fleming, R. J., and S. H. Bradshaw (1992), Contamination of subsurface drainage systems during manure spreading, paper presented at the 1992 International Winter Meeting, American Society of Agricultural Engineers, Nashville.

Flint, L.E., and A.L. Flint. (2002), Porosity. In: Dane, J.H., Topp, G.C. (Eds.), *Methods of Soil Analysis Part 4*, *Physical Methods*, Soil Science Society of America, Inc., Madison WI, pp241-254.

Flury, M., H. Fluhler, W.A. Jury, and J. Leuenberger. (1994), Susceptibility of soils to preferential flow of water - A field-study, *Water Resources Research* 30:1945-1954.

Forkel, C., and M. A. Celia (1992), Numerical simulation of unsaturated flow and contaminant transport with density and viscosity dependence, In: T.F. Russell et al. (Eds.) *Computational methods in water resources IX*, *Vol. 2: Mathematical modeling in water resources*, pp. 351-358, Elsevier Applied Science, Boston.

Frison, A., I. Cousin, D. Montagne, and S. Cornu. (2009), Soil hydraulic properties in relation to local rapid soil changes induced by field drainage: a case study, *European Journal of Soil Science* 60:662-670.

Gärdenäs, A.I., J. Simunek, N. Jarvis, and M.T. van Genuchten. (2006), Two-dimensional modelling of preferential water flow and pesticide transport from a tile-drained field, *Journal of Hydrology* 329:647-660.

Gardner, W.R. (1958), Some steady-state solutions of the unsaturated moisture flow equation with application to evaporation from a water table, *Soil Science* 85:228-232.

Gee, G.W., and D. Or. (2002), Particle-size analysis. p.255-293, In: J.H. Dane and G.C. Topp. (Eds.), *Methods of Soil Analysis Part 4, Physical Methods*, Soil Science Society of America, Inc., Madison.

Gerke, H. H. (2006), Preferential flow descriptions for structured soils, *Journal of Plant Nutrition and Soil Science*, 169:382-400.

Gerke, H. H., and M. T. van Genuchten (1993a), A dual-porosity model for simulating the preferential movement of water and solutes in structured porous-media, *Water Resources Research*, 29:305-319.

Gerke, H. H., and M. T. van Genuchten (1993b), Evaluation of a 1st-order water transfer term for variably saturated dual-porosity flow models, *Water Resources Research*, 29:1225-1238.

Gerke, H. H., and J. M. Köhne (2002), Estimating hydraulic properties of soil aggregate skins from sorptivity and water retention, *Soil Science Society of America Journal*, 66:26-36.

Gerke, H.H., J. Dusek, T. Vogel, and J.M. Köhne. (2007), Two-dimensional dual-permeability analyses of a bromide tracer experiment on a tile-drained field, *Vadose Zone Journal* 6:651-667.

Ghezzehei, T.A., and D. Or. (2000), Dynamics of soil aggregate coalescence governed by capillary and rheological processes, *Water Resources Research* 36:367-379.

Gish, T. J., K. J. S. Kung, D. C. Perry, J. Posner, G. Bubenzer, C. S. Helling, E. J. Kladivko, and T. S. Steenhuis (2004), Impact of preferential flow at varying irrigation rates by quantifying mass fluxes, *Journal of Environmental Quality*, 33:1033-1040.

Gottschall, N., M. Edwards, E. Topp, P. Bolton, M. Payne, W.E. Curnoe, B.B. Coelho, and D.R. Lapen. (2009), Nitrogen, Phosphorus, and Bacteria Tile and Groundwater Quality Following Direct Injection of Dewatered Municipal Biosolids into Soil, *Journal of Environmental Quality* 38:1066-1075.

Hawkins, C.L., E.M. Rutledge, M.C. Savin, M.J. Shipitalo, and K.R. Brye. (2008), A sand layer deters burrowing by Lumbricus terrestris L., *Soil Science* 173:186-194.

Haws, N. W., P. S. C. Rao, J. Simunek, and I. C. Poyer (2005), Single-porosity and dual-porosity modelling of water flow and solute transport in subsurface-drained fields using effective field-scale parameters, *Journal of Hydrology*, 313:257-273.

Helsel, D.R., and R.M. Hirsch. (2002), Chapter A3, Statistical methods in water resources. In: *Techniques of Water-Resources Investigations of the United States Geological Survey, Book 4, Hydrologic Analysis and Interpretation*. United States Geological Survey.

Hofmann, N. (2008), A geographical profile of livestock manure production in Canada, 2006, *EnviroStats*, 2:12-16.

Hoorman, J. J., and M. J. Shipitalo (2006), Subsurface drainage and liquid manure, *Journal of Soil and Water Conservation*, 61:94A-97A.

Hu, W., M.G. Shao, Q.J. Wang, J. Fan, and R. Horton. (2009), Temporal changes of soil hydraulic properties under different land uses, *Geoderma* 149:355-366.

Hundal, S.S., G.O. Schwab, and G.S. Taylor. (1976), Drainage system effects on physical properties of a lakebed clay soil, *Soil Science Society of America Journal* 40:300-305.

Jarvis, N.J. (2007), A review of non-equilibrium water flow and solute transport in soil macropores: principles, controlling factors and consequences for water quality, *European Journal of Soil Science 58*:523-546.

Jaynes, D. B., S. I. Ahmed, K. J. S. Kung, and R. S. Kanwar (2001), Temporal dynamics of preferential flow to a subsurface drain, *Soil Science Society of America Journal*, 65:1368-1376.

Keener, H. M., J. J. Hoorman, and M. H. Klingman (2006), Rheology and flowability properties of liquid dairy and swine waste, paper presented at the 2006 Annual International Meeting of the American Society of Agricultural and Biological Engineers, Oregon.

Kladivko, E.J., G.E. Vanscoyoc, E.J. Monke, K.M. Oates, and W. Pask. (1991), Pesticide and nutrient movement into subsurface tile drains on a silt loam soil in Indiana, *Journal of Environmental Quality* 20:264-270.

Kladivko, E. J., J. Grochulska, R. F. Turco, G. E. Van Scoyoc, and J. D. Eigel (1999), Pesticide and nitrate transport into subsurface tile drains of different spacings, *Journal of Environmental Quality*, 28:997-1004.

Kladivko, E. J., L. C. Brown, and J. L. Baker (2001), Pesticide transport to subsurface tile drains in humid regions of North America, *Critical Reviews in Environmental Science and Technology*, 31:1-62.

Kladivko, E. J., J. R. Frankenberger, D. B. Jaynes, D. W. Meek, B. J. Jenkinson, and N. R. Fausey (2004), Nitrate leaching to subsurface drains as affected by drain spacing and changes in crop production system, *Journal of Environmental Quality*, 33:1803-1813.

Köhne, J. M., H. H. Gerke, and S. Köhne (2002), Effective diffusion coefficients of soil aggregates with surface skins, *Soil Science Society of America Journal*, 66:1430-1438.

Köhne, J. M., and H. H. Gerke (2005), Spatial and temporal dynamics of preferential bromide movement towards a tile drain, *Vadose Zone Journal*, 4:79-88.

Köhne, J. M., S. Köhne, and J. Simunek (2009), A review of model applications for structured soils: a) Water flow and tracer transport, *Journal of Contaminant Hydrology*, 104:4-35.

Kumar, M., H. D. Bartlett, and N. N. Mohsenin (1972), Flow properties of animal waste slurries, *Transactions of the ASAE*, 15:718-722.

Kung, K. J. S., T. S. Steenhuis, E. J. Kladivko, T. J. Gish, G. Bubenzer, and C. S. Helling (2000), Impact of preferential flow on the transport of adsorbing and non-adsorbing tracers, *Soil Science Society of America Journal*, 64:1290-1296.

Lal, R., and N.R. Fausey. (1993), Drainage - tillage effects on a Crosby-Kokomo soil association in Ohio IV. Soil physical properties, *Soil Technology* 6:123-135.

Landry, H., C. Lague, and M. Roberge (2004), Physical and rheological properties of manure products, *Applied Engineering in Agriculture*, 20:277-288.

Lapen, D. R., E. Topp, C. D. Metcalfe, H. Li, M. Edwards, N. Gottschall, P. Bolton, W. Curnoe, M. Payne, and A. Beck (2008a), Pharmaceutical and personal care products in tile drainage following land application of municipal biosolids, *Science of the Total Environment*, *399*(1-3), 50-65.

Lapen, D. R., E. Topp, M. Edwards, L. Sabourin, W. Curnoe, N. Gottschall, P. Bolton, S. Rahman, B. Ball-Coelho, M. Payne, S. Kleywegt, N. McLaughlin. (2008b), Effect of liquid municipal biosolid application method on tile and ground water quality, *Journal of Environmental Quality*, 37:925-936.

Larsson, M. H., N. J. Jarvis, G. Torstensson, and R. Kasteel (1999), Quantifying the impact of preferential flow on solute transport to tile drains in a sandy field soil, *Journal of Hydrology*, 215:116-134.

Laubel, A., O. H. Jacobsen, B. Kronvang, R. Grant, and H. E. Andersen (1999), Subsurface drainage loss of particles and phosphorus from field plot experiments and a tile-drained catchment, *Journal of Environmental Quality*, 28:576-584.

Lauren, J.G., R.J. Wagenet, J. Bouma, and J.H.M. Wosten. (1988), Variability of saturated hydraulic conductivity in a Glossaquic Hapludalf with macropores, *Soil Science* 145:20-28.

Lennartz, B., J. Michaelsen, W. Wichtmann, and P. Widmoser (1999), Time variance analysis of preferential solute movement at a tile-drained field site, *Soil Science Society of America Journal*, 63:39-47.

Lin, H. S., K. J. McInnes, L. P. Wilding, and C. T. Hallmark (1997), Low tension water flow in structured soils, *Canadian Journal of Soil Science*, 77:649-654.

Lin, H.S., K.J. McInnes, L.P. Wilding, and C.T. Hallmark. (1998), Macroporosity and initial moisture effects on infiltration rates in vertisols and vertic intergrades, *Soil Science* 163:2-8.

Logsdon, S.D., R.R. Allmaras, L. Wu, J.B. Swan, and G.W. Randall. (1990), Macroporosity and its relation to saturated hydraulic conductivity under different tillage practices, *Soil Science Society of America Journal* 54:1096-1101.

Macrae, M. L., M. C. English, S. L. Schiff, and M. Stone (2007), Intra-annual variability in the contribution of tile drains to basin discharge and phosphorus export in a first-order agricultural catchment, *Agricultural Water Management*, 92:171-182.

Mallants, D., B.P. Mohanty, A. Vervoort, and J. Feyen. (1997), Spatial analysis of saturated hydraulic conductivity in a soil with macropores, *Soil Technology* 10:115-131.

Mallawatantri, A.P., B.G. McConkey, and D.J. Mulla. (1996), Characterization of pesticide sorption and degradation in macropore linings and soil horizons of Thatuna silt loam, *Journal of Environmental Quality* 25:227-235.

McIntyre, D. S. (1958), Permeability Measurements of Soil Crusts Formed By Raindrop Impact, *Soil Science*, 85:185-189.

McKenzie, B.M., and A.R. Dexter. (1993), Size and orientation of burrows made by the earthworms Aporrectodea-Rosea and A-Caliginosa, *Geoderma* 56:233-241.

Messing, I., and N. J. Jarvis (1993), Temporal variation in the hydraulic conductivity of a tilled clay soil as measured by tension infiltrometers, *Journal of Soil Science*, 44:11-24.

Millington, R., and J. P. Quirk (1961), Permeability of porous solids, *Transactions of the Faraday Society*, 57:1200-1207.

Mohanty, B.P., M.D. Ankeny, R. Horton, and R.S. Kanwar. (1994), Spatial analysis of hydraulic conductivity measured using disc infiltrometers, *Water Resources Research* 30:2489-2498.

Mohanty, B.P., R. Horton, and M.D. Ankeny. (1996), Infiltration and macroporosity under a row crop agricultural field in a glacial till soil, *Soil Science* 161:205-213.

Mohanty, B. P., R. S. Bowman, J. M. H. Hendrickx, J. Simunek, and M. T. van Genuchten (1998), Preferential transport of nitrate to a tile drain in an intermittent-flood-irrigated field: Model development and experimental evaluation, *Water Resources Research*, 34:1061-1076.

Moorman, T. B., D. B. Jaynes, C. A. Cambardella, J. L. Hatfield, R. L. Pfeiffer, and A. J. Morrow (1999), Water quality in Walnut Creek watershed: Herbicides in soils, subsurface drainage, and groundwater, *Journal of Environmental Quality*, 28:35-45.

Moret, D., and J. L. Arrúe (2007), Characterizing soil water-conducting macro- and mesoporosity as influenced by tillage using tension infiltrometry, *Soil Science Society of America Journal*, 71:500-506.

Mori, Y., T. Maruyama, and T. Mitsuno. (1999), Soft x-ray radiography of drainage patterns of structured soils, *Soil Science Society of America Journal* 63:733-740.

Mubarak, I., J. C. Mailhol, R. Angulo-Jaramillo, P. Ruelle, P. Boivin, and M. Khaledian (2009), Temporal variability in soil hydraulic properties under drip irrigation, *Geoderma*, 150:158-165.

Munyankusi, E., S.C. Gupta, J.F. Moncrief, and E.C. Berry. (1994), Earthworm macropores and preferential transport in a long-term manure applied Typic Hapludalf, *Journal of Environmental Quality* 23:773-784.

Murphy, B. W., T. B. Koen, B. A. Jones, and L. M. Huxedurp (1993), Temporal variation of hydraulic properties for some soils with fragile structure, *Australian Journal of Soil Research*, 31:179-197.

Neuman, S. P. (1990), Universal scaling of hydraulic conductivities and dispersivities in geologic media, *Water Resources Research*, *26*:1749-1758.

Nielsen, D.R., J.W. Biggar, and K.T. Erh. (1973), Spatial variability of field-measured soil-water properties, *Hilgardia* 42:215-259.

Nimmo, J. R. (2007), Simple predictions of maximum transport rate in unsaturated soil and rock, *Water Resources Research*, 43:W05426

Nuutinen, V., S. Poyhonen, E. Ketoja, and J. Pitkänen. (2001), Abundance of the earthworm *Lumbricus terrestris* in relation to subsurface drainage pattern on a sandy clay field, *European Journal of Soil Biology* 37:301-304.

Nuutinen, V., and K.R. Butt. (2003), Interaction of *Lumbricus terrestris* L. burrows with field subdrains, *Pedobiologia* 47:578-581.

Ophori, D. U. (1998), The significance of viscosity in density-dependent flow of groundwater, *Journal of Hydrology*, 204:261-270.

Ontario Geological Survey. (1986), Aggregate resources inventory of the Township of Zorra, Oxford County, Aggregate Resources Inventory Paper 61, p.35.

Parlange, J.Y. (1972), Theory of water movement in soils: 4. Two and three dimensional steady infiltration, *Soil Science* 113:96-101.

Perret, J., S.O. Prasher, A. Kantzas, and C. Langford. (1999), Three-dimensional quantification of macropore networks in undisturbed soil cores, *Soil Science Society of America Journal* 63:1530-1543.

Philip, J.R. (1968), Steady infiltration from buried point sources and spherical cavities, *Water Resources Research* 4:1039-1047.

Philip, J.R. (1985), Reply to "Comments on steady infiltration from spherical cavities", *Soil Science Society of America Journal* 49:788-789.

Pitkänen, J., and V. Nuutinen. (1997), Distribution and abundance of burrows formed by *Lumbricus terrestris* L and *Aporrectodea caliginosa* Sav. in the soil profile, *Soil Biology & Biochemistry* 29:463-467.

Prodanovic, P. and S. Simonovic. (2004), Generation of synthetic design storms for the Upper Thames River basin. CFCAS project report V: Assessment of Water Resources Risk and Vulnerability to Changing Climatic Conditions

Reynolds, W.D. (2008), Saturated hydraulic properties: laboratory methods. p1013-1024, In: M.R. Carter and E.G. Gregorich (Eds.). *Soil sampling and methods of analysis, 2nd Edition*. CRC Press, Boca Raton.

Reynolds, W.D. (2008), Unsaturated hydraulic properties: Field tension infiltrometer. p1107-1128, In: M.R. Carter and E.G. Gregorich (Eds.). *Soil sampling and methods of analysis*, *2nd Edition*. CRC Press, Boca Raton.

Reynolds, W.D., and D.E. Elrick. (1991), Determination of hydraulic conductivity using a tension infiltrometer, *Soil Science Society of America Journal* 55:633-639.

Reynolds, W.D., and W.D. Zebchuk. (1996), Use of contact material in tension infiltrometer measurements, *Soil Technology* 9:141-159.

Reynolds, W.D., D.E. Elrick, and E.G. Youngs. (2002), Single-ring and double- or concentric-ring infiltrometers. p.821-826, In: J.H. Dane and G.C. Topp. (Eds.), *Methods of Soil Analysis Part 4, Physical Methods*, Soil Science Society of America, Inc., Madison.

Reynolds, W.D., and G.C. Topp. (2008), Soil water analyses: principles and parameters. p. 913-937. In: M.R. Carter and E.G. Gregorich (Eds.). *Soil sampling and methods of analysis, 2nd Edition*. CRC Press, Boca Raton.

Richard, T. L., and T. S. Steenhuis (1988), Tile drain sampling of preferential flow on a field scale, *Journal of Contaminant Hydrology*, 3:307-325.

Ringrose-Voase, A.J. (1996), Measurement of soil macropore geometry by image analysis of sections through impregnated soil, *Plant and Soil* 183:27-47.

Rosenbom, A. E., R. Therrien, J. C. Refsgaard, K. H. Jensen, V. Ernstsen, and K. E. S. Klint (2009), Numerical analysis of water and solute transport in variably-saturated fractured clayey till, *Journal of Contaminant Hydrology*, 104:137-152.

Royer, T. V., M. B. David, and L. E. Gentry (2006), Timing of riverine export of nitrate and phosphorus from agricultural watersheds in Illinois: Implications for reducing nutrient loading to the Mississippi River, *Environmental Science & Technology*, 40:4126-4131.

Rudolph, D., and G. Parkin. (1998), Partitioning of solutes from agricultural fields within the hydrologic system at two sites in Southern Ontario and the subsequent impact on adjacent aquatic ecosystems. COESA Report No.: RES/MON-010/97.

Russo, D., and E. Bresler. (1981), Soil hydraulic properties as stochastic processes: 1. An analysis of field spatial variability, *Soil Science Society of America Journal* 45:682-687.

Sado, E.V., and U.J. Vagners. (1975), Quaternary geology of the Lucan area, Southern Ontario. Ontario Division of Mines, Preliminary map, P. 1048 Geological Series, scale 1:50000.

Scanlon, B. R., I. Jolly, M. Sophocleous, and L. Zhang (2007), Global impacts of conversions from natural to agricultural ecosystems on water resources: Quantity versus quality, *Water Resources Research*, 43:W03437

Schaap, M. G., F. J. Leij, and M. T. van Genuchten (2001), ROSETTA: a computer program for estimating soil hydraulic parameters with hierarchical pedotransfer functions, *Journal of Hydrology*, 251:163-176.

Schwartz, R. C., A. S. R. Juo, and K. J. McInnes (2000), Estimating parameters for a dual-porosity model to describe non-equilibrium, reactive transport in a fine-textured soil, *Journal of Hydrology*, 229:149-167.

Shiel, R.S., M.A. Adey, and M. Lodder. (1988), The effect of successive wet/dry cycles on aggregate size distribution in a clay texture soil, *Journal of Soil Science* 39:71-80.

Shipitalo, M.J., and F. Gibbs. (2000), Potential of earthworm burrows to transmit injected animal wastes to tile drains, *Soil Science Society of America Journal* 64:2103-2109.

Shipitalo, M.J., V. Nuutinen, and K.R. Butt. (2004), Interaction of earthworm burrows and cracks in a clayey, subsurface-drained, soil, *Applied Soil Ecology* 26:209-217.

Simunek, J., N.J. Jarvis, M.T. van Genuchten, and A. Gärdenäs. (2003), Review and comparison of models for describing non-equilibrium and preferential flow and transport in the vadose zone, *Journal of Hydrology* 272:14-35.

Simunek, J., M. Sejna, and M. T. van Genuchten (2006), The HYDRUS Software package for simulating two- and three-dimensional movement of water, heat, and multiple solutes in variably-saturated media, User manual, Version 1.0 edited, p. 173, PC Progress, Prague, Czech Republic.

Skaggs, R. W., M. A. Breve, and J. W. Gilliam (1994), Hydrologic and water quality impacts of agricultural drainage, *Critical Reviews in Environmental Science and Technology*, 24:1-32.

Sollins, P., and R. Radulovich. (1988), Effects of soil physical structure on solute transport in a weathered tropical soil, *Soil Science Society of America Journal* 52:1168-1173.

Stamm, C., R. Sermet, J. Leuenberger, H. Wunderli, H. Wydler, H. Fluhler, and M. Gehre (2002), Multiple tracing of fast solute transport in a drained grassland soil, *Geoderma*, 109:245-268.

Starr, J.L. (1990), Spatial and temporal variation of ponded infiltration, *Soil Science Society of America Journal* 54:629-636.

Steenhuis, T. S., T. L. Richard, M. B. Parlange, S. O. Aburime, L. D. Geohring, and J. Y. Parlange (1988), Preferential flow influences on drainage of shallow sloping soils, *Agricultural Water Management*, 14:137-151.

Stewart, J.B., C.J. Moran, and J.T. Wood. (1999), Macropore sheath: quantification of plant root and soil macropore association, *Plant and Soil* 211:59-67.

Sudicky, E. A., J. A. Cherry, and E. O. Frind (1983), Migration of contaminants in groundwater at a landfill: A case study. 4. A natural-gradient dispersion test, *Journal of Hydrology*, 63: 81-108.

Therrien, R., R. G. McLaren, E. A. Sudicky, and S. M. Panday (2009), Hydrogeosphere: A three-dimensional numerical model describing fully-integrated subsurface and surface flow and solute transport. Groundwater Simulations Group.

Thomas, G. W., and R. E. Phillips (1979), Consequences of water movement in macropores, *Journal of Environmental Quality*, 8:149-152.

Thompson, M.L., P. Singh, S. Corak, and W.E. Straszheim. (1992), Cautionary notes for the automated-analysis of soil pore-space images, *Geoderma* 53:399-415.

Tomer, M. D., D. W. Meek, D. B. Jaynes, and J. L. Hatfield (2003), Evaluation of nitrate nitrogen fluxes from a tile-drained watershed in central Iowa, *Journal of Environmental Quality*, 32:642-653.

Trojan, M.D., and D.R. Linden. (1998), Macroporosity and hydraulic properties of earthworm-affected soils as influenced by tillage and residue management, *Soil Science Society of America Journal* 62:1687-1692.

Turpin, K. M., D. R. Lapen, E. Topp, M. J. L. Robin, M. Edwards, W. E. Curnoe, B. B. Coelho, N. B. McLaughlin, and M. Payne (2007a), Tine-influenced infiltration patterns and informing timing of liquid amendment applications using brilliant blue dye tracers, *Biosystems Engineering*, 98:235-247.

Turpin, K. M., D. R. Lapen, M. J. L. Robin, E. Topp, M. Edwards, W. E. Curnoe, G. C. Topp, N. B. McLaughlin, B. B. Coelho, and M. Payne (2007b), Slurry-application implement tine modification of soil hydraulic properties under different soil water content conditions for silt-clay loam soils, *Soil & Tillage Research*, 95:120-132.

Udawatta, R. P., P. P. Motavalli, H. E. Garrett, and J. J. Krstansky (2006), Nitrogen losses in runoff from three adjacent agricultural watersheds with claypan soils, *Agriculture Ecosystems & Environment*, 117:39-48.

van de Graaff, R.H.M. (1979), Size of subsoil blocky peds in relation to textural parameters, depth and drainage. In: Emerson, W.W., Bond, R.D., Dexter, A.R. (Eds.), *Modification of Soil Structure*. John Wiley & Sons, New York, pp. 87-96.

van Es, H. M. (1993), Evaluation of temporal, spatial, and tillage-induced variability for parameterization of soil infiltration, *Geoderma*, 60:187-199.

van Es, H. M., C. B. Ogden, R. L. Hill, R. R. Schindelbeck, and T. Tsegaye (1999), Integrated assessment of space, time, and management-related variability of soil hydraulic properties, *Soil Science Society of America Journal*, 63:1599-1608.

van Genuchten, M. T. (1980), A closed-form equation for predicting the hydraulic conductivity of unsaturated soils, *Soil Science Society of America Journal*, 44:892-898.

Vieira, S.R., D.R. Nielsen, and J.W. Biggar. (1981), Spatial variability of field-measured infiltration rate, *Soil Science Society of America Journal* 45:1040-1048.

Villholth, K.G., K.H. Jensen, and J. Fredericia. (1998), Flow and transport processes in a macroporous subsurface-drained glacial till soil - I: Field investigations, *Journal of Hydrology* 207:98-120.

Villholth, K. G., N. J. Jarvis, O. H. Jacobsen, and H. de Jonge (2000), Field investigations and modeling of particle-facilitated pesticide transport in macroporous soil, *Journal of Environmental Quality*, 29:1298-1309.

Vogel, T., H.H. Gerke, R. Zhang, and M.T. Van Genuchten. (2000), Modeling flow and transport in a two-dimensional dual-permeability system with spatially variable hydraulic properties, *Journal of Hydrology* 238:78-89.

Walkley, A. and I.A. Black. 1934. An examination of the Degtjareff method for determining organic carbon in soils: Effect of variations in digestion conditions and of inorganic soil constituents, *Soil Science* 63:251-263.

Watson, K.W., and R.J. Luxmoore. (1986), Estimating macroporosity in a forest watershed by use of a tension infiltrometer, *Soil Science Society of America Journal* 50:578-58.

Weiler, M., and F. Naef. (2003), An experimental tracer study of the role of macropores in infiltration in grassland soils, *Hydrological Processes* 17:477-493.

White, I., and M.J. Sully. (1987). Macroscopic and microscopic capillary length and time scales from field infiltration, *Water Resources Research* 23:1514-1522

Yeh, T.C.J., L.W. Gelhar, and A.L. Gutjahr. (1985), Stochastic analysis of unsaturated flow in heterogeneous soils. 2. Statistically anisotropic media with variable alpha, *Water Resources Research* 21:457-464.

Zehe, E., and H. Fluhler (2001), Preferential transport of isoproturon at a plot scale and a field scale tile-drained site, *Journal of Hydrology*, 247:100-115.

Zhou, X., H. S. Lin, and E. A. White (2008), Surface soil hydraulic properties in four soil series under different land uses and their temporal changes, *Catena*, 73:180-188.

Appendix A

Kintore soil data

Table A.1. Physical properties of topsoil.

Sample Name	Bulk Density	Organic Matter	Gravel	Sand	Very Fine Sand	Fine Sand	Medium Sand	Coarse Sand	Very Coarse Sand	Silt	Clay	Texture
	g/cm3	% dry					%					
P1-1A	1.21	6.4	5.3	51.2	12.8	19.1	11.7	4.6	3.1	34.3	14.6	Loam
P1-2A	1.22	6.2	5.7	53.9	13.2	20.6	12.8	4.9	2.3	31.6	14.5	Fine sandy loam
P1-3A	1.18	6.3	7.2	52.0	13.4	20.5	11.8	3.9	2.4	33.5	14.4	Fine sandy loam
P1-1B	1.25	5.8	6.1	54.1	12.9	19.7	13.1	5.3	3.2	33.0	12.9	Fine sandy loam
P1-2B	1.13	6.2	7.7	55.2	14.1	20.3	14.2	5.2	1.5	30.1	14.6	Fine sandy loam
P1-3B	1.25	6.6	9.8	54.0	13.0	20.1	12.7	5.6	2.7	32.5	13.4	Fine sandy loam
P2-1A	1.44	3.2	4.1	46.1	14.8	19.7	7.9	2.5	1.4	37.7	16.3	Loam
P2-2A	1.37	3.3	4.1	48.3	15.6	20.7	8.3	2.5	1.3	36.4	15.3	Loam
P2-3A	1.33	3.2	2.6	48.5	16.3	19.9	8.2	2.6	1.5	36.8	14.7	Loam
P2-1B	1.42	3.3	1.4	49.5	16.4	21.2	8.3	2.5	1.1	36.8	13.7	Loam
P2-2B	1.52	3.0	2.9	49.5	16.3	20.7	8.7	2.6	1.4	36.5	14.0	Loam
P2-3B	1.54	3.0	2.8	51.2	16.8	22.1	8.6	2.8	0.8	34.8	14.0	Loam
P3-1A	1.12	5.3	1.1	31.7	10.9	9.5	6.8	2.9	1.7	47.9	20.4	Loam
P3-2A	1.11	5.4	3.8	29.5	9.4	9.6	6.0	2.5	1.8	50.6	19.8	Silt loam
P3-3A	1.14	5.0	2.2	31.9	10.2	10.9	7.0	2.6	1.2	48.8	19.3	Loam
P3-1B	1.18	5.3	8.1	29.2	10.2	9.4	5.9	2.3	1.4	49.0	21.8	Loam
P3-2B	1.03	5.4	0.8	29.8	10.1	9.6	6.6	2.6	0.8	49.1	21.1	Loam
P3-3B	1.07	5.1	3.6	30.8	11.1	10.3	5.6	2.2	1.2	47.1	22.1	Loam

Notes

Sample analysis performed by University of Guelph - Agriculture and Food Laboratory

Sample name: P1-2A denotes plot 1, position 2 along sample row A; where row A is above tile drain

Table A.2. Physical properties of B horizon

Sample Name	Bulk Density	Gravel	Sand	Very Fine Sand	Fine Sand	Medium Sand	Coarse Sand	Very Coarse Sand	Silt	Clay	Texture
	g/cm3					%					
P1-1-85	1.92	8.6	30.1	9.5	10.1	5.7	3.5	1.3	53	16.8	Silt loam
P1-2-100	1.97	5.1	26.6	8.7	8	4.9	3	1.7	56.6	16.8	Silt loam
P1-3-50	1.94	12.8	35.1	11.3	11.8	6.3	3.7	1.7	49.2	15.7	Loam
P1-3-50	1.74	9.9	33.9	10.5	10.8	5.9	3.5	2.9	51.8	14.3	Silt loam
P2-1-50	1.71	0.9	56.5	31.3	20.5	2.7	1	0.6	39.4	4.1	VF sandy loam
P2-2-100	2.09	5.6	49.6	18.5	16.9	6.9	4.2	2.6	43.8	6.6	Sandy loam
P2-3-100	2.03	6.2	52.7	20.7	19.8	6.6	3.2	1.8	41.5	5.8	VF sandy loam
P2-4-70	1.91	3.5	49.7	19.6	17.2	6.4	3.1	2.8	42	8.3	Loam
P2-5-40	1.76	1.6	64.6	24.6	30.6	5.9	1.7	1.2	31.6	3.7	F sandy loam
P2-6-75	2.03	9.3	51.7	18.9	18	7.3	3.9	3	42	6.2	Sandy loam
P3-1-40	1.7	0	38.2	11.4	15.8	9	1.6	0.3	45.6	16.2	Loam
P3-2-50	1.49	3.7	38.1	12.4	12.9	8.5	2.5	1.4	42.5	19.4	Loam
P3-3-50	1.75	6.5	48.4	14.7	16.8	11	3.9	1.5	42.5	9.1	Loam
P3-4-80	1.52	9.1	69.3	8.3	20.5	22.1	12.1	5.9	23.7	7	Sandy loam
P3-5-80	1.83	33.6	94	2.4	11.7	34.6	30.2	14.6	4.4	1.6	Sand
P3-6-50	1.71	11.4	56.7	16.7	19.2	12	5	3.3	34.3	9.1	F sandy loam

Notes

Sample analysis performed by University of Guelph - Agriculture and Food Laboratory

Sample name: P1-2-100 denotes plot 1, sample 2, with a maximum sample depth of 100 cm

Appendix B

Kintore infiltration test data

Table B.1. Infiltration test and soil water content data, plot 1, August 2009.

X	Y	α (cm^{-1})					K - TI (cm d^{-1})					K - Dual Ring (cm d^{-1})	Initial Water Content	Final Water Content
		Applied Tension Interval (cm)					Applied Tension (cm)							
(m)	(m)	15-10	10-5	5-2	2-1	1-0	10	5	2	1	0			
0	0	0.06	0.08	0.45	1.15	0.73	1.82	4.56	25.18	83.38	167.53	46.76	0.31	0.43
1.93	0.05	0.04	0.15	0.66	0.72	1.16	3.00	11.73	102.33	219.26	716.74	114.51	0.29	0.44
3.7	0	0.02	0.13	0.43	0.74	0.43	3.83	14.05	64.53	135.58	198.15	152.06	0.28	0.44
5.3	0.1	0.07	0.15	0.75	0.23	0.30	4.05	13.67	139.62	157.50	221.22	146.54	0.21	0.43
0.25	1	0.03	0.14	0.43	1.08	0.38	1.80	6.73	31.48	90.96	120.79	24.94	0.3	0.44
2.15	1	0.03	0.11	0.70	0.94	0.47	1.66	5.99	65.32	160.93	243.83	93.99	0.29	0.45
3.5	0.91	0.06	0.14	0.59	0.59	0.58	4.13	13.11	93.22	168.12	300.53	103.66	0.25	0.45
5.25	1.06	0.08	0.14	0.80	0.96	0.66	1.77	5.41	76.29	196.30	368.53	122.25	0.31	0.45
0.25	3.14	0.08	0.14	0.43	1.07	0.93	1.77	5.05	23.89	74.02	187.10	23.65	0.31	0.45
2.1	3.35	0.06	0.14	0.44	1.11	0.90	2.16	6.75	32.71	105.23	255.94	94.79	0.31	0.43
3.6	3.34	0.04	0.10	0.48	1.62	-	2.60	8.04	47.02	517.10	636.33	88.88	0.3	0.44
5.35	3.2	0.06	0.16	0.66	0.75	0.99	2.26	8.20	72.90	158.94	435.26	98.67	0.37	0.45

Notes

Tile drain axis is Y = 0

\- denotes a value less than 0 was obtained and was therefore not used for subsequent analysis per Reynolds (2008)

Table B.2. Infiltration test and soil water content data, plot 1, September 2009.

X	Y	α (cm^{-1})					K - TI (cm d^{-1})					K - Dual Ring (cm d^{-1})	Initial Water Content	Final Water Content
		Applied Tension Interval (cm)					Applied Tension (cm)							
(m)	(m)	15-10	10-5	5-2	2-1	1-0	10	5	2	1	0			
0	0.1	0.04	0.08	0.26	1.27	1.60	2.10	5.18	17.02	70.64	353.52	95.35	0.16	0.44
1.9	0.05	0.03	0.09	0.32	1.34	1.17	1.90	5.56	20.69	88.20	282.33	171.26	0.22	0.44
4.4	0.1	0.04	0.07	0.25	1.29	0.84	1.96	4.60	15.41	63.20	142.64	258.48	0.21	0.43
0.25	1	0.02	0.09	0.34	1.00	1.06	1.65	5.18	20.53	61.51	177.52	134.61	0.22	0.44
2.45	1.3	0.00	0.07	0.29	0.81	2.52	1.68	7.10	25.38	66.32	867.58	147.26	0.2	0.42
4.65	1.1	0.04	0.05	0.18	0.52	1.18	1.79	3.68	9.90	20.58	71.26	249.46	0.25	0.44
0.2	3.35	0.03	0.07	0.23	0.45	1.19	2.52	6.52	18.57	34.59	121.96	50.88	0.2	0.43
2.35	3.75	0.03	0.09	0.25	1.81	1.89	1.39	3.84	11.94	86.08	572.91	193.46	0.28	0.4
4.3	3.4	0.01	0.07	0.29	0.82	1.90	2.16	7.10	25.40	66.40	460.06	90.94	0.13	0.43

Notes

Tile drain axis is Y = 0

Table B.3. Infiltration test and soil water content data, plot 2, August 2009.

X	Y	α (cm^{-1})					K - TI (cm d^{-1})					K - Dual Ring (cm d^{-1})	Initial Water Content	Final Water Content
		Applied Tension Interval (cm)					Applied Tension (cm)							
(m)	(m)	15-10	10-5	5-2	2-1	1-0	10	5	2	1	0			
0	0	0.02	0.07	0.46	0.37	0.45	1.26	4.37	23.34	33.76	54.42	2.22	0.23	0.36
2.54	0.18	0.00	0.11	0.20	0.27	0.64	1.82	7.34	15.96	24.71	51.67	9.34	0.21	0.35
3.72	0	0.00	0.18	0.57	0.35	2.03	1.88	10.91	66.74	102.71	874.75	21.78	0.19	0.35
5.8	-0.3	0.00	0.13	0.34	0.56	1.92	1.80	8.41	29.14	58.33	427.12	122.42	0.21	0.34
-0.18	1.14	-	0.14	0.34	0.64	0.32	0.20	4.07	14.26	26.79	34.30	19.80	0.26	0.36
2.52	1.41	-	0.14	0.05	0.24	0.07	-	2.49	3.42	4.58	3.42	40.64	0.24	0.3
3.3	1.54	0.11	0.05	0.47	0.41	1.73	3.41	6.26	36.82	60.76	378.32	12.30	0.21	0.34
5.89	1.43	-	0.07	0.34	0.79	0.79	11.08	3.54	14.52	34.81	76.30	12.25	0.23	0.34
0.72	3.65	0.02	0.11	0.28	0.11	0.57	2.47	8.70	20.08	24.80	56.45	4.85	0.21	0.34
2.69	3.66	0.06	0.11	0.32	0.34	0.55	2.02	5.40	17.41	26.07	47.60	2.15	0.23	0.35
4.22	3.62	0.03	0.11	0.36	0.29	0.99	2.97	9.33	32.59	48.01	144.37	20.94	0.23	0.37
6	3.41	0.04	0.08	0.31	0.46	0.66	2.10	5.35	18.45	31.67	63.37	35.03	0.21	0.32

Notes

Tile drain axis is Y = 0

- denotes a value less than 0 was obtained and was therefore not used for subsequent analysis per Reynolds (2008)

Table B.4. Infiltration test and soil water content data, plot 2, September 2009.

X	Y	α (cm^{-1})					K - TI (cm d^{-1})					K - Dual Ring (cm d^{-1})	Initial Water Content	Final Water Content
		Applied Tension Interval (cm)					Applied Tension (cm)							
(m)	(m)	15-10	10-5	5-2	2-1	1-0	10	5	2	1	0			
0	0.1	0.07	0.05	0.19	0.99	1.19	2.11	3.76	11.13	36.18	120.04	50.18	0.15	0.36
1.7	-0.05	0.04	0.08	0.56	1.09	0.94	2.10	5.88	45.18	140.14	353.94	36.05	0.13	0.42
4.35	-0.05	-	0.08	0.30	0.90	2.03	0.69	5.33	19.04	54.13	425.63	41.63	0.19	0.34
0.1	1.05	-	0.05	0.07	1.32	2.78	0.04	1.83	4.50	24.98	413.08	31.66	0.18	0.35
2.05	1.5	0.04	0.07	0.21	0.59	1.09	1.96	4.39	12.20	26.33	81.77	25.45	0.11	0.38
4.1	1.55	0.00	0.07	0.30	0.85	2.73	1.63	6.89	25.07	68.15	1091.00	49.79	0.12	0.41
0	3.4	0.03	0.06	0.25	0.67	0.91	2.36	6.08	19.55	43.65	110.34	17.53	0.15	0.36
2.45	3.1	0.00	0.05	0.28	0.90	0.92	0.98	4.36	16.27	45.20	113.40	16.67	0.2	0.35
4.4	2.9	0.00	0.07	0.36	0.69	1.07	1.38	6.04	25.79	56.69	170.53	16.05	0.18	0.35

Notes

Tile drain axis is Y = 0

- denotes a value less than 0 was obtained and was therefore not used for subsequent analysis per Reynolds (2008)

Table B.5. Infiltration test and soil water content data, plot 3, August 2008.

X	Y	α (cm^{-1}) Applied Tension Interval (cm)					K - TI (cm d^{-1}) Applied Tension (cm)					K - Dual Ring (cm d^{-1})	Initial Water Content	Final Water Content
(m)	(m)	15-10	10-5	5-2	2-1	1-0	10	5	2	1	0			
0	0.05	-	0.13	0.29	0.58	3.16	1.28	6.62	20.25	42.38	1075.32	16.56	0.3	0.41
2.3	0.22	0.00	0.10	0.25	0.41	1.34	1.16	4.79	12.95	22.92	95.93	224.88	0.26	0.4
4.55	0.35	-	0.14	0.51	0.81	0.85	1.67	9.54	54.96	128.86	301.70	405.21	0.24	0.41
7.05	0.2	-	0.09	0.42	0.87	1.99	1.01	6.21	30.28	79.56	602.96	312.80	0.23	0.39
0.3	1.18	0.00	0.10	0.31	0.89	1.14	1.63	7.01	24.41	66.74	212.70	450.05	0.19	0.4
2.15	1.46	0.04	0.12	0.52	1.13	1.39	2.09	6.74	42.43	139.67	567.77	335.70	0.2	0.43
3.95	1.3	-	0.14	0.44	0.96	0.54	1.23	8.05	38.18	102.31	168.56	208.61	0.26	0.4
6.1	1.2	0.03	0.14	0.18	1.44	0.60	2.17	6.71	15.68	76.55	131.65	163.34	0.27	0.41
0.8	3.3	0.05	0.14	0.52	0.63	1.09	2.90	9.77	57.55	114.15	351.24	1153.73	0.21	0.41
2.3	3.4	0.05	0.13	0.45	1.35	0.50	3.87	12.06	61.02	236.94	363.38	347.96	0.23	0.41
4.3	3.38	-	0.09	0.33	0.93	0.92	1.16	6.88	26.46	73.75	184.70	122.08	0.19	0.4
6.1	3.3	0.01	0.11	0.33	1.40	1.29	2.39	8.82	33.07	149.77	544.88	549.64	0.17	0.39

Notes
Tile drain axis is Y = 0
- denotes a value less than 0 was obtained and was therefore not used for subsequent analysis per Reynolds (2008)

Table B.6. Infiltration test and soil water content data, plot 1, November 2008.

X	Y	α (cm^{-1}) Applied Tension Interval (cm)				K - TI (cm d^{-1}) Applied Tension (cm)				K - Dual Ring (cm d^{-1})	Initial Water Content	Final Water Content
(m)	(m)	10-5	5-2	2-1	1-0	5	2	1	0			
0	0	0.15	0.26	0.44	1.44	3.96	10.37	18.76	86.32	84.12	0.36	0.42
4.5	0	0.09	0.54	0.69	1.11	6.42	43.09	90.87	284.80	273.33	0.32	0.43
9	0	0.16	0.29	0.90	1.75	4.46	13.29	37.75	225.06	47.63	0.34	0.42
0	2	0.14	0.29	0.77	3.49	2.64	8.10	20.62	717.80	11.62	0.36	0.42
4.5	2	0.09	0.31	0.57	2.96	3.92	13.24	27.43	569.31	2.06	0.37	0.43
9	2	0.11	0.40	0.67	1.88	1.86	7.98	17.38	119.75	16.51	0.33	0.43

Notes
Tile drain axis is Y = 0

Table B.7. Infiltration test and soil water content data statistical analysis, plot 1, August 2009.

Parameter	Row	α (cm^{-1}) Applied Tension Interval (cm)					K - TI ($cm\ d^{-1}$) Applied Tension (cm)					K - Dual Ring ($cm\ d^{-1}$)	Initial Water Content	Final Water Content
		15-10	10-5	5-2	2-1	1-0	10	5	2	1	0			
Arithmetic Mean	1	0.05	0.13	0.57	0.71	0.65	3.18	11.00	82.91	148.93	325.91	114.97	0.27	0.44
	2	0.05	0.13	0.63	0.89	0.52	2.34	7.81	66.58	154.08	258.42	86.21	0.29	0.45
	3	0.06	0.14	0.50	1.14	0.94	2.20	7.01	44.13	213.82	378.66	76.50	0.32	0.44
Maximum	1	0.07	0.15	0.75	1.15	1.16	4.05	14.05	139.62	219.26	716.74	152.06	0.31	0.44
	2	0.08	0.14	0.80	1.08	0.66	4.13	13.11	93.22	196.30	368.53	122.25	0.31	0.45
	3	0.08	0.16	0.66	1.62	0.99	2.60	8.20	72.90	517.10	636.33	98.67	0.37	0.45
Minimum	1	0.02	0.08	0.43	0.23	0.30	1.82	4.56	25.18	83.38	167.53	46.76	0.21	0.43
	2	0.03	0.11	0.43	0.59	0.38	1.66	5.41	31.48	90.96	120.79	24.94	0.25	0.44
	3	0.04	0.10	0.43	0.75	0.90	1.77	5.05	23.89	74.02	187.10	23.65	0.30	0.43
CV (%)	1	42.93	26.53	27.91	53.08	58.22	31.84	40.12	59.35	37.78	80.23	42.09	15.96	1.33
	2	55.04	10.12	25.58	23.49	23.45	50.97	45.77	39.14	29.05	40.62	49.30	9.15	1.12
	3	31.35	18.30	21.54	31.62	4.76	15.46	20.78	48.52	95.97	53.12	46.35	9.93	2.16
Std Dev	1	0.02	0.03	0.16	0.38	0.38	1.01	4.41	49.21	56.26	261.48	48.39	0.04	0.01
	2	0.03	0.01	0.16	0.21	0.12	1.19	3.58	26.06	44.76	104.97	42.50	0.03	0.01
	3	0.02	0.02	0.11	0.36	0.04	0.34	1.46	21.41	205.20	201.13	35.46	0.03	0.01
Shapiro-Wilks Statistic	1	0.95	0.86	0.88	0.95	0.94	0.91	0.80	0.99	0.99	0.71	0.86	0.87	0.73
	2	0.85	0.63	0.98	0.87	0.98	0.68	0.76	0.96	0.90	0.98	0.87	0.89	0.63
	3	0.94	0.92	0.77	0.94	0.98	0.98	0.89	0.95	0.78	0.94	0.73	0.75	0.86
Shapiro-Wilks P	1	0.52	0.49	0.66	0.58	0.68	0.97	0.21	0.05	0.07	0.03	0.52	0.62	0.05
	2	0.47	0.00	0.14	0.57	0.20	0.01	0.11	0.43	0.87	0.23	0.56	0.74	0.00
	3	0.65	0.89	0.12	0.68	0.51	0.14	0.74	0.63	0.14	0.64	0.05	0.08	0.54
Shapiro-Wilks H	1	FALSE	FALSE	FALSE	FALSE	FALSE	FALSE	FALSE	FALSE	FALSE	TRUE	FALSE	FALSE	TRUE
	2	FALSE	TRUE	FALSE	FALSE	FALSE	TRUE	FALSE	FALSE	FALSE	FALSE	FALSE	FALSE	TRUE
	3	FALSE	FALSE	FALSE	FALSE	FALSE	FALSE	FALSE	FALSE	FALSE	FALSE	FALSE	FALSE	FALSE
Rank-Sum P	1-2	0.83	0.89	0.69	0.69	0.89	0.34	0.49	0.89	0.69	0.89	0.34	0.66	0.09
	1-3	0.57	0.86	0.89	0.20	0.40	0.20	0.34	0.34	1.00	0.69	0.20	0.11	0.40
Rank-Sum H	1-2	FALSE	FALSE	FALSE	FALSE	FALSE	FALSE	FALSE	FALSE	FALSE	FALSE	FALSE	FALSE	FALSE
	1-3	FALSE	FALSE	FALSE	FALSE	FALSE	FALSE	FALSE	FALSE	FALSE	FALSE	FALSE	FALSE	FALSE

Notes

Row 1 is immediately over, and row 3 is furthest from, the tile drain

Table B.8. Infiltration test and soil water content data statistical analysis, plot 1, September 2009.

Parameter	Row	α (cm^{-1}) Applied Tension Interval (cm)					K - TI ($cm\ d^{-1}$) Applied Tension (cm)					K - Dual Ring ($cm\ d^{-1}$)	Initial Water Content	Final Water Content
		15-10	10-5	5-2	2-1	1-0	10	5	2	1	0			
Arithmetic Mean	1	0.04	0.08	0.28	1.30	1.20	1.99	5.11	17.70	74.01	259.49	175.03	0.20	0.44
	2	0.02	0.07	0.27	0.78	1.59	1.71	5.32	18.60	49.47	372.12	177.11	0.22	0.43
	3	0.03	0.08	0.26	1.03	1.66	2.02	5.82	18.63	62.36	384.97	111.76	0.20	0.42
Maximum	1	0.04	0.09	0.32	1.34	1.60	2.10	5.56	20.69	88.20	353.52	258.48	0.22	0.44
	2	0.04	0.09	0.34	1.00	2.52	1.79	7.10	25.38	66.32	867.58	249.46	0.25	0.44
	3	0.03	0.09	0.29	1.81	1.90	2.52	7.10	25.40	86.08	572.91	193.46	0.28	0.43
Minimum	1	0.03	0.07	0.25	1.27	0.84	1.90	4.60	15.41	63.20	142.64	95.35	0.16	0.43
	2	0.00	0.05	0.18	0.52	1.06	1.65	3.68	9.90	20.58	71.26	134.61	0.20	0.42
	3	0.01	0.07	0.23	0.45	1.19	1.39	3.84	11.94	34.59	121.96	50.88	0.13	0.40
CV (%)	1	18.48	16.53	12.55	2.65	31.80	5.29	9.37	15.28	17.34	41.34	46.64	16.35	1.32
	2	98.23	26.00	31.62	31.15	51.14	4.17	32.24	42.55	50.81	116.19	35.56	11.27	2.66
	3	39.09	16.16	11.83	68.50	24.54	28.59	29.89	36.11	41.67	60.96	65.80	36.91	4.12
Std Dev	1	0.01	0.01	0.03	0.03	0.38	0.11	0.48	2.71	12.84	107.28	81.63	0.03	0.01
	2	0.02	0.02	0.08	0.24	0.81	0.07	1.72	7.91	25.13	432.35	62.98	0.03	0.01
	3	0.01	0.01	0.03	0.70	0.41	0.58	1.74	6.73	25.98	234.66	73.53	0.08	0.02
Shapiro-Wilks Statistic	1	0.75	1.00	0.85	0.92	0.99	0.96	0.99	0.95	0.95	0.97	1.00	0.87	0.75
	2	1.00	0.99	0.96	0.99	0.81	0.91	1.00	0.96	0.83	0.85	0.83	0.99	0.75
	3	0.75	0.88	0.93	0.93	0.75	0.96	0.88	1.00	0.98	0.92	0.94	1.00	0.75
Shapiro-Wilks P	1	0.00	0.07	0.48	0.89	0.29	0.81	0.47	0.85	0.88	0.71	0.15	0.60	0.00
	2	0.12	0.38	0.80	0.43	0.30	0.83	0.27	0.81	0.37	0.47	0.38	0.44	0.00
	3	0.00	0.63	0.95	0.99	0.01	0.80	0.64	0.03	0.52	0.93	0.95	0.15	0.00
Shapiro-Wilks H	1	TRUE	FALSE	FALSE	FALSE	FALSE	FALSE	FALSE	FALSE	FALSE	FALSE	FALSE	FALSE	TRUE
	2	FALSE	FALSE	FALSE	FALSE	FALSE	FALSE	FALSE	FALSE	FALSE	FALSE	FALSE	FALSE	TRUE
	3	TRUE	FALSE	FALSE	FALSE	TRUE	FALSE	FALSE	TRUE	FALSE	FALSE	FALSE	FALSE	TRUE
Rank-Sum P	1-2	0.40	0.50	1.00	0.10	0.70	0.10	1.00	1.00	0.20	1.00	1.00	0.50	1.00
	1-3	0.10	0.80	0.40	0.70	0.20	0.70	0.70	1.00	0.70	0.70	0.40	1.00	0.30
Rank-Sum H	1-2	FALSE	FALSE	FALSE	FALSE	FALSE	FALSE	FALSE	FALSE	FALSE	FALSE	FALSE	FALSE	FALSE
	1-3	FALSE	FALSE	FALSE	FALSE	FALSE	FALSE	FALSE	FALSE	FALSE	FALSE	FALSE	FALSE	FALSE

Notes

Row 1 is immediately over, and row 3 is furthest from, the tile drain

Table B.9. Infiltration test and soil water content data statistical analysis, plot 2, August 2009.

Parameter	Row	α (cm^{-1})					K - TI (cm d^{-1})					K - Dual Ring (cm d^{-1})	Initial Water Content	Final Water Content
		Applied Tension Interval (cm)					Applied Tension (cm)							
		15-10	10-5	5-2	2-1	1-0	10	5	2	1	0			
Arithmetic Mean	1	0.00	0.12	0.39	0.39	1.26	1.69	7.76	33.80	54.88	351.99	38.94	0.21	0.35
	2	0.11	0.10	0.30	0.52	0.73	4.90	4.09	17.25	31.74	123.09	21.25	0.24	0.34
	3	0.04	0.10	0.32	0.30	0.69	2.39	7.20	22.13	32.64	77.95	15.74	0.22	0.35
Maximum	1	0.02	0.18	0.57	0.56	2.03	1.88	10.91	66.74	102.71	874.75	122.42	0.23	0.36
	2	0.11	0.14	0.47	0.79	1.73	11.08	6.26	36.82	60.76	378.32	40.64	0.26	0.36
	3	0.06	0.11	0.36	0.46	0.99	2.97	9.33	32.59	48.01	144.37	35.03	0.23	0.37
Minimum	1	0.00	0.07	0.20	0.27	0.45	1.26	4.37	15.96	24.71	51.67	2.22	0.19	0.34
	2	0.11	0.05	0.05	0.24	0.07	0.20	2.49	3.42	4.58	3.42	12.25	0.21	0.30
	3	0.02	0.08	0.28	0.11	0.55	2.02	5.35	17.41	24.80	47.60	2.15	0.21	0.32
CV (%)	1	200.00	37.78	40.72	31.56	65.69	16.99	34.89	66.91	63.61	110.96	144.43	7.78	2.33
	2	-	45.88	57.88	46.93	100.64	114.13	38.82	81.35	73.09	140.36	63.08	8.86	7.51
	3	47.98	14.77	9.46	49.17	29.29	18.03	29.42	31.89	32.70	57.41	97.23	5.25	6.03
Std Dev	1	0.01	0.05	0.16	0.12	0.83	0.29	2.71	22.61	34.91	390.58	56.24	0.02	0.01
	2	-	0.05	0.17	0.24	0.73	5.59	1.59	14.04	23.19	172.76	13.40	0.02	0.03
	3	0.02	0.02	0.03	0.15	0.20	0.43	2.12	7.06	10.67	44.75	15.30	0.01	0.02
Shapiro-Wilks Statistic	1	0.63	0.99	0.99	0.90	0.81	0.74	0.99	0.84	0.91	0.86	0.76	0.94	0.94
	2	-	0.82	0.87	0.98	0.92	0.95	0.95	0.90	0.99	0.78	0.80	1.00	0.89
	3	0.99	0.78	0.99	0.98	0.81	0.91	0.80	0.77	0.83	0.76	0.91	0.73	1.00
Shapiro-Wilks P	1	0.00	0.05	0.06	0.82	0.25	0.06	0.07	0.38	0.97	0.53	0.09	0.63	0.63
	2	-	0.30	0.63	0.24	0.87	0.89	0.60	0.82	0.10	0.15	0.20	0.01	0.81
	3	0.06	0.13	0.06	0.25	0.24	0.91	0.21	0.11	0.36	0.10	0.96	0.05	0.01
Shapiro-Wilks H	1	TRUE	FALSE	FALSE	FALSE	FALSE	FALSE	FALSE	FALSE	FALSE	FALSE	FALSE	FALSE	FALSE
	2	-	FALSE	FALSE	FALSE	FALSE	FALSE	FALSE	FALSE	FALSE	FALSE	FALSE	TRUE	FALSE
	3	FALSE	FALSE	FALSE	FALSE	FALSE	FALSE	FALSE	FALSE	FALSE	FALSE	FALSE	TRUE	TRUE
Rank-Sum P	1-2	-	0.83	0.86	0.49	0.34	0.63	0.06	0.20	0.69	0.34	0.89	0.20	0.43
	1-3	0.80	0.57	0.49	0.49	0.69	0.03	1.00	0.69	0.49	0.69	0.69	0.66	0.77
Rank-Sum H	1-2	-	FALSE	FALSE	FALSE	FALSE	FALSE	FALSE	FALSE	FALSE	FALSE	FALSE	FALSE	FALSE
	1-3	FALSE	FALSE	FALSE	FALSE	FALSE	TRUE	FALSE	FALSE	FALSE	FALSE	FALSE	FALSE	FALSE

Notes

Row 1 is immediately over, and row 3 is furthest from, the tile drain

- denotes insufficient data to calculate parameter due to removal of negative TI values

Table B.10. Infiltration test and soil water content data statistical analysis, plot 2, September 2009.

Parameter	Row	α (cm^{-1})					K - TI (cm d^{-1})					K - Dual Ring (cm d^{-1})	Initial Water Content	Final Water Content
		Applied Tension Interval (cm)					Applied Tension (cm)							
		15-10	10-5	5-2	2-1	1-0	10	5	2	1	0			
Arithmetic Mean	1	0.06	0.07	0.35	1.00	1.38	1.64	4.99	25.11	76.82	299.87	42.62	0.16	0.37
	2	0.04	0.06	0.19	0.92	2.20	1.21	4.37	13.93	39.82	528.62	35.64	0.14	0.38
	3	0.01	0.06	0.29	0.75	0.97	1.57	5.49	20.54	48.51	131.42	16.75	0.18	0.35
Maximum	1	0.07	0.08	0.56	1.09	2.03	2.11	5.88	45.18	140.14	425.63	50.18	0.19	0.42
	2	0.04	0.07	0.30	1.32	2.78	1.96	6.89	25.07	68.15	1091.00	49.79	0.18	0.41
	3	0.03	0.07	0.36	0.90	1.07	2.36	6.08	25.79	56.69	170.53	17.53	0.20	0.36
Minimum	1	0.04	0.05	0.19	0.90	0.94	0.69	3.76	11.13	36.18	120.04	36.05	0.13	0.34
	2	0.04	0.05	0.07	0.59	1.09	0.04	1.83	4.50	24.98	81.77	25.45	0.11	0.35
	3	0.00	0.05	0.25	0.67	0.91	0.98	4.36	16.27	43.65	110.34	16.05	0.15	0.35
CV (%)	1	32.58	23.09	54.40	9.59	41.27	49.86	22.00	70.96	72.34	53.29	16.71	19.50	11.15
	2	-	17.76	61.21	39.93	43.65	84.65	57.92	74.64	61.63	97.32	35.49	27.70	7.89
	3	173.21	18.08	19.72	17.15	9.64	45.09	17.84	23.56	14.68	25.80	4.43	14.24	1.63
Std Dev	1	0.05	0.02	0.19	0.10	0.57	0.82	1.10	17.82	55.57	159.81	7.12	0.03	0.04
	2	-	0.01	0.12	0.37	0.96	1.03	2.53	10.39	24.54	514.44	12.65	0.04	0.03
	3	0.02	0.01	0.06	0.13	0.09	0.71	0.98	4.84	7.12	33.90	0.74	0.03	0.01
Shapiro-Wilks Statistic	1	-	0.75	0.95	1.00	0.91	0.75	0.93	0.91	0.88	0.91	0.99	0.96	0.92
	2	-	0.89	0.99	0.97	0.77	0.88	1.00	0.98	0.77	0.96	0.93	0.85	1.00
	3	0.75	0.99	0.92	0.83	0.81	0.94	0.77	0.97	0.84	0.79	0.99	0.99	0.75
Shapiro-Wilks P	1	-	0.00	0.88	0.17	0.86	0.02	0.97	0.85	0.62	0.86	0.46	0.73	0.93
	2	-	0.69	0.45	0.63	0.11	0.62	0.02	0.55	0.10	0.75	0.95	0.51	0.00
	3	0.00	0.44	0.91	0.37	0.26	0.92	0.09	0.68	0.42	0.17	0.36	0.44	0.00
Shapiro-Wilks H	1	-	TRUE	FALSE	FALSE	FALSE	TRUE	FALSE	FALSE	FALSE	FALSE	FALSE	FALSE	FALSE
	2	-	FALSE	FALSE	FALSE	FALSE	FALSE	TRUE	FALSE	FALSE	FALSE	FALSE	FALSE	TRUE
	3	TRUE	FALSE	FALSE	FALSE	FALSE	FALSE	FALSE	FALSE	FALSE	FALSE	FALSE	FALSE	TRUE
Rank-Sum P	1-2	-	0.30	0.40	0.70	0.40	0.40	1.00	0.70	0.40	1.00	0.40	0.40	1.00
	1-3	-	0.30	1.00	0.20	0.20	1.00	0.40	1.00	1.00	0.20	0.10	0.50	0.90
Rank-Sum H	1-2	-	FALSE	FALSE	FALSE	FALSE	FALSE	FALSE	FALSE	FALSE	FALSE	FALSE	FALSE	FALSE
	1-3	-	FALSE	FALSE	FALSE	FALSE	FALSE	FALSE	FALSE	FALSE	FALSE	FALSE	FALSE	FALSE

Notes

Row 1 is immediately over, and row 3 is furthest from, the tile drain

- denotes insufficient data to calculate parameter due to removal of negative TI values

Table B.11. Infiltration test and soil water content data statistical analysis, plot 3, August 2008.

Parameter	Row	α (cm^{-1})					K - TI (cm d^{-1})					K - Dual Ring (cm d^{-1})	Initial Water Content	Final Water Content
		Applied Tension Interval (cm)					Applied Tension (cm)							
		15-10	10-5	5-2	2-1	1-0	10	5	2	1	0			
Arithmetic Mean	1	0.00	0.12	0.37	0.66	1.83	1.28	6.79	29.61	68.43	518.98	239.86	0.26	0.40
	2	0.02	0.13	0.36	1.10	0.92	1.78	7.13	30.18	96.32	270.17	289.43	0.23	0.41
	3	0.04	0.12	0.41	1.08	0.95	2.58	9.38	44.53	143.65	361.05	543.35	0.20	0.40
Maximum	1	0.00	0.14	0.51	0.87	3.16	1.67	9.54	54.96	128.86	1075.32	405.21	0.30	0.41
	2	0.04	0.14	0.52	1.44	1.39	2.17	8.05	42.43	139.67	567.77	450.05	0.27	0.43
	3	0.05	0.14	0.52	1.40	1.29	3.87	12.06	61.02	236.94	544.88	1153.73	0.23	0.41
Minimum	1	0.00	0.09	0.25	0.41	0.85	1.01	4.79	12.95	22.92	95.93	16.56	0.23	0.39
	2	0.00	0.10	0.18	0.89	0.54	1.23	6.71	15.68	66.74	131.65	163.34	0.19	0.40
	3	0.01	0.09	0.33	0.63	0.50	1.16	6.88	26.46	73.75	184.70	122.08	0.17	0.39
CV (%)	1	-	19.89	32.51	32.11	54.39	21.95	29.35	61.91	68.15	81.96	69.24	12.02	2.38
	2	89.59	15.01	41.37	21.97	45.22	24.48	8.83	40.94	33.80	74.45	44.77	17.75	3.45
	3	55.72	19.07	22.70	33.82	35.55	43.81	22.96	38.88	48.39	40.77	81.50	12.91	2.38
Std Dev	1	-	0.02	0.12	0.21	1.00	0.28	1.99	18.33	46.64	425.34	166.08	0.03	0.01
	2	0.02	0.02	0.15	0.24	0.42	0.44	0.63	12.35	32.56	201.15	129.57	0.04	0.01
	3	0.02	0.02	0.09	0.36	0.34	1.13	2.15	17.31	69.51	147.19	442.81	0.03	0.01
Shapiro-Wilks Statistic	1	-	0.94	0.94	0.92	0.96	0.94	0.93	0.93	0.96	0.96	0.96	0.92	0.86
	2	0.94	0.91	0.98	0.92	0.88	0.91	0.78	0.93	0.93	0.78	0.95	0.84	0.83
	3	0.81	0.97	0.87	0.90	0.97	0.99	0.99	0.86	0.96	0.96	0.94	0.99	0.86
Shapiro-Wilks P	1	-	0.70	0.64	0.89	0.43	0.74	0.80	0.87	0.49	0.40	0.45	0.92	0.54
	2	0.95	0.92	0.23	0.95	0.64	0.99	0.15	0.76	0.80	0.13	0.63	0.41	0.32
	3	0.28	0.30	0.56	0.87	0.36	0.06	0.04	0.53	0.42	0.46	0.72	0.06	0.54
Shapiro-Wilks H	1	-	FALSE	FALSE	FALSE	FALSE	FALSE	FALSE	FALSE	FALSE	FALSE	FALSE	FALSE	FALSE
	2	FALSE	FALSE	FALSE	FALSE	FALSE	FALSE	FALSE	FALSE	FALSE	FALSE	FALSE	FALSE	FALSE
	3	FALSE	FALSE	FALSE	FALSE	FALSE	FALSE	TRUE	FALSE	FALSE	FALSE	FALSE	FALSE	FALSE
Rank-Sum P	1-2	-	0.89	0.89	0.03	0.20	0.20	0.34	0.89	0.49	0.49	0.89	0.51	0.71
	1-3	-	1.00	0.49	0.11	0.20	0.11	0.11	0.20	0.20	0.89	0.34	0.06	1.00
Rank-Sum H	1-2	-	FALSE	FALSE	TRUE	FALSE	FALSE	FALSE	FALSE	FALSE	FALSE	FALSE	FALSE	FALSE
	1-3	-	FALSE	FALSE	FALSE	FALSE	FALSE	FALSE	FALSE	FALSE	FALSE	FALSE	FALSE	FALSE

Notes

Row 1 is immediately over, and row 3 is furthest from, the tile drain

- denotes insufficient data to calculate parameter due to removal of negative TI values

Table B.12. Infiltration test and soil water content data intra-plot comparison data, plot 1.

Parameter	Date	α (cm^{-1})					K - TI (cm d^{-1})					K - Dual Ring (cm d^{-1})	Initial Water Content	Final Water Content
		Applied Tension Interval (cm)					Applied Tension (cm)							
		15-10	10-5	5-2	2-1	1-0	10	5	2	1	0			
Arithmetic Mean	Aug	0.05	0.13	0.57	0.91	0.68	2.57	8.61	64.54	172.28	321.00	92.56	0.29	0.44
	Sep	0.03	0.08	0.27	1.03	1.48	1.91	5.42	18.31	61.95	338.86	154.63	0.21	0.43
Maximum	Aug	0.08	0.16	0.80	1.62	1.16	4.13	14.05	139.62	517.10	716.74	152.06	0.37	0.45
	Sep	0.04	0.09	0.34	1.81	2.52	2.52	7.10	25.40	88.20	867.58	258.48	0.28	0.44
Minimum	Aug	0.02	0.08	0.43	0.23	0.30	1.66	4.56	23.89	74.02	120.79	23.65	0.21	0.43
	Sep	0.00	0.05	0.18	0.45	0.84	1.39	3.68	9.90	20.58	71.26	50.88	0.13	0.40
CV (%)	Aug	40.32	17.64	24.98	37.82	41.09	36.90	41.27	54.70	68.29	58.55	45.39	13.00	1.89
	Sep	51.68	18.20	18.46	42.20	36.19	17.37	23.70	29.41	35.40	76.36	45.93	21.36	3.08
Std Dev	Aug	0.02	0.02	0.14	0.35	0.28	0.95	3.55	35.30	117.64	187.95	42.01	0.04	0.01
	Sep	0.02	0.01	0.05	0.44	0.54	0.33	1.28	5.39	21.93	258.75	71.02	0.04	0.01
Shapiro-Wilks Statistic	Aug	0.91	0.89	0.86	0.94	0.95	0.82	0.86	0.93	0.67	0.85	0.92	0.86	0.80
	Sep	0.89	0.93	0.98	0.95	0.91	0.99	0.92	0.95	0.89	0.90	0.96	0.97	0.77
Shapiro-Wilks P	Aug	0.37	0.22	0.09	0.81	0.59	0.03	0.11	0.73	0.00	0.08	0.54	0.09	0.02
	Sep	0.39	0.91	0.10	0.56	0.61	0.03	0.82	0.60	0.43	0.51	0.46	0.29	0.03
Shapiro-Wilks H	Aug	FALSE	FALSE	FALSE	FALSE	FALSE	TRUE	FALSE	FALSE	TRUE	FALSE	FALSE	FALSE	TRUE
	Sep	FALSE	FALSE	FALSE	FALSE	FALSE	TRUE	FALSE	FALSE	FALSE	FALSE	FALSE	FALSE	TRUE
Rank-Sum P		0.04	0.00	0.00	0.50	0.00	0.11	0.04	0.00	0.00	0.86	0.05	0.00	0.03
Rank-Sum H		TRUE	TRUE	TRUE	FALSE	TRUE	FALSE	TRUE	TRUE	TRUE	FALSE	FALSE	TRUE	TRUE

Table B.13. Infiltration test and soil water content data intra-plot comparison data, plot 1.

Parameter	Date	α (cm^{-1})					K - TI (cm d^{-1})					K - Dual Ring (cm d^{-1})	Initial Water Content	Final Water Content
		Applied Tension Interval (cm)					Applied Tension (cm)							
		15-10	10-5	5-2	2-1	1-0	10	5	2	1	0			
Arithmetic Mean	Aug	0.05	0.11	0.34	0.40	0.89	2.82	6.35	24.39	39.75	184.34	25.31	0.22	0.34
	Sep	0.05	0.06	0.28	0.89	1.52	1.47	4.95	19.86	55.05	319.97	31.67	0.16	0.37
Maximum	Aug	0.11	0.18	0.57	0.79	2.03	11.08	10.91	66.74	102.71	874.75	122.42	0.26	0.37
	Sep	0.07	0.08	0.56	1.32	2.78	2.36	6.89	45.18	140.14	1091.00	50.18	0.20	0.42
Minimum	Aug	0.02	0.05	0.05	0.11	0.07	0.20	2.49	3.42	4.58	3.42	2.15	0.19	0.30
	Sep	0.03	0.05	0.07	0.59	0.91	0.04	1.83	4.50	24.98	81.77	16.05	0.11	0.34
CV (%)	Aug	78.20	33.22	38.75	46.72	72.45	101.56	40.92	66.01	63.40	139.36	129.98	8.35	5.46
	Sep	35.44	19.35	48.58	25.51	51.48	52.33	31.17	58.72	63.34	100.13	43.20	20.68	7.72
Std Dev	Aug	0.04	0.04	0.13	0.19	0.65	2.86	2.60	16.10	25.20	256.89	32.90	0.02	0.02
	Sep	0.02	0.01	0.14	0.23	0.78	0.77	1.54	11.66	34.87	320.38	13.68	0.03	0.03
Shapiro-Wilks Statistic	Aug	0.85	0.96	0.92	0.96	0.86	0.59	0.97	0.82	0.85	0.66	0.64	0.91	0.89
	Sep	0.90	0.92	0.91	0.96	0.75	0.93	0.93	0.90	0.75	0.72	0.90	0.93	0.83
Shapiro-Wilks P	Aug	0.34	0.30	0.50	0.48	0.10	0.00	0.25	0.03	0.07	0.00	0.00	0.46	0.21
	Sep	0.85	0.71	0.52	0.43	0.01	0.91	0.94	0.41	0.02	0.01	0.46	0.99	0.09
Shapiro-Wilks H	Aug	FALSE	FALSE	FALSE	FALSE	FALSE	TRUE	FALSE	TRUE	FALSE	TRUE	TRUE	FALSE	FALSE
	Sep	FALSE	FALSE	FALSE	FALSE	TRUE	FALSE	FALSE	FALSE	TRUE	TRUE	FALSE	FALSE	FALSE
Rank-Sum P		0.66	0.01	0.17	0.00	0.02	0.18	0.27	0.59	0.21	0.05	0.08	0.00	0.04
Rank-Sum H		FALSE	TRUE	FALSE	TRUE	TRUE	FALSE	FALSE	FALSE	FALSE	FALSE	FALSE	TRUE	TRUE

Appendix C

Kintore macroporosity data

Table C.1. Plot 1 macropore area fraction data.

Position (m)			Macropore area fraction attributable to:						
X	Y	Z	Fractures	0.05 -0 .5	0.5 - 0.8	0.8 - 1.0	1.0 - 1.2	Total	Total w/o fractures
				(cm in diameter cylindrical pores)					
0	0	-0.02	0.0002	0.0025	0.0001	0.0000	0.0000	0.0028	0.0026
0	0	-0.12	0.0000	0.0015	0.0005	0.0000	0.0000	0.0020	0.0019
0	0	-0.3	0.0003	0.0024	0.0003	0.0003	0.0000	0.0032	0.0030
0	0	-0.64	0.0000	0.0003	0.0000	0.0000	0.0000	0.0003	0.0003
1.93	0.05	-0.02	0.0002	0.0037	0.0000	0.0000	0.0000	0.0039	0.0037
1.93	0.05	-0.1	0.0001	0.0029	0.0000	0.0000	0.0000	0.0030	0.0029
1.93	0.05	-0.3	0.0002	0.0017	0.0017	0.0003	0.0000	0.0038	0.0036
1.93	0.05	-0.7	0.0000	0.0005	0.0001	0.0000	0.0000	0.0006	0.0006
3.7	0	-0.02	0.0004	0.0026	0.0003	0.0000	0.0000	0.0033	0.0029
3.7	0	-0.14	0.0000	0.0020	0.0003	0.0000	0.0000	0.0023	0.0023
3.7	0	-0.39	0.0003	0.0012	0.0003	0.0005	0.0000	0.0024	0.0020
3.7	0	-0.64	0.0000	0.0005	0.0000	0.0000	0.0000	0.0005	0.0005
5.3	0.1	-0.02	0.0001	0.0041	0.0002	0.0000	0.0000	0.0044	0.0043
5.3	0.1	-0.15	0.0000	0.0020	0.0003	0.0000	0.0000	0.0024	0.0023
5.3	0.1	-0.45	0.0002	0.0005	0.0003	0.0000	0.0000	0.0010	0.0008
5.3	0.1	-0.76	0.0000	0.0003	0.0000	0.0000	0.0000	0.0003	0.0003
0.25	1	-0.02	0.0001	0.0026	0.0000	0.0000	0.0000	0.0027	0.0026
0.25	1	-0.13	0.0000	0.0016	0.0000	0.0000	0.0000	0.0016	0.0016
0.25	1	-0.27	0.0000	0.0026	0.0007	0.0003	0.0000	0.0036	0.0036
0.25	1	-0.65	0.0000	0.0008	0.0000	0.0000	0.0000	0.0008	0.0008
2.15	1	-0.02	0.0001	0.0023	0.0003	0.0000	0.0000	0.0028	0.0026
2.15	1	-0.14	0.0000	0.0022	0.0001	0.0003	0.0000	0.0027	0.0026
2.15	1	-0.37	0.0004	0.0010	0.0005	0.0003	0.0000	0.0022	0.0018
2.15	1	-0.72	0.0000	0.0008	0.0000	0.0000	0.0000	0.0008	0.0008
3.5	0.91	-0.02	0.0002	0.0048	0.0003	0.0000	0.0000	0.0053	0.0051
3.5	0.91	-0.15	0.0000	0.0023	0.0007	0.0000	0.0000	0.0030	0.0030
3.5	0.91	-0.32	0.0003	0.0013	0.0002	0.0000	0.0000	0.0018	0.0015
3.5	0.91	-0.68	0.0000	0.0007	0.0000	0.0000	0.0000	0.0007	0.0007
5.25	1.06	-0.02	0.0002	0.0035	0.0000	0.0000	0.0000	0.0036	0.0035
5.25	1.06	-0.15	0.0000	0.0022	0.0011	0.0000	0.0000	0.0033	0.0033
5.25	1.06	-0.39	0.0001	0.0008	0.0003	0.0003	0.0000	0.0015	0.0014
5.25	1.06	-0.74	0.0000	0.0004	0.0000	0.0000	0.0000	0.0004	0.0004
0.25	3.14	-0.02	0.0003	0.0027	0.0001	0.0000	0.0000	0.0031	0.0028
0.25	3.14	-0.17	0.0001	0.0023	0.0005	0.0000	0.0000	0.0028	0.0028
0.25	3.14	-0.32	0.0005	0.0014	0.0009	0.0003	0.0000	0.0031	0.0026
0.25	3.14	-0.7	0.0000	0.0005	0.0000	0.0003	0.0000	0.0007	0.0007
2.1	3.35	-0.02	0.0003	0.0026	0.0003	0.0000	0.0000	0.0032	0.0029
2.1	3.35	-0.17	0.0000	0.0019	0.0006	0.0000	0.0000	0.0025	0.0025
2.1	3.35	-0.39	0.0003	0.0010	0.0002	0.0010	0.0000	0.0025	0.0022
2.1	3.35	-0.74	0.0000	0.0008	0.0000	0.0000	0.0000	0.0008	0.0008
3.6	3.34	-0.02	0.0002	0.0043	0.0002	0.0000	0.0000	0.0047	0.0046
3.6	3.34	-0.17	0.0000	0.0018	0.0003	0.0000	0.0000	0.0022	0.0022
3.6	3.34	-0.38	0.0000	0.0003	0.0005	0.0003	0.0000	0.0010	0.0010
3.6	3.34	-0.71	0.0000	0.0006	0.0000	0.0000	0.0000	0.0006	0.0006
5.35	3.2	-0.02	0.0002	0.0027	0.0001	0.0000	0.0000	0.0030	0.0028
5.35	3.2	-0.17	0.0000	0.0025	0.0007	0.0000	0.0000	0.0032	0.0031
5.35	3.2	-0.44	0.0002	0.0014	0.0008	0.0000	0.0000	0.0024	0.0022
5.35	3.2	-0.71	0.0000	0.0005	0.0000	0.0000	0.0000	0.0005	0.0005

Notes

Tile drain axis is Y = 0

Table C.2. Plot 2 macropore area fraction data.

Position (m)			Macropore area fraction attributable to:						
X	Y	Z	Fractures	0.05 -0 .5	0.5 - 0.8	0.8 - 1.0	1.0 - 1.2	Total	Total w/o fractures
				(cm in diameter cylindrical pores)					
0	0	-0.02	0.0001	0.0045	0.0009	0.0000	0.0000	0.0055	0.0054
0	0	-0.15	0.0001	0.0021	0.0023	0.0000	0.0000	0.0044	0.0043
0	0	-0.27	0.0000	0.0046	0.0020	0.0005	0.0000	0.0072	0.0072
0	0	-0.51	0.0000	0.0004	0.0007	0.0000	0.0000	0.0011	0.0011
0	0	-0.94	0.0000	0.0002	0.0000	0.0000	0.0000	0.0002	0.0002
2.54	0.18	-0.02	0.0001	0.0059	0.0008	0.0000	0.0000	0.0068	0.0067
2.54	0.18	-0.1	0.0001	0.0038	0.0005	0.0000	0.0000	0.0043	0.0043
2.54	0.18	-0.28	0.0000	0.0030	0.0035	0.0000	0.0000	0.0065	0.0065
2.54	0.18	-0.61	0.0000	0.0004	0.0002	0.0000	0.0000	0.0007	0.0007
2.54	0.18	-0.97	0.0001	0.0004	0.0000	0.0000	0.0000	0.0005	0.0004
3.72	0	-0.02	0.0001	0.0048	0.0015	0.0000	0.0000	0.0063	0.0062
3.72	0	-0.12	0.0000	0.0028	0.0008	0.0003	0.0000	0.0039	0.0039
3.72	0	-0.3	0.0000	0.0025	0.0036	0.0005	0.0000	0.0067	0.0067
3.72	0	-0.61	0.0000	0.0005	0.0002	0.0000	0.0000	0.0007	0.0007
3.72	0	-0.95	0.0001	0.0004	0.0000	0.0000	0.0000	0.0005	0.0004
5.8	-0.3	-0.02	0.0002	0.0048	0.0008	0.0000	0.0000	0.0057	0.0056
5.8	-0.3	-0.16	0.0000	0.0027	0.0027	0.0005	0.0000	0.0059	0.0059
5.8	-0.3	-0.34	0.0000	0.0023	0.0026	0.0003	0.0000	0.0051	0.0051
5.8	-0.3	-0.63	0.0000	0.0004	0.0000	0.0000	0.0000	0.0005	0.0004
5.8	-0.3	-1	0.0002	0.0004	0.0000	0.0000	0.0000	0.0006	0.0004
-0.18	1.14	-0.02	0.0001	0.0045	0.0012	0.0000	0.0000	0.0058	0.0057
-0.18	1.14	-0.06	0.0001	0.0026	0.0010	0.0000	0.0000	0.0037	0.0036
-0.18	1.14	-0.21	0.0000	0.0053	0.0024	0.0003	0.0000	0.0079	0.0079
-0.18	1.14	-0.51	0.0001	0.0002	0.0000	0.0000	0.0000	0.0003	0.0002
-0.18	1.14	-0.85	0.0000	0.0005	0.0001	0.0000	0.0000	0.0006	0.0006
2.52	1.41	-0.02	0.0002	0.0038	0.0014	0.0000	0.0000	0.0054	0.0052
2.52	1.41	-0.07	0.0002	0.0027	0.0014	0.0000	0.0000	0.0042	0.0041
2.52	1.41	-0.2	0.0000	0.0036	0.0029	0.0008	0.0000	0.0073	0.0073
2.52	1.41	-0.54	0.0000	0.0006	0.0000	0.0000	0.0000	0.0006	0.0006
2.52	1.41	-0.77	0.0000	0.0004	0.0000	0.0000	0.0000	0.0004	0.0004
3.3	1.54	-0.02	0.0002	0.0045	0.0007	0.0000	0.0000	0.0053	0.0051
3.3	1.54	-0.08	0.0001	0.0027	0.0012	0.0003	0.0000	0.0042	0.0042
3.3	1.54	-0.18	0.0000	0.0018	0.0027	0.0000	0.0000	0.0045	0.0045
3.3	1.54	-0.54	0.0000	0.0005	0.0001	0.0000	0.0000	0.0006	0.0006
3.3	1.54	-0.84	0.0000	0.0004	0.0000	0.0000	0.0000	0.0004	0.0004
5.89	1.43	-0.3	0.0000	0.0033	0.0031	0.0003	0.0000	0.0066	0.0066
5.89	1.43	-0.63	0.0000	0.0004	0.0002	0.0000	0.0000	0.0006	0.0006
5.89	1.43	-0.9	0.0000	0.0003	0.0000	0.0000	0.0000	0.0003	0.0003
0.72	3.65	-0.02	0.0001	0.0051	0.0009	0.0000	0.0000	0.0060	0.0060
0.72	3.65	-0.1	0.0000	0.0025	0.0009	0.0003	0.0000	0.0037	0.0037
0.72	3.65	-0.23	0.0000	0.0029	0.0010	0.0005	0.0000	0.0044	0.0044
0.72	3.65	-0.49	0.0000	0.0003	0.0012	0.0000	0.0000	0.0015	0.0015
0.72	3.65	-0.85	0.0000	0.0003	0.0000	0.0000	0.0000	0.0003	0.0003
2.69	3.66	-0.02	0.0001	0.0046	0.0018	0.0000	0.0000	0.0064	0.0064
2.69	3.66	-0.15	0.0000	0.0029	0.0015	0.0000	0.0000	0.0044	0.0044
2.69	3.66	-0.33	0.0000	0.0014	0.0033	0.0003	0.0000	0.0050	0.0050
2.69	3.66	-0.62	0.0000	0.0004	0.0001	0.0000	0.0000	0.0005	0.0005
2.69	3.66	-1	0.0000	0.0002	0.0000	0.0000	0.0000	0.0002	0.0002
4.22	3.62	-0.02	0.0001	0.0037	0.0011	0.0000	0.0000	0.0048	0.0048
4.22	3.62	-0.15	0.0000	0.0028	0.0014	0.0003	0.0000	0.0044	0.0044
4.22	3.62	-0.31	0.0000	0.0027	0.0032	0.0005	0.0000	0.0063	0.0063
4.22	3.62	-0.58	0.0001	0.0003	0.0001	0.0000	0.0000	0.0005	0.0004
4.22	3.62	-0.95	0.0000	0.0004	0.0000	0.0000	0.0000	0.0004	0.0004

Notes

Tile drain axis is Y = 0

Table C.3. Plot 3 macropore area fraction data.

Position (m)			Macropore area fraction attributable to:						
X	Y	Z	Fractures	0.05 -0 .5	0.5 - 0.8	0.8 - 1.0	1.0 - 1.2	Total	Total w/o fractures
				(cm in diameter cylindrical pores)					
0.0000	0.5000	-0.0200	0.0003	0.0020	0.0003	0.0000	0.0000	0.0026	0.0023
0.0000	0.5000	-0.1500	0.0005	0.0025	0.0007	0.0008	0.0000	0.0045	0.0040
0.0000	0.5000	-0.2000	0.0002	0.0020	0.0036	0.0018	0.0000	0.0075	0.0074
0.0000	0.5000	-0.5000	0.0000	0.0001	0.0009	0.0013	0.0000	0.0023	0.0023
2.3000	0.2200	-0.0200	0.0002	0.0024	0.0003	0.0005	0.0000	0.0035	0.0032
2.3000	0.2200	-0.1500	0.0005	0.0041	0.0020	0.0010	0.0004	0.0081	0.0076
2.3000	0.2200	-0.2800	0.0001	0.0021	0.0021	0.0013	0.0000	0.0057	0.0056
2.3000	0.2200	-0.5000	0.0000	0.0002	0.0008	0.0023	0.0000	0.0033	0.0033
4.5500	0.3500	-0.0200	0.0002	0.0040	0.0007	0.0015	0.0000	0.0064	0.0062
4.5500	0.3500	-0.1500	0.0007	0.0031	0.0024	0.0025	0.0017	0.0104	0.0097
4.5500	0.3500	-0.2500	0.0003	0.0025	0.0023	0.0031	0.0008	0.0089	0.0086
4.5500	0.3500	-0.5000	0.0000	0.0002	0.0012	0.0023	0.0000	0.0037	0.0037
7.0500	0.2000	-0.0200	0.0003	0.0035	0.0010	0.0008	0.0000	0.0056	0.0053
7.0500	0.2000	-0.1500	0.0007	0.0029	0.0014	0.0023	0.0000	0.0072	0.0066
7.0500	0.2000	-0.3000	0.0001	0.0020	0.0020	0.0005	0.0000	0.0046	0.0046
7.0500	0.2000	-0.5000	0.0000	0.0002	0.0011	0.0025	0.0000	0.0039	0.0039
0.3000	1.1800	-0.0200	0.0002	0.0043	0.0006	0.0008	0.0000	0.0058	0.0056
0.3000	1.1800	-0.1500	0.0003	0.0052	0.0021	0.0018	0.0000	0.0094	0.0091
0.3000	1.1800	-0.2200	0.0001	0.0032	0.0037	0.0023	0.0000	0.0093	0.0092
0.3000	1.1800	-0.5000	0.0000	0.0004	0.0025	0.0031	0.0000	0.0059	0.0059
2.1500	1.4600	-0.0200	0.0003	0.0033	0.0007	0.0003	0.0000	0.0045	0.0042
2.1500	1.4600	-0.1500	0.0005	0.0032	0.0025	0.0010	0.0000	0.0073	0.0067
2.1500	1.4600	-0.2700	0.0002	0.0022	0.0029	0.0031	0.0000	0.0084	0.0082
2.1500	1.4600	-0.5000	0.0000	0.0001	0.0016	0.0018	0.0000	0.0034	0.0034
3.9500	1.3000	-0.0200	0.0002	0.0049	0.0007	0.0003	0.0000	0.0060	0.0058
3.9500	1.3000	-0.1500	0.0006	0.0037	0.0032	0.0025	0.0008	0.0108	0.0103
3.9500	1.3000	-0.3000	0.0001	0.0022	0.0029	0.0036	0.0004	0.0092	0.0091
3.9500	1.3000	-0.5000	0.0000	0.0002	0.0029	0.0028	0.0000	0.0060	0.0060
6.1000	1.2000	-0.0200	0.0001	0.0044	0.0007	0.0003	0.0000	0.0054	0.0053
6.1000	1.2000	-0.1500	0.0008	0.0038	0.0036	0.0036	0.0004	0.0121	0.0114
6.1000	1.2000	-0.2800	0.0001	0.0020	0.0025	0.0008	0.0004	0.0057	0.0056
6.1000	1.2000	-0.5000	0.0000	0.0003	0.0019	0.0015	0.0000	0.0038	0.0038
0.8000	3.3000	-0.0200	0.0003	0.0047	0.0007	0.0025	0.0000	0.0082	0.0079
0.8000	3.3000	-0.1500	0.0007	0.0040	0.0019	0.0015	0.0008	0.0089	0.0083
0.8000	3.3000	-0.2800	0.0001	0.0016	0.0026	0.0015	0.0004	0.0062	0.0061
0.8000	3.3000	-0.5000	0.0000	0.0002	0.0017	0.0031	0.0000	0.0049	0.0049
2.3000	3.4000	-0.0200	0.0003	0.0041	0.0010	0.0015	0.0000	0.0069	0.0067
2.3000	3.4000	-0.1500	0.0000	0.0039	0.0018	0.0005	0.0000	0.0062	0.0062
2.3000	3.4000	-0.2700	0.0000	0.0023	0.0034	0.0018	0.0000	0.0074	0.0074
2.3000	3.4000	-0.5000	0.0000	0.0002	0.0016	0.0023	0.0000	0.0040	0.0040
4.3000	3.3800	-0.0200	0.0002	0.0048	0.0005	0.0015	0.0000	0.0070	0.0068
4.3000	3.3800	-0.1500	0.0008	0.0041	0.0025	0.0015	0.0000	0.0089	0.0081
4.3000	3.3800	-0.2500	0.0002	0.0025	0.0044	0.0025	0.0000	0.0096	0.0094
4.3000	3.3800	-0.5000	0.0000	0.0002	0.0020	0.0028	0.0000	0.0050	0.0050
6.1000	3.3000	-0.0200	0.0003	0.0041	0.0011	0.0013	0.0000	0.0068	0.0065
6.1000	3.3000	-0.1500	0.0006	0.0046	0.0033	0.0031	0.0004	0.0120	0.0113
6.1000	3.3000	-0.2800	0.0001	0.0024	0.0043	0.0033	0.0004	0.0106	0.0105
6.1000	3.3000	-0.5000	0.0000	0.0002	0.0016	0.0038	0.0000	0.0056	0.0056

Notes

Tile drain axis is Y = 0

Table C.4. Rank-sum P values for the inter-row effective porosity comparison using the results from the Dunn and Phillips (1991) analysis.

Date	Comparison Test	Effective Pore Dia. [cm] 0.02 - 0.03	0.03 - 0.06	0.06 - 0.15	0.15 - 0.3	0.3 - 1.0	0.03 - 1.0
Aug 09	Plot 1: Rows 1-2	0.31	0.49	0.89	0.34	0.89	0.69
	Plot 1: Rows 1-3	0.40	0.34	0.34	0.69	0.89	0.49
Sep 09	Plot 1: Rows 1-2	0.40	1.00	0.70	0.10	1.00	1.00
	Plot 1: Rows 1-3	0.40	0.40	1.00	0.70	0.40	0.40
Aug 09	Plot 2: Rows 1-2	0.31	0.20	0.46	0.69	0.34	0.11
	Plot 2: Rows 1-3	0.03	1.00	0.69	0.49	0.69	0.34
Sep 09	Plot 2: Rows 1-2	0.80	1.00	0.70	0.40	0.70	1.00
	Plot 2: Rows 1-3	0.90	0.70	1.00	0.40	0.20	0.70
Aug 08	Plot 3: Rows 1-2	0.26	0.69	1.00	0.34	0.34	0.89
	Plot 3: Rows 1-3	0.31	0.34	0.34	0.20	0.69	0.34

Table C.5. Rank-sum P values for the intra-plot effective porosity comparison using the results from the Dunn and Phillips (1991) analysis.

Effective Pore Dia. [cm]	Comparison Plot1 Aug - Sep	Plot 2 Aug - Sep
0.02 - 0.03	0.34	0.91
0.03 - 0.06	0	0.12
0.06 - 0.15	0	0.27
0.15 - 0.3	0	0.01
0.3 - 1.0	0.24	0.04
0.03 - 1.0	0	0.70

Table C.6. Rank-sum P values for the inter-plot effective porosity comparison using the results from the Dunn and Phillips (1991) analysis.

Effective Pore Dia. [cm]	Comparison			
	Plot 1 vs Plot 2 Aug 2009	Plot 1 vs Plot 2 Sep 2009	Plot 1 vs Plot 3 Aug 2009 / Aug 2008	Plot 2 vs Plot 3 Aug 2009 / Aug 2008
0.02 - 0.03	0.05	0.44	0.01	0.89
0.03 - 0.06	0.08	0.28	0.71	0.14
0.06 - 0.15	0.00	0.86	0.01	0.24
0.15 - 0.3	0.00	0.22	0.11	0.00
0.3 - 1.0	0.16	0.55	0.22	0.02
0.03 - 1.0	0.00	0.55	0.09	0.02

Appendix D

Soil analysis process pictures

a) Tension (left) and double ring (right) infiltration tests,

b) Dye application

c) Rough Excavation

d) Finished excavation

e) Macropore counting surface preparation

f) Macropore counting

(photo courtesy of Sara Esmaeili)

g) Photography

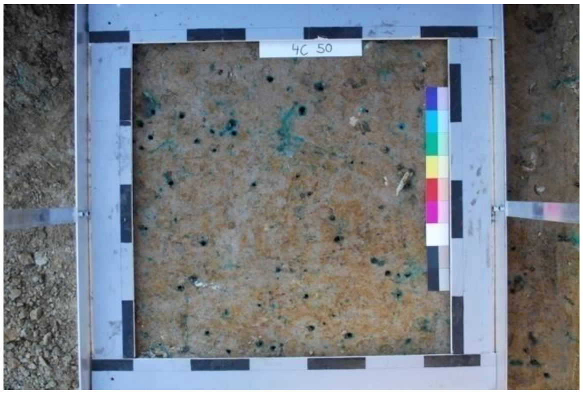

Appendix E

Tile discharge, tracer and climate data

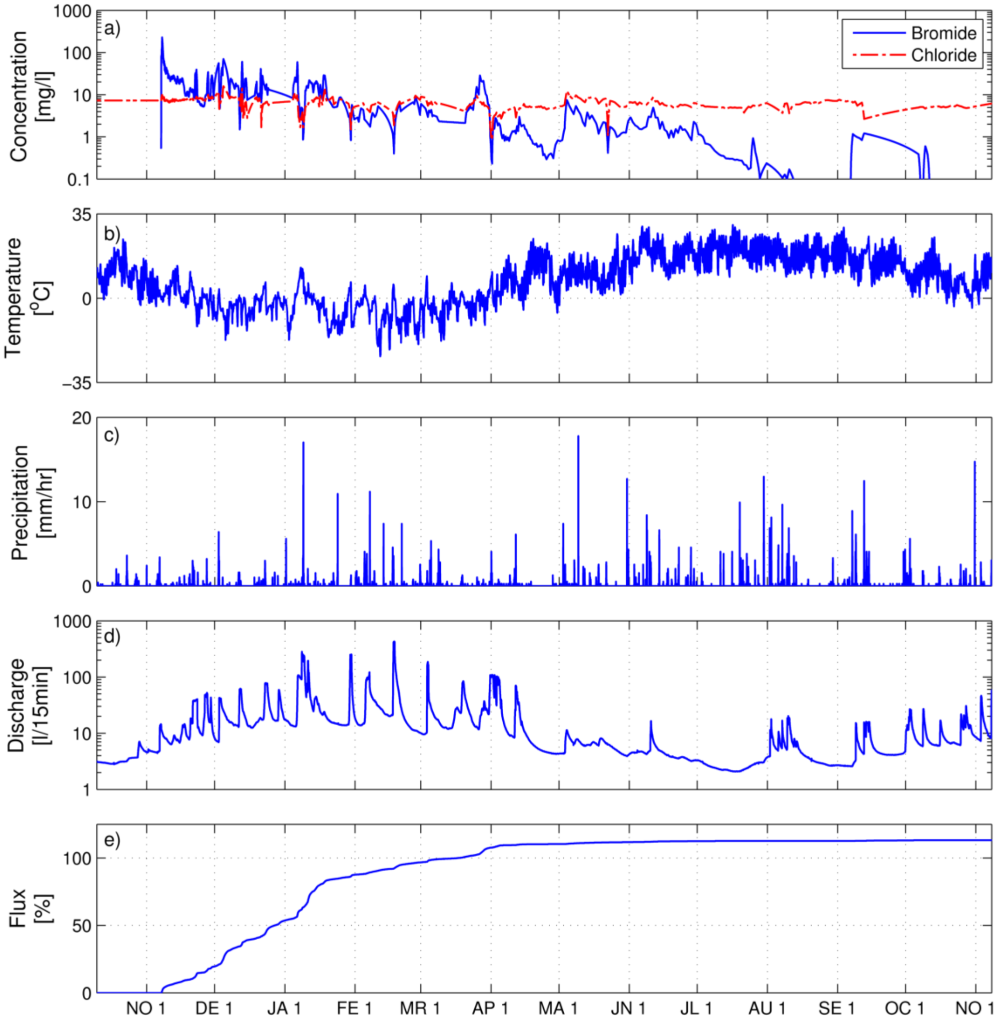

Figure E.1. Bromide and chloride concentration in the tile effluent (a), temperature (b), precipitation (c), modelled tile discharge (d), and bromide (as % of initial mass applied) captured by the tile drain (e), between October 2007 and November 2008.

Appendix F

Residual tracer distribution in plot 1 soil cores extracted Sept 2008

Position			Concentration	
X	Y	Z	Cl	Br
	[m]		[mg/l]	
0	0.25	-0.12	33.74	30.02
0	0.25	-0.35	36.05	39.10
0	0.25	-0.57	64.44	23.49
0	0.25	-0.81	51.08	9.83
0	0.25	-1.04	45.34	0.00
0	0.25	-1.21	53.83	0.00
0	0.25	-1.39	25.19	0.00
0	0.25	-1.57	36.89	16.30
0	0.25	-1.74	32.41	0.00
3	0.25	-0.26	63.84	30.63
3	0.25	-0.48	51.29	11.17
3	0.25	-0.79	45.60	0.00
3	0.25	-1.02	52.13	0.00
3	0.25	-1.25	29.58	0.00
3	0.25	-1.48	30.52	0.00
3	0.25	-1.71	44.79	0.00
6	0.25	-0.17	9.43	13.09
6	0.25	-0.35	18.40	14.66
6	0.25	-0.52	22.60	14.62
6	0.25	-0.75	23.04	0.00
6	0.25	-0.94	29.46	0.00
6	0.25	-1.14	31.63	0.00
6	0.25	-1.34	25.05	0.00
6	0.25	-1.53	19.04	0.00
6	0.25	-1.73	96.23	0.00
0	0.75	-0.21	32.67	35.44
0	0.75	-0.48	139.32	54.72
0	0.75	-0.64	42.52	0.00
0	0.75	-0.85	44.93	0.00
0	0.75	-1.07	34.35	0.00
0	0.75	-1.28	33.92	0.00
0	0.75	-1.50	19.55	0.00
0	0.75	-1.71	26.12	0.00
3	0.75	-0.21	14.70	4.52
3	0.75	-0.47	107.10	11.64
3	0.75	-0.76	37.03	0.00
3	0.75	-0.93	40.87	0.00
3	0.75	-1.09	27.32	0.00
3	0.75	-1.25	39.08	0.00
3	0.75	-1.42	35.22	0.00
3	0.75	-1.58	19.86	0.00
3	0.75	-1.75	20.98	0.00
6	0.75	-0.22	5.32	8.52
6	0.75	-0.48	133.04	34.33
6	0.75	-0.67	29.27	0.00
6	0.75	-0.85	31.14	0.00
6	0.75	-1.02	57.28	0.00
6	0.75	-1.20	20.50	0.00
6	0.75	-1.39	33.49	0.00
6	0.75	-1.56	26.74	0.00
6	0.75	-1.74	25.82	0.00
0	1.75	-0.21	127.89	115.71
0	1.75	-0.48	205.18	31.70
0	1.75	-0.75	127.73	10.68
0	1.75	-0.94	42.67	0.00
0	1.75	-1.14	35.51	0.00
0	1.75	-1.34	15.91	0.00
0	1.75	-1.53	29.11	0.00
0	1.75	-1.74	26.21	0.00
6	1.75	-0.21	21.08	16.89
6	1.75	-0.48	118.35	8.72
6	1.75	-0.65	27.32	0.00
6	1.75	-0.84	33.20	0.00
6	1.75	-1.02	24.87	0.00
6	1.75	-1.20	80.98	0.00
6	1.75	-1.38	20.45	0.00
6	1.75	-1.56	23.55	0.00
6	1.75	-1.74	24.69	0.00
6	1.75	-0.22	13.59	15.95
6	1.75	-0.48	109.08	10.47
6	1.75	-0.79	42.76	0.00
6	1.75	-0.98	21.33	0.00
6	1.75	-1.16	25.81	0.00
6	1.75	-1.36	25.57	0.00
6	1.75	-1.55	40.29	0.00
6	1.75	-1.74	25.44	0.00
0	3.75	-0.04	60.11	13.29
0	3.75	-0.28	72.26	5.62
0	3.75	-0.49	132.35	17.36
0	3.75	-0.71	62.47	0.00
0	3.75	-0.86	27.16	0.00
0	3.75	-1.01	18.48	0.00
0	3.75	-1.16	17.78	0.00
0	3.75	-1.31	24.03	0.00
0	3.75	-1.46	42.58	0.00
0	3.75	-1.61	46.09	0.00
0	3.75	-1.76	19.45	0.00
3	3.75	-0.10	77.77	3.62

Position			Concentration	
X	Y	Z	Cl	Br
	[m]		[mg/l]	
3	3.75	-0.31	75.40	4.86
3	3.75	-0.49	134.42	5.50
3	3.75	-0.76	33.34	0.00
3	3.75	-0.92	40.27	0.00
3	3.75	-1.08	32.80	0.00
3	3.75	-1.25	27.06	0.00
3	3.75	-1.42	45.43	0.00
3	3.75	-1.58	38.90	0.00
3	3.75	-1.75	25.33	0.00
6	3.75	-0.04	10.06	1.81
6	3.75	-0.27	95.94	5.98
6	3.75	-0.49	52.83	0.00
6	3.75	-0.67	30.08	0.00
6	3.75	-0.88	35.41	0.00
6	3.75	-1.08	43.51	0.00
6	3.75	-1.30	28.99	0.00
6	3.75	-1.51	23.95	0.00
6	3.75	-1.72	43.77	3.47
0	6	-0.02	19.28	26.78
0	6	-0.18	17.38	9.59
0	6	-0.35	55.76	0.00
0	6	-0.52	25.67	0.00
0	6	-0.65	33.25	0.00
0	6	-0.91	39.41	0.00
0	6	-1.17	27.87	0.00
0	6	-1.44	31.78	0.00
0	6	-1.70	38.51	0.00
3	6	-0.23	16.71	2.62
3	6	-0.48	78.43	0.00
3	6	-0.73	30.01	0.00
3	6	-0.90	23.69	0.00
3	6	-1.06	34.60	0.00
3	6	-1.24	28.61	0.00
3	6	-1.41	51.67	0.00
3	6	-1.58	26.92	0.00
3	6	-1.75	29.33	0.00
6	6	-0.08	12.81	2.81
6	6	-0.29	14.86	3.50
6	6	-0.50	12.58	3.17
6	6	-0.73	28.68	0.00
6	6	-0.90	41.04	0.00
6	6	-1.07	47.62	0.00
6	6	-1.24	27.17	0.00
6	6	-1.40	24.40	0.00
6	6	-1.58	29.59	0.00
6	6	-1.75	35.63	0.00

Appendix G

Sebringville tile drain nutrient concentration data converted for 2D model application

Sebringville Plot 205-2002 56.1m3/ha LSM surface banding application

AAFC field data - based on a 9m x 220m 12 row application plot				**Data adjusted for a 1cm thick x 450cm 6 row model domain**			
Hours Post Appl.	Tile Flow [ml/s]	NH_4 Conc. [ug/ml]	Total P [ug/ml]	Days Post Appl.	Tile Flow [cm^3/d]	NH4 [C/C_0]	Total P [C/C_0]
0.00	0.15	0.00	0.05	0.0000	0.29	0.0000	0.0000
0.05	-	0.01	0.05	0.0021	-	0.0000	0.0000
0.38	-	0.00	0.008	0.0158	-	0.0000	0.0000
0.62	-	0.00	0.05	0.0258	-	0.0000	0.0001
0.77	-	0.00	0.05	0.0320	-	0.0000	0.0000
0.88	-	0.00	0.05	0.0367	-	0.0000	0.0001
1.00	-	0.00	0.05	0.0417	-	0.0000	0.0001
1.12	-	0.00	0.05	0.0467	-	0.0000	0.0001
1.45	-	0.00	0.05	0.0604	-	0.0000	0.0001
2.27	-	0.42	0.11	0.0946	-	0.0001	0.0001
3.27	-	2.08	0.20	0.1363	-	0.0006	0.0002
4.27	-	3.04	0.19	0.1779	-	0.0008	0.0002
5.27	-	2.57	0.10	0.2196	-	0.0007	0.0001
6.27	-	2.10	0.09	0.2613	-	0.0006	0.0001
7.27	-	1.72	0.04	0.3029	-	0.0005	0.0000
8.27	-	1.44	0.04	0.3446	-	0.0004	0.0000
9.27	-	1.23	0.04	0.3863	-	0.0003	0.0000
24	1.89	0.39	0.04	1.0000	3.71	0.0001	0.0000
48	2.17	0.00	0.012	2.0000	4.26	0.0000	0.0000

Note: the C/Co calcs are based on a 3.6g/kg initial concentration for NH4 and a 1g/kg initial concentration for P

(-) denotes no observed flow

Sebringville Plot 108-2002 74.8m3/ha LSM Injection application

AAFC field data - based on a 9m x 220m 12 row application plot				Data adjusted for a 1cm thick x 450cm 6 row model domain			
Hours Post Appl.	Tile Flow [ml/s]	NH_4 [ug/ml]	Total P [ug/ml]	Days Post Appl.	Tile Flow [cm^3/d]	NH4 [C/C_0]	Total P [C/C_0]
0.00	1.67	0.00	0.04	0.00	3.28	0.0000	0.0000
0.20	-	0.00	0.005	0.01	-	0.0000	0.0000
0.67	-	9.45	0.48	0.03	-	0.0026	0.0005
0.80	-	20.50	3.12	0.03	-	0.0057	0.0031
0.90	-	306.56	2.50	0.04	-	0.0852	0.0025
1.10	-	125.00	5.80	0.05	-	0.0347	0.0058
1.40	-	48.70	1.80	0.06	-	0.0135	0.0018
1.70	-	46.30	2.12	0.07	-	0.0129	0.0021
2.02	-	137.00	3.37	0.08	-	0.0381	0.0034
2.80	-	76.00	2.51	0.12	-	0.0211	0.0025
3.40	-	33.00	1.86	0.14	-	0.0092	0.0019
3.90	-	16.50	1.65	0.16	-	0.0046	0.0017
4.97	-	16.50	1.35	0.21	-	0.0046	0.0014
6.05	-	12.50	0.98	0.25	-	0.0035	0.0010
7.15	-	9.82	1.02	0.30	-	0.0027	0.0010
8.15	-	7.83	0.67	0.34	-	0.0022	0.0007
9.15	-	4.22	0.57	0.38	-	0.0012	0.0006
10.15	-	6.29	0.93	0.42	-	0.0017	0.0009
11.15	-	7.62	0.62	0.46	-	0.0021	0.0006
12.15	-	4.95	0.84	0.51	-	0.0014	0.0008
13.15	-	4.14	0.62	0.55	-	0.0012	0.0006
14.15	-	3.58	0.72	0.59	-	0.0010	0.0007
24	4.63	2.20	0.39	1.00	9.09	0.0006	0.0004
48	5.06	0.79	0.16	2.00	9.94	0.0002	0.0002

Note: the C/Co calcs are based on a 3.6g/kg initial concentration for NH4 and a 1g/kg initial concentration for P

Sebringville Plot 208-2002 74.8m3/ha LSM Injection application

AAFC field data - based on a 9m x 220m 12 row application plot				Data adjusted for a 1cm thick x 450cm 6 row model domain			
Hours Post Appl.	Tile Flow [ml/s]	NH_4 [ug/ml]	Total P [ug/ml]	Days Post Appl.	Tile Flow [cm^3/d]	NH4 [C/C_0]	Total P [C/C_0]
0.00	0	0	0	0.0000	0.00	0.0000	0.0000
0.08	-	0	0	0.0033	-	0.0000	0.0000
0.42	-	6.20	0.38	0.0175	-	0.0017	0.0004
0.70	-	39.2	6.89	0.0292	-	0.0109	0.0069
0.88	-	96.4	7.18	0.0367	-	0.0268	0.0072
1.05	-	107.0	3.10	0.0438	-	0.0297	0.0031
1.17	-	24.1	3.80	0.0488	-	0.0067	0.0038
1.32	-	100.0	5.57	0.0550	-	0.0278	0.0056
1.50	-	32.8	3.86	0.0625	-	0.0091	0.0039
1.87	-	39.1	4.13	0.0779	-	0.0109	0.0041
1.98	-	38.4	3.50	0.0825	-	0.0107	0.0035
2.03	-	41.5	4.05	0.0846	-	0.0115	0.0041
2.22	-	40.5	4.02	0.0925	-	0.0113	0.0040
2.53	-	27.2	3.73	0.1054	-	0.0076	0.0037
3.07	-	31.7	3.60	0.1279	-	0.0088	0.0036
3.6	-	15.6	2.05	0.1500	-	0.0043	0.0021
4.2	-	37.64	2.65	0.1750	-	0.0105	0.0027
5.47	-	26.86	1.63	0.2279	-	0.0075	0.0016
6.47	-	23.18	0.97	0.2696	-	0.0064	0.0010
7.47	-	19.99	1.53	0.3113	-	0.0056	0.0015
8.47	-	16.40	0.82	0.3529	-	0.0046	0.0008
9.47	-	15.88	1.61	0.3946	-	0.0044	0.0016
10.47	-	13.73	1.03	0.4363	-	0.0038	0.0010
11.47	-	11.82	0.77	0.4779	-	0.0033	0.0008
12.47	-	10.45	0.86	0.5196	-	0.0029	0.0009
24	2.34	8.43	1.00	1.0000	4.59	0.0023	0.0010
48	2.31	3.42	0.44	2.0000	4.54	0.0010	0.0004

Note: the C/Co calcs are based on a 3.6g/kg initial concentration for NH4 and a 1g/kg initial concentration for P

Appendix H

Extended dual-permeability model evaluation for tile discharge.

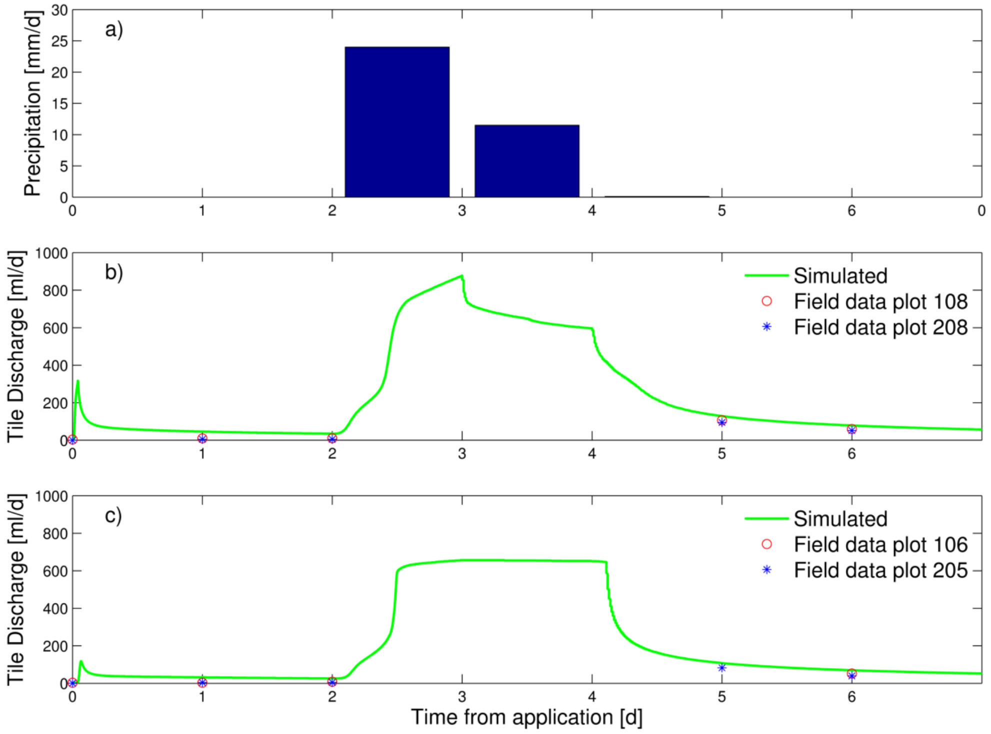

Figure H.1. Flow evaluation for the seven day time interval following LSM application at Sebringville during 2002.

Box (a) shows precipitation received, (b) shows tile discharge at the 74 m^3 ha^{-1} injection plots, and (c) shows tile discharge at the 56 m^3/ha surface banding plots. Note that the soil properties are slightly different between injection and surface banding plots (as explained in chapter 5), hence the slightly different hydraulic response to precipitation between (b) and (c). There were no field measurements of tile discharge obtained during the peak hydrologic response to the precipitation (day 3 and 4).

Appendix I

Dual-permeability model water and solute exchange parameter sensitivity.

In order to assess the influence of the solute and water exchange parameter values on the simulation results, 1 dimensional infiltration was simulated with different exchange parameter values. For the water exchange term, α_w, values ranged from 0.006 to 60.0 $cm^{-1}d^{-1}$ and for the solute exchange term, α_s, values ranged from 0.05 to 500.0 d^{-1}. In the case of both parameters, values were altered by a factor of 10 between each simulation. Results for the sensitivity analysis simulations are presented in Figure I.1, which shows the vertical mass distribution for the matrix and macropore continuum and Figure I.2, which shows the water flux and NH_4 breakthrough curves across the bottom boundary of the 1D domain. Base case scenario for the simulations was $\alpha_w = 0.6$ $cm^{-1}d^{-1}$ and $\alpha_s = 5.0$ d^{-1}. In order to evaluate each parameter individually, in the simulations where the water exchange term was adjusted, the solute exchange term was held constant, and conversely when the solute exchange term was adjusted, the water exchange term was held constant. The 1D parameter sensitivity simulations were run for a 48 hour time period. Flow boundary conditions in the domain consisted of a type 1, fixed pressure surface on the bottom of the domain and a surface water boundary at the top of the domain. Loading rates on the surface water boundary were equal to those used in 74.8 m^3 ha^{-1} liquid swine manure (LSM) injection simulations. Pressure head on the bottom boundary was set to 0 throughout the entire simulation to allow free drainage. Soil matrix and macropore hydraulic properties used in the sensitivity tests are given in Tables I.1 and I.2 respectively.

Table I.1. Soil matrix properties used in exchange parameter sensitivity tests.

Location / Soil Class	Depth (cm)	$\theta_{r,m}$ (-)	$\theta_{s,m}$ (-)	α_m (cm^{-1})	n_m (-)	$K_{s,m}$ ($cm \cdot d^{-1}$)
Sebringville ON / Huron Silt Loam	0-20	0.07	0.42	0.006	1.61	4.5
	20-150	0.08	0.4	0.008	1.48	1.3

Table I.2. Macropore properties used in exchange parameter sensitivity tests.

Depth (cm)	$\theta_{r,f}$ (-)	α_f (cm-1)	n_f (-)	w_f (cm3 cm-3)	$\theta_{s,f}$ (-)	$K_{s,f,z}$ (cm d-1)	$*K_{s,f,x}$ (cm d-1)
0-20	0.05	0.1	2	0.01	0.9	39273	4.5
20-70	0.05	0.1	2	0.02	0.9	15088	1.3

Breakthrough and drainage curves presented in Figure I.2 show the influence that the two exchange parameters have on NH_4 and water flux across the fixed head boundary on the bottom of the domain. Reducing the water exchange term causes more water to drain through the soil matrix flow regime while reducing the solute exchange term induces higher concentrations of NH_4 in the macropore discharge. Intuitively these observations for both parameters make sense. Lowering the water exchange coefficient decreases the ability of water to move between the relatively low K soil matrix and the higher K macropore regions of the simulated soil column, therefore causing more water to be retained in the matrix which ultimately leads to higher matrix discharge. Lowering the solute exchange coefficient reduces the amount of dispersive mass flux between the matrix and macropores and hence causes more mass to be retained in the macropore water. Since there is noticeably more discharge through the macropores than the matrix for the simulations where the water exchange coefficient was set to 0.6 $cm^{-1}d^{-1}$, reducing the amount of NH_4 diffusion into the matrix increases the total mass of NH_4 flushed through the domain during the simulation. Increasing the solute exchange coefficient from the base case value of 5.0 d^{-1} had a double pronged effect on the shape of the NH_4 breakthrough curve by delaying the NH_4 arrival time at the bottom boundary of the domain and by decreasing the concentration gradient between the matrix and macropore zones. For both simulations where the solute exchange coefficient was increased from the base case, NH_4 concentrations were in nearly constant equilibrium between the matrix and macropore discharge water exiting the bottom of the domain.

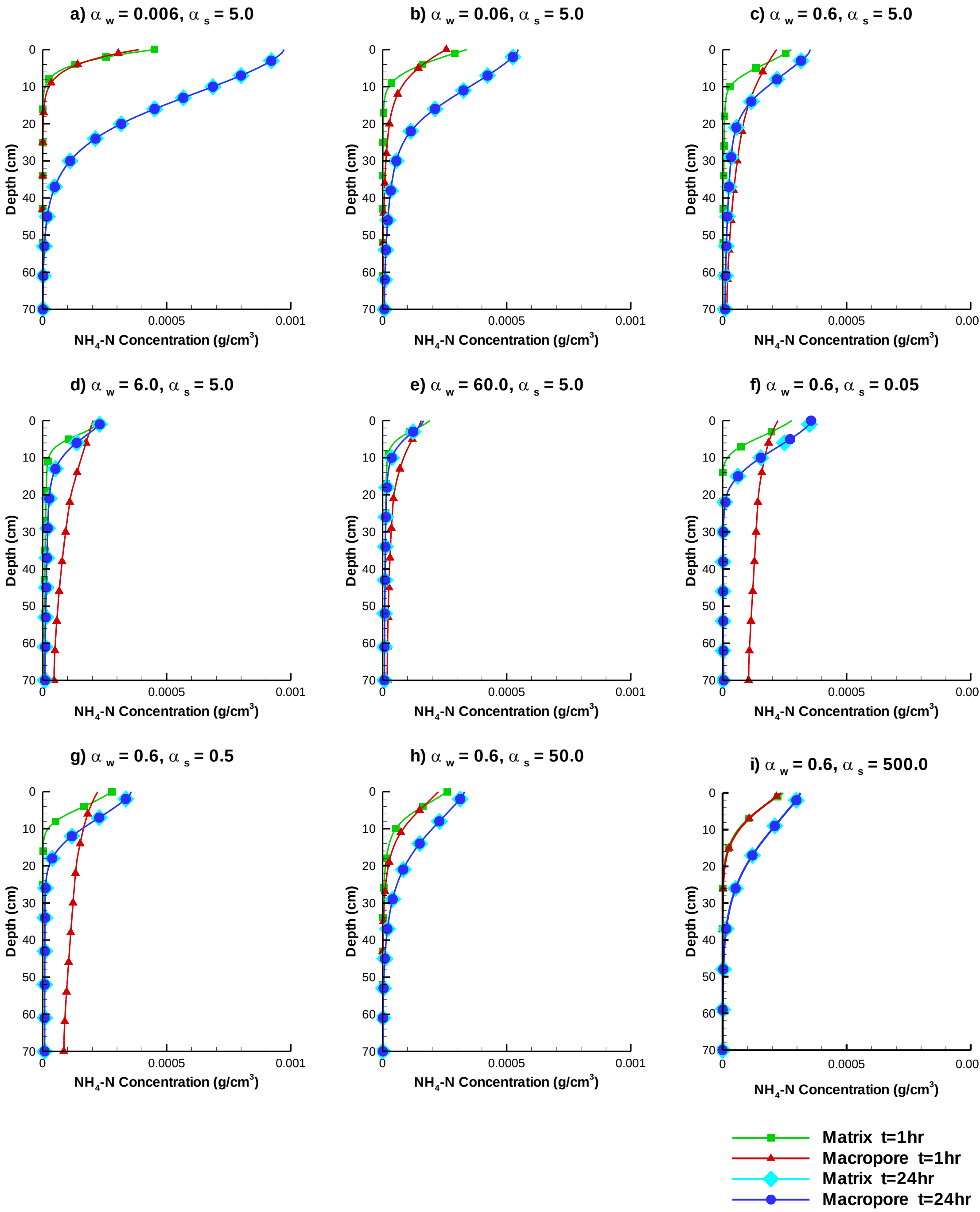

Figure I.1. Stored NH_4 mass in the soil matrix and macropore continuums vs. depth, at time = 2days for each of the nine different combinations of water and solute exchange parameter combinations considered in the 1D parameter sensitivity analysis.

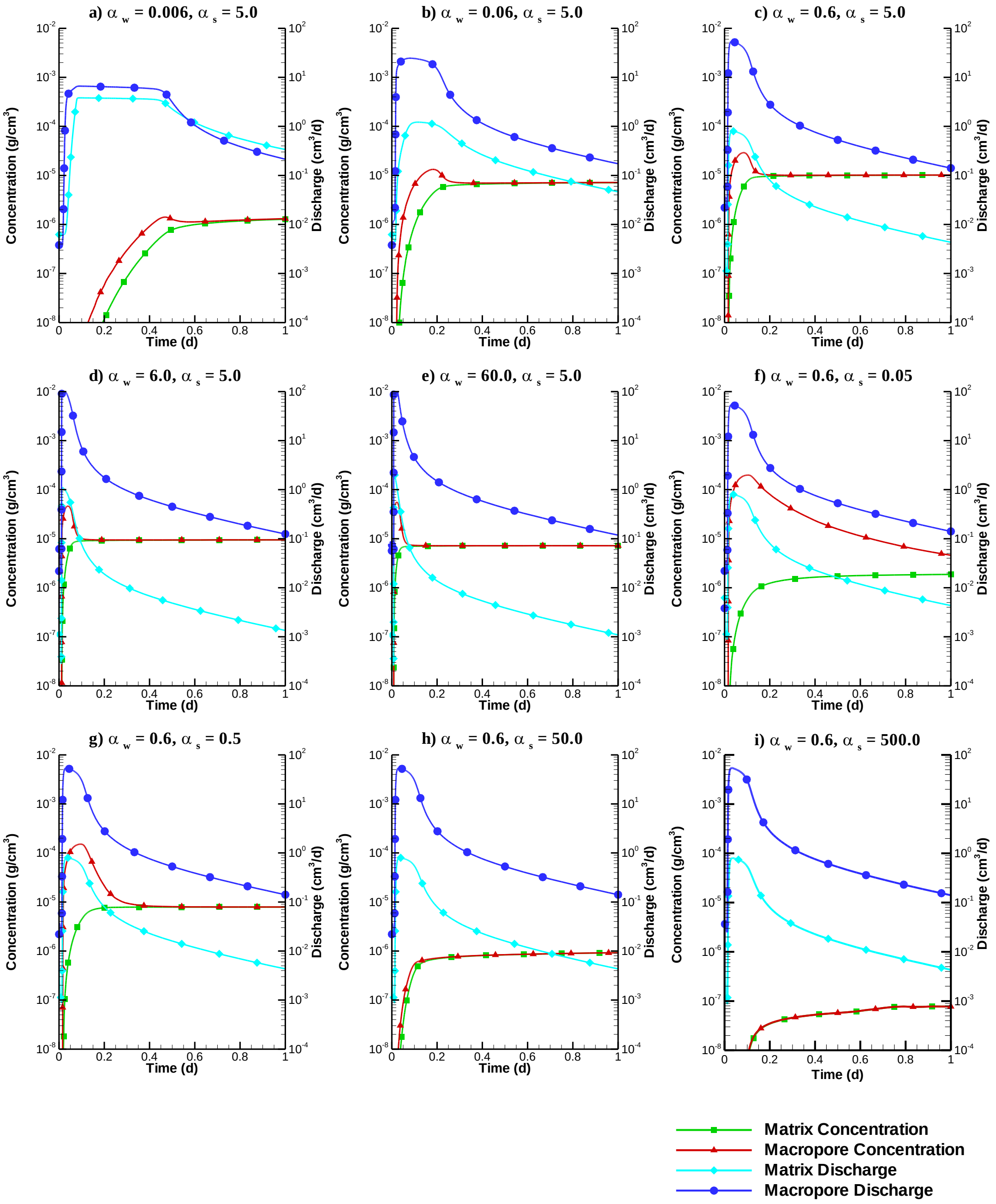

Figure I.2. NH_4 breakthrough curves and water drainage rates for the soil matrix and macropore continuums for each of the nine different water and solute exchange parameter combinations used in the parameter sensitivity analysis.

Appendix J

Density influence on liquid manure movement in macroporous soil.

In order to establish if density factors have the ability to significantly affect the flow and transport of surface applied water and solutes to tile drains and shallow groundwater, a set of numerical simulations was conducted. Results from this work can offer insight into the significance of fluid density on liquid swine manure (LSM) flux to tile drains and groundwater. It is important to note that viscosity effects (which in the case of liquid manure have the potential to be significant) were not included here. Due to current limitations in the ability of HydroGeoSphere (Therrien et al., 2009) to simulate flow and transport of dense fluids in an unsaturated domain, all simulations were conducted using fully saturated conditions so accordingly, results from this work are somewhat of an approximation. To provide insight on how density can affect the numerical solution under a range of different conditions, three sets of simulations were conducted. For all simulations, a 1cm x 1cm x 100cm (X, Y, Z) rectangular grid was used. Vertical (Z axis) discretization was 1cm. Simulations are all based on the movement of a conservative solute. The longitudinal dispersivity coefficient was set to 10 cm and the free-solution diffusion coefficient was set to 20e-6 cm^2 s^{-1}.

J1. Hydrostatic Domain

For the first set of simulations, the domain was initially hydrostatic with equal, type 1 (fixed head) flow boundaries on both the top and bottom. Dense solute was introduced into the domain via type 1, C_o = 1, (fixed concentration) transport boundaries which were active for a 1 day time interval at the beginning of the 20 day total simulation period. All transport which occurred in the first set of simulations was induced by either density driven advection combined with dispersion or, in the simulations where density was not considered, dispersion only. To determine the effect of density gradients on the numerical solution, three different solute densities (2 times, 1.1 times and 1.0 times that of water) were considered. Three different soil types were included in the simulations. These were homogeneous silt loam with a K of 11 cm d^{-1}, homogeneous sand with a K of 322 cm d^{-1}and a macroporous silt loam with matrix K of 11 cm d^{-1} and macropore K of 6000 cm d^{-1}. For the fluid and solute exchange parameters required by the dual-permeability solution that was used to simulate the macroporous silt loam, values were set to 0.6 cm^{-1}d^{-1} and 5 d^{-1} respectively. Figure J.1 shows the vertical solute distribution at t = 0.1 d and t = 2.0 d for each of the three relative densities considered.

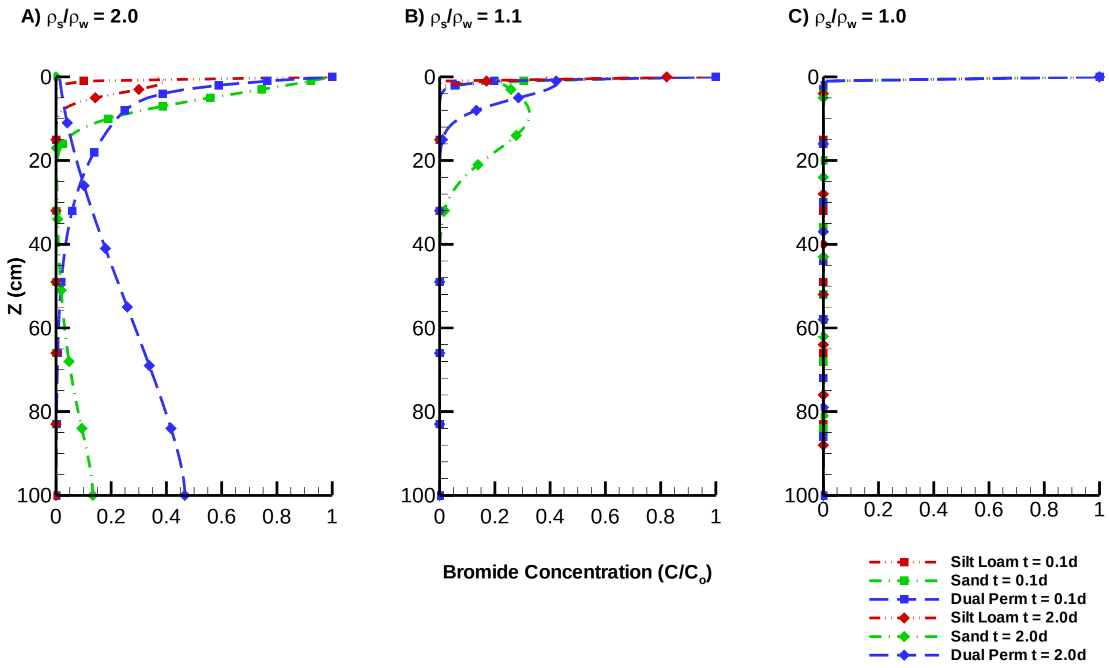

Figure J.1. Vertical solute distribution within an initially hydrostatic domain for infiltrating fluids with densities of (A) 2, and (B) 1.1 times that of water (C). Time intervals of 0.1 and 2.0 days are presented in each plot, for each of the three soil types.

Results presented in Figure J.1 show that in a saturated, initially hydrostatic flow field, dense fluid can effectively sink over relatively short time periods. Figure J.1 a) and b) shows that the amount of solute distribution is strongly dependent on density and soil type with the greatest amount of density driven solute flux occurring in the macroporous silt loam and sand soils with mixtures that have a density twice that of water. Figure J.1 c) shows that molecular dispersion effects had very little influence on mass distribution. If LSM is considered to have a density ~10% greater than water, such as the case in Figure J.1 B), it is unlikely that density effects would significantly increase the rate of LSM flux to tile drains under hydrostatic conditions.

J2. Steady-state Flow – Unit Gradient

For the second set of simulations, the domain was initially flowing under steady-state conditions with a unit hydraulic gradient imposed by type 1 boundary conditions top and bottom. Transport boundary conditions, density gradients and soil types were the same as those used in the first set of simulations. Because of the comparatively fast solute transport times through the domain (relative to the simulations in section J1), the results, which are shown in Figure J.2, are plotted as concentration observed at the bottom of the domain vs. time.

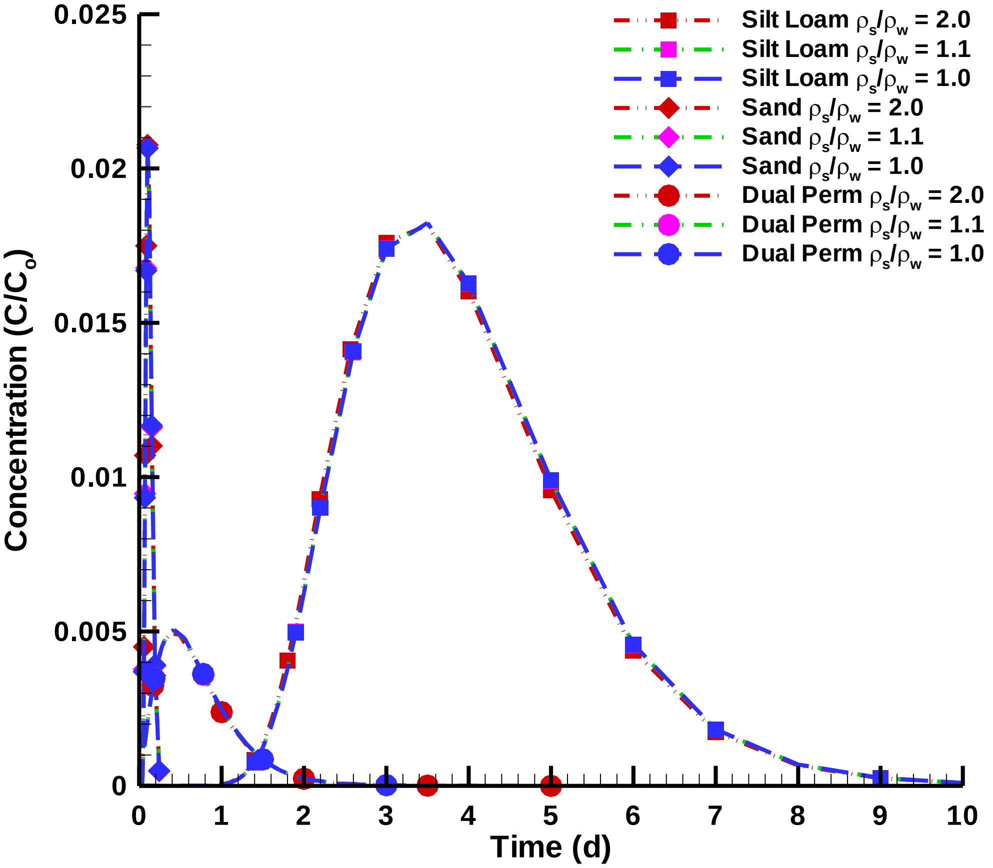

Figure J.2. Solute concentration as observed at the bottom of the domain vs. time for each of the three soil types and each of the three density gradients. A unit hydraulic gradient was imposed across the domain.

Figure J.2 shows that under steady-state flow conditions imposed by a unit gradient in a saturated domain, density has little noticeable effect on solute flux. It is therefore unlikely that density would affect LSM flux when flow is driven by gravity induced hydraulic gradients within a soil profile (regardless of soil type).

J3. Steady-state Flow – 0.1 Gradient

Simulations described in section J3 are similar to those in section J2 with the exception that the hydraulic gradient was reduced by a factor of 10, from 1 to 0.1. Results are again plotted as time vs. concentration along the bottom boundary of the domain and are presented in Figure J.3.

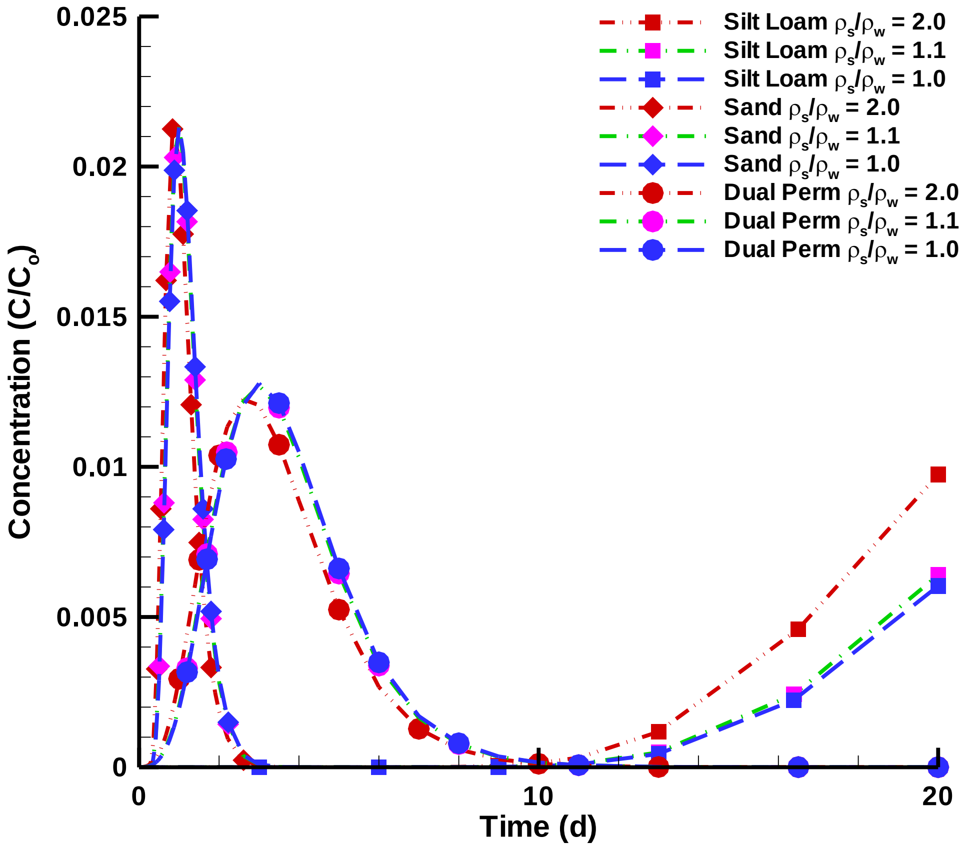

Figure J.3. Breakthrough curves as observed at the bottom of the domain with a 0.1 hydraulic gradient.

When the results shown in Figure J.3 are compared to the results shown in Figure J.2 it is apparent that the relative influence of density on solute flux increases when ambient fluid velocity decreases. However, there is still no indication that density effects could significantly increase the rate at which LSM reaches tile drains.